



Université
de Toulouse

THÈSE

En vue de l'obtention du

DOCTORAT DE L'UNIVERSITÉ DE TOULOUSE

Délivré par l'Université Toulouse III – Paul Sabatier
Discipline ou spécialité : *Sciences et Génie des Matériaux*

Co-tutelle avec l' Universidade Federal do Rio Grande Do Sul

Présentée et soutenue par **Mônica Jung de Andrade**
Le *05 octobre 2010*

**Titre: STUDY OF ELECTRICAL PROPERTIES OF 2- AND 3-
DIMENSIONAL CARBON NANOTUBES NETWORKS**

JURY

<i>S. BINOTTO FAGAN</i>	<i>Professeur</i>	<i>Centro Univ. Franciscano, UNIFRA</i>	<i>Rapporteur</i>
<i>K. MASENELLI-VARLOT</i>	<i>Professeur</i>	<i>Inst. Univ. France, INSA de Lyon</i>	<i>Rapporteur</i>
<i>C. de FRAGA MALFATTI</i>	<i>Professeur</i>	<i>Univ. Federal do Rio Grande Do Sul</i>	<i>Examineur</i>
<i>J.M. HOHEMBERGER</i>		<i>Petróleo Brasileiro, PETROBRAS</i>	<i>Examineur</i>
<i>L.A. FERREIRA COELHO</i>	<i>Professeur</i>	<i>Univ. do Estado de Santa Catarina</i>	<i>Examineur</i>
<i>C.P. BERGMANN</i>	<i>Professeur</i>	<i>Univ. Federal do Rio Grande Do Sul</i>	<i>Directeur de thèse</i>
<i>A. PEIGNEY</i>	<i>Professeur</i>	<i>Université de Toulouse</i>	<i>Directeur de thèse</i>
<i>C. ESTOURNES</i>	<i>Dir. Recherches</i>	<i>CNRS, Toulouse</i>	<i>Directeur de thèse</i>

Ecole doctorale : *Sciences de la Matière*
Unités de Recherche : *CIRIMAT Institut Carnot*
Directeurs de Thèse : *A. Peigney, C. Estournés, C.P. Bergmann*



Université
de Toulouse

THÈSE

En vue de l'obtention du

DOCTORAT DE L'UNIVERSITÉ DE TOULOUSE

Délivré par l'université Toulouse III – Paul Sabatier
Discipline ou spécialité : Sciences et Génie des Matériaux

Co-tutelle avec l' Universidade Federal do Rio Grande Do Sul

Présentée et soutenue par Mônica Jung de Andrade
Le 05 octobre 2010

**Titre: STUDY OF ELECTRICAL PROPERTIES OF 2- AND 3-
DIMENSIONAL CARBON NANOTUBES NETWORKS**

JURY

S. BINOTTO FAGAN	Professeur	Centro Univ. Franciscano, UNIFRA	Rapporteur
K. MASENELLI-VARLOT	Professeur	Inst. Univ. France, INSA de Lyon	Rapporteur
C. de FRAGA MALFATTI	Professeur	Univ. Federal do Rio Grande Do Sul	Examineur
J.M. HOHEMBERGER		Petróleo Brasileiro, PETROBRAS	Examineur
L.A. FERREIRA COELHO	Professeur	Univ. do Estado de Santa Catarina	Examineur
C.P. BERGMANN	Professeur	Univ. Federal do Rio Grande Do Sul	Directeur de thèse
A. PEIGNEY	Professeur	Université de Toulouse	Directeur de thèse
C. ESTOURNES	Dir. Recherches	CNRS, Toulouse	Directeur de thèse

Ecole doctorale : Sciences de la Matière
Unités de Recherche : CIRIMAT Institut Carnot
Directeurs de Thèse : A. Peigney, C. Estournés, C.P. Bergmann

MINISTÉRIO DA EDUCAÇÃO
UNIVERSIDADE FEDERAL DO RIO GRANDE DO SUL

Escola de Engenharia
Programa de Pós-Graduação de Engenharia de Minas, Metalúrgica e de
Materiais – PPGE-3M

STUDY OF ELECTRICAL PROPERTIES OF 2- AND 3-
DIMENSIONAL CARBON NANOTUBES NETWORKS

Mônica Jung de Andrade

Thesis in co-tutelle to obtain the title of Doctor in Engineering

Porto Alegre
2010

MINISTÉRIO DA EDUCAÇÃO
UNIVERSIDADE FEDERAL DO RIO GRANDE DO SUL

Escola de Engenharia
Programa de Pós-Graduação de Engenharia de Minas, Metalúrgica e de
Materiais – PPGEM

**STUDY OF ELECTRICAL PROPERTIES OF 2- AND 3-
DIMENSIONAL CARBON NANOTUBES NETWORKS**

Mônica Jung de Andrade
Mestre em Engenharia

Thesis presented to the Programa de Pós-Graduação em Engenharia de Minas, Metalúrgica e de Materiais – PPGE-3M, as part of the requirements to obtain the title of Doctor in Engineering.

Area of concentration: Science and Technology of Materials.

Porto Alegre
2010

This thesis was judged in order to obtain the title of Doctor in Engineering, in the area of Science and Technology of Materials and approved in its final format by the Thesis Advisor and Board of Examiners of the Course of Post-graduation.

Thesis Advisor at UFRGS (Brazil): Prof. Dr. Carlos Pérez Bergmann

Thesis Advisor at UPS (France): Prof. Dr. Alain Peigney
Dr. Claude Estournès

Board of Examiners: Prof. Dr. Karine Masenelli-Varlot
Prof. Dr. Solange Binotto Fagan
Prof. Dr. Célia de Fraga Malfatti
Dr. João Marcos Hohemberger
Prof. Dr. Luiz Antônio Ferreira Coelho

Prof. Dr. Carlos Pérez Bergmann
Coordinator of PPGE-3M

ACKNOWLEDGMENTS

First of all, I am in really debt with my family and my boyfriend, who generously understood my absences and supported me along all the period of this work even at separated continents for long periods. Even without knowing, they were many times my incentive to persue my dreams through their example of lifes and this work I dedicate to them.

I deeply acknowledge the opportunities of learning research with so many special people that generously received me in their laboratories and Universities:

Prof. Alain Peigney, Dr.Claude Estournès and Dr. Alicia Weibel for sharing their knowledge and teaching me that research need patience and persistence. Their scientific rigidity and attention along all the period at Université Paul Sabatier (Toulouse, France) and during the writing/correction of this manuscript greatly affected my formation and are acknowledged. Their criterious revising of this work favoured great improvements on it. I also acknowledge Prof. Alain Peigney and Dr. Alicia Weibel for the scanning electron microscope imaging.

Dr. Siegmar Roth for his enthusiasm for teaching science, culture and history. Dr. Viera Skakalova for her cherished endearment and concern. The nice moments at Max Planck Institut für Festkörperforschung (Stuttgart, Germany) with intercultural exchanges in the group and unequal opportunities given to develop ideas and discussions strongly contributed to my formation.

Prof. Carlos Pérez Bergmann, from Universidade Federal do Rio Grande do Sul (Porto Alegre, Brazil), to believe, support and incentive my work since undergraduate studies, giving no limits to the curious student with many dreams.

Thank you as well for all my friends and colleagues from Brazil and abroad for their support and nice environment of working: my colleagues at LACER and the multicultural families of the unforgettable 4C11 in Stuttgart and the brotherhood 0169 in Toulouse. I also thank all the technicians from Max Planck Institut für Festkörperforschung (Stuttgart, Germany) and from CIRIMAT/CNRS/Université Paul Sabatier (Toulouse, France) that helped me during many analyses and also in the spark-plasma sintering.

SUMMARY

LIST OF FIGURES	XV
LIST OF TABLES	XXI
LIST OF ABBREVIATIONS	XXIII
GLOSSARY	XXVII
ABSTRACT	XXIX
RESUMÉ	XXXI
RESUMO	XXXIII
1 INTRODUCTION	35
1.1 JUSTIFICATIVE	39
2 OBJECTIVE	41
2.1 GENERAL OBJECTIVE	41
2.2 SPECIFIC OBJECTIVES	41
3 LIMITATIONS OF THE RESEARCH WORK	43
4 BIBLIOGRAPHIC REVISION	45
4.1 CNT - STRUCTURE, TYPE, SYNTHESIS AND CHARACTERIZATION	45
4.1.1 <i>Structure and types of carbon nanotubes</i>	45
4.1.2 <i>Synthesis of carbon nanotubes</i>	47
4.1.3 <i>Characterization of carbon nanotubes and its networks</i>	51
4.2 PRODUCTION OF 2D AND 3D CNTNS	56
4.2.1 <i>2D CNTNs</i>	56
4.2.2 <i>3D CNTNs in insulator matrices</i>	58
4.3 CNTs-SiO ₂ NANOCOMPOSITES	59
4.3.1 <i>Dispersion</i>	59
4.3.2 <i>Densification</i>	60
4.3.3 <i>SPS method</i>	61
4.4 ELECTRICAL PROPERTIES OF CARBON NANOTUBES AND ITS NETWORKS.....	63
4.4.1 <i>Intrinsic properties of CNTs affecting their electrical conductivity</i>	66
4.4.2 <i>Properties of CNTNs affecting the electrical conductivity</i>	70
5 MATERIALS AND METHODS	79
5.1 CARBON NANOTUBES	79
5.1.1 <i>Commercial CNTs</i>	79
5.1.2 <i>Synthesis and extraction of DWCNT</i>	80
5.2 PRODUCTION OF CNTNS IN 2D AND 3D SYSTEMS.....	81
5.2.1 <i>Two dimensional systems</i>	81
5.2.2 <i>Three dimensional systems</i>	84
5.3 CHARACTERIZATION METHODS	87
5.3.1 <i>Spectroscopic and optical characterizations</i>	88
5.3.2 <i>Zeta potential</i>	89
5.3.3 <i>Electron and Atomic Force Microscopies</i>	89
5.3.4 <i>Electrical conductivity and properties of percolation</i>	90
5.3.5 <i>Carbon content</i>	93
5.3.6 <i>Specific surface area</i>	93
5.3.7 <i>Density determination</i>	93
5.3.8 <i>X-ray diffraction</i>	94
6 RESULTS AND DISCUSSIONS	95
6.1 CHARACTERIZATION OF CNTS	95
6.1.1 <i>Summary of characterization of the commercial CNTs</i>	108
6.2 CNTNS IN 2D SYSTEM	110
6.2.1 <i>Summary of 2D CNTNs</i>	118

6.3	CNTNs IN 3D SYSTEM: DWCNT-SiO ₂ NANOCOMPOSITES	119
6.3.1	<i>DWCNTs synthesis and characterization</i>	119
6.3.2	<i>DWCNTs Functionalization</i>	130
6.3.3	<i>Nanocomposite powders</i>	145
6.3.4	<i>Dense F-DWCNT-SiO₂ Nanocomposites</i>	150
6.3.5	<i>Summary of 3D CNTNs</i>	187
CONCLUSIONS		193
ATTACHMENTS		196
REFERENCES		204

LIST OF FIGURES

Figure 4.1 (A) Vectors \vec{C}_n and \vec{T} defined by the indices (n,m) [52]; (B) the three different structures of CNTs: armchair, zigzag and chiral.....	47
Figure 4.2 Typical Raman spectrum from SWCNT bundles.....	52
Figure 4.3 Schematic diagram of a CNTN immersed into a matrix: (A) with good compatibility with the matrix and fully densified; (B) with good compatibility with the matrix, but with remaining porosity; (C) with bad interface interaction with the matrix and non-ideally dispersed.....	60
Figure 4.4 Schematic diagram of SPS device.....	62
Figure 4.5 Pathway of CNTs connected, where L^{ce} is the equivalent straight length of each CNT, L^p is the length of the connected CNTs path and L^{pe} is the equivalent length of the CNTs path [35].	67
Figure 4.6 Schematic representation of the CNT structure after an oxidation process.	70
Figure 4.7 Schematic diagram of interacting CNTs bundles in a γ angle (top) and in parallel (bottom), where L^B and d^B are the length and width of the bundles [150].	75
Figure 5.1 Schematic diagram of the post-growth techniques used in this work to prepare 2D CNTNs: spray-coating, dip-coating, filtration method and electrophoretic deposition.	83
Figure 5.2 Schematic diagram of the steps for the preparation of 3D CNTNs using <i>F</i> -DWCNTs embedded in silica matrix SiO ₂ : (i) functionalization of DWCNTs; (ii) dispersion of the <i>F</i> -DWCNTs into acid aqueous solution with the aid of probe sonication; (iii) <i>in-situ</i> production of silica (precursor: tetraethylorthosilicate, TEOS) over <i>F</i> -DWCNTs through organic sol-gel route; (iv) calcination of the nanocomposite xerogel; (v) densification of the calcinated powder through spark-plasma sintering (SPS).....	85
Figure 5.3 Schematic diagram of the overall experimental procedure to produce CNTNs in 2D (spray-coating, dip-coating, filtration method and electrophoretic deposition) and 3D - in liquid with chloroform or in silica prepared by sol-gel and densified by spark-plasma sintering (SPS).....	88
Figure 5.4 Schematic diagram of apparatus used for electrical measurements of (a) 3D CNTNs in a liquid electric insulator matrix; (b) 2D CNTNs; (c) 3D CNTNs embedded in silica matrix.....	91
Figure 5.5 Configuration for the electrical conductivity measurements of CNTNs in 2D systems using Pd/Au (200/2000 Å) electrodes that were deposited by the technical service of Max Planck Institute for Solid State Research.	92
Figure 6.1 TEM micrographs of SWCNT (mainly gathered in bundles). Black arrows as other carbon impurities (disordered carbon) and blue arrows as metal NPs. 96	96

Figure 6.2 TEM micrographs of (A) MWCNT-I and (B) MWCNT-I-short: Red arrows as defects, black arrows as other carbon impurities and blue arrows as metal NPs.	96
Figure 6.3 TEM micrographs of MWCNT-II: Red arrows/circle as defects, black arrows as other carbon impurities and blue arrows as metal NPs.....	96
Figure 6.4 Raman spectra of CNTs at $\lambda = 632.8$ nm (normalized to D*): (A) SWCNT (inset: <i>RBM</i>); (B) MWCNT-I, MWCNT-I-short, MWCNT-II and graphite.....	98
Figure 6.5 Electrical conductivity of the carbon suspensions in chloroform at 1.5 V DC (0.104 V/cm) during sonication: carbon content (mg/mL) versus electrical conductivity. Both in logarithmic scale.....	101
Figure 6.6 Electrical conductivity of the carbon suspensions in chloroform at 1.5 V DC (0.104 V/cm) during sonication: vol.% of nanomaterial (log scale) versus electrical conductivity (log scale). Inset: vol.% of nanomaterial (linear scale) versus electrical conductivity (log scale).	102
Figure 6.7 Conductivity versus reduced volume for HiPco SWCNTs (both in logarithmic scale). Below 1 mg/mL of CNTs (reduced volume = 3.7) the conductivity follows a linear correlation. The CNT concentration (mg/mL) is indicated for each point.	105
Figure 6.8 Measured conductivities of HiPco SWCNT dynamic 3D CNTNs in chloroform in comparison to calculated conductivities by modified rule of mixtures considering an aspect ratio (L/d) of 7000 and $\beta=0.2$	106
Figure 6.9 Surface resistance (log scale) versus transmittance of a commercial ITO and other data from literature [136] in comparison to several CNTNs prepared through different techniques using similar material of literature (HiPco SWCNTs): dip-coating (DC), filtration method (FM), spray-coating (SC) and electrophoretic deposition (ED). Eye-guide auxiliary line to visualize the tendency.....	111
Figure 6.10 FESEM micrograph at 25 kx of magnification of a dip-coated CNTN (red arrow: CNT loop).....	112
Figure 6.11 Transmittance (%) versus concentration per area of several CNTNs prepared through different techniques with HiPco SWCNTs in comparison with other data from literature using similar material [136].	113
Figure 6.12 Surface conductance (log scale) versus concentration per area of several CNTNs prepared through different techniques with HiPco SWCNTs in comparison with other data from literature using similar material [136].....	113
Figure 6.13 Surface conductance (log scale) versus reduced concentration (log scale) of several CNTNs prepared through different techniques with HiPco SWCNTs in comparison with other data from literature using similar material [136]. Inset: Power law fitting of the surface conductance (log scale) of SWCNT random 2D networks versus reduced concentration to obtain the constant of dimensionality.	114
Figure 6.14 Schematic diagram (note: CNTs and surfactant are not in the real proportions) of the effect in the electrical conductivity of CNTNs with and without surfactant.	115
Figure 6.15 Surface resistance (log scale) versus transmittance of the pioneer work of M.W.Rowell <i>et al.</i> [83] reported using Arc-Discharge SWCNTs (AD-SWCNTs)	

in comparison to the CNTNs prepared by filtration method (FM) using different commercial CCVD CNTs: HiPco SWCNT, DWCNT-I and MWCNT-I.....	117
Figure 6.16 Possible applications for ultrathin CNTNs produced in this work (based on [136])......	118
Figure 6.17 XRD patterns from DWCNTs: (A) before and (B) after extraction of magnesia (DWCNT), with an inset (C) of the filtrated solution after extraction with chloridric acid.	121
Figure 6.18 TEM micrographs of home-made DWCNTs after extraction with HCl. Red arrows as defects (“kinks”) and blue arrows as metal NPs.....	122
Figure 6.19 Raman spectra at different regions from DWCNT-C (DWCNT sample with the highest average $I_{D/G}$: 17%). Inset left: <i>RBM</i> spectra at different regions (coloured lines) and average <i>RBM</i> (black line). Inset right: average Raman spectrum.	124
Figure 6.20 Electrical conductivity of the carbon suspensions (volume percent) in chloroform at 1.5 V DC (0.104 V/cm) during sonication (dynamic network) of different batches of DWCNTs.....	126
Figure 6.21 Measured conductivities of DWCNT-E dynamic 3D CNTNs (used for wet route) in chloroform in comparison to calculated conductivities (modified rule of mixtures) considering an aspect ratio (L/d) of 23300.	128
Figure 6.22 Conductivity <i>versus</i> reduced volume for DWCNT-E (both in logarithmic scale). The CNT concentration (mg/mL) is indicated for each point.	129
Figure 6.23 Zeta potential curve of CNTs non-functionalized (DWCNTs) and functionalized (using a reflux step) with acid nitric (<i>F</i> -DWCNTs/ HNO_3), with acids nitric and sulphuric (<i>F</i> -DWCNTs/ $HNO_3/2SO_4$) and with acids nitric, sulphuric and chloridric (<i>F</i> -DWCNTs/ $HNO_3/H_2SO_4/HCl$).	131
Figure 6.24 Qualitative stability test at pH 3.6 for functionalization with HNO_3/H_2SO_4 -HCl (aqueous suspension with ~1 mg/mL) at different times: T_0 is just after preparation of suspension, T_1 is after 24h, T_2 is after 48h and T_3 is after one week.	133
Figure 6.25 <i>F</i> -DWCNT: (a) XRD pattern of the material after rinsing with deionized water and (b) first filtrated solution after the chemical oxidation step.	134
Figure 6.26 TEM images of (a) <i>F</i> -DWCNT-B and (b) <i>F</i> -DWCNT-E (material used for wet route). Red arrows as defects (“kinks”), black arrows as other carbon impurities and blue arrows as metal NPs.	135
Figure 6.27 Average Raman spectra at $\lambda = 632.8$ nm (normalized to D^*) of <i>F</i> -DWCNT samples from different batches in comparison to original material. Inset: upshift in D^* after functionalization.....	137
Figure 6.27 (<i>Continued</i>)	138
Figure 6.28 Normalized (by the mass and then by $C=C$ peak at $\sim 1630cm^{-1}$) Infrared spectra of DWCNTs-II before (black line) and after (red line) chemical oxidation from (a) DWCNTs-E, (b) DWCNTs-B and (c) DWCNTs-C.....	141
Figure 6.29 Electrical conductivity of the carbon suspensions in chloroform at 1.5 V DC (0.104 V/cm) during sonication of different batches of <i>F</i> -DWCNTs: dried in	

stove (F-DWCNT-B and F-DWCNT-C) and dried in dessicator (F-DWCNT-D and F-DWCNT-E).....	143
Figure 6.30 FESEM image of a nanocomposite powders D (a) and W (b) prepared using dry (2.97 vol.% of average carbon content) or wet (6.43 vol.% of average carbon content) DWCNTs, respectively.....	147
Figure 6.31 Raman spectra at $\lambda = 632.8$ nm (normalized to D^*) of a nanocomposite powder obtained by (A) dry route and (B) wet route (containing 6.43 vol.% of carbon): coloured lines are spectra from different regions of the same sample and black line is the average spectra.	149
Figure 6.32 SPS parameters used to densify the W set of nanocomposites. Inset: electric current applied during SPS densification.	157
Figure 6.33 Raman spectra at $\lambda = 632.8$ nm normalized by G band done in different regions of the sample (coloured lines as inset) for each sample from dry route: (a) D1 (0.22 wt.%); (b) D2 (0.22 wt.%); (c) D3 (0.22 wt.%); (d) D4 (0.29 wt.%); (e) D5 (2.44 wt.%). Black line: Average Raman spectra of the respective densified F-DWCNT-SiO ₂ nanocomposites.....	160
Figure 6.33 (Continued)	161
Figure 6.33 (Continued)	162
Figure 6.34 Raman spectra at $\lambda = 632.8$ nm normalized by G band done in different regions of the sample (colored lines as inset) for each sample from wet route: (a) W2 (0.15 wt.%); (b) W3 (0.47 wt.%); (c) W4 (0.48 wt.%); (d) W6 (5.32 wt.%). Average Raman (black line) spectra of samples from respective densified F-DWCNT-SiO ₂ nanocomposites.	164
Figure 6.35 FESEM image of a fractured surface of F-DWCNT-SiO ₂ nanocomposite obtained by dry route: (a,b) sample D1 (0.22 wt.%); (c) sample D2 (0.22 wt.%); (d) sample D3 (0.22 wt.%); (e,f) sample D4 (0.29 wt.%); (g,h) sample D5 (2.44 wt.%).	167
Figure 6.36 (A) FESEM image of a fractured surface of F-DWCNT-SiO ₂ (0.29 wt.% of carbon) nanocomposite obtained by dry route; (B) Evidence of wettability of the F-DWCNT by the silica matrix.	168
Figure 6.37 FESEM images of the fracture surface of F-DWCNT-SiO ₂ nanocomposites obtained through the wet route: (a) sample W1 (0.12 wt.%); (b) sample W3 (0.47 wt.%);(c,d) sample W4 (0.48 wt.%); (e,f) sample W5 (1.27 wt.%); (g,h) sample W6 (5.32 wt.%).	172
Figure 6.38 Electrical conductivity measured for the F-DWCNT-silica nanocomposites (D and W series) measured by two-probe method.....	177
Figure 6.39 Electrical conductivity measured for the F-DWCNT-silica nanocomposites measured by two-probe method (straight line below) in comparison to expected from modified rule of mixtures (dash-dot line above) using a $L/d=23300$ and $\beta=0.2$ (Equation 4.13b) and its probability of percolation (Equation 4.2), considering critical volume fraction (Φ_{CVF}) of F-DWCNT measured by dynamic percolation (0.003 vol.%).	179
Figure 6.40 (A) Electrical conductivity <i>versus</i> various CNT content (vol.%) for CNT-ceramic nanocomposites (non-aligned CNTNs) in insulator matrices (<i>note: assuming densities of 3.98 g/cm³ and 2.23 g/cm³ for alumina and borosilicate,</i>	

<i>respectively</i> [98]): <i>F</i> -DWCNT-SiO ₂ nanocomposites from this work in comparison with data from literature [29,30,94,99,100b,126,190-196,199,200]. (B) Same enlarged graph for the low contents.	186
Figure 0.1 Schematic diagram of the molecule of sodium dodecyl sulfate, SDS.....	196
Figure 0.2 Typical spectral transmission including Fresnel reflection loss. The uppermost nearly straight line indicates the calculated Fresnel reflection loss of two uncoated surfaces. Path length of 10 mm.	197
Figure 0.3 Schematic diagram of the reaction of silanization of the surface of silica glass substrate by reacting with 3.Aminopropyltriethoxysilan (APS).	197
Figure 0.4 Schematic diagram of the reaction of silanization of the surface of silica glass substrate by reacting with 3.Aminopropyltriethoxysilan (APS).	198
Figure 0.5 Normalized electrical conductivity (~1 mg/mL) of the carbon suspensions in chloroform at 1.5 V DC (0.104 V/cm) during sonication of HiPco-SWCNT and DWCNT along time.	199
Figure 0.6 Conductivity of MWCNT-I suspensions in chloroform <i>versus</i> its reduced volume (both in logarithmic scale). The CNT concentration (mg/mL) is indicated for each point.	199
Figure 0.7 Conductivity of MWCNT-I-short suspensions in chloroform <i>versus</i> its reduced volume (both in logarithmic scale). The CNT concentration (mg/mL) is indicated for each point.	200
Figure 0.8 Conductivity of MWCNT-II suspensions in chloroform <i>versus</i> its reduced volume (both in logarithmic scale). The CNT concentration (mg/mL) is indicated for each point.	200
Figure 0.9 (A) AFM image (height data type with Z range of 30 nm) evidence of alignment of dip-coating first adsorbed layer (blue arrow is the direction of dipping and black arrow shows CNT loop); (B) and increase of bundling with number of dippings.....	201
Figure 0.10 Infrared spectra of KBr pill without CNTs.	202
Figure 0.11 XRD pattern of a pure silica sample with apparent slight beginning of crystallization (black arrow).	202
Figure 0.12 XRD patterns of the <i>F</i> -DWCNT-SiO ₂ materials after consolidation by SPS composites obtained by wet route.	203

LIST OF TABLES

Table 1.1 Main properties of individual CNTs.....	36
Table 4.1 Examples of carbon structures with different aspect ratio and their percolation as 3D network in insulator matrices.....	65
Table 5.1 Main characteristics of the commercial CNTs given by the producers: aspect ratio measured by producers (TEM and SEM), carbon content wt.% (measured by thermal gravimetric analysis, TGA under air, or elementary analysis, EA) and other impurities (not mentioned or by ICP, inductively coupled plasma)	80
Table 6.1 Main characteristics of the CNTs studied in this work: carbon content wt.% (measured by flash-combustion method or informed by producer that measured by thermal gravimetric analysis or elementary analysis), aspect ratio measured by producers (TEM and SEM) and calculated D/G ratios measured by Raman spectroscopy ($\lambda = 632$ nm) for the carbon materials in comparison with a graphite.....	99
Table 6.2 Observed aspect ratios for various commercial carbon materials, in comparison to the calculated aspect ratios through the observed critical volume.	104
Table 6.3 Electrical conductivity of free standing papers produced from different carbon materials, compared with the same materials' conductivities in liquid medium in the dynamic mode, at the highest concentration measured (around 5 mg/mL).....	108
Table 6.4 Comparison of the average roughnesses of commercial ITO over glass with CNTNs using HiPco SWCNTs and prepared by different techniques (all with similar transparency, around 85 % at 550 nm): dip-coating (DC), filtration method (FM), spray-coating (SC) and electrophoretic deposition (ED). Size of each analyzed area: $210.25 \mu\text{m}^2$	116
Table 6.5 Main characteristics of the DWCNTs studied in this work: average carbon content wt.% (measured by flash-combustion method: two measurements for each sample) and calculated D/G ratios measured by Raman spectroscopy ($\lambda = 632$ nm) for the carbon materials in comparison with a graphite.....	125
Table 6.6 Main characteristics of the DWCNTs after their functionalization: average carbon content wt.% (measured by flash-combustion method: two measurements for each sample) and average $I_{D/G}$ ratios measured by Raman spectroscopy ($\lambda = 632$ nm) for the carbon materials in comparison to original material.	139
Table 6.7 Examples of studies of sintering parameters by SPS with pure silica: silica powder, SPS parameters, final density by Archimedes, relative density (considering amorphous silica) and general aspect.	153
Table 6.8 Densities of F-DWCNT silica nanocomposites measured by Archimedes method with their statistic deviation between brackets in comparison to their SPS parameters, carbon content and relative density (by considering full silica amorphous).....	156

Table 6.9 D and W samples microstructural analysis (selected only “clean” type of fracture for these analyses).....	171
Table 6.10 Electrical conductivity of F-DWCNT-SiO ₂ nanocomposites obtained by the dry (D samples) and wet (W samples) routes measured by two-probe method.	174
Table 0.1 Main characteristics of substrate used for the deposition of 2D CNTNs..	196

LIST OF ABBREVIATIONS

CNT(s)	Carbon nanotube(s).
CNF(s)	Carbon nanofiber(s).
SWCNT(s)	Single-walled Carbon nanotube(s).
DWCNT(s)	Double-walled Carbon nanotube(s).
MWCNT(s)	Multi-walled Carbon nanotube(s).
CNTN(s)	Carbon nanotubes network(s).
2D	Two-dimensional
3D	Three-dimensional
vol.%	Volume per cent
wt.%	Weight per cent
(C)CVD	(Catalytical) Chemical Vapor Deposition.
NP(s)	Nanoparticle(s).
θ	Chiral angle.
\vec{C}_h	Chiral vector.
\vec{T}	Translational symmetry vector (parallel to tube axis).
\vec{a}_1 and \vec{a}_2	Unit vectors of the graphene.
<i>RBM</i>	Radial Breathing mode.
<i>D</i>	“Diamond” or “defect” mode.
<i>G</i>	Tangential mode.
<i>D*</i>	<i>D*</i> -band also known as second order <i>G'</i> -band; overtone of <i>D</i> mode.
$I_{D/G}$	Ratio between the intensities of <i>D</i> and <i>G</i> modes.
I_{D/D^*}	Ratio between the intensities of <i>D</i> and <i>D*</i> modes.

TGA	Thermogravimetric analysis.
EA	Elementary analysis.
AFM	Atomic force microscopy.
(HR)TEM	(High Resolution) Transmission Electron Microscopy.
(FE)SEM	(Field Emission) Scanning Electron Microscopy.
FTIR	Fourier Transform Infrared Spectroscopy.
ICP	Inductively Coupled Plasma
C _n	Carbon content in weight per cent.
SG	Specific gravity.
W	Weight of the sample. Subscripts <i>air</i> and <i>water</i> refer to the measurement in air and in water, respectively.
XRD	X-ray diffraction.
PU	Polyurethane.
PC	Polycarbonate.
PI	Polyimide.
PET	Poly(ethylene terephthalate).
PVDF	Poly(vinylidene fluoride).
<i>HiPco</i>	High Pressure Carbon Monoxide.
SDS	Sodium dodecyl sulphate.
<i>F-CNT(s)</i>	Functionalized Carbon nanotube(s).
TEOS	Tetraethylorthosilicate.
<i>r</i>	Molar ratio of water per tetraethylorthosilicate.
ITO	Indium tin oxide (solid solution of 90% In ₂ O ₃ and 10% SnO ₂ by weight).
SC	Spray-coating.
DC	Dip-coating.

ED	Electrophoretic deposition.
FM	Filtration method.
SPS	Spark-Plasma Sintering.
HIP	High-pressure cold quasi-isostatic pressing.
HP	Hot-pressing.
ξ	Probability at which CNTs percolate.
$\Phi_{CVF} (A_{CAF})$	Volume (area) fraction of carbon nanotubes in which the percolation process begins (also called critical volume fraction).
$\Phi_F (A_F)$	Volume (area) fraction of carbon nanotubes.
P_{CNT}	Carbon nanotubes density per area (CNT/ μm^2).
P_{CNT}^C	Critical carbon nanotubes density per area (CNT/ μm^2).
$\sigma (R)$	Electrical conductivity (resistivity). Subscripts <i>C</i> , <i>M</i> and <i>F</i> refer to the composite, matrix and filler (in this case, CNTs), respectively.
$\sigma_0 (R_0)$	Constant of proportionality: electrical conductivity (resistivity) of the filler.
σ_{MAX}	Maximal electrical conductivity.
V	Volume of electrical conductive “fillers” “(in this case, the carbon nanotubes).
τ	Critical exponent that represents the dimensionality of the network.
V_{ex}	Total excluded volume. For randomly oriented infinitely thin cylinders it gives a value of 1.4.
V_e	Excluded volume.
N_c	Critical number density of objects in the system.
D	Diameter of the filler.
L	Length of the filler.
D_{AV}	Average diameter of bundles.

L_{AV}	Average length of bundles.
L^{ce}	Equivalent straight length of each CNT.
L^p	Length of the connected CNTs path.
L^{pe}	Equivalent length of the CNTs path.
β	Parameter depends on the orientation of the filler and it is 0.2 if it is a random orientation in a tridimensional volume and considered as 0.35 if its orientation is randomic in the two dimensional plane.
α	Parameter depends on the dimensions of the filler and can be calculated by Equation 0.1.
H	Distance between the electrodes.
A	Area of the electrodes.
W	Length of the electrodes.
R_s	Surface (or sheet) resistance (or resistivity).
T	Optical transmittance of the network.
α_{CNT}	Absorbance coefficient (whose value is $2.875 \times 10^{-6} \mu\text{m}^2$ for a light wavelength of 550 nm, assuming CNTs with 0.5 μm length and diameter of 1.2 nm).
$\rho_{ARCHIMEDES}$	Archimedes density.
$\rho_{GEOMETRICAL}$	Geometrical density.
Agg	Parameter of dispersity related to the size and frequency of aggregates.
Bdl	Parameter of dispersity related to size of bundles.

GLOSSARY

<i>Nanoscale</i>	At least one dimensional scale in the order of nanometer (10^{-9} meters).
<i>Bundles</i>	Integral number N of carbon nanotubes aligned parallel to a common axis, which is termed the bundle axis.
<i>Aggregates</i>	Bundles of carbon nanotubes held together in an disorderly manner.
<i>Buckypaper</i>	Self-standing papers of carbon nanotubes by filtering a solution containing carbon nanotubes, which leads to a compaction of the carbon nanotubes.
<i>Surface resistance</i>	In plane resistance of a square () with contacts at opposite sides, unit is Ω/sq (sometimes $\Omega/$ or Ω or Ω_{sq}). Sometimes the term surface (or sheet) resistivity is used in literature instead of surface (or sheet) resistance.
Ohms per square	Is an alternate common unit (generally denoted " Ω/sq "), which is dimensionally equal to an Ohm, but is exclusively used for sheet resistance. This is an advantage, because a sheet resistance of " 1Ω " could be taken out of context and misinterpreted as a <i>bulk</i> resistance of 1 Ohm, while a sheet resistance of " $1\Omega/\text{sq}$ " cannot be so misinterpreted. The reason for the name "Ohms per square" is that a square sheet with sheet resistance 1 Ohm/square has an actual resistance of 1 Ohm, regardless of the size of the square. (For a square, $L = W$, so $R_S = R$.) The unit can be thought of as, loosely, "Ohms per aspect ratio".
<i>Kinks</i>	Atomic-scale deviations from the perfect hexagonal lattice of carbon nanotubes (CNTs) manifest themselves as 'kinks' at the junctions between

nanotube portions of different diameters. Under certain growth conditions, MWNTs exhibit helical, coil or zig-zag morphologies with kinks connecting adjacent segments, leading to a curvature in the CNT.

ABSTRACT

Two and three dimensional carbon nanotube networks (2D- and 3D-CNTNs) were prepared over silica glass substrate and in silica matrix, respectively. Several types of CNTs (single-, double- and multi-walled carbon nanotubes, SWCNTs, DWCNTs and MWCNTs, respectively) were characterized by transmission electron microscopy, Raman spectroscopy and carbon analysis, while their aptitudes to form a percolating network were compared by measurement of their electrical conductivity in dynamic suspensions in chloroform. The conductivity of SWCNTs and DWCNTs suspensions well follow the power law of the percolation theory, with an exponent close to the theoretical value of a 3D network. The SWCNTs suspensions present the higher maximum normalized conductivity ($3.08 \text{ S}\cdot\text{cm}^2/\text{g}$) whereas the DWCNTs suspensions present the lower percolation thresholds (0.002-0.06 vol.%) which led to choose SWCNTs for the preparation of 2D-CNTNs and DWCNTs for the preparation of CNT-silica nanocomposites (3D-CNTNs).

To produce 2D-CNTNs, SWCNTs aqueous suspensions containing sodium dodecyl sulphate were deposited over amorphous silica substrates using four different techniques : dip-coating, filtration, spray-coating and electrophoretic deposition. Most of the 2D-CNTNs formed a percolating network whose electrical conductivity well followed the power law, with an exponent around 1.29, which is in agreement with theoretical predictions. Dip-coating and electrophoretic deposition provided the smoothest CNTNs and might be an interesting option for solar cell applications. The obtained characteristics of surface conductance and transparency in the UV also demonstrated their possible applications in displays, touch screens, shielding in cathode tubes and electrostatic dissipation.

CNT-silica matrix nanocomposites (3D-CNTNs) were prepared by the sol-gel route, using DWCNTs which were previously submitted to a mild functionalization, their dispersion being carried out by probe sonication. The materials were fully densified by spark-plasma sintering. The dispersion state of CNTs was evaluated by field emission scanning electron microscopy and correlated with the electrical properties. The comparison of two variations in the preparation route (ie: the DWCNT were dried or not after their fonctionnalization) led to a good correlation between the dispersions states (presence and size of CNTs aggregates) and the percolation thresholds. For the "Dry" route, the percolation operates at only 0.35 vol.% DWCNT, which is lower that the values reported for CNT-silica nanocomposites. For the "Wet" one, the more conductive material shows an electrical conductivity (1.56 S/cm) higher than the values reported for similar materials. In spite that the dispersion of CNTS could be still improved, the achieved electrical conductivity of these nanocomposites is still high enough for their use in antielectrostatic or heating applications.

RESUMÉ

Des réseaux de nanotubes de carbone (CNTs) en deux ou trois dimensions (2D- et 3D-CNTNs) ont été préparés respectivement sur substrat de silice amorphe et dans une matrice silice. Plusieurs types de CNTs (mono-, double- et multi-parois, respectivement SWCNTs, DWCNTs et MWCNTs) ont été caractérisés par microscopie électronique à transmission, spectroscopie Raman et analyse élémentaire du carbone, et leurs aptitudes à former un réseau percolant ont été comparées par mesure de la conductivité électrique de suspensions dynamiques de ces CNTs dans le chloroforme. La conductivité des suspensions de SWCNTs et de DWCNTs obéit à la loi de puissance de la théorie de percolation, avec un exposant proche de la valeur théorique d'un réseau 3D. Celle des suspensions de SWCNTs présentent une conductivité normalisée maximale ($3.08 \text{ S.cm}^2/\text{g}$) tandis que celle des suspensions de DWCNTs présente le plus faible seuil de percolation (0.002-0.06 vol.%) ce qui a conduit à choisir les SWCNTs pour la préparation des 2D-CNTNs et les DWCNTs pour la préparation des nanocomposites CNT-silice (3D CNTNs).

Les 2D-CNTNs ont été préparés par dépôt de suspensions aqueuses de SWCNTs contenant du dodecyl sulfate de sodium sur de la silice amorphe, par quatre techniques différentes: trempage, filtration, spray et dépôt électrophorétique. Les 2D-CNTNs forment un réseau percolant dont la conductivité électrique obéit à la loi de puissance, avec un exposant d'environ 1.29, ce qui est en bon accord avec les prédictions théoriques. Les dépôts effectués par trempage et les dépôts électrophorétiques conduisent aux films les plus lisses et peuvent constituer une option intéressante pour des applications dans les cellules solaires. La conductance de surface et la transparence obtenues dans l'UV laissent espérer des applications possibles dans les écrans d'affichage, les écrans tactiles, les tubes cathodiques et les films destinés à dissiper les charges électrostatiques.

Les nanocomposites CNT-silice (3D-CNTNs) ont été préparés par sol-gel, en utilisant des DWCNTs qui furent d'abord soumis à un traitement doux de fonctionnalisation, leur dispersion étant réalisée par sonication avec une sonde. Les matériaux ont été ensuite complètement densifiés par "spark-plasma sintering". Les états de dispersion des CNTs ont été évalués par microscopie électronique à balayage à émission de champ et corrélé aux propriétés électriques. La comparaison de deux variantes de la méthode de préparation (*i.e.*: DWCNT séchés ou non séchés après leur fonctionnalisation) a conduit à une bonne corrélation entre les états de dispersion (présence et taille des agrégats de CNTs) et les seuils de percolation. Pour la voie sèche, la percolation intervient pour seulement 0.35 vol.% DWCNT, ce qui est plus faible que les valeurs publiées pour les nanocomposites CNT-silice. Pour la voie humide, le matériau le plus conducteur présente une conductivité électrique (1.56 S/cm) plus élevée que celles publiées pour des matériaux similaires. Bien que l'état de dispersion des CNTs puisse encore être amélioré, la conductivité électrique obtenue pour ces nanocomposites est déjà suffisamment élevée pour leur utilisation pour évacuer les charges électrostatiques ou comme éléments chauffants.

RESUMO

Redes bi- e tridimensionais de nanotubos de carbono (2D e 3D-RNTCs) foram preparadas sobre substratos de vidro de sílica e em matriz de sílica, respectivamente. Vários tipos de nanotubos de carbono (nanotubos de carbono de paredes simples, dupla e multicamadas, NTCPs, NTPDs e NTPMs respectivamente) foram caracterizados por microscopia eletrônica de transmissão, espectroscopia Raman e análise de carbono, enquanto que as suas aptidões para formar uma rede de percolação foram comparadas através da medição da suas condutividades elétricas em suspensões dinâmicas em clorofórmio. A condutividade das suspensões de NTCPs e NTPDs seguiram a lei de potência da teoria de percolação, com expoente próximo ao valor teórico de uma rede 3D. As suspensões de NTCPs apresentaram $3.08 \text{ S}\cdot\text{cm}^2/\text{g}$, enquanto que as suspensões de NTPDs apresentaram o menor teor crítico para percolação (0.002-0.06% vol.) o que levou a escolher NTCPs para a preparação de 2D-RNTCs e NTPDs para a preparação de nanocompósitos CNT-sílica (3D-RNTCs).

Para produzir em 2D-RNTCs, suspensões aquosas de NTCPs contendo dodecil sulfato de sódio foram depositadas sobre substratos de sílica amorfa utilizando quatro diferentes técnicas: *dip-coating*, filtração, deposição por *spray* e deposição eletroforética. A maioria das 2D-RNTCs formaram uma rede de percolação cuja condutividade elétrica também seguiu a lei de potência, com expoente em torno de 1.29, que está de acordo com as previsões teóricas. *Dip-coating* e deposição eletroforética resultaram nas mais suaves RNTCs sendo uma opção interessante para aplicações em células solares. As características obtidas de condutância de superfície e de transparência no UV também demonstraram suas possíveis aplicações em *displays*, telas de toque, blindagem em tubos catódicos e dissipação eletrostática.

Nanocompósitos de NTCs em matriz de sílica (3D-RNTCs) foram preparados pela rota *sol-gel*, utilizando NTPDs que foram previamente submetidos a uma funcionalização branda e sua dispersão foi realizada com ultrassom de ponta. Os materiais foram totalmente densificados por *spark-plasma sintering*. O estado de dispersão dos nanotubos de carbono foi avaliado por microscopia eletrônica de varredura por emissão de campo e correlacionados com as propriedades elétricas. A comparação das duas variações na rota de preparação (ou seja: os NTPDs foram secos ou não após a sua funcionalização) levou a uma boa correlação entre os estados dispersões (presença e tamanho dos agregados de NTCs) e os pontos críticos de percolação. Para a rota "seca", a percolação opera em apenas 0.35 vol. % de NTPDs, que é inferior aos valores reportados para nanocompósitos de sílica contendo NTCs. Para a rota "úmida", o material mais condutor apresenta uma condutividade elétrica (1.56 S/cm) maior do que o relatado por materiais similares. Apesar de que a dispersão de NTCs poderia ser ainda melhor, as condutividades elétricas obtidas destes nanocompósitos já são altas o suficiente para seu uso em elementos de aquecimento ou antieletrostáticos.

1 INTRODUCTION

Carbon nanotubes (CNTs) have unique physical and chemical properties (as summarized in Table 1.1), yielding more than 60000 publications in the last 19 years (according to Science Citation Index, ISI).

Already in 1952 Radushkevich and Lukyanovich presented in a soviet journal called *Journal of Physical Chemistry* [1] several transmission electron microscopy (TEM) images from some tubular nanostructures made of carbon, whose diameter was around 50 nm. However, probably due to “cold war” and to limitations of access to soviet publications, this report was ignored by others researchers. Even though it is possible that CNTs have been produced from vapor phase using methane as carbon source [2] before the soviets, CNTs could not be visualized since TEM was not invented on that period yet. Twenty four years after the soviets, Oberlin, Endo and Koyama also showed TEM images of hollow carbon structures produced by chemical vapor deposition [3]. In 1979, Abrahamson, Wiles and Rhoades also presented evidences of production of hollow carbon filaments by arc discharge using carbon electrodes in a nitrogen atmosphere at low pressure during the 14^o Biennial Conference on Carbon at Penn State University [4]. In 1987, a patent was registered in USA by Howard G. Tennent for *Hyperion Catalysis* for the production of “cylindrical discrete carbon fibril” with constant diameter between 3.5 and 70 nm and length about 102 times the diameter, with an outer region of multiple essentially continuous layers of ordered carbon atoms and a distinct inner core region, each of the layers and core disposed substantially concentrically about the cylindrical axis of the fibril [5]. However, it was only after Iijima published in 1991 about CNTs showing high resolution transmission electron microscopy images (HRTEM) and their interpretation as fringes of cylindrical and concentric curved graphene walls of multi-walled carbon nanotubes (MWCNTs) [6] that many scientists focused their work on CNTs research.

The most used technique for the synthesis of CNTs is catalytical chemical vapor deposition (CCVD) since it allows the large scale production of CNTs and low-cost processes, which permits their further applications. Most of the commercial producers of CNTs have been using this technique.

Table 1.1 Main properties of individual CNTs.

Aspect ratio	Length of nanometers to centimeters [7], but usually in the order of micrometers. Diameter can range from 0.4 nm [7,8] to 100 nm [9,10], but usually is between 1 nm to 20 nm [7].
Electrical conductivity	Metallic (ballistic transport), semiconducting <i>p</i> -, <i>n</i> -doped or ambipolar [7]. Operating current density $\sim 10^9$ A/cm ² (Cu $\sim 10^6$ A/cm ²) [7]
Thermal conductivity	~ 6000 W.K ⁻¹ m ⁻¹ (single-walled carbon nanotubes, SWCNTs) to 3000 W.K ⁻¹ m ⁻¹ (multi-walled carbon nanotubes, MWCNTs) along the axis (Cu ~ 400 W.K ⁻¹ m ⁻¹) [7]
Specific surface area	100-1300 m ² /g for closed CNTs [11]
Specific gravity	0.5-3 g.cm ⁻³ [12]
Mechanical property	$E \sim 640$ GPa (SWCNTs) - 1060 GPa (MWCNTs) [7] $\sigma \sim 23 - 63$ GPa (tensile strength of double-walled carbon nanotubes, DWCNTs) [7]
Chemical property	Chemically inert [7]
Temperature stability	Vacuum: SWCNT 460-520°C (0.4 nm confined inside AlPO ₄ ⁻⁵ zeolite crystal) [7]; while MWCNT 2900°C [13]. Air atmosphere: 700°C (theoretical study) [14].

The unique dimension (nanometric diameter, aspect ratio of 10^3 - 10^6) of CNTs combined with an unusual high electrical conductivity make them ideal components for electric circuits, for example. The dimension of an object is informally defined as the minimum number of coordinates needed to specify each point on the object. CNTs are generally considered as one dimensional structures.

For practical purposes, thin films of CNTs are generally considered as two-dimensional CNTs networks (2D CNTNs) since the property of interest being evaluated (generally electrical or thermal conductivity) is along the plane on which they are lying and their thicknesses are usually not higher than 200 nm [15].

Some of the applications of 2D CNTNs are: (i) antielectrostatic coatings; (ii) electrochromic or electrically heated windshields [16]; (iii) field-emitters [17]; (iv) energy applications [18]; (v) displays [19]; (vi) electromagnetic screening and touch panels; (vii) transistors [20] for logic elements in macroelectronic systems or for

optical elements with highly anisotropic properties; (viii) sensors [21]; (ix) optoelectronics [22]; and (x) diodes [23].

Great efforts recently have been focused in the replacement of indium tin oxide (ITO) by transparent, electrical conductive films of CNTs and the north-american companies Eikos Inc and Unidym Inc. are in the way to achieve this goal [24]. Some of the advantages of transparent 2D CNTNs over the conventionally used (indium tin oxide films) are: (i) sources of Indium are in short supply (will finish soon) and ITO is expensive; (ii) CNTNs are not fragile (ITO cracks when used in the current generation of touch screen displays) and can be deposited over flexible substrates (next-generation rollable displays).

In a three-dimensional system the depth can not be neglected. Since CNTs length vary from nanometres to centimetres [7], but usually in the order of micrometers, a CNT network (CNTN) with more than a micron of thickness will be considered as a three-dimensional system. Thus, three-dimensional CNTNs would include composites reinforced by CNTs, forests of CNTs, CNTs suspensions and CNTs yarns.

Three dimensional CNTNs in an electrical insulator medium, like silica (SiO_2) matrix for example, combine high mechanical, electrical, and chemical performance of CNTs [7], while silica enables the composites to be stable in harsh environments (such as high temperatures and strong acids/bases), no degradation under high optical flux and easy to fabricate [25]. Thus, these combined properties of percolating CNTNs embedded in silica can also have many potential applications, including opto-electronic devices [26], antielectrostatic components [27], heating elements [28] and electromagnetic interference shielding devices [29].

For all these applications, CNTs should form 2- or 3-dimensional (2D or 3D, respectively) percolating networks, which are facilitated by their high aspect ratio and electrical conductivity, leading to the achievement of percolation threshold at concentrations two orders of magnitude lower (< 0.1 vol.%) than those of networks formed from other sp^2 carbon forms. In solid composites or coatings, one of the main challenges is the random dispersion of CNTs to enable the formation of pathway between the electrodes in an electric circuit [7]. For example, MWCNT- SiO_2 nanocomposites up to 10 vol.% of MWCNTs processed by spark-plasma sintering (SPS) achieved maximal conductivity (σ_{MAX}) of only 0.65 S/cm [30]. According to

other reports [31,32], CNTs can also create such percolating networks and conduct electric current in a liquid medium. In this case, the connections between the suspended tubes are dynamic (Brownian motion and, eventually, liquid agitation).

The main aspects that affect the final electrical conductivity of CNTNs are: metallic/semiconducting ratio [7,33,34], effective aspect ratio of CNTs [35], presence of impurities (like amorphous carbon, catalytic particle and surfactant) [36,37], defects in the graphitic structure of CNTs [36,38], charge transfer by “vicinity doping” of semiconducting CNTs [7,36,39,40,41], distribution of CNTs (random or aligned, for example) [42], state of dispersion of CNTs in the CNTN [43,44,45], contacts between CNTs or its bundles [43] and amount of CNTs [46-49].

The electrical conductivity of an electrical conductor network depends on the critical volume for the percolation threshold (V_c) (which depends on the aspect ratio of the “filler”), the volume of electrical conductive “fillers” (V) and the dimensionality of the network represented by a critical exponent τ : $\sigma \propto (V - V_c)^\tau$ [46-49].

According to Stauffer [46], the theoretical value of τ in 2D would be 1.3, while in 3D it would be in the order of 2.05, similar to the 1.94 value proposed in the early eighties by Balberg *et al.* [47]. However, the theoretical value of τ is still not a consensus in the CNT community, in particular for 3D systems of randomly distributed and randomly oriented CNTs with aspect ratio of the order of 10^2 - 10^3 , the conductivity exponent ranges from 1.2 to 1.6, which is close to the conductivity exponent for 2D systems that range from 1.1 to 1.4 [48], up to 7.6 [49].

For convenience, along this thesis, whenever the words resistance/conductance, resistivity/conductivity and insulator/conductor are used alone it is related to electrical properties.

1.1 JUSTIFICATIVE

In this context, the interest of this study is to prepare CNTNs in 2D and 3D systems, including films, CNTs in suspension and composites containing CNTs, to investigate some of the main parameters that affect their electrical conductivity and to check the percolation thresholds (V_c) and the critical exponents (τ). The study of the electrical properties of 2D and 3D CNTNs would facilitate to predict and select the parameters and materials required for the preparation of these networks for a specific application. Different types of CNTs and techniques of preparation were tested to produce 2D CNTNs. In the case of 3D composites, DWCNTs have been selected since functionalization can occur in the outer wall without damage to the inner tube [50], which keeps its intrinsically electronic properties, and its lower density than MWCNTs usually demands lower load of CNTs to achieve percolation. To study the electrical conductivity of the CNTs themselves in a 3D system, electrical insulator mediums were chosen (silica and chloroform).

2 OBJECTIVE

2.1 GENERAL OBJECTIVE

The objective in this thesis was to investigate the electrical conductivity of 2D (over quartz substrate) and 3D (in chloroform and in silica matrix) CNTNs prepared with CCVD-CNTs. This analysis has as objective to optimize the selection of CNTs and parameters of preparation of CNTNs in order to their further possible applications.

2.2 SPECIFIC OBJECTIVES

In order to achieve this general objective it was required the following specific objectives:

- Production of DWCNTs by the CCVD route of Centre Interuniversitaire de Recherche et d'Ingénierie des Matériaux-CIRIMAT;
- Characterization of commercial and produced CCVD-CNTs - aspect ratio, defects in the graphite structure and purity (carbon content);
- Dispersion of CNTs in aqueous solution by using surfactant (for preparation of 2D CNTNs) or mild covalent functionalization (for preparation of CNT-SiO₂ composites) both aided by probe sonication;
- Preparation of the 2D and 3D CNTNs (films and suspension in chloroform respectively);
- Preparation of 3D CNTNs in silica (*in-situ* synthesis of CNT-SiO₂ composites and their densification by Spark Plasma Sintering, SPS)
- Characterization of CNTNs and nanocomposites;
- Comparison of 2D CNTNs prepared by different techniques using commercial CCVD-SWCNT;
- Comparison of 2D CNTNs prepared with different commercial CCVD-CNTs;
- Comparison of 3D CNTNs of CCVD-CNTs ideally dispersed in a liquid matrix at constant probe sonication (chloroform matrix case);

- Comparison of 3D CNTNs of “ideally dispersed” *F*-DWCNTs in a liquid (chloroform) at constant probe sonication) with 3D CNTNs of *F*-DWCNTs in a composite (silica matrix).

3 LIMITATIONS OF THE RESEARCH WORK

This work is restricted to the studies of CNTs obtained by catalytical chemical vapor deposition (CCVD) since it is the most promising technique for the large scale production of CNTs.

The amorphous carbon and metallic particles were not quantified in the CNTs and no specific treatment was done to eliminate them. The commercial purified materials were not extra purified and, in the case of the home-made produced CNTs, the purification step was restricted to an acid treatment with HCl to dissolve the magnesia (MgO) support and part of the catalytic metal nanoparticles.

It is also important to outline that the evaluation of CNTs aspect ratio might be in fact CNTs bundles aspect ratio.

In the case of 2D CNTNs, the CNTNs were prepared with non-functionalized commercial CNTs and dispersed with the aid of surfactant (sodium dodecyl sulfate, SDS). The 2D systems were evaluated by the surface resistance (also called sheet resistance or resistivity), which is the standard procedure in literature, since the thickness evaluation of these 2D CNTNs is generally associated with relatively high uncertainty bars. Therefore, as generally reported in literature, surface resistance was then correlated with the measured transparency of the CNTNs at the visible light (550 nm wavelength), an important relation for applications. From its transparency the concentration of CNTs per area was calculated.

The electrical conductivities of 3D CNTNs non-functionalized (commercial and home-made produced) and functionalized (home-made produced) CNTs were compared only in the case of an ideal state of dispersion (i.e. for the liquid composites). The ideal case of dispersion was considered as that obtained in insulator liquid (using chloroform as insulator medium since it is the less toxic and highly apolar liquid medium, with dielectric constant of 4.8069) with constant probe sonication (to avoid agglomeration) after stabilization of the electric current. These 3D CNTNs were limited to a concentration of CNTs of about 0.3 vol.% mainly due to evaporation of solvent (low evaporation point of chloroform and great increase of thermal conductivity at high concentrations) and increase of viscosity of solution.

Therefore, this study is concentrated in CNTNs with low volume content of CNTs and always using an ice bath to avoid evaporation of the chloroform.

For the non ideal state of dispersion of 3D CNTNs (composites: silica matrix), only functionalized CNTs (*F*-CNTs) were evaluated. In this case, since the classical route of sol-gel requires to work in the presence of alcohol or extreme pH [25], it is difficult to obtain a relatively good dispersion with surfactants and non-oxidized CNTs. Moreover, surfactants would cause a decrease of the conductivity through physical barrier in the intertube contacts [37] and, consequently, to the formation of pathway. Archimedes method was used to evaluate the density of the nanocomposites.

The dispersion of *F*-DWCNTs in the silica matrix was evaluated only by field-emission-gun scanning electron microscopy (FESEM) of surfaces of fractured materials. There was no access to X-ray tomography (resolution of about 200 microns), to focused ion beam (mesoscopic scale) or to 4D electron tomography (use small volume, but with excellent resolution; would enable the visualization of the three-dimensional structural complexity of CNT nanocomposite at the nanoscale though high-contrast tomographic reconstructions enabled by differences in the energy-loss spectrum of plasmon-loss electrons [51]).

4 BIBLIOGRAPHIC REVISION

4.1 CNT - structure, type, synthesis and characterization

4.1.1 Structure and types of carbon nanotubes

Carbon nanotubes (CNTs) are considered as nearly one-dimensional structures according to their aspect ratio: high length (usually micrometers) over their diameter (0.7 - 100 nanometers). CNTs can be visualized as graphene sheets (Figure 4.1) that have been rolled into a tube with two hemispheres of fullerene as end caps [39]. The simplest CNT is composed by one tube and is called singlewalled carbon nanotube (SWCNT). The structure of each tube depends on its diameter and on the symmetry of the hexagonal plane of the tube (twist of the graphene to form a tube). These features are defined by the angle of the hexagon helix around the tube axis, the so called chiral angle (represented as $\theta(\vec{a}_1, \vec{a}_2)$). Therefore, SWCNTs are completely described by the vectors \vec{C}_h (called chiral vector) and \vec{T} (called translational symmetry vector) in a planar graphene sheet (Figure 4.1A) [52]. The chiral vector, represented by a pair of integers (n,m) , would be the circumference of the SWCNT and is a function of the modulus of the vectors \vec{a}_1 and \vec{a}_2 . The translational symmetry vector is the vector parallel to SWCNT axis and is a function of the pair of integers (n,m) and of the vectors \vec{a}_1 and \vec{a}_2 . Where \vec{a}_1 and \vec{a}_2 are the unit vectors of the graphene plane.

According to the chiral angle, SWCNTs can be classified as chiral or achiral. CNTs with θ between 0 and 30° are chiral and present chiral vector (n,m) . Achiral CNTs present a specular plane and correspond to the chiral angles $\theta = 0$ and 30°, known as zigzag $(n,0)$ and armchair (n,n) configurations, respectively. These configurations can be visualized in Figure 4.1B.

The helicity has a significant implication on the electronic properties of the CNTs. According to the indices n and m , SWCNTs with similar diameters or interatomic bonds can be metallic or semiconducting. A simple rule based on the structure of the SWCNT is obtained for classifying SWCNTs regarding their electronic properties: if $n = m$ the SWCNT is metallic; if $n - m$ is multiple of 3, the nanotube is

semiconducting with a very small band gap, otherwise it is a moderate semiconductor [7,39]. In general, a batch of CNTs is composed by CNTs with different helicities and, besides the company NanoIntegris already uses an efficient method to separate them [53], it is still expensive for general composite applications, for example.

SWCNTs have diameters typically in the range of 0.4–2 nm [33]. If all chiral vectors were equally probable, 1/3 of the total SWCNTs would be metallic while the remaining 2/3, semiconducting, which was also confirmed experimentally [33]. During its growth process, SWCNTs form hexagonal-packed bundles and the distance between the walls of two nanotubes is nearby the interlayer distance in graphite (3.35-3.41 Å) [33,54].

CNTs can also be composed by two or a series of graphene sheets coaxially wrapped into cylinders, known as doublewalled (DWCNTs) and multiwalled (MWCNTs) CNTs, respectively. A good control of the number of walls is already possible in the synthesis process [7].

Each cylinder would be a SWCNT of different helicities that is still well defined by its n,m chiral indices. However, in DWCNTs and MWCNTs the metallicity is affected by the inter-walls interactions [55] and in both cases the majority of CNTs is metallic CNTs [56-58]. In the case of bundles, the interaction surface of adjacent nanotubes is small; while in DWCNTs the interaction surface between the two shells is 100%.

It is expected charge transfer and/or orbital mixing to occur between the two walls of a DWCNT caused by inter-walls coupling interactions [55,56]. The interaction between the inner and outerwalls of DWCNTs was indirectly confirmed by nuclear-magnetic-resonance measurements that showed that DWCNTs have a highly uniform metallic character [57]. Furthermore, theoretical study showed that a small charge transfer from the outer wall to the inner wall occurs in every DWCNT [55]. This was experimentally confirmed by photoemission spectroscopy [59]. The orbital mixing between the walls also can explain the measured redshift of the resonance in the Raman measurements of DWCNTs [60]. Zolyomi *et al.* concluded that the observed charge transfer and orbital mixing together can cause a semiconductor-to-metal transition of DWCNTs, but not obligatory near-universal metallicity [55b].

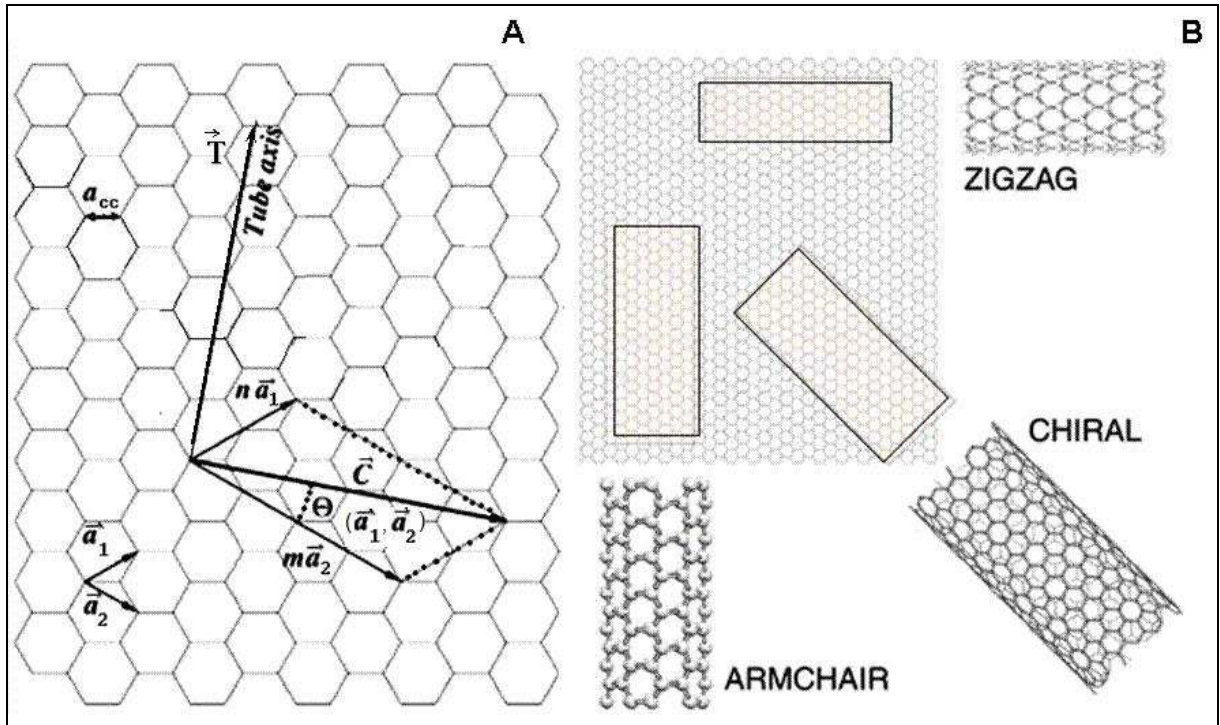


Figure 4.1 (A) Vectors \vec{C}_h and \vec{T} defined by the indices (n,m) [52]; (B) the three different structures of CNTs: armchair, zigzag and chiral.

The typical inter-walls spacing in DWCNTs and MWCNTs is ~ 0.34 nm [7,39]. This distance closely corresponds to the interlayer distance in graphite [39] and it increases with the decrease of number of the concentric tubes. MWCNTs have diameters that vary in the range of ~ 20 nm (grown by the arc-discharge method) to 100 nm (obtained by CCVD) [7], but also some CCVD MWCNTs are composed of 5-10 walls and are only of 10-20 nm in diameter [40]. Large diameter tubes are found to have a greater density of defects (i.e., vacancies or interstitials) than small CNTs [7].

4.1.2 Synthesis of carbon nanotubes

The synthesis methods of CNTs can be divided into: (i) methods at high temperatures, which include arc discharge and laser ablation; and (ii) methods at moderated temperatures, which correspond mainly to catalytic chemical vapor deposition (CCVD).

High temperature growth processes (like arc-growth or laser ablation) synthesize CNTs with low contents of defects (less than methods at moderated

temperatures), thus good crystallization states [7,34,39]. As a consequence, these CNTs exhibit metallic temperature dependence (resistance linearly decreases with increase temperature of synthesis due to less defects acting as scattering centers for conduction of electrons). A great amount of disordered carbon is produced by arc-growth (especially sp^3 like carbon: only 1-2 wt% of CNTs are obtained after purification by thermal treatment), whereas laser ablation produces the most pure SWCNTs with good crystallization state as well [7,34,39]. In the other hand, CNTs prepared by CCVD methods (moderated temperatures) are usually much longer (few tens to hundreds of micrometers) than those obtained by arc-discharge (few nanometers to micrometers) [61].

The arc discharge method consists to vaporize carbon atoms by plasma of inert gas (helium or argon) ignited by high currents that pass through opposing carbon anode and cathode. The temperature in the plasma region is extremely high (3000 °C to 4000 °C). The first observed MWCNTs (with diameters between 2 and 30 nm) were grown in an arc-discharge process using electrodes of pure graphite [6]. A breakthrough in MWCNT growth by arc discharge was first made by Ebbesen and Ajayan [62] who reported the growth and purification of high quality MWCNTs at the gram level. In order to produce SWCNTs however, graphite-metal electrodes are needed [6,63].

Guo *et al.* [64] have shown that SWCNTs can be produced by direct laser vaporization using laser ablation method. In this method a transition metal-graphite composite target is ablated by means of intense laser pulses. The target is mounted in a high-temperature furnace, with a maximum temperature of 1200 °C. During laser ablation, a flow of Ar gas passes through the growth chamber to carry the grown CNTs downstream and to collect them on a cold finger. In contrast to the arc-discharge method, laser vaporization produces a better quality final product (little amorphous carbon deposit).

The CCVD method is based on the catalytic decomposition of a carbonaceous gas on metal nanoparticles (NPs) [7,34,39,61]. The formation of CNTs typically occurs between 600 °C and 1000 °C (depending on the carbon source). This method is cheaper compared to the two previous ones and allows producing large scale amounts of CNTs. In contrast to the arc-discharge method and laser ablation that produce low yields through intermittent syntheses, the CCVD method can produce

grams-scale batches of CNTs [61,65] and can be used in a continuous production using technologies such as fluidized bed reactors [66]. Since all CNTs used in this work were produced by CCVD a more detailed description is in the following sequence.

The CCVD process

The CCVD method is based on: (i) gas-phase catalysts (High Pressure of CO process or vertical EtOH vapor systems), when the metallic catalyst cluster is formed by the introduction of a gas-phase precursor; or (ii) solid-phase catalysts, when the metallic catalyst is supported over a substrate (silicon wafers or oxide powder support, for example). Initially, carbon containing molecules are decomposed (role of the catalyst in the decomposition: catalytic decomposition). Then, carbon is dissolved inside the metallic cluster. When the carbon concentration is high enough, the strong C-C interactions outside the metal dominate, leading to the precipitation in a curved graphene sheet and the formation of the CNTs (nucleation and growth) [67].

The *HiPco* process was developed by P. Nikolaev *et al.* [68] and it stands for high pressure carbon monoxide (30–50 atm). In this CCVD method SWCNT are made by high-temperature (900–1100 °C) decomposition of flowing CO on catalytic clusters of iron. The clusters are formed *in situ*: Fe is added to the gas flow in the form of $\text{Fe}(\text{CO})_5$, which decomposes and Fe atoms condense into clusters. The nanotubes grow in suspension in the vapor phase and are collected out onto cold surfaces.

Planar catalyst supports are usually wafers (generally silicon) with an oxidized surface layer on which a thin metallic layer of transition metal is deposited (by dip-coating the wafer in a solution containing the metals precursors followed by thermal decomposition to form metallic NP or by sputtering, for example) to act as catalyst [7]. This approach is mainly used to produce vertically aligned CNTs, characterized by a root growth type with an equal rate of growth, in which lateral interactions keep them growing vertically. It is also an interesting technique to produce electronic devices or connections since it is possible to synthesize horizontally aligned CNTs (by applying an electric field or by flux control or by using the crystalline orientation of the substrate) [7].

CCVD using a powder catalytic material is one of the most promising techniques for the mass production of CNTs. The catalytic material is composed of a precursor of the corresponding metal (usually transition metals, such as Fe, Co or Ni sometimes with addition of other elements such as Mo and W) dispersed on the grain surface of an oxide powder which acts as support material (generally Al_2O_3 , SiO_2 , zeolites or MgO), which forms the catalytic material [7,39]. In this case, CNTs grow by either surface or bulk carbon diffusion and it can be either base or tip growth (depending on the catalyst type, the hydrocarbon source, and the growth temperature). The oxide powder must have a high surface area to avoid the metallic NPs coalescence, which is harmful for CNT synthesis. The carbonaceous gas can be either hydrocarbons (CH_4 , C_2H_4 , C_2H_2 ,...) or CO, generally mixed with H_2 , N_2 or Ar, which act as carrier gas (N_2 or Ar) or reducing agent (H_2). The diameter of the CNTs is mainly controlled by the diameter of metallic catalytic particles (kept at a nanometric size) [7,39]. There are two main methods to prepare the catalytic materials: (a) the impregnation of a substrate with a solution of transition metal salt; and (b) the preparation of a solid solution between an oxide of a catalytic metallic element and a chemically inert and thermally stable host oxide.

a) In the impregnation method, the catalytic material is prepared by simply drying a stirred mixture of an oxide powder and a metal salt solution, followed by a thermal treatment that decomposes the salt to form the catalytic metal oxide. At the end, a subsequent reduction treatment is required in order to form the catalytic metal NP.

b) The metal NP can be prepared *in situ* in an oxide powder (via wet chemical reaction followed by a thermal treatment, or solution combustion synthesis) by selective reduction of an oxide solid solution. Their coalescence is normally avoided by using inert and thermally stable host oxides such as Al_2O_3 , MgO , MgAl_2O_4 , and a sufficiently low content of transition element. This method, developed by the *Centre Interuniversitaire de Recherche et d'Ingénierie des Matériaux* (CIRIMAT) at Université Paul Sabatier in Toulouse (France) [61,65], used in the present work for the synthesis of the DWCNTs will be briefly discussed in the next chapter.

4.1.3 Characterization of carbon nanotubes and its networks

4.1.3.1 Raman spectroscopy

It is the major technique used to characterize the CNTs since it can provide like a “fingerprint” of CNTs and it is also sensible to the direct environment of the CNTs (if they are in bundles, surrounded by surfactant, etc) [69]. All allotropic forms of carbon are active in Raman spectroscopy, but according to the carbon form, the position, width and relative intensity of the bands are modified. CNTs present three characteristic modes in Raman spectroscopy (Figure 4.2): the radial breathing mode (*RBM*), the disordered-induced mode (*D* band) and the tangential or high-energy modes (*G* band). The *RBM* is visible only for SWCNTs and DWCNTs, and corresponds to the atomic vibration of the C atoms in the radial direction (appearing between $120 \text{ cm}^{-1} < \omega_{RBM} < 250 \text{ cm}^{-1}$ for SWCNTs with diameters within $1 \text{ nm} < d < 2 \text{ nm}$). The *D* band (generally around 1340 cm^{-1}) is related to the presence of disordered carbon or structural defects in CNTs and usually the ratio of intensities of *D* and *G* bands is used to have an idea of the “quality” of the graphitic structure. Thus, a high *D/G* ratio, here called $I_{D/G}$, indicates the presence of a lot of disordered carbon or defects in the graphitic structure of the CNTs. The main differences between *D* bands from CNTs and graphite are that in CNTs it presents small linewidths (40 cm^{-1} down to 7 cm^{-1}) and it appears at lower frequencies than sp^2 -based carbons (this last feature is even more pronounced in low diameter CNTs) [69]. This $I_{D/G}$ ratio is also used to verify the degree of deleterious effects of a chemical functionalization into the graphitic structure of carbon nanofibers (CNFs) [70] and nanotubes [71]. For example, concentrated nitric and sulfuric acids in contact to CNFs by sonication for 24h can increase $I_{D/G}$ by 328% in comparison to pristine material [70]. The *G* band gives information about the metallic character of the CNTs in resonance with a given laser line and it is typically around 1580 cm^{-1} .

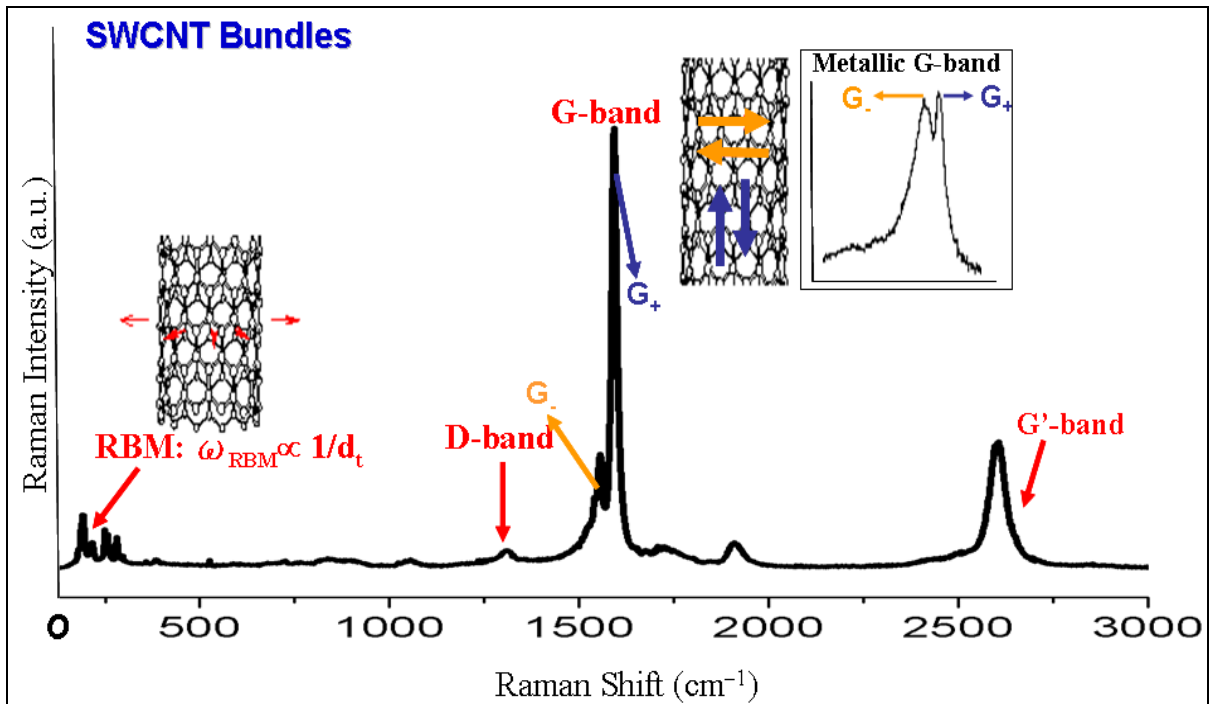


Figure 4.2 Typical Raman spectrum from SWCNT bundles.

Some limitations of this technique are that: (i) it is not possible to quantify the amount of CNTs in a mixture with other carbonaceous structures; (ii) only the carbon forms in resonance with the specific energy line that is being used will be detected by Raman spectroscopy.

4.1.3.2 Microstructural characterization

Even though other techniques like atomic force microscopy (AFM) and scanning tunneling microscopy (STM) started to be more diffused among other microstructural techniques to visualize CNTs, transmission electron microscopy (TEM) and field-emission-gun scanning electron microscopy (FESEM) are still the main used techniques to study their microstructure. The structure of CNTs was first visualized and described in 1991 with the aid of a high resolution TEM (HRTEM) [6] and it is still the technique that allows the direct observation of details of their morphology (diameter of the CNTs, number of walls, filling and presence of defects). FESEM also has been greatly used to observe the “quality” (morphology, presence of impurities) of the sample and to have an idea of length of CNTs. However, one of its limitations is the small scale of the sample (especially in non-homogeneous

samples), which is typically 10^{-12} – 10^{-13} g for (FE)SEM observations [72] and for TEM this amount can be several orders less.

Atomic force microscopy (AFM) can also be used to visualize CNTs, but at lower magnifications than HRTEM. It is possible to get informations about the diameter of CNTs/bundles, length of CNTs/bundles and roughness of 2D CNTNs. It has the same limitation of small scale of sample. In the case of STM it is usually used to visualize the structure of individual CNTs in the resolution of atoms, so that even the chirality of the CNT can be visualized.

FESEM observations can be used to characterize the dispersion of the 2D (films) and 3D CNTNs (composites), the observation of the fractured surfaces giving satisfactory idea in the latter case. Another quite recent technique in the case of 3D CNTNs is the 3D spectral tomography, which can provide more qualitative information than FESEM images [51,73] since it allows the visualization of the 3D structure, but few research centers have access to it. It enables the visualization of the three-dimensional structural complexity of CNT nanocomposite at the nanoscale though high-contrast tomographic reconstructions enabled by differences in the energy-loss spectrum of plasmon-loss electrons [51].

4.1.3.3 Carbon content

Thermogravimetric analysis and elementary analysis by the flash combustion method are some of the most commonly used methods to determine the amount of carbon present in a sample containing CNTs [61]. Even though amorphous carbon present lower temperature of oxidation than CNTs, the evaluation of its relative quantity is quite difficult since the oxidation temperature also depends in other factors like density, flow of the oxidant gas, heating rate, morphology of the powder, quantity and nature of metal nanoparticles, etc. The residual mass at the end of the final combustion of the carbonaceous material is constituted by oxide of residues of the metal catalyst that were not removed during the purification process.

4.1.3.4 Fourier Transform Infrared Spectroscopy

Fourier Transform Infrared Spectroscopy (FTIR) provides specific information about chemical bonding and molecular structures, making it useful for analyzing organic materials and certain inorganic materials. During FTIR analysis, the specimen is subjected to a modulated IR beam. The specimen's transmittance and reflectance of the infrared rays at different frequencies is translated into an IR absorption plot consisting of reverse peaks. Chemical bonds vibrate at characteristic frequencies, and when exposed to infrared radiation, they absorb the radiation at frequencies that match their vibration modes (characteristic to that molecule, as a "fingerprint"). By interpreting the infrared absorption spectrum, the chemical bonds in a molecule can be determined. FTIR spectra of pure compounds are generally so unique that they are like a molecular "fingerprint". For most common materials, the spectrum of an unknown compound can be identified by comparison to a library of known compounds. For the case of CNTs, infrared is most commonly used to verify the presence of groups attached to CNTs during the synthesis and mainly post-synthesis of CNTs. For example, to detect the carboxylation (characterized by C=O, C-O and O-H groups) of CNFs/CNTs after chemical functionalization by their contact with nitric (and sulphuric and chloridric) acid(s) [70,71,74,75]. According to the strength of the functionalization treatment, the correspondent bands of carboxylation can be more [70,71,74] or less [75] intense.

4.1.3.5 Zeta potential

Zeta potential is based on the electrokinetic of (un)charged particles in a liquid medium. It corresponds to the electric potential in the junction between the Stern layer and the diffusive layer that surround each particle in the liquid medium. If the charge of the particles is high enough, they will remain discrete, disperse and in suspension, while reducing or eliminating the charge has the opposite effect (agglomeration). In practice, modulated values of 30 mV or higher means stable dispersions. Particle charge can be controlled by modifying the suspending liquid (by pH or change of ionic species in the solution) or by modifying the surface of the particle (by chemical functionalization, for example) [76]. For CNTs suspensions, this method can be used to study the most efficient ways to get a stable dispersion in

order to prepare a composite, for example. As demonstrated by Hu *et al.* [76], functionalized CNTs containing carboxylic groups can generate high modulated value of Zeta potential, leading to stable dispersions of CNTs.

4.1.3.6 UV-Vis spectroscopy

It allows the determination of light absorption in a sample (spectrophotometry) and it uses light from the visible UVA (315 to 400 nm) up to near infrared (750 to 1400 nm) ranges [77]. In the study of CNTs, it can be useful to determine the stability of a suspension and in the study of transparent electrical conductive CNTNs. In order to determine the light absorption (or transparency) in the region of ultraviolet (generally wavelength of 550 nm is used for this evaluation) for 2D CNTNs quartz substrates can be a good alternative because they do not absorb in this range of spectrum (see Figure 0.2 in the attachment section).

4.1.3.7 Electrical conductivity

One method to estimate the conductivity of CNTs is to produce self-standing papers (so called *buckypapers*) by filtering a CNT solution, which leads to a compaction of the CNTs. However, the preparation of such *buckypapers* are time consuming and require relatively high amounts of CNTs (> 50 mg) and the packing of CNTs can vary even using the same sample, varying the amount of internal porosity of the material. Their apparent density is very dependent on the morphology of the carbon material. This variation causes significant changes in the thickness of the free standing paper but does not reflect the real cross-section area of the CNTs (area of solid material with its interconnections). Because of that we preferred to normalize the conductivity by the density of the *buckypaper*.

In the case of evaluation of 2D CNTNs, since the evaluation of thickness of these 2D CNTNs is generally associated with relatively high uncertainties the standard procedure in literature is to measure the surface resistance, its unity being the Ohm but it is generally notated in Ohm per square (Ohm/sq.) to avoid the confusion with volume resistance [58,78]. These results are then correlated with the measured transparency of the CNTNs at the visible light (usually 550 nm wavelength

is used), an important relation for applications and from this measurement the concentration of CNTs per area can be determined [58,78].

Electrical conductivity of an unique CNT or a bundle of it is also possible through the deposition (usually dip-coating or spray-coating is chosen) of thin 2D CNTN over a substrate with markers followed by localization of the CNT by AFM to allow the deposition of electrodes over it through lithographic techniques. By last, the substrate is transferred to a chip carrier and wires are connected between the chip carrier and the electrodes over the CNTs, allowing the measurement [58].

4.2 Production of 2D and 3D CNTNs

4.2.1 2D CNTNs

There have been several reports on ultra-thin electrical conductive CNTNs that are optically transparent since 2002 [79] due to their wide range of applications, as already described in the introduction section. Strategic areas like production of energy by environmentally friendly way [17] has been one of the most interesting topics for 2D CNTNs. Inexpensive organic solar cells that can be painted or printed on flexible plastic sheets were developed by the New Jersey Institute of Technology [80] and used a mixture of CNTs and fullerenes to form snake-like structures.

According to their purpose, they might be produced with different morphologies (random or aligned), transmittance/absorbance in the UV region (typically 550 nm is the wavelength of evaluation), surface electrical resistance and average roughness. The techniques for the production of these CNTNs can be classified into post-growth or direct growth methods [81].

In the first case, most of the techniques require suspensions of CNTs to deposit CNTs on a substrate. Generally, they might be summarized by the following steps: (i) synthesis of CNTs, (ii) purification of the CNTs, (iii) dispersion with probe/bath sonication of the CNTs in a suspension (with the aid of surfactants or chemical functionalization), and (iv) deposition over the desired substrate. Examples of post-growth techniques are spray-coating (or air-brushing) [78], vacuum filtration method [82,83], spin-coating [84] and dip-coating [85]. There is also a solid-state

post-growth technique that allows the production of aligned CNTNs from spinnable CNT forests, but still few groups have this technology [86]. The main advantages of these methods are the possibility of use of purified CNTs and the deposition of CNTNs on several substrates and, in some cases, even with different shapes of substrates. However, when CNTs are deposited over a substrate, depending on the techniques used, they can be in bundles of diameter of order 50 nm containing a large number of more or less parallel CNTs (due to *van der Waals* interactions between the CNTs). These bundles join and intersect with other bundles to form the complete CNTNs. A brief description is given in the sequence about some post-growth techniques used in this work (spray-coating, vacuum filtration and dip-coating).

Spray-coating [78] consists of applying a network over a substrate with the aid of an air-brush pistol and typically gives CNTNs in the form of “linked islands” of CNTs due to the droplets generated at the nozzle of the pistol. In this method, the flocculation of the CNTs in the solvent prior to exiting the nozzle remains a problem, as well the loss of material in the over spray at the edges of the work piece and in the aerosol generated.

Filtration method [82,83] usually gives more dispersed deposits of CNTNs. In this case, a suspension is filtrated with a cellulose nitrate membrane and then the deposited network over the membrane is transferred for the desired substrate by dissolving the membrane in organic solvent, like acetone.

Dip-coating method [85] leads to the production of relatively aligned CNTNs, by the liquid flow. The alignment of the CNTs is dependent on the speed of dipping (the lower the speed, the more aligned are the CNTs, but more bundles are also formed). To achieve a good alignment the attraction force between the dry surface and the nanotube should be higher than the forces acted on the nanotube by the liquid front [87]. Besides this deposition method can generate quite smooth films, it is quite time consuming to obtain comparably thick films and others coupling agents to silanize the surface might be required to speed up the process.

The direct growth techniques can provide CNTNs composed of several millimeters long CNTs and aligned (by the gases flow or substrate structure) CNTNs, so that they already reach a percolation threshold at lower concentration of CNTs than post-growth techniques [88]. However, as there is no purification step, the

by-products from the synthesis (e.g. amorphous carbon and other allotropic forms of carbon with low aspect ratio) are deleterious for the optical transmittance of these networks and do not contribute to the electrical conductivity.

4.2.2 3D CNTNs in insulator matrices

4.2.2.1 Solid medium - ceramic matrix composites

The addition of CNTs in ceramic composites is a promising field for several applications and several reports were focused on them [89,90], but there are relatively few if compared to polymer composites. Particularly, the huge aspect ratio and outstanding electrical properties of CNTs give rise to percolation in insulator matrix at a much lower content than any other additives [91].

In order to prepare 3D CNTNs embedded in a matrix one can achieve this by mechanical mixing [92], sol-gel [93] or *in-situ* growth [94], for example.

One of the challenges on preparing such CNTNs is the dispersion step and it will depend on the method chosen. Generally mechanical mixing does not provide an homogeneous dispersion at a molecular level, but this might be better achieved by sol-gel (*in-situ* synthesis of ceramic matrix) [93] or much better by *in-situ* growth of CNTs (by CCVD) [94]. In the sol-gel case, the CNTs can be dispersed in aqueous [95] or alcohol [96] medium either with the aid of surfactants [95,96] or by chemical functionalization with strong acids [95], both using either probe or bath sonication. In the case of *in-situ* synthesis of CNTs, to achieve a good dispersion of CNTs in the matrix (support) it is important to have a good dispersion of the catalyst metal NPs. This approach can lead to quite dispersed CNTs in the matrix, providing high electrical conductivity: 2.8 to 4 S/cm for 5.7 wt.% of carbon in a CNT-Fe-Al₂O₃ composite densified by uniaxial hot-pressing at 43 MPa in graphite dies, in a primary vacuum, at 1500°C [94]. A drawback from this technique is that the matrix should be in the form of a high surface area powder and should not react with the metal NP at the temperature of CNTs synthesis.

4.3 CNTs-SiO₂ nanocomposites

Due to the good chemical interaction between CNTs and silica without altering their original properties [97], CNTs-silica composites can have many applications (as previously reported in the introduction section) [26,29]. Moreover, the relatively low thermal expansion coefficient of silica ($0.4 \times 10^{-6} \text{ } ^\circ\text{C}^{-1}$) [98] might help to avoid some sintering problems since CNTs also present quite low value of this coefficient. CNTs-SiO₂ nanocomposites have already been reported since 2001 [93], but few works were devoted to electrical conductivity of these composites [29,30,99,100b]. Silica glass presents an electrical conductivity about 10^{-20} S/cm [98]. The main challenges to obtain such dense nanocomposites are the dispersion of CNTs in the matrix and the densification of the final product [29,30,99,100].

The lowest loading that has been reported to present percolation was 1 vol.% for MWCNT-SiO₂ composites [100b], with an electrical conductivity of about 10^{-10} S/cm . Higher CNTs contents resulted in much higher conductivities. For example, 0.08 and 0.65 S/cm were measured for 5 and 10 vol.% MWCNTs-SiO₂ composite, respectively [30].

4.3.1 Dispersion

The high surface area and aspect ratio of CNTs associated with their high hydrophobicity make it really difficult to disperse them properly in any medium at concentrations required for their application in composites. Generally, CNTs are found to be in bundles or aggregates due to their strong *van der Waals* interactions. For example, the energy of attraction in a region of 10 nm in contact of two SWCNTs is about 250 kJ (or 0.5 eV/nm for SWCNT-SWCNT contact) [7,101]. To overcome the first difficulty, CNTs can either be synthesized *in-situ* in the ceramic powder [94] or the ceramic precursor can be synthesized around CNTs dispersed in a solvent [93] (with aid of chemical functionalization or use of surfactants, followed by sonication).

Therefore, to improve the dispersion of CNTs into SiO₂, various approaches have already been tested as modification of the interface (by use of surfactants [29,99,100b], chemical functionalization [102]) and also methods of composite preparation (attrition mill with colloidal SiO₂ [30] or *in-situ* production of silica by organic [29,100b,102] or inorganic [99] sol-gel routes).

4.3.2 Densification

In the case of 3D CNTNs, the morphology of the CNTNs will depend not only on the characteristics of the CNTNs themselves, but also on the densification of the final composite, as shown in Figure 4.3.

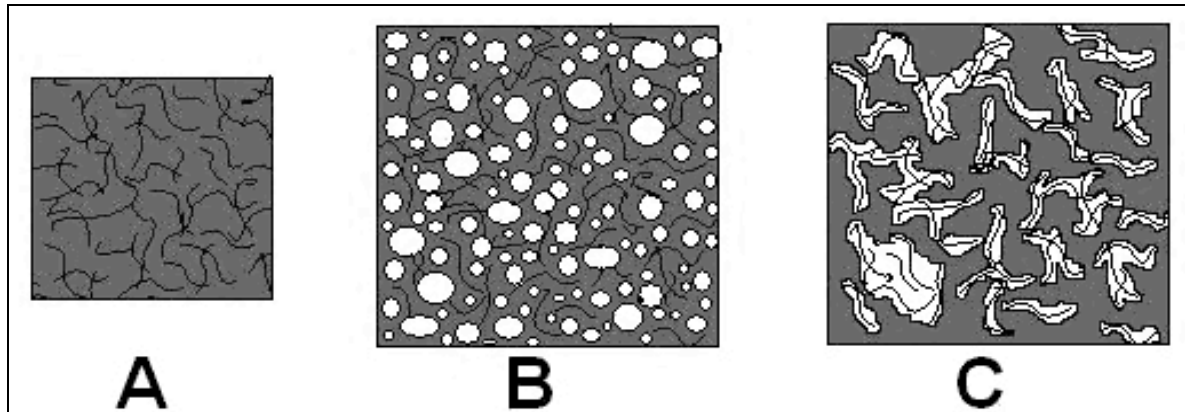


Figure 4.3 Schematic diagram of a CNTN immersed into a matrix: (A) with good compatibility with the matrix and fully densified; (B) with good compatibility with the matrix, but with remaining porosity; (C) with bad interface interaction with the matrix and non-ideally dispersed.

The incorporation of CNTs into silica glass is detrimental to densification, particularly due to an increase of softening point that fibres generally cause in glass matrices [103]. Indeed, Ning *et al.* [100d] reported a decrease of relative density accompanied by an increase of porosity with the increase of MWCNTs content into silica matrix for composites obtained by hot-pressing (HP). Consequently, several techniques have also been tested to densify these composites, including heat-treatment in inert atmosphere [99], hot-pressing (HP) [29,100b], high-pressure cold quasi-isostatic pressing (HIP) [102] and spark-plasma sintering (SPS) [30].

According to literature, the more efficient densification methods seem to be HIP [102], HP [29,100d] and SPS [30].

In the HIP technique the powder is usually placed in a lead container, which acts as a pressure-transmitting medium and the compaction (at pressures in the order of 8 GPa, for example) is accomplished in a toroidal-type high-pressure chamber at room temperature that provides the required quasi-hydrostatic pressure around the sample [102].

The HP technique is a well-known method to densify materials that consists of filling a cylindrical matrix (mostly graphite) with the powder bed and then applying via punches (mostly graphite) an uniaxial pressure and through resistance heating elements surrounding the matrix it is exposed simultaneously to a high temperature.

SPS, also known as pulse electric current or field assisted sintering technique was proposed in 1989 to be the next generation of sintering methods [104]. SPS is a sintering method for rapid consolidation of materials in short time frames (seconds to minutes) and at temperatures lower than that needed by other techniques. Furthermore, it has an advantage of almost suppressing grain growth over conventional sintering methods. Since this sintering method was used in the present work, a more detailed description is given.

4.3.3 SPS method

Figure 4.4 displays a schematic diagram for this technique. It is a method that applies an uniaxial pressure with a fast heating, which is applied by a high intensity dc pulsed electric current passing directly through the mold of graphite containing the powder.

Thus, the graphite mold and punches act as heating elements. The electric field not only generates Joule heat, providing conditions for hot compaction, but can also influence diffusion mass transport (mostly through electric field induced diffusion, electromigration and electroplasticity mechanisms) [105]. It is believed that micro-sparks are generated when this pulsed current reaches particle contact points and this would increase the diffusion kinetics in surface grain boundary [106]. However, high heating rates with short dwell times can cause inhomogeneous sintered parts due to temperature gradients [107]. These temperature gradients within the sample are also influenced by the electrical properties of the materials, as well as the thermal and electric contact resistances. Vanmeensel *et al.* [108] proved theoretically and experimentally that thermal distribution in the sample is mainly dependent on contact resistance of contacting parts and on the electrical properties of the sample. The temperature field, the current and the power needed during SPS are greatly influenced by the thermal and electrical resistances in the contacts between the sample and the tool components. Therefore, the reproducibility of the

results depends on the repeatability of contact properties. In insulator materials the current flows only through the tool components (punch and dies) [109], while in samples that are more conductive than graphite, it flows mainly by the sample itself. If the current passes through tool components, heat losses may be compensated by the radiation from exposed tool surfaces, but if it is not compensated, temperature is largely non homogeneous [108]. Even though this technique has been investigated already for 18 years, the mechanism of sintering is still unknown due to the complexity of the thermal, electrical and mechanical processes that may be involved in the SPS [110,111]. It is assumed that, depending on the material treated, mechanisms like vaporization–condensation, plastic deformation, surface-, grain boundary-, and volume-diffusions might occur during the sintering and densification by SPS, but this has not yet been proved [112]. It is not clear also if plasma is generated by pulse electric current.

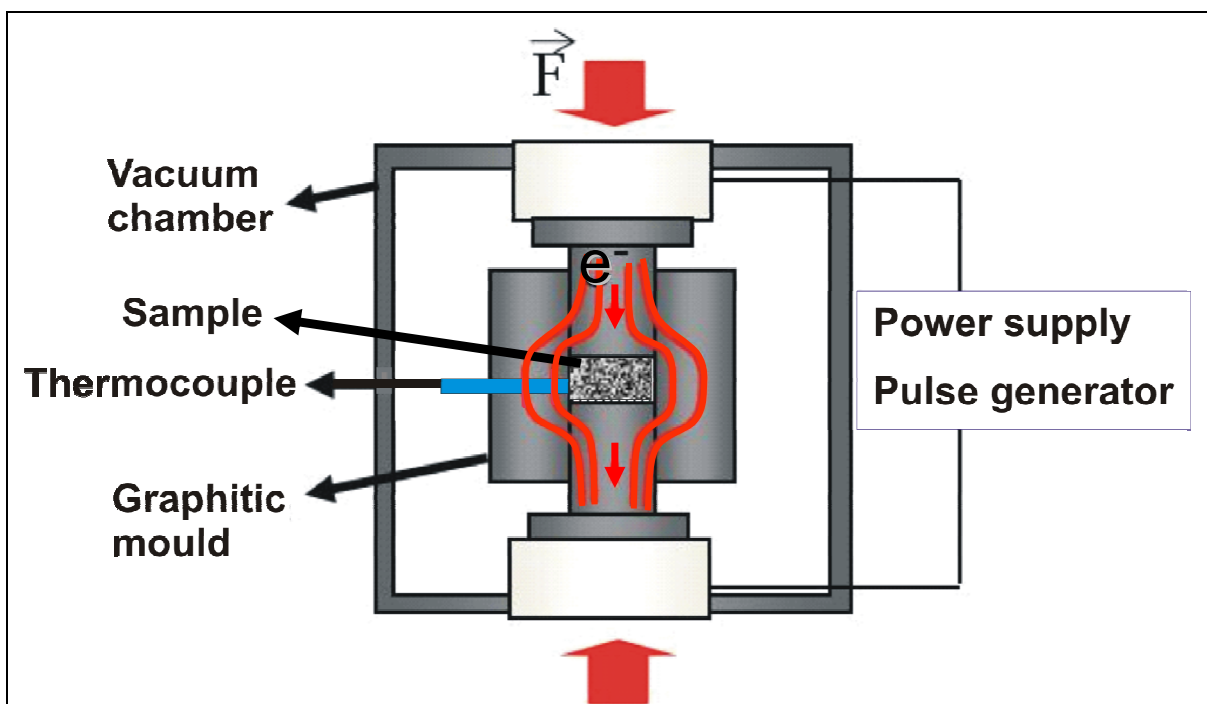


Figure 4.4 Schematic diagram of SPS device.

4.4 Electrical properties of carbon nanotubes and its networks

As mentioned before, CNTs can have metallic or semiconducting behavior, generating electrical conductivities that can reach 10^5 S/cm or only 0.1-100 S/cm, respectively [7,34]. In a DWCNT with one tube metallic and the other semiconducting, low energy properties characteristic of metallic tubes predominate, while if both the constituent tubes are metallic, a much more complicated situation in the case of band crossings can arise [55-57]. Therefore, in the case of DWCNTs and MWCNTs it is quite difficult to predict their behaviors.

Electrical resistance was first measured for bundles of MWCNTs yielding electrical conductivity of 1.5×10^2 S/cm at 300 K [113]. Later, Ando *et al.* [114] managed to evaluate the resistance of isolated MWCNTs and reported a conductivity of 1.8×10^3 S/cm, while Langer *et al.* [115] found 10^4 S/cm for a single MWCNT.

In the case of ropes of metallic SWNTs, Thess *et al.* calculated the conductivity to be around 10^4 S/cm at 300 K [116] by measuring the resistance directly with a four-point technique (one of their measured values was 0.34×10^4 S/cm). That means a difference of one order of magnitude between a rope of metallic SWCNTs and a metallic SWCNT [7,34].

Aligned three-dimensional CNTNs such as fibers and yarns made from ultralong (mm to cm) uniquely MWCNTs can achieve an electrical conductivity in the order of 10^2 S/cm [117]. This is the same order of magnitude of that reported for MWCNTs bundles [113] and about one [114] to two [115] orders of magnitude lower than that calculated for a single MWCNT. For comparison, unaligned 3D CNTN composed only by DWCNTs in the form of densified pellets prepared by SPS achieved an electrical conductivity as high as 1.65×10^3 S/cm [118].

When CNTs are dispersed over a substrate or in a matrix, CNTs can form 2- or 3-dimensional (2D or 3D, respectively) percolating networks that permit to conduct electrical current through them with small amount of material (< 0.1 vol.%). Table 4.1 presents a summary of carbon structures with different aspect ratios in comparison to their typical electrical conductivities and prices, as well as their percolating properties in 3D CNTNs embedded in a matrix. In spite that carbon black is still the most economical option, the higher electrical conductivity of CNTs in comparison to other carbon forms and the continuous effort of producers to decrease their costs are great attractives for future applications. Moreover, CNTs require much lower contents (1-2

orders of magnitude) than other carbon forms to percolate due to their high aspect ratios, which could be quite interesting to avoid any deleterious consequences of other properties that can be important for specific applications (like transparency in solar cells applications, or mechanical properties in ceramic matrix composites for example). According to the state of dispersion, anisotropy, purity of sample, effective aspect ratio, compatibility with the matrix and densification, the percolation threshold can greatly vary.

Several studies on the electrical conductivity of SWCNTs networks were reported and the values range from 400 to 6600 S/cm [43].

The resistance of CNTNs depends on the resistance due to intertube junctions (major role at CNTs concentrations below the percolation threshold) and on the resistance along the CNT itself (predominates at CNTs concentrations above the percolation threshold). Therefore, these two distinct sources of resistance depend on the properties of individual CNTs (defects [36,38], doping level of semiconducting CNTs [7,36,39-41], effective aspect ratio [35], purity [36,37] and metallic to semiconducting volume fraction [7,33,34]) and of the CNTN itself (volume fraction of CNTs in the CNTN [46-49], state of dispersion of CNTs into the CNTN [43-45], anisotropy [42] and contacts between CNTs or its bundles [43]).

For example, long CNTs will lead to a low number of interbundle/intertube junctions in a given path (when straight longer CNTs are used the electric current will be able to percolate through the CNTs passing through less contact points and the final electrical conductivity will be higher than a CNTN with shorter CNTs), while the smaller is the diameter of bundles; the higher are the number of conductive paths [43]. According to Buldum *et al.* [119], the resistance associated with the intertube contacts can be a function of the geometry and chirality of the CNTs.

The presence of impurities (such as carbon nanofibres, amorphous carbon and surfactants) or of structural defects in CNTs cause electron scattering relative to an ideal structure [36], which is deleterious to the electrical conductivity. And impurities not only have lower ability to conduct than CNTs, but also can also decrease the transparency of the final product [36-38].

Table 4.1 Examples of carbon structures with different aspect ratio and their percolation as 3D network in insulator matrices.

	Filler particle			3D network				
	σ_{DC} along axis (S/cm)	Specific gravity (g/cm ³)	Price per gram (€, 1 USD = 0.7667 €)	Matrix	Percolation threshold	σ_{MAX} (S/cm)	Aspect ratio	τ
Graphite particles (single crystal graphite flakes)	(1.25-2.5) x 10 ⁴ (in the basal plane) or 2 to 3 orders lower (normal to basal plane) [35]	2.25 [12]	0.0038335*	PU	0.7 vol.% [120]	~10 ⁻² (at 2 vol.%)	200	-
				PC	10.5 vol.% [121]	1.7 x 10 ⁻² (at 26.1 vol.%)	~1.65	-
Carbon black	-	1.9 [98]	0.0075**	PC	2.5 vol.% [121]	2 x 10 ⁻¹ (at 6.9 vol.%)	-	-
				PU	4.6 vol.% [122]	6.8 x 10 ⁻⁵ (at 6.02 vol.%)	L = - d ~ 30 nm	2.165
Carbon fiber	5.5x10 ² -9x10 ³ [7]	1.7 - 2.2 [7]	-	PI	0.24 vol.% [123]	2 x 10 ⁻¹ (at 7 vol.%)	100 - 200	3.1
				PC	9.0 vol.% [121]	9.5 x 10 ⁻² (at 27.1 vol.%)	8 - 11	-
SWCNT	Metallic – 10 ⁵ [34] Semiconducting – 0.1-100 [34] (1/3 metallic CNTs [33])	1.2-1.4 [7,12]	150-230	Epoxy	0.0052 vol.% [124]	10 ⁻⁴ (at 0.1 vol.%)	153-668	2.7 (+0.4/-0.8)
				Epoxy	0.0085 vol.% [124]	1 x 10 ⁻⁷ (at 0.04 wt.%)	55-321	3.1 (+1.2/-1.7)
				PI	0.05 vol.% [125]	4 x 10 ⁻² (at 5.7 vol.%)	2500-3333	2.77 (± 0.24)
DWCNT	Majority metallic characteristic CNTs [56,57]	1.5 [7] - 1.8 [12,126]	120	Epoxy	0.3 wt.% [127]	10 ⁻⁴ (at 2.5 wt.%)	L = - d ≤ 3nm	1.4-1.8
				PVDF	0.23 vol.% [128]	3 x 10 ⁻³ (at 0.4 vol.%)	133-2667	1.91
MWCNT	1.8 x 10 ³ [114]- 10 ⁴ [115] (majority metallic CNTs [58])	1.3 – 2.0 [7,12]	120	Epoxy	0.0025 wt.% [129]	2 x 10 ⁻² (at 1 wt.%)	~500	1.2
				PET	0.9 wt.% [130]	3 x 10 ⁻⁴ (at 9 wt.%)	1000	2.2

* Seab Gems Ltd. (Tanzania); ** Cabot Corporation (United States of America); *** Nanocyl S.A. (Belgium); PU= polyurethane; PC= polycarbonate; PI= polyimide; PET= poly(ethylene terephthalate); PVDF= poly(vinylidene fluoride)

4.4.1 Intrinsic properties of CNTs affecting their electrical conductivity

4.4.1.1 One-dimensional Transport

Due to its nanoscale, the transport of electrons in a CNT is governed by quantum effects and will occur only in the direction of its length [7], which is the same behavior observed in “quantum wires” [131]. Because of this, CNTs are generally considered as one-dimensional structures. However, this is valid only when their diameter is smaller than the electron mean free path, while, if the length is larger than it, the current flow could be described as diffusive/two-dimensional transport [40]. Moreover, the absence of defects and phonons also are requirements to allow a ballistic conductor.

4.4.1.2 Structure

According to the structure of CNTs, they can have either metallic or semiconducting behavior. Theoretically, the metallic ones (CNTs for which $\frac{m+2n}{3}$ is an integer) would be able to achieve a density of electric current 1000 times higher than metals like copper or silver [132]. Unfortunately, it is not possible up to now to control the synthesis of CNTs in order to produce only metallic or semiconducting CNTs. Besides many researchers [133,134] reported strategies for the separation of the desired CNTs, it was only in 2006 that Arnold *et al.* [135] solved the problems in the scalability through density gradient ultracentrifugation (DGU). This technique enabled a technical and commercial solution to the sorting of carbon nanotubes (yields of DGU process can exceed 10% in most cases, depending on the original raw material used) and in 2007 the north-american company NanoIntegris [53] has scaled up the separation of metallic and semiconducting CNTs. NanoIntegris has achieved over a 10,000x increase in production capacity since 2007, achieving the kilogram/year level (further scale-up is possible and will be continued once the market for SWNTs increases).

4.4.1.3 Aspect ratio and waviness

The percolation threshold is the critical value at which the long-range connectivity (percolation) first occurs. Therefore, the higher is the aspect ratio of the

electrical conductive component; the lower is its critical concentration to achieve percolation. For a 2D CNTN, for example, the critical content of CNTs, P_{CNT}^C [CNTs/ μm^2], has been correlated to the length of the CNTs, L_{CNT} [μm], according the following relation [136]:

$$P_{CNT}^C = \frac{(4.236/L_{CNT})^2}{\pi} \quad \text{Equation 4.1}$$

Nonstraightness (or waviness) has already found to influence the fraction of CNTs at which the percolation process begins (critical concentration of CNTs per area, P_{CNT}^C , or critical volume fraction, Φ_{CVF}) [35], which means that aspect ratio and nonstraightness affect the percolation threshold of CNTNs, as shown in Figure 4.5. However, in practice, it is still quite difficult and time consuming to evaluate the length of CNTs (L_{CNT}) or their effective length (L^{ce}).

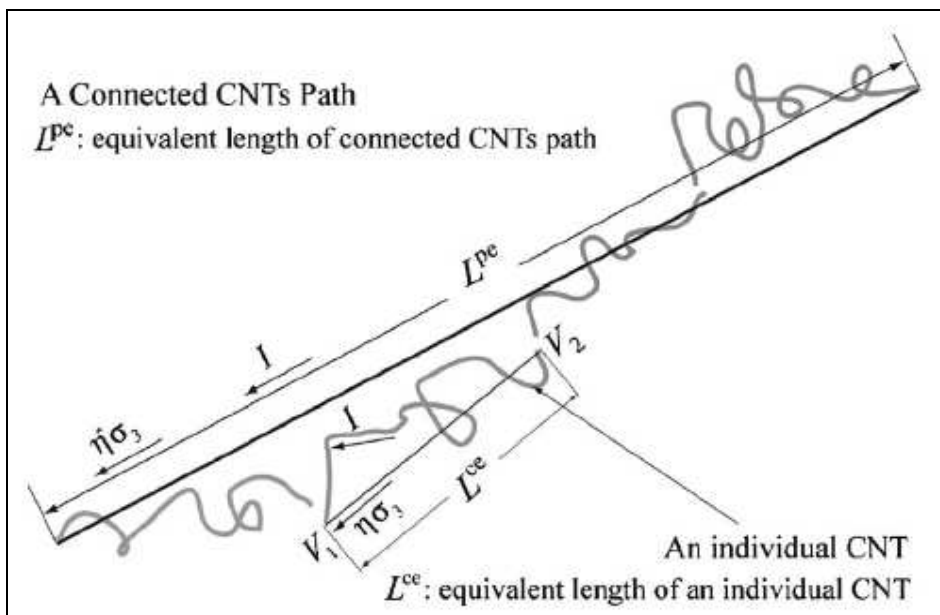


Figure 4.5 Pathway of CNTs connected, where L^{ce} is the equivalent straight length of each CNT, L^p is the length of the connected CNTs path and L^{pe} is the equivalent length of the CNTs path [35].

4.4.1.4 Defects, functionalization and doping

Like in any other material, the presence of structural defects strongly affects the electrical conductivity of CNTs. Defects act as points of dispersion (scattering centers) for the conduction of electrons, so increasing their number lowers the conductivity. For example, the presence of a structural defect in an armchair CNT

(with metallic behavior) might lead to a semiconductive behavior around these defects [38]. One example of structural defect is the so called Stone-Wales defects, which consist of groups of one pentagon and one pair of heptagons created by the rearrangement of the covalent bonds [137]. If these defects propagate along its structure, it might lead to a decrease of diameter and maybe to its rupture. Others examples of defects are: “kinks”, variations in diameter, change of number of walls, bamboo features, etc. Generally, MWCNTs present higher probability of presence of defects than SWCNTs. However, if defects are in the outer wall of MWCNTs, the electrons can still migrate from their outer to their inner wall and extend their electrically conductive pathway [50].

Structural defects can be originated from the synthesis method or from the processing of composites, for example. Generally high temperature methods generate more defect free CNTs. One of the steps that can introduce defects in the structure during the preparation of composites is in the dispersion of CNTs. In order to disperse them in aqueous solution, for example, the most efficient way is the use of surfactants or oxidizing agents both followed by sonication. According to the parameters of the sonication (intensity and sonication time) and the oxidizing agents (concentration, temperature and time in contact), one might create defects in the graphitic structure of CNTs. Indeed, in a systematic study on aqueous suspensions of SWCNTs, Henrich *et al.* [138] confirmed by atomic force microscopy that the distribution of lengths of CNTs depends on the time of sonication and this distribution decrease with time. Attrition milling is also found to create defects in the structure of CNTs, as well as shortening. Chemical oxidation also can shorts the CNTs and this might be controlled by the concentration and/or time in contact with acids [139].

The reactions of chemical functionalization can be divided into two main groups: physical or chemical adsorption. The most used physical adsorption methods (or non-covalent functionalization) are based on the use of surfactants. This process has the advantage of preserving the electronic structure of the aromatic surface of CNTs since the sp^2 structure and the bounds between the carbon atoms are maintained. However, the use of surfactant is generally avoided in nanocomposites since it remains in the nanocomposite and could decrease transport properties [36] by increasing the intertube resistance (wrapping of the CNTs). The functionalization by chemical adsorption or covalent interaction is an alternative to disperse CNTs in many solvents through the modification of the walls and tips of the CNTs. The

process of functionalization of CNTs consists of linking external elements to superficial atoms of the material, adsorbing functional groups that will modify their superficial properties. This procedure changes the wettability and adsorption properties of CNTs. Generally CNTs are not structurally perfect, presenting defects in their walls. Moreover, the extremities of CNTs are sites of high reactivity when compared with atoms along the cylinder(s) but they represent a very small part of the long CNTs. The unique structure of CNTs does not hinder the existence of unsaturated valences of carbon atoms located in external defects and their extremities where the carbon atoms present some sp^3 character and, still, between the layers, in the case of MWCNTs. Different methods exist to allow this grafting of functional groups onto the surface of the material and they can be chemically or thermally introduced. Treatments with acids or plasma are the most used.

The most commonly used oxidizing agents used to disperse CNTs in aqueous solutions are based on nitric acid or nitric acid associated with sulfuric acid (1:3 by volume of nitric acid per sulphuric acid). These oxidizing treatments can lead to shortening of the CNTs, holes in the sidewalls and a high density of oxygen containing groups (mainly carboxyl groups, but also carbonyl and/or hydroxyl groups), as represented in Figure 4.6. All these features will depend on how strong was the oxidation process (according to the temperature used, the acids concentrations, the use of sonication and the time in contact with the CNTs). When a strong process is used (with reflux, for example), the nitronium ion (NO_2^+) [140], also present in HNO_3/H_2SO_4 solutions, might even dissolve small-diameter (0.9-1.1 nm) metallic CNTs (charge transfer from m-SWCNTs to NO_2^+ : NO_2^+ can easily attack δ electrons in aromatic rings, leading to nitration). An extra addition of HCl at the end of the treatment with HNO_3/H_2SO_4 solution would not attack the CNTs, but would help to form carboxyl functional groups at the CNTs ends [95].

As it can be expected, a decrease of the electrical conductivity in composites after a strong functionalization of CNTs has already been reported [141]. However, it was also reported that it is even possible to increase the conductivity with functionalization when it is made in a mild way [142]. Barros *et al.* [143] suggested that SWCNTs behave as donors after the acidic treatment, with a charge transfer occurring from the nanotubes to the $-COOH$ groups.

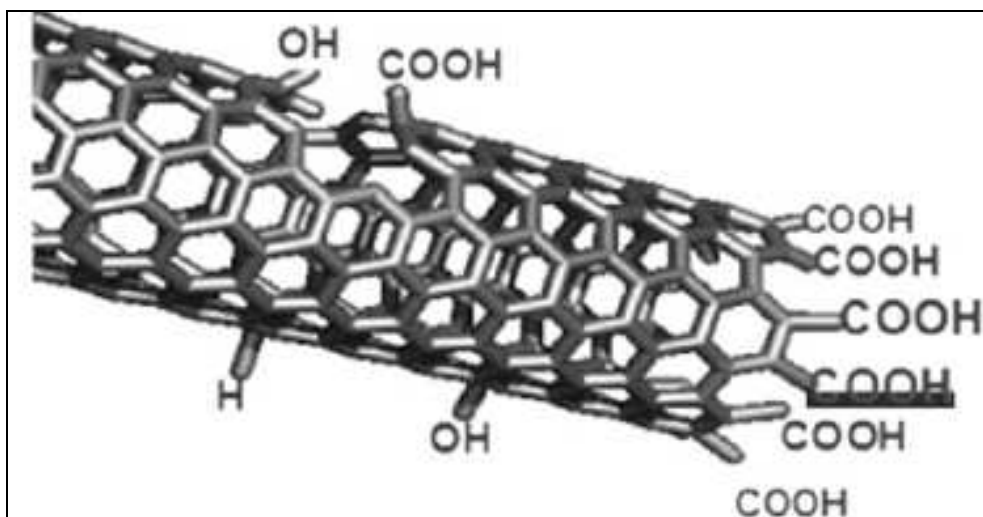


Figure 4.6 Schematic representation of the CNT structure after an oxidation process.

For a *realistic* graphene based nanotube a finite doping (extrinsic semiconduction) is inevitable due to the presence of adsorbates from the ambient medium, which would cause charge transfer [40]. Basically, two types of doping have been reported: (i) by adsorption of atoms and molecules in the CNTs; (ii) substitutional doping. Examples of doping by adsorption have been reported by Skákalová *et al.* [41] demonstrating that the electrical conductivity of SWCNT *buckypaper* can increase with ionic-acceptor dopings (like SOCl_2 , iodine, H_2SO_3 , etc.). The most reported examples of substitutional doping are the substitutions of an atom of carbon in a semiconducting CNT by boron (less electrons than carbon) or nitrogen (more electrons than carbon) atom to obtain a p-type or n-type semiconductor, respectively [39].

Raman spectroscopy (vibrational mode shift) and electrical conductivity at low temperatures (typically from 10K to 300K) are the most common techniques used to determine the charge transfer characteristics (which can be a doping or interaction of CNTs when they are embedded in a matrix) of CNTs [41].

4.4.2 Properties of CNTNs affecting the electrical conductivity

4.4.2.1 Phenomenon of Percolation

The percolation theory was firstly introduced by Broadbent and Hammersley [144] to understand the permeation of a gas in a porous medium. It is about statistic properties of randomly distributed objects disposed in a regular network. The

transport properties of these systems depend on their geometrical and morphological characteristics.

The critical volume fraction of filler at which a percolating network is initially formed depends strongly on the aspect ratio of the filler species and is referred as the percolation threshold. When the concentration of the filler is lower than the critical volume fraction, the property of the matrix is dominating, while when it is higher, the property of the filler is dominating. Since Φ_{CVF} denotes the volume fraction at which the percolation process begins and due to the random distribution nature of CNTs, the percolation of CNTs occur for a range of volume fractions above Φ_{CVF} . This is explained by the probability at which CNTs percolate (ξ), which increases from 0 to 1 as Φ_F increase from Φ_{CVF} to 1. For the sake of developing a simple model, Deng *et al.* proposed the following equation (Equation 4.2), which is valid for the whole realistic range of Φ_F [35]:

$$\xi = \frac{\sqrt[3]{\phi_F} - \sqrt[3]{\phi_{CVF}}}{1 - \sqrt[3]{\phi_{CVF}}}, \quad (\Phi_{CVF} \leq \Phi_F < 1) \quad \text{Equation 4.2}$$

Assuming a random orientation of CNTs in an insulator matrix, the classical percolation theory predicts that, above the percolation threshold, the conductivity of 2D and 3D CNTNs should be:

$$\sigma \alpha (A_F - A_{CAF})^\tau, \quad \text{for 2D CNTNs} \quad \text{Equation 4.3}$$

or

$$\sigma \alpha (\phi_F - \phi_{CVF})^\tau, \quad \text{for 3D CNTNs} \quad \text{Equation 4.4}$$

Where σ is the electrical conductivity of the composite, Φ_F (A_F) is the volume (area) fraction of the conducting filler phase, Φ_{CVF} (A_{CAF}) is the critical volume (area) fraction for the percolation threshold and τ is a critical exponent that indicates the dimensionality of the network [46].

In the case of 3D CNTNs, the value of the critical volume fraction can be calculated by [120]:

$$\phi_{CVF} = 1 - \exp\left(\frac{-V_{ex}V}{V_e}\right) \quad \text{Equation 4.5}$$

Where V is the volume of the filler (in this case, CNTs); V_e is the excluded volume of each filler; and V_{ex} ($V_{ex} = N_c V_e$ with N_c as critical number density of objects in the system) is the total excluded volume (between 1.4, for randomly oriented infinitely thin cylinders, and 2.8, for spheres [120]). For the calculation of the critical volume of real cylindrical particles, these values should be considered as the lowest and highest limits.

Taking into account that the volume of a hemisphere is $1/2 (4/3 \pi r^3)$ and that of a cylinder is $\pi r^2 L$, where r is the radius ($d/2$) and L is the length, the volume of CNTs, considering as end capped cylinders would be:

$$V = \pi \left(\frac{4}{3} \left(\frac{d}{2} \right)^3 + L \left(\frac{d}{2} \right)^2 \right) \quad \text{Equation 4.6}$$

The excluded volume V_e (excluded area in two dimensions) of an object is defined as the volume (area) around an object into which the center of another similar object is not allowed to enter if overlapping of the two objects is to be avoided. It depends on the aspect ratio of the “filler” and for CNTs in random distribution can be calculated by [120,145]:

$$V_e = \frac{4\pi}{3} d^3 + 2\pi d^2 L + \frac{\pi}{2} dL^2 \quad \text{Equation 4.7}$$

Where d is the diameter and L is the length of the “filler” (CNTs, in this case).

If the diameter of the CNTs is known, based on Equations 4.5, 4.6 and 4.7 it is possible to calculate their theoretical length:

$$\left(\frac{\pi d}{2} \right) L^2 + \left[\pi d^2 \left(2 + \frac{V_{ex}}{4 \ln(1 - \phi_{CVF})} \right) \right] L + \frac{\pi d^3}{3} \left(4 + \frac{V_{ex}}{2 \ln(1 - \phi_{CVF})} \right) = 0 \quad \text{Equation 4.8}$$

Celzard *et al.* [120] forecasted that for fillers with an aspect ratio higher than one hundred, like CNTs, the percolation threshold would be in the range of

0.24-1.35 vol.%. Experimentally, values as low as 0.0025 wt.% were already reported for MWCNTs [129]. As demonstrated in Table 4.1, the critical concentrations observed experimentally for unaligned CNTNs can be much lower than that predicted by the classical percolation theory, proving that the molecular interactions and alignment of the filler might influence the formation of a percolation network and showing the limitations of the percolation theory in the case of CNTs [146].

4.4.2.2 Thickness of CNTNs (2D systems)

The thinnest CNTNs with SWCNTs, like the individual semiconducting SWCNTs, present semiconducting behaviors (hopping conduction), while thick CNTNs with SWCNTs (free standing film) show more metallic behavior [58].

The electrical properties of CNTNs in 2D systems are generally given in the literature as the surface resistance (in Ohm/sq or Ω/\square) compared to the transparency (at $\lambda = 550$ nm) of the network [78,83-85,136]. Surface resistance (or conductance) is applicable to two-dimensional systems where the thin film is considered to be a two-dimensional entity. It is analogous to resistivity as used in three-dimensional systems. When the term surface resistance (or conductance) is used, the current must be flowing along the plane of the sheet, not perpendicular to it.

This is the most relevant information for practical applications and also due to the high error bars (caused by heterogeneity on the nanometer scale) and difficulty on the thickness measurement of such thin CNTNs. Combining both the modified Beer's law and percolation theory Kaempgen *et al.* found a quantitative relationship between the density of the CNT network and its transparency, as follows [136]:

$$P_{CNT} = \frac{\ln T}{-\alpha_{CNT}} \quad \text{Equation 4.9}$$

Where T is the optical transmittance of the network at 550 nm, α_{CNT} is the absorbance coefficient (whose value is $1.15 \times 10^{-5} \mu\text{m}^2$ for a light wavelength of 550 nm [136]), and P_{CNT} corresponds to the CNT density per area (CNT/ μm^2). Furthermore, the surface resistivity of thin networks also strongly depends on its density. Combining both the modified Beer's law and the percolation theory yields a new equation which fits a transparency *versus* resistivity plot very accurately, and

which validity has been demonstrated for the entire range of transmittance (0-100%) [136]:

$$R = R_0 (P_{CNT} - P_{CNT}^C)^{-\tau} \text{ or, alternatively, } \sigma = \sigma_0 (P_{CNT} - P_{CNT}^C)^{\tau} \quad \text{Equation 4.10}$$

Where P_{CNT}^C is the critical concentration of CNTs per area (CNT/ μm^2) and can be calculated as indicated in Equation 4.1.

4.4.2.3 Type of contact

According to some studies [147], the intertube interactions in a bundle of SWCNTs can either open a gap in metallic CNTs or reduce the gap of semiconducting CNTs. The contact resistance between CNTs is strongly dependent on the atomic structures in the contact region, the contact length (Figure 4.7), the nanotube diameter and the nanotubes structural relaxation. Measurements indicated that the junction resistance between SWCNTs can range from 100-400 k Ω for metal/metal or semiconducting/semiconducting junctions to two orders of magnitude higher for a metal/semiconducting junction [148]. However, theoretical calculations [119] reported that metal/semiconducting junction can even reach contact resistance two orders of magnitude higher than that reported by measurements [148]. Imperfect contacts and the presence of impurities lead to larger resistance values. However, in the case of DWCNTs or MWCNTs these interactions lead to more complex behaviors that make it difficult to predict [149]. Besides it is believed that great part of the current pass through the outer tube of a MWCNT, each CNT is comprised of concentric tubes that can be of different metallicity behavior and might interact between each other [50].

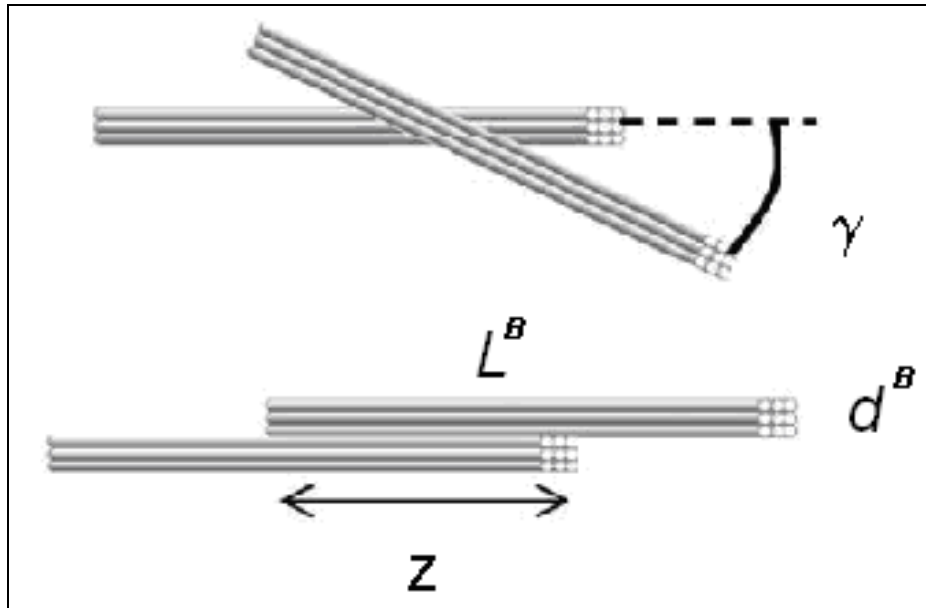


Figure 4.7 Schematic diagram of interacting CNTs bundles in a γ angle (top) and in parallel (bottom), where L^B and d^B are the length and width of the bundles [150].

4.4.2.4 Morphology of network

The strong intertube *van der Waals'* force often leads to a highly aggregated state, which significantly inhibits the state of dispersion of CNT. Therefore, the morphology of the CNTNs will influence the number of contacts between CNTs, and consequently in the final electrical conductivity. The conductivity σ_{dc} of CNTNs is expected to be inversely proportional to the average diameter of bundles (D_{av}) [43,44], but it is quite difficult to estimate the average diameter of bundles of CNTs, especially in a composite. Measurements of Hecht *et al.* [43] also indicated that the conductivity of CNTNs is proportional to the average bundle length of bundles (L_{av}) for bundles of similar diameters.

The morphology of CNTNs is affected by the processing and dispersion methods. The better dispersed are the CNTs, the lower is the concentration of CNTs needed to achieve the percolation threshold. The non-ideal state normally consists of bundles or clusters interconnected, where the later case will be expected to require higher amounts of CNTs to achieve the percolation threshold. In the other hand, it was reported that longer mixing time or higher screw speed during melt-mixing of the composites has a direct impact on the L/d (leading to attrition of MWCNTs and followed by their shortening), resulting in lower electrical conductivity [141].

Moreover, the density and the alignment of CNTNs strongly influence the electrical conductivity of the network. These parameters can be adjusted according to

the method of preparation selected. For example, by applying an electric field it is possible to achieve a high alignment of CNTs, so that the electrical conductivity measured perpendicularly to the alignment will be quite low, while in the direction of alignment it will be higher than an anisotropic CNTN with same density of CNTs. In the case of CNTNs density, two things are enclosed: the concentration of CNTs and the CNTN density itself. For 2D networks obtained by a filtration method [82], for example, more dense and homogeneous CNTNs are obtained than with spray-coating CNTNs [78].

Behnam *et al.* [42] theoretically predicted that a minimum resistivity of thick nanotube films occurs for a partially aligned nanotube film rather than for a perfectly aligned one. Moreover, they also found that values of the minimum resistivity and of the power law critical exponents strongly depend on the CNTs length, nanotube density per layer and distance between electrodes, as well as on the direction of measurement (case of strongly aligned films).

In the case of 3D CNTNs, more specifically ceramic composites, it was reported that spark-plasma sintering (SPS) can generate high densification [151] and is preferable to other sintering techniques. MWCNT-SiO₂ composites densified by SPS led to huge increases of the electrical conductivity when compared the composites and the matrix (silica σ_{DC} is about 10⁻²⁰ S/cm [98]): 10⁻¹⁰ S/cm was achieved with 1 vol.% of MWCNTs [100b], while 0.08 and 0.65 S/cm were measured for 5 and 10 vol.% MWCNTs-SiO₂ [30], respectively.

The effect of the dispersion of the CNTs in the CNTN has also been demonstrated by Li *et al.* [45] with entangled bundles and well dispersed individual CNTs in epoxy matrix.

Numerous models have been developed to predict properties of two phase composites. A simple mathematical model to estimate the electrical conductivity of composite materials with discontinuous fillers is the modified “rule of mixtures” [152]:

$$\sigma_C = \alpha\beta\sigma_F\phi_F + \sigma_M\phi_M \quad \text{Equation 4.11}$$

Where σ is the electrical conductivity, ϕ is the volume fraction and the subscripts C , M and F refer to the composite, matrix and filler (in this case, CNTs), respectively. The parameter β depends on the orientation of the filler and it is 0.2 if it is a random orientation in a tridimensional volume and considered as 0.35 if its

orientation is random in the two dimensional plane. The parameter α depends on the dimensions of the filler and can be calculated through the following equations [152]:

$$\alpha = 1 - \left[\frac{\tanh\left(a \frac{L}{d}\right)}{a \frac{L}{d}} \right] \text{ and } a = \sqrt{\frac{-3\sigma_M}{2\sigma_M \ln \phi_F}} \quad \text{Equation 4.12}$$

Where L and d are the length and diameter of the filler, respectively.

The exact values of some of the parameters used in Equations 4.11-4.12 are unknown, but considering the order of magnitude of the values encountered in the literature, the values used along this work were: $\sigma_M \sim 10^{-20}$ S/cm for silica [98] and 2.67×10^{-10} S/cm for pure chloroform (also known as trichloromethane) [153]. For CNTs, σ_{DC} (σ_F in Equation 4.11) along their axis was taken as 10^5 S/cm and 10 S/cm for metallic and semiconducting CNTs, respectively. Thus, in fact, two types of fillers with very different electrical conductivities are present. The proportion of semiconducting CNTs is 2/3 in the SWCNTs [33], while in DWCNTs and MWCNTs samples are mainly metallic. We propose a modification of the Equation 4.11 to take into account the three constituents: the two types of fillers, metallic and semiconducting CNTs (F_1, α_1 and F_2, α_2 respectively) and the matrix. In this case, it was considered 2/3 semiconducting in SWCNTs, while 2/3 metallic in DWCNTs. It is important to note that this equation does neither consider the intertube resistances nor the porosity of the system. Thus, this equation is neither appropriate for too porous materials nor for CNT contents below the CNT percolation threshold value (since intertube junction resistance predominates).

$$\sigma_C = \alpha_1 \beta \sigma_{F1} \phi_{F1} + \alpha_2 \beta \sigma_{F2} \phi_{F2} + \sigma_M \phi_M \quad \text{Equation 4.13}$$

5 MATERIALS AND METHODS

5.1 Carbon Nanotubes

All CCVD-CNTs (home-made produced and commercial ones) were characterized by electrical conductivity measurements, Raman spectroscopy and TEM. Their carbon content was measured by flash combustion method. All studies with commercial CNTs (their characterization and preparation of 2D CNTNs or 3D CNTNs in chloroform) were carried out during the studies at Max-Planck Institute für Festkörperforschung (Stuttgart, Germany), while the studies with home-made DWCNTs (their characterization and study in 3D systems: chloroform and silica) were carried out at Institut Carnot CIRIMAT at the Université Paul Sabatier (Toulouse, France).

5.1.1 Commercial CNTs

In the case of 2D CNTNs deposited over glass substrate and 3D CNTNs in chloroform medium, the commercial SWCNTs from Carbon Nanotechnologies Inc. (CNI Technology, USA) were studied and compared to other commercial CNTs: MWCNT-I (Nanocyl, Belgium), MWCNT-I-short (Nanocyl, Belgium) and MWCNT-II (Baytubes, Germany). Further details about these products obtained with the producers are described in Table 5.1. For this entire study, the CNTs were used as received.

Table 5.1 Main characteristics of the commercial CNTs given by the producers: aspect ratio measured by producers (TEM and SEM), carbon content wt.% (measured by thermal gravimetric analysis, TGA under air, or elementary analysis, EA) and other impurities (not mentioned or by ICP, inductively coupled plasma)

Material	Average Aspect ratio	Carbon content (wt.%)	Other impurities
SWCNT	550 (d ~ 1.2 nm, L ~ 0.66 μm)	~ 85 (TGA)	~5.9 wt.% (by ICP) of Fe (metal catalyst)
MWCNT-I	750 (d ~ 10 nm, L ~ 7.5 μm)	90 (TGA)	Fe and Co (metal catalyst)
MWCNT-I-short	370 (d ~ 10 nm, L ~ 3.7 μm)	~ 90 (TGA)	Fe and Co (metal catalyst)
MWCNT-II	379 (d ~ 14.5 nm, L ~ 5.5 μm)	> 95 (EA)	< 1 wt.% (by ICP) of Co (metal catalyst)

5.1.2 Synthesis and extraction of DWCNT

In the case of 3D CNTNs embedded in silica matrix, non-commercial CCVD-DWCNTs (thereafter called DWCNTs) were used. They were prepared at Institut Carnot CIRIMAT at the Université Paul Sabatier (France). These CNTs were also submitted to electrical measurements of 3D CNTNs in chloroform medium.

These DWCNTs were produced by CCVD using the route developed by Flahaut *et al.* [154]. Briefly, the catalytic material $Mg_{0.99}Co_{0.075}Mo_{0.025}O$ was prepared by solution combustion synthesis and then reduced in a H_2-CH_4 mixture (18 mol% CH_4 , heating and cooling rates of $5^\circ C \cdot min^{-1}$, temperature $1000^\circ C$, no dwell). This procedure allowed obtaining a DWCNT-CoMo-MgO composite powder that was then characterized by flash-combustion method to evaluate the carbon content.

In order to extract the DWCNTs, magnesia had to be dissolved. Thus, the DWCNT-CoMo-MgO composite powder was submitted to an acid attack by HCl at room temperature [154], which does not attack CNTs. The acid solution containing the DWCNTs was then filtered using an ultrafine membrane ($0.45 \mu m$) and rinsed with abundant deionized water. Initially, the extracted CNTs were dried in vacuum/stove, but later a non-dry route was developed to avoid agglomeration of CNTs. According to Flahaut *et al.* [154], this method of production of CNTs leads to

samples in which 77% of CNTs are DWCNTs with median inner and outer diameters of 1.35 nm (from 0.53 to 2.53 nm) and 2.05 nm (from 1.23 to 3.23 nm), respectively.

5.2 Production of CNTNs in 2D and 3D systems

Once CNTs were characterized, 2D and 3D CNTNs systems were produced and characterized as presented in the general schematic diagram in Figure 5.3. Two dimensional CNTNs with various concentrations of CNTs were prepared using HiPco SWCNTs. For the sake of comparison, different techniques were tested to produce 2D CNTNs (Figure 5.1): filtration method (FM), spray-coating (SC), dip-coating (DC) and electrophoretic deposition (ED). Furthermore, to have an idea of the effect of using different types of CNTs, 2D CNTNs of HiPco SWCNTs by FM were compared to 2D CNTNs of the commercial CCVD-CNTs MWCNT-I prepared by the same method. To prepare 3D CNTNs embedded in silica matrix (Figure 5.2), DWCNTs were used at different concentrations during the sol-gel process. To ensure a good dispersion of the nanotubes in the silica matrix they were functionalized (hereafter called *F-DWCNT*) prior to their dispersion. To densify these nanocomposites, spark plasma sintering (SPS) was used.

5.2.1 Two dimensional systems

CNTNs in a 2D system were prepared at Max-Planck Institut für Festkörperforschung (Stuttgart, Germany). These CNTNs were deposited on pre-silanized (3-Aminopropyltriethoxysilane, Fluka) vitreous silica substrates (Heraeus Quarzglas, SUPRASIL: more specifications in attachment) using four different methods [81]: dip-coating (DC), filtration method (FM), spray-coating (SC) and electrophoretic deposition (ED). The surface of these substrates had been previously cleaned with acetone and isopropanol with aid of bath sonication. To ensure a good adhesion of CNTs to the substrates, the later were left few minutes in contact with 3-aminopropyl-triethoxysilane water solution, except in the case of electrophoretic deposition. To compare these different preparation techniques between them, aqueous suspensions of HiPco SWCNTs (with ≤ 1 mg/mL) were used. To prepare

these suspensions, an aqueous solution of 1 wt.% sodium dodecyl sulphate (SDS; M.W. 288.38 g) was used in which SWCNTs were dispersed with aid of a probe sonicator UP200s Dr. Hielscher at 50% of the power output (titanium rod of a diameter of 14 mm). In order to avoid heating during sonication, the suspension was maintained into an ice/water bath. To avoid great damage to the SWCNTs, the sonication was maintained not longer than 35 min based on literature [138,155]. From these suspensions, CNTNs were deposited on silica substrates using the four different methods (Figure 5.1).

In order to evaluate the suitability of different CNTs materials for use in the preparation of CNTNs, other CNTNs were also prepared by filtration method, using MWCNT-I.

In order to remove the surfactant present in the suspension, all CNTNs deposited over the substrates were washed with deionized water by immersion.

Spray-coated CNTNs were prepared according to the work developed by Kaempgen *et al.* [78]. Briefly, it was performed using a commercial air brush pistol by adjusting the air flow (~1 bar) and spraying the CNTs suspension over the glass substrates over a hot plate (~140°C) to immediately dry the droplets. During this process, the substrate was being turned from time to time to obtain a homogeneous covering.

Dip-coating was performed using pre-selected conditions with the aid of a home-made apparatus. Briefly, a speed around 33.8 μm per second was used: higher speeds of dipping resulted in lower conductivities, probably due to turbulence increase and the shear force might have detached the nanotubes from the substrate. Between each dip, a pause (~1 min) was done to aid the evaporation of part of the solvent. The humidity of the atmosphere was monitored (HT-200 Voltcraft) and controlled (with aid of gas flow and vapors) to be about 80%.

For the filtration method, suspensions with different concentrations were filtrated trough a cellulose nitrate membrane (0.45 μm). The surface of the membrane containing CNTN was then carefully placed in contact with the glass substrate (taking care to not leave bubbles). After that, they were submitted to an acetone bath that dissolved slowly the membrane (acetone was changed 2-3 times until the complete dissolution of the membrane).

Electrophoretic deposited 2D transparent CNTNs were prepared according to the method developed during the period at Max-Planck Institut für

Festkörperforschung [156]. Briefly, an electrical conductive thin layer (10 nm) of aluminium was deposited (using thermal evaporation at the technical service from Max-Planck Institute für Festkörperforschung) on the glass substrate. This thin layer acted as the anode (positive electrode), while a copper electrode was used as cathode. For the deposition of CNTs, these two electrodes were immersed in a CNTs suspension and a voltage was then applied between them (electric field of ~ 25 V/cm) leading to the migration of the CNTs to the anode. During this process, the reduction of oxygen anions (electrolysis of water) at the anode generates the oxidation of the aluminium layer, and it becomes transparent. The electrophoretic deposition of CNT transparent films takes only few seconds. More details of the developed technique are reported on [156].

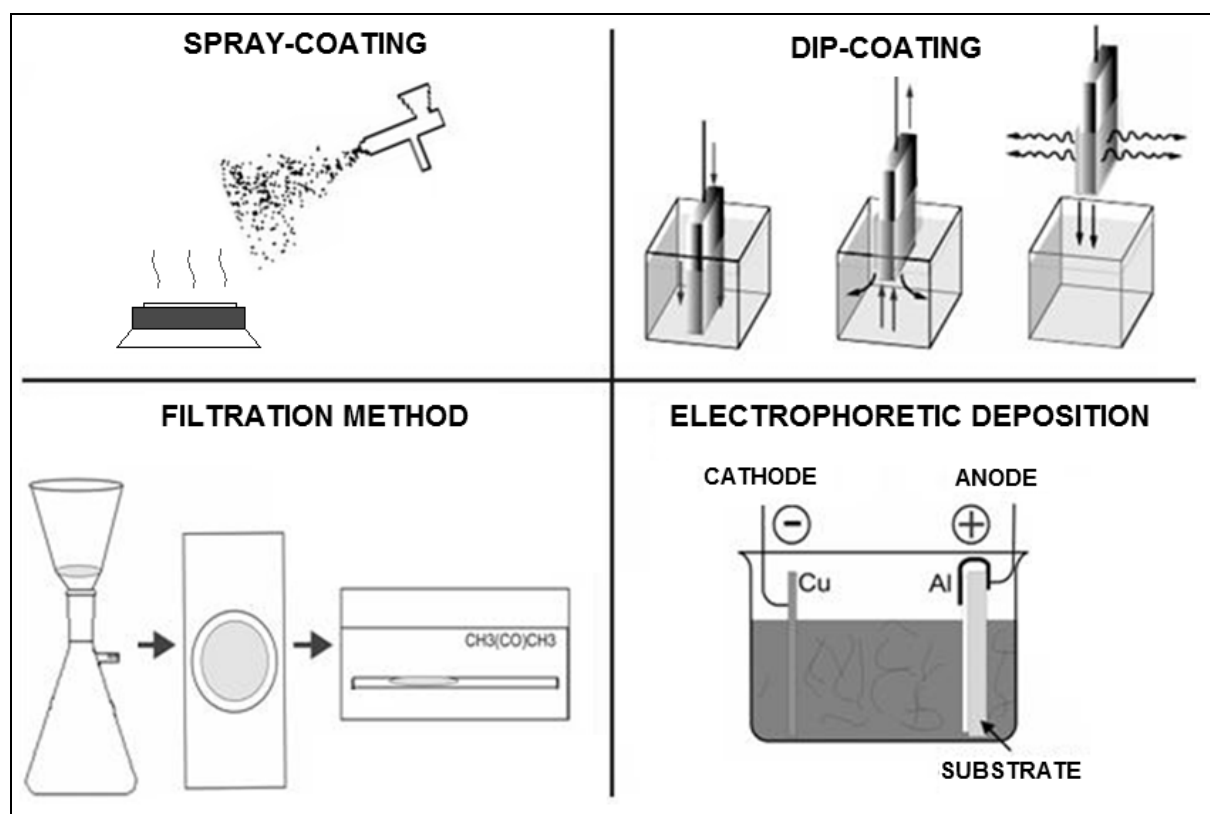


Figure 5.1 Schematic diagram of the post-growth techniques used in this work to prepare 2D CNTNs: spray-coating, dip-coating, filtration method and electrophoretic deposition.

5.2.2 Three dimensional systems

5.2.2.1 CNTNs suspensions – chloroform medium

Considering that CNTs can also create such percolating networks and conduct electric current in a liquid insulating medium, CNTs suspended in chloroform was considered as the ideal case of dispersion since it was under constant sonication. In this case, the contacts between the suspended CNTs are dynamic (Brownian motion and, eventually, liquid agitation).

The electrical conductivity measurements in chloroform (dielectric constant: ~4.81) were performed under constant sonication. The value of the current intensity was taken after its stabilization and before its decrease due to cutting of the CNTs. During these measurements, two processes occur: breakage of agglomerates and cutting of the CNTs. Only CNTs which have been dried (80-100°C in stove or at room temperature in dessicator) before their dispersion in chloroform were used.

5.2.2.2 Silica matrix nanocomposites

In order to prepare these composites, the sol-gel method was selected since it can allow a good dispersion of the CNTs at the nanometric or molecular level in the silica matrix. Another interesting property of the sol-gel matrix is that it contains many pores capable of encapsulating the guest molecules [25], metal NPs [25], and more recently, CNTs [93].

In this context, the classical organic route of the sol-gel method was chosen for convenience and nitric acid (HNO₃, 67%) was used as the acid catalyst since it can be most easily eliminated through calcination at 400°C for 2h before the densification by SPS. Furthermore, CNTs wrapped with surfactant would increase the intertube/interbundle resistance [36]. Therefore, a preliminary study of different functionalization routes was required. The stability and ability of dispersion of different kind of functionalized CNTs solutions in the presence of nitric acid (or its counterpart for basic pH) was evaluated by zeta potential in different pH media and by observing its tendency of agglomeration with time.

Once the functionalization route was selected, the preparation of *F*-DWCNTs-SiO₂ composites was performed. It can be divided into the following steps (Figure 5.2): (i) functionalization of DWCNTs; (ii) dispersion of *F*-DWCNTs in acid aqueous

solution; (iii) *in-situ* sol-gel preparation with the *F*-DWCNTs dispersion; (iv) calcination of the xerogel powder; (v) densification of the CNT-SiO₂ composite by SPS.

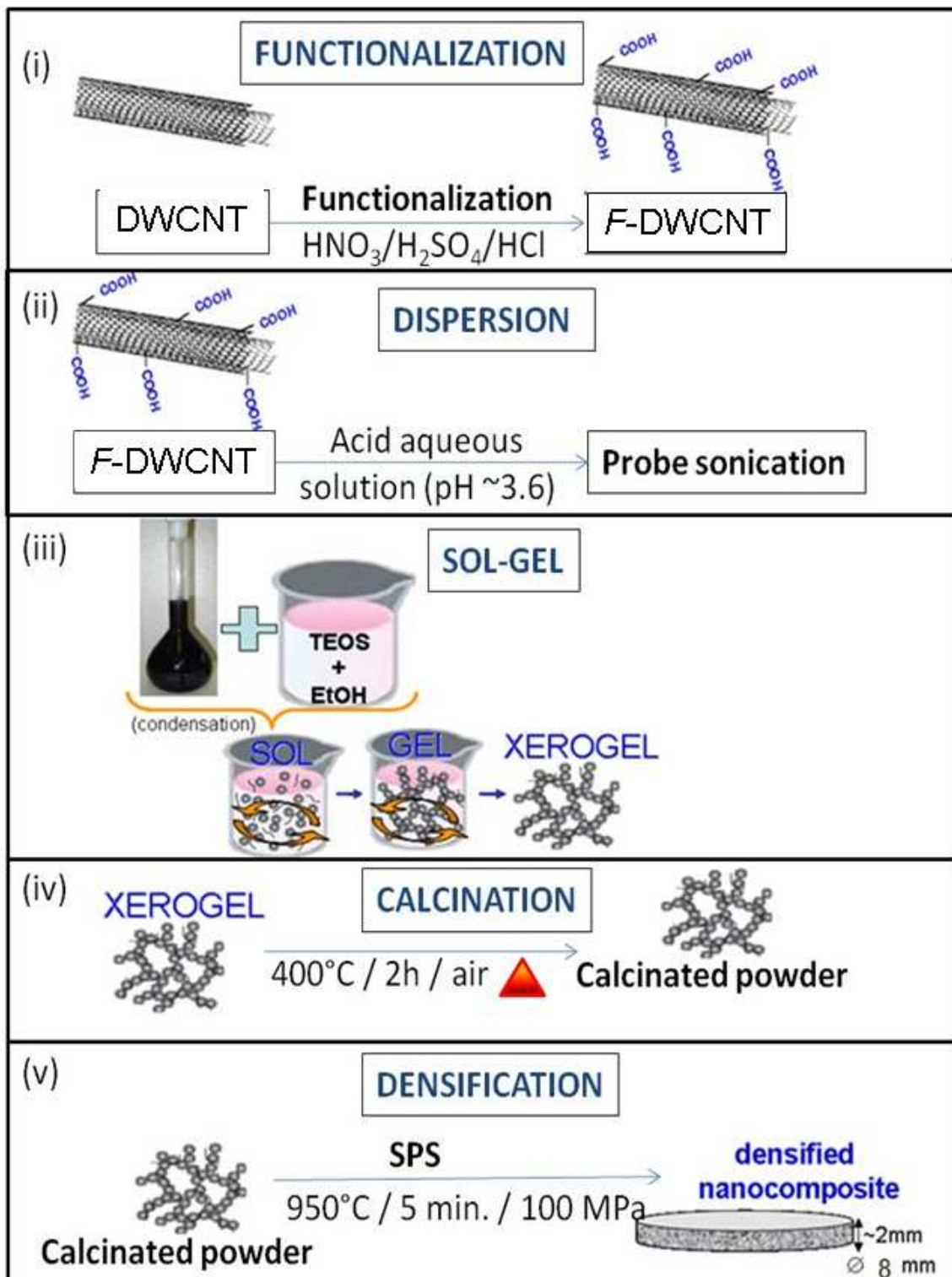


Figure 5.2 Schematic diagram of the steps for the preparation of 3D CNTNs using *F*-DWCNTs embedded in silica matrix SiO₂: (i) functionalization of DWCNTs; (ii) dispersion of the *F*-DWCNTs into acid aqueous solution with the aid of probe sonication; (iii) *in-situ* production of silica (precursor: tetraethylorthosilicate, TEOS) over *F*-DWCNTs through organic sol-gel route; (iv) calcination of the nanocomposite xerogel; (v) densification of the calcinated powder through spark-plasma sintering (SPS).

Pre-tests with the most used functionalizations (carboxylic) were carried out and a “soft” route that avoids reflux and use of a sonication bath instead was adopted. Thus, DWCNTs produced by CCVD were acid-functionalized using nitric, sulphuric and chloridric acids based on the work of Chen *et al.* [95]. Briefly, CNTs are submitted to a mixture of nitric and sulfuric acids (1:3) for 24h (with the first 10 minutes in a sonication bath with an ice/water bath and then left with magnetic stirring). After that, HCl is added for 10 minutes in contact during magnetic stirring. Finally, the mixture is diluted and neutralized, followed by filtration through a 0.45 μm pore size membrane and abundant rinsing with deionized water. Then, a nitric acid aqueous solution containing undried *F*-DWCNTs was prepared with the aid of sonication probe (Bioblock Scientific Vibracell 75042). Initially, pH around 2 was used, but later pH around 4 was selected since the suspensions would be more stable according to tests of zeta potential (further details are shown in the next chapter). To avoid great damage to the CNTs, the sonication was not longer than 35 min based on literature [138,155].

These suspensions were incorporated while magnetic stirring into an alcoholic solution containing tetraethylorthosilicate (TEOS, 98-99%) as silica precursor, followed by one minute of sonication and then let to gelify while stirring. For the sake of comparison, a product without CNTs (pure SiO_2) was prepared by the same route. Initially, the molar ratio r of water to TEOS was varied (4.5, 16.4, 20), but then in order to decrease the concentration of CNTs in aqueous suspension, it was fixed to 20 (based on Brinker *et al.* [25]). Finally, the molar ratio of ethanol (EtOH, 99.9%) to TEOS was used at 0.3 (based on Brinker *et al.* [25]). The xerogels were grinded and calcinated in air at 400°C. After that, the carbon contents in the so-obtained composites powders were evaluated by flash combustion method. These powders were densified by SPS (Dr. Sinter 2080, SPS Syntex Inc. at the *Plateforme Nationale CNRS de Frittage-Flash - PNF2*, Toulouse) using a 20 mm (initially) or 8 mm (last set of samples) inner diameter graphite die. The SPS parameters were chosen according to some preliminary tests (described in the next chapter) which allowed achieving quite high densifications. The used temperature (950°C) was quite lower than the temperatures at which the carboreduction of silica occurs (1500-1700°C)

[157], while the vacuum and short time of sintering warranted by SPS would help to minimize damage to *F*-DWCNTs.

The densified composites were then characterized by field-emission-gun scanning electron microscopy (FESEM) of fractured surfaces, specific gravity measurements, Raman spectroscopy, X-ray diffraction and electrical conductivity measurements. These techniques are briefly described in the following section, while the results of the characterizations of the samples are presented and discussed in chapter 6.

5.3 Characterization Methods

To evaluate the electrical conductivity of the CNTNs and to obtain an evaluation of the CNTs aspect ratio, experiments with 3D CNTNs in the chloroform medium with various concentrations of CNTs (DWCNT, *F*-DWCNT and commercial ones) in a dynamic mode were performed through the technique developed during the period of research work at Max-Planck Institut für Festkörperforschung [158]. Other techniques of evaluation include, in the case of 2D CNTNs: electrical conductivity measurement by 4 points (as surface resistance/conductance), UV-Vis transparency at 550 nm by UV-Vis spectroscopy and roughness by atomic force microscopy. In the case of 3D CNTNs embedded in silica matrix, the other characterizations include: electrical conductivity by 2 points, density, field-emission-gun scanning electron microscopy and X-ray diffraction. Further details about the characterizations indicated in Figure 5.3 are described, as follows.

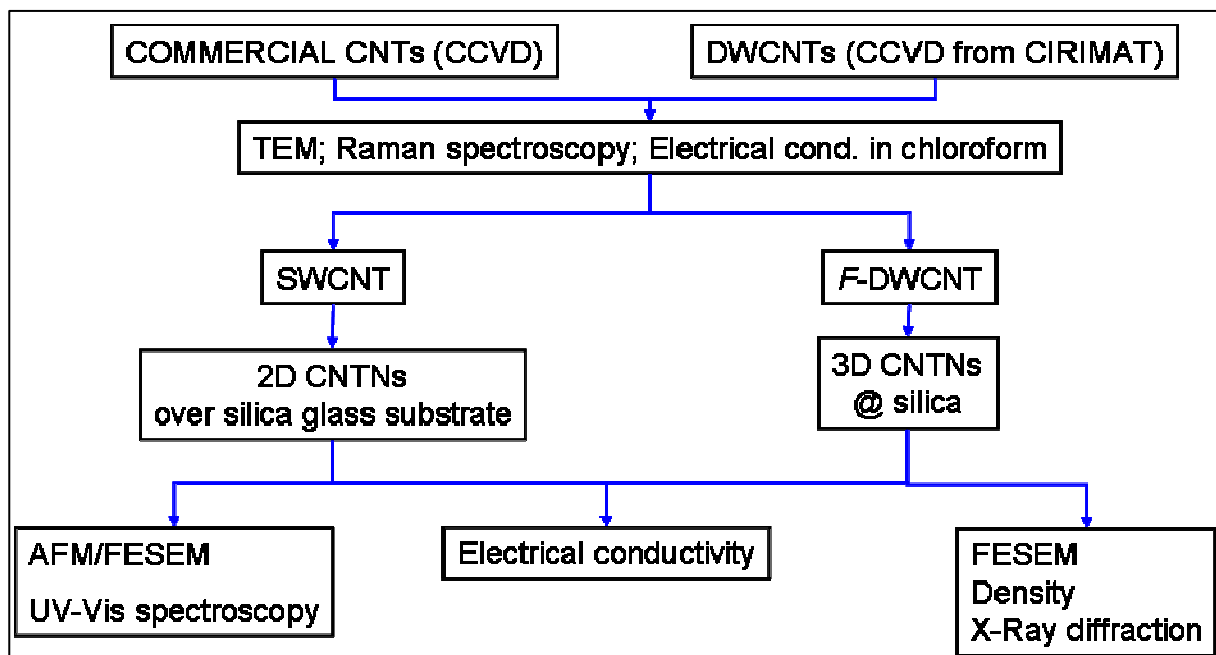


Figure 5.3 Schematic diagram of the overall experimental procedure to produce CNTNs in 2D (spray-coating, dip-coating, filtration method and electrophoretic deposition) and 3D - in liquid with chloroform or in silica prepared by sol-gel and densified by spark-plasma sintering (SPS).

5.3.1 Spectroscopic and optical characterizations

5.3.1.1 Raman Spectroscopy

Raman spectroscopy measurements of the (*F*-)CNTs and *F*-DWCNTs-SiO₂ nanocomposites were done with a 20x objective lenses with a 632.82 nm laser line (1.96 eV energy line) and a laser power of about 4 mW (Jobin Yvon-LabRam spectrometer). These measurements were carried at Max-Planck Institut für Festkörperforschung and at the “service commun de spectroscopie Raman” of Université Paul Sabatier.

5.3.1.2 UV-Vis spectroscopy

A Perkin Elmer Lambda 2 spectrometer was used to evaluate the transmittance of the 2D CNTNs. A commercial ITO with 100 nm of thickness over glass was used as comparison. These measurements were carried out at Max-Planck Institut für Festkörperforschung.

5.3.1.3 Fourier Transform Infrared spectroscopy

Functionalized DWCNTs were characterized by infrared (IR) spectroscopy (Bruker FT-IR spectrometer) in order to check the presence of carboxylic groups after functionalization of DWCNTs. For comparison, DWCNTs before functionalization step were also analyzed. These measurements were carried out at CIRIMAT at Université Paul Sabatier.

5.3.2 Zeta potential

Pre-tests of zeta potential measurements (Malvern Instruments DTS5300) of functionalized and non-functionalized DWCNT were carried out at various pH (with additions of nitric acid or ammonia hydroxide). The results obtained by zeta potential are discussed in the next chapter. These tests were carried out at CIRIMAT at Université Paul Sabatier.

5.3.3 Electron and Atomic Force Microscopies

Transmission electron microscopy (TEM, Philips CM 200 from Max-Planck Institut für Festkörperforschung, and JEOL JEM 1011 from “service commun TEMSCAN” at Université Paul Sabatier) were used to characterize the (*F*-)CNTs themselves, while observations of the 3D CNTs embedded in silica matrix (fracture surface of the *F*-DWCNTs-SiO₂ nanocomposites) were carried out with a field-emission-gun scanning electron microscopy (FESEM, JEOL 6700F from “service commun TEMSCAN” at Université Paul Sabatier) mainly to evaluate the state of dispersion of the *F*-DWCNTs in the matrix. All characterizations involving DWCNTs were carried out in CIRIMAT at Université Paul Sabatier (Toulouse, France), while others (commercial CNTs) were carried out at Max-Planck Institut für Festkörperforschung.

AFM (Veeco Digital Instruments model Nanoscope IIIA) was used to evaluate the roughness (important for some applications) and state of dispersion of the 2D CNTNs. A commercial ITO with 100 nm of thickness over glass was used as comparison. All these characterizations involving 2D CNTNs were carried out at Max-Planck Institut für Festkörperforschung.

5.3.4 Electrical conductivity and properties of percolation

The electrical conductivity of CNTs and CNTNs was evaluated according to schematic diagram demonstrated in Figure 5.4 which is briefly summarized as follows.

The electrical conductivity in 3 dimensional systems was calculated by the relation:

$$\sigma_{DC} = \frac{I * H}{V * A} \quad \text{Equation 5.1}$$

Where σ is the electrical conductivity, I is the electric current measured between the electrodes, V is the voltage applied between the electrodes, H is the distance between the electrodes and A is the area of the electrodes.

As previously explained, in the case of 2 dimensional systems the surface resistance was calculated by the relation:

$$R_s = \frac{R * W}{H} \quad \text{Equation 5.2}$$

Where R_s is the surface resistance, R is the resistance of the 2D CNTNs, H is the distance between the electrodes and W is the length of the electrodes.

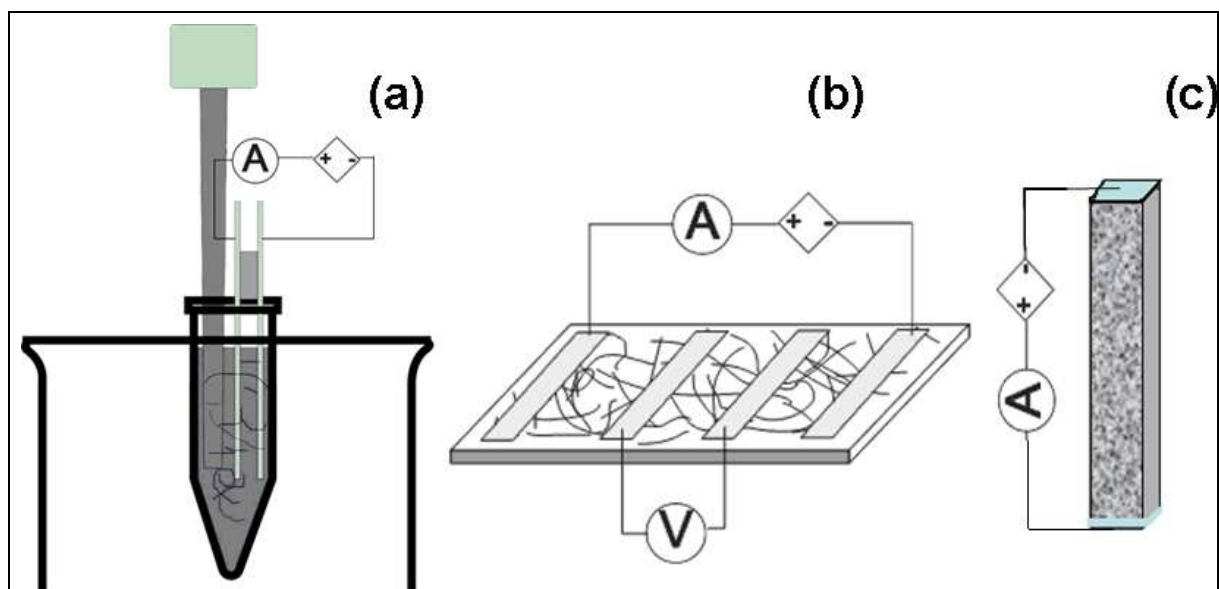


Figure 5.4 Schematic diagram of apparatus used for electrical measurements of (a) 3D CNTNs in a liquid electric insulator matrix; (b) 2D CNTNs; (c) 3D CNTNs embedded in silica matrix.

A new alternative method was proposed [158] during the period at Max-Planck Institut für Festkörperforschung to measure electrical conductivity of dispersions of CNTs (with the aid of probe sonication) in an electric insulator liquid (chloroform, CHCl_3), where the CNTs would behave similarly as in solid electric insulating matrices. For these measurements, chloroform stabilized with about 0.6% of ethanol was obtained from VWRTM International with purity of 99.8% (water content about 0.05%). More details about this method were described in [158]. To maintain a dispersed state of CNTs in the liquid and avoid the nanotubes to be aligned by the electric field, a probe sonicator (UP100H Dr.Hielscher, with a titanium probe of 2.5 mm diameter, and using a power output of 20%) and a low voltage are used for these experiments. Briefly, an electric field of 0.104 V/cm is applied between two copper electrodes (typical distance of ~3 mm) and the electric current flows in the suspension of CNTs through the network of CNTs that is formed (Figure 5.4a). Higher electric fields without ultrasound sonication make CNTs to form a percolation pathway quite rapidly due to alignment and make them move toward the electrodes due to electrophoretic forces [158]. The concentration of CNTs in the suspension can be adjusted and volumes of 2-3 mL use to be quite enough for such measurements, while the quantity of CNTs necessary to these experiments is relatively small (few milligrams). The values for each concentration were considered as the maximum achieved along time, typically at 10-15 min (see attachment). The measurement of the electrical conductivity of CNT suspension in liquid allows the determination of the

value of the percolation threshold concentration, by way of systematically tuning the amount of CNTs in the liquid. As it can be expected, the conductivity is also highly sensitive to the purity of the material, the kind of material (SWCNTs, DWCNTs or MWCNTs in the present study) and its aspect ratio. This is a quite useful method to compare or select different kinds of materials to be used in a composite for electrical applications, for example.

For comparison, *buckypapers* were also prepared (at Max-Planck Institut für Festkörperforschung) by dispersing CNTs in an aqueous solution containing 1% of sodium dodecyl sulphate (SDS) with the aid of a sonicator probe and then passing this solution through a filtration membrane (0.2 μm porosity). The final thickness of these *buckypapers* was about 50 μm . The conductivity of these self standing papers of CNTs was measured using 4 probes electrodes, a continuous current source and a nanovoltmeter (Keithley Instruments).

Electrical conductivity of the CNTNs in 2D systems was also measured (at Max Planck Institute für Festkörperforschung) in a 4 probe configuration (Figure 5.4b) using Keithley Instruments. In order to that, 4 electrodes of Pd/Au (200/2000 \AA thickness) with 3 mm of length were deposited (by the technical service of Max Planck Institute für Festkörperforschung) over the transparent CNTNs with the aid of an evaporation mask (about 0.25 mm of distance between the two outer pairs of electrodes and about 0.5 mm between the inner pair), as shown in Figure 5.5a. After that, it was placed into a chip carrier and wires were also placed between the Pd/Au layers and the electrodes from the chip carrier. A special support was used to place the chip carrier and characterize the CNTNs (as displayed in Figure 5.5b). A commercial ITO with 100 nm of thickness over glass was used as comparison.

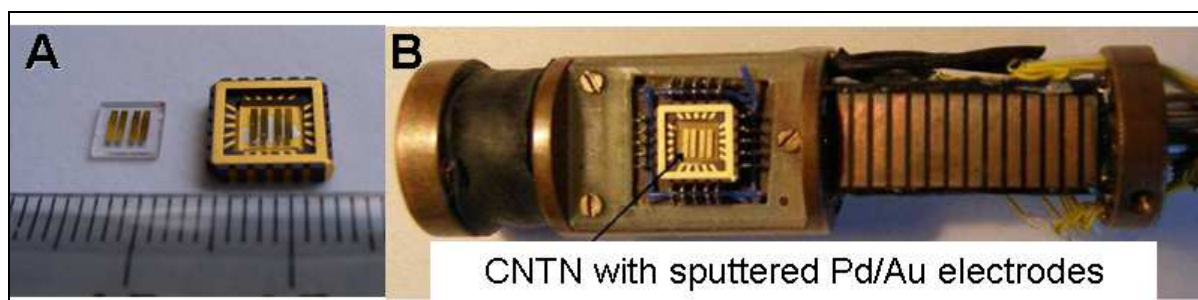


Figure 5.5 Configuration for the electrical conductivity measurements of CNTNs in 2D systems using Pd/Au (200/2000 \AA) electrodes that were deposited by the technical service of Max Planck Institute for Solid State Research.

To measure the electrical conductivity of the *F*-DWCNT-SiO₂ composites (at CIRIMAT at Université Paul Sabatier), the densified samples were cut (Buehler Isomet 4000) and polished (Buehler Phoenix 4000) into bars. The two square faces of the sample in contact with the electrodes were coated with silver paint in order to reduce discrepancies arising from microroughness. Then, the electrical conductivity of the *F*-DWCNT-SiO₂ nanocomposite was measured using a Philips PM2525 apparatus (Figure 5.4c).

5.3.5 Carbon content

The carbon content (C_n , wt. %) in the CNT-nanocomposite powders was measured by the flash-combustion method. It consists of a preheating of the powder at 925°C followed by fast heating at 1800°C for about 1 s and measuring the amount of produced CO₂. The accuracy of the measurements is ± 2 % and each measurement uses few milligrams of sample. These evaluations were carried out at the *Centre National de la Recherche Scientifique (CNRS)* in Toulouse (France).

5.3.6 Specific surface area

The specific surface area (m²/g) of a CNT-nanocomposite and a pure silica powders were calculated according to the measurements carried out with Brunauer-Emmet-Teller single-point method at Micromeritics AutoMate 23 FlowSorb II-2300 (at CIRIMAT at Université Paul Sabatier) using N₂ adsorption at liquid-N₂ temperature. The accuracy of the measurements is ± 3 % and each measurement uses tens of milligrams of sample.

5.3.7 Density determination

The relative densities of the SPS densified samples were calculated for nanocomposites whom the matrix is amorphous by taking into account the specific gravity of the sample and the theoretical density according to the carbon content of the sample, considering that the specific gravity of amorphous silica is 2.2 g/cm³ [98] and the specific gravity of DWCNTs is 1.8 g/cm³ [12,126]. The Archimed's method was chosen to check all samples and few of them (the ones that seem more porous) were cross checked with geometrical measurements (dividing the weight of the

sample in air by its volume). Firstly, the sample is weighed in air and then in water. Specific gravity can then be calculated using the formula $SG = \frac{W_{air}}{W_{air} - W_{water}}$, where W_{air} is the weight of the sample in air (measured in some unit of force) W_{water} is the weight of the sample in water (measured in the same units).

Alternatively, for too porous materials, the relative density can be calculated directly by calculating the density of a sample (after weighting and measurements of its dimensions) and dividing it by the (known/calculated) theoretical density.

For these measurements it was used a KERN ARJ 220-4M balance with an uncertainty of ± 0.00028 g. These measurements were carried out at CIRIMAT at Université Paul Sabatier.

5.3.8 X-ray diffraction

XRD patterns of the *F*-DWCNT-SiO₂ nanocomposites were recorded in the range 10-100° (2θ) using a Bruker D4 Endeavor diffractometer (at CIRIMAT at Université Paul Sabatier) equipped with a Cu K_{α} radiation tube ($\lambda = 1.5406$ Å). Counts were registered every 0.02° (2θ).

6 RESULTS AND DISCUSSIONS

6.1 Characterization of CNTs

Figures 6.1-6.3 show TEM micrographs of the CNTs materials used in this work. The typical average diameters of commercial CNTs seem to be in good agreement with the characteristic data informed by the producers (Table 5.1). SWCNT's diameters in TEM observations (Figure 6.1) varied from 0.6 to 1.4 nm and generally gathered in bundles of tens of nanometers. All MWCNT samples (Figures 6.2 and 6.3) look very similar, even though, as demonstrated later by the results obtained from our new method, they exhibit quite different electrical properties in percolating networks. The outer diameter distribution for MWCNT-I and MWCNT-I-short is about 4–20 nm (Figure 6.2), while for MWCNT-II it varies between 5–21 nm (Figure 6.3), as measured by TEM.

Regarding other carbon structures besides CNTs, disordered carbon, carbon fibers and graphitic shells were easily observed (black arrows in Figures 6.1-6.3) in MWCNT-II, but also visualized in MWCNT-I(-short) and SWCNT samples. Generally, MWCNTs use to have higher $I_{D/G}$ ratios (in Raman spectra) than SWCNTs due to their sp^3 defects and this is in good agreement with the low $I_{D/G}$ ratio in the later ones (Table 6.1). While in the case of MWCNTs disordered carbon was observed as great deposits (MWCNT-II) or as graphite shells, in SWCNTs (mainly as bundles) it is observed a lot of disordered carbon around their outer walls (Figure 6.1A2). Defects (red arrows in Figures 6.2 and 6.3) were observed in all MWCNTs (MWCNT-I, MWCNT-I-short and MWCNT-II). It is possible to observe topological defects like variations in diameter, Lchange of number of walls, etc. No such defects were observed in SWCNTs. It was possible to observe encapsulated metal NPs in all CNTs (blue arrows in Figures 6.1-6.3). Micrographs show that in SWCNT samples all metal NPs (~5.9 wt.% Fe by Inductive Coupled Plasma analysis according to producer) are attached to the NTCs, while in MWCNT-I (Fe and Co according to producer) and MWCNT-II (< 1 wt.% Co by elementary analysis according to producer) the metal NPs can also be found surrounded by disordered carbon or graphitic shells (black arrows).

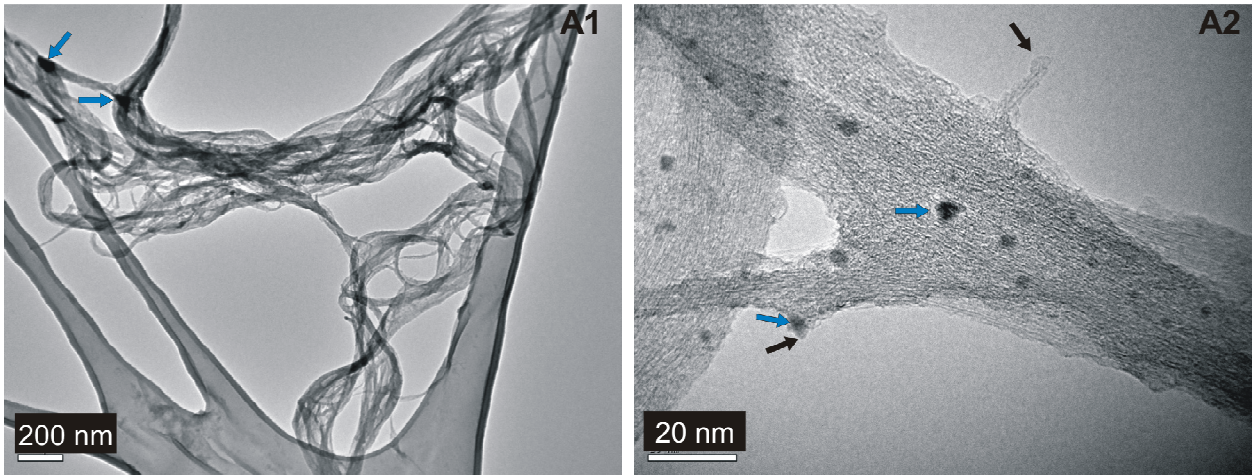


Figure 6.1 TEM micrographs of SWCNT (mainly gathered in bundles). Black arrows as other carbon impurities (disordered carbon) and blue arrows as metal NPs.

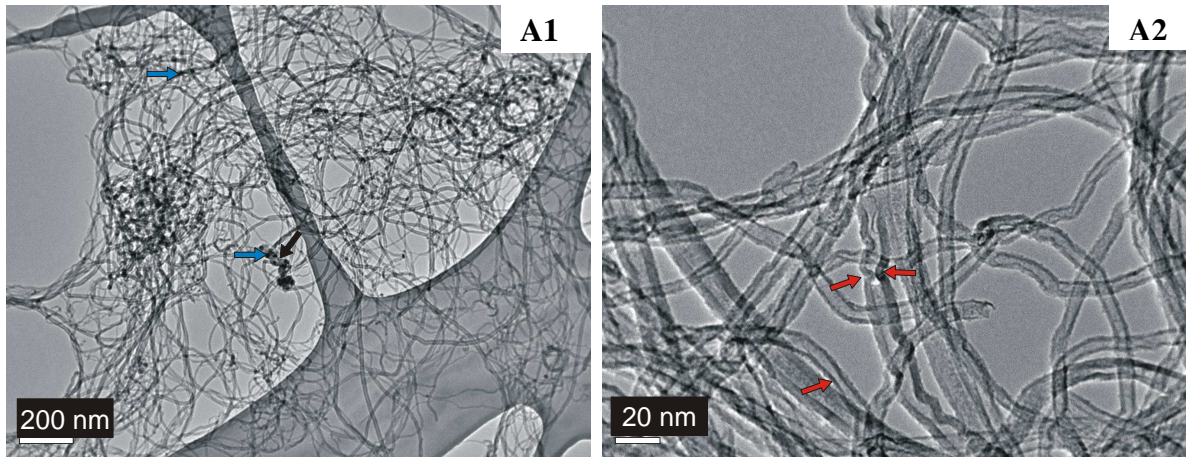


Figure 6.2 TEM micrographs of (A) MWCNT-I and (B) MWCNT-I-short: Red arrows as defects, black arrows as other carbon impurities and blue arrows as metal NPs.

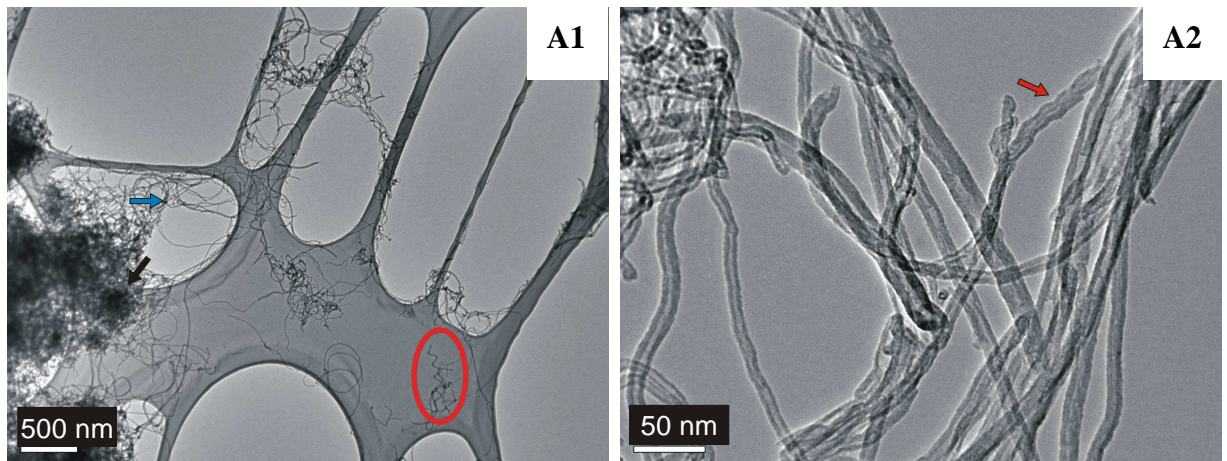


Figure 6.3 TEM micrographs of MWCNT-II: Red arrows/circle as defects, black arrows as other carbon impurities and blue arrows as metal NPs.

Figure 6.4 shows Raman spectra of all commercial CNTs and of a commercial graphite for comparison. All the spectra are normalized to the D^* mode at about 2600 cm^{-1} , which does not depend on defect concentration [159].

Raman spectra of the SWCNT sample is shown in Figure 6.4A. As could be expected, the radial breathing modes (*RBM*) at low frequencies ($196\text{-}296\text{ cm}^{-1}$) are only visualized for HiPco SWCNTs, which have a diameter distribution centered on 1.2 nm [78,158]. As indicated in Table 6.1, besides SWCNT product has the lowest carbon content (81.3-85 wt.%) in comparison to other CNTs, it presents the lowest $I_{D/G}$ (0.05) and I_{D/D^*} (0.43). The lower intensity of the ratio between the Diamond (or “defect”) mode (*D*) at about 1302 cm^{-1} , induced by sp^3 electronic states (considered as defects in the planar sp^2 graphitic structure), and the tangential mode (*G*) at about 1580 cm^{-1} of SWCNT sample indicates that HiPco SWCNT product contains less structural defects or sp^3 carbon like material than any MWCNT material. In the case of SWCNTs, the strong signal of the graphene tangential mode is strongly affected by the resonance effect, which impairs the reliability of the $I_{D/G}$ (*D/G* ratio); some reports, therefore, use I_{D/D^*} (*D/D** ratio) instead [159], which is listed in Table 6.1.

Raman spectra of graphite and MWCNTs (Figure 6.4B) differ from the spectra of the SWCNT sample mainly by the absence of the *RBM* feature. Since the resonance effect in MWCNTs is small, a structural disorder is well characterized by the ratio of the *D* to *G* modes intensities. The values of this ratio are summarized in Table 6.1 and demonstrate that the graphite studied in the work has far less sp^3 defects than MWCNTs. As could be expected, a slightly higher number of defects is present in MWCNT-I-short ($I_{D/G}=1.69$) than in MWCNT-I (longer tubes: $I_{D/G}=1.67$). However, besides MWCNT-II exhibits the highest carbon content (95-95.6 wt.%) in comparison to other CNTs, the highest $I_{D/G}$ (1.75) is indicative of disorderly structure. This coincides with the observations from TEM images (Figures 6.2 and 6.3). Indeed, TEM observations of MWCNT-II (Figure 6.3) showed a great amount of disordered carbon and topological defects, which could be considered as reflecting defects in its structure.

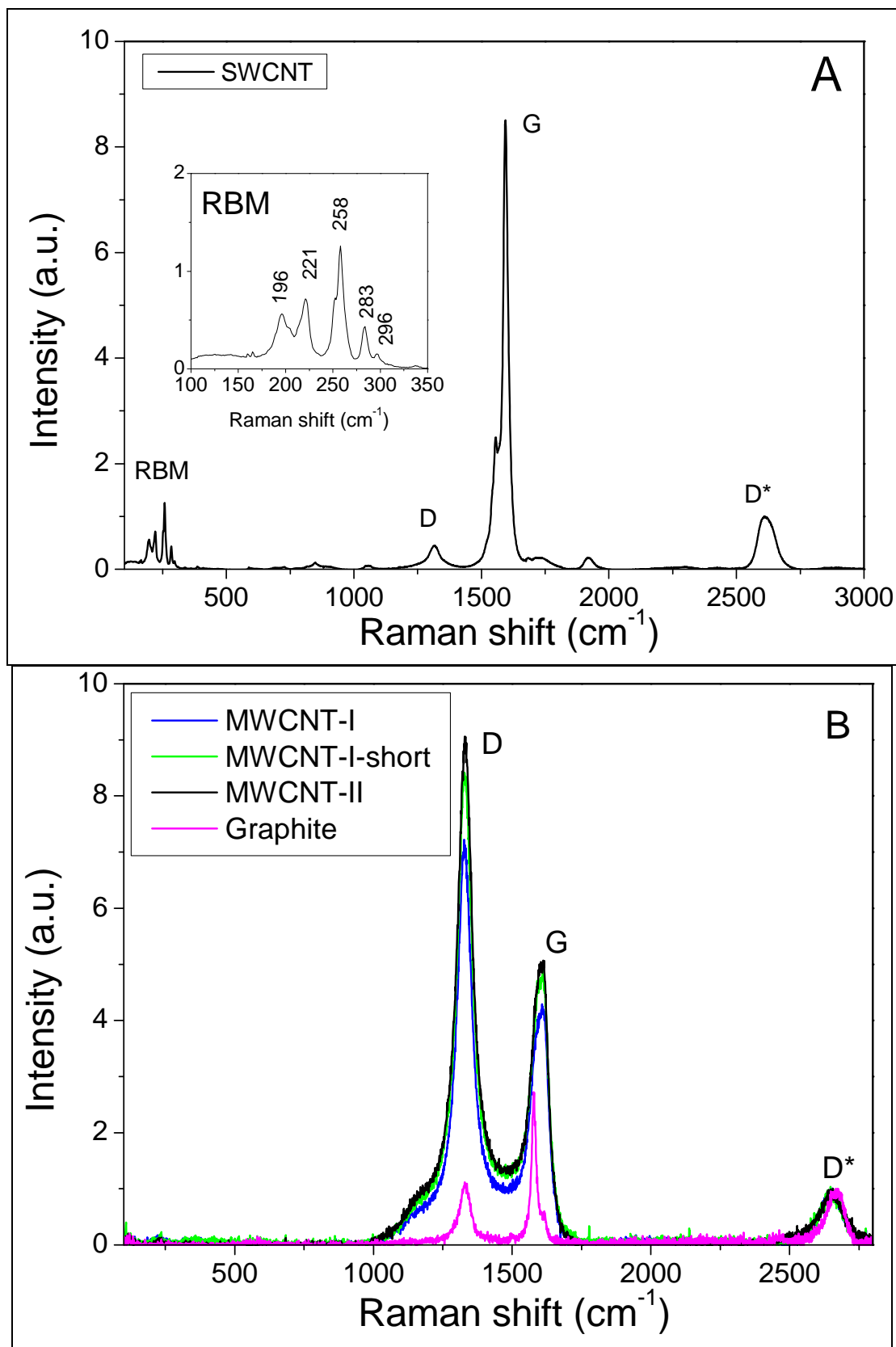


Figure 6.4 Raman spectra of CNTs at $\lambda = 632.8$ nm (normalized to D*): (A) SWCNT (inset: RBM); (B) MWCNT-I, MWCNT-I-short, MWCNT-II and graphite.

Table 6.1 Main characteristics of the CNTs studied in this work: carbon content wt.% (measured by flash-combustion method or informed by producer that measured by thermal gravimetric analysis or elementary analysis), aspect ratio measured by producers (TEM and SEM) and calculated D/G ratios measured by Raman spectroscopy ($\lambda = 632 \text{ nm}$) for the carbon materials in comparison with a graphite.

	Carbon content wt.%	Average Aspect ratio provided by producers (average)	D/D* ratio, I_{D/D^*} (Raman)	D/G ratio, $I_{D/G}$ (Raman)
SWCNT	81.3(± 1.6)* 85**	550 (d ~ 1.2 nm, L ~ 0.66 μm)	0.43	0.05
MWCNT-I	90.4(± 1.8)* 90**	750 (d ~ 10 nm, L ~ 7.5 μm)	-	1.67
MWCNT-I-short	87.7(± 1.8)*	370 (d ~ 10 nm, L ~ 3.7 μm)	-	1.69
MWCNT-II	95.6(± 1.9)* >95***	379 (d ~ 14.5 nm, L ~ 5.5 μm)	-	1.75
Graphite	-	-	-	0.4

* Flash combustion method; ** thermal gravimetric analysis; *** elementary analysis.

The electrical conductivities of CNTs at different concentrations in chloroform measured under sonication are shown in Figures 6.5 (nanomaterial in mg/mL) and 6.6 (nanomaterial in vol.%). At the lowest concentration (below the percolation point) the conductivity measured for most of these CNTs and for graphite fluctuates in the range of 10^{-9} - 10^{-8} S/cm. This is probably due to small contamination (in the carbon materials or in the chloroform itself) that act as ions (ionic conduction) increasing the conductivity of the medium. However, after the percolation is reached, the conductivity through the CNT networks surpasses the conductivity of the liquid matrix by several orders of magnitude.

At high concentrations of CNTs (above the percolation threshold), the conductivities of the suspensions are approximately the same whatever the CNTs, but at lower concentrations (just below the percolation threshold), they differ. This means that the difference of aspect ratio is more significant than the intrinsic conductivity of the CNTs.

It is possible to observe that MWCNT-I, MWCNT-I-short and HiPco SWCNT have lower percolation thresholds values (one order of magnitude) than MWCNT-II

(0.009 vol.%, 0.016 vol.% and 0.01 vol.% against 0.07 vol.%, respectively) presumably due to their higher general aspect ratio than MWCNT-II. Besides the aspect ratio of MWCNT-II is supposed to be similar to MWCNT-I-short, this difference could be related to: (i) the high $I_{D/G}$ ratio of MWCNTs-II, which would be an indicative of a larger presence of disordered carbon (decreasing effective amount of CNTs implying that the aspect ratio of whole carbon material is lower than MWCNT-I-short contributing for percolation at lower contents); (ii) the diameter of MWCNT-II on TEM images can be larger than 14.5 nm (limitation of average value instead of distribution), thus the aspect ratio might have been slightly superestimated. After percolation, it is interesting to note that at low concentrations of CNTs (just after percolation), MWCNT-I presents higher conductivities than others CNTs, while at maximum concentration HiPco SWCNT has a slightly higher conductivity than MWCNT-I. This might be due to the fact that at lower concentrations, the conductivity is dominated by the electrical resistance of the intertube contacts (aspect ratio), while at higher concentrations the intrinsic resistance of the CNTs starts to play the dominant role.

As can be observed in Figures 6.5 and 6.6, the suspension of graphite particles with the highest used concentration does not exhibit any measurable value of electrical conductivity. This reflects the fact that the aspect ratio of graphite particles is many orders of magnitude lower than that of CNTs.

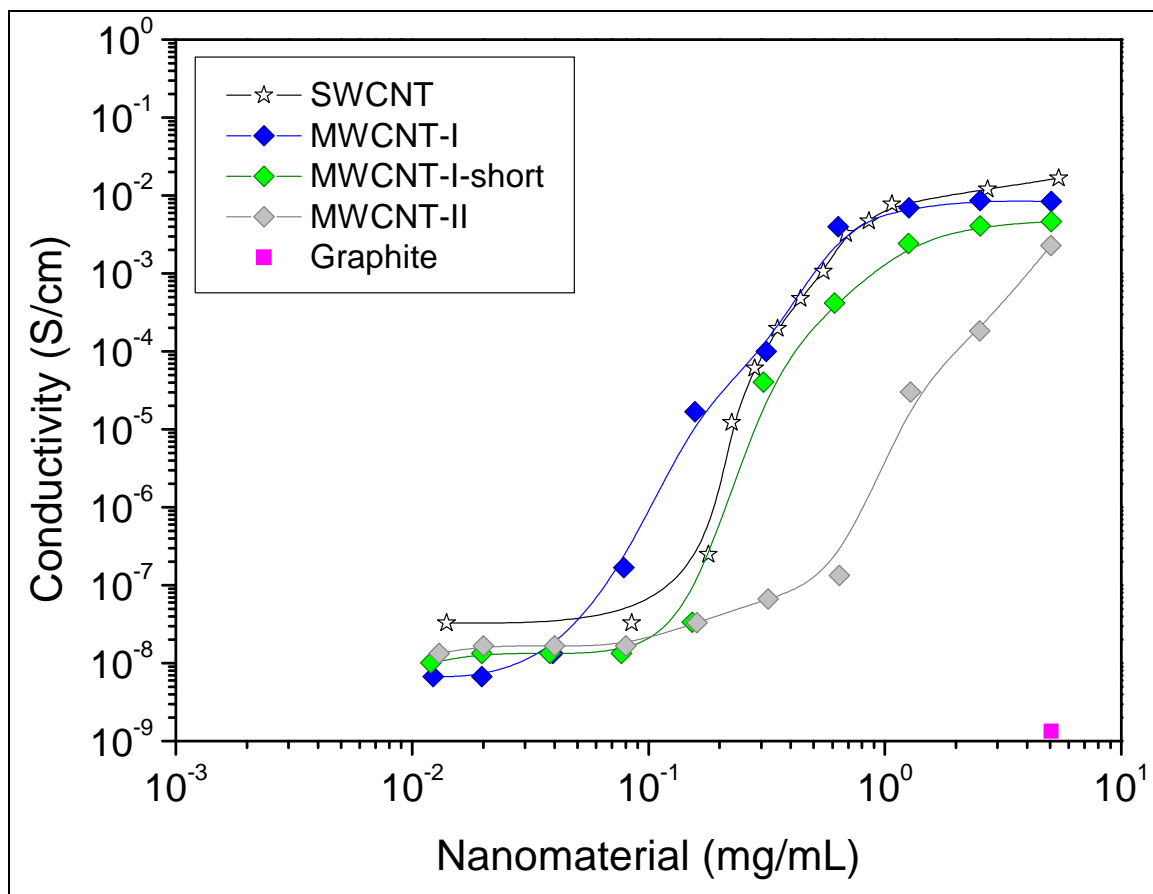


Figure 6.5 Electrical conductivity of the carbon suspensions in chloroform at 1.5 V DC (0.104 V/cm) during sonication: carbon content (mg/mL) versus electrical conductivity. Both in logarithmic scale.

According to the diagram of densities recently reported by Laurent *et al.* [12], the theoretical density of graphite is 2.25 g/cm^3 and that of SWCNTs with diameter of 1.2 nm is around $2.2\text{-}2.3 \text{ g/cm}^3$. In the case of MWCNTs, the number of walls also affects the density. Thus, for MWCNTs-I(-short) if the average diameter is 10 nm with around 4-5 walls maximum the density would be 1.3 g/cm^3 and for MWCNTs-II, with an average diameter of 14.5 nm and around 8-10 walls, the theoretical density is 1.7 g/cm^3 . Taking these values into account, it is possible to plot the electrical conductivity versus the carbon content (here considered all carbon content is CNT in the case of nanotubes), as volume percents (Figure 6.6), which is later compared with the plots for 2D CNTNs and 3D CNTNs embedded in silica matrix.

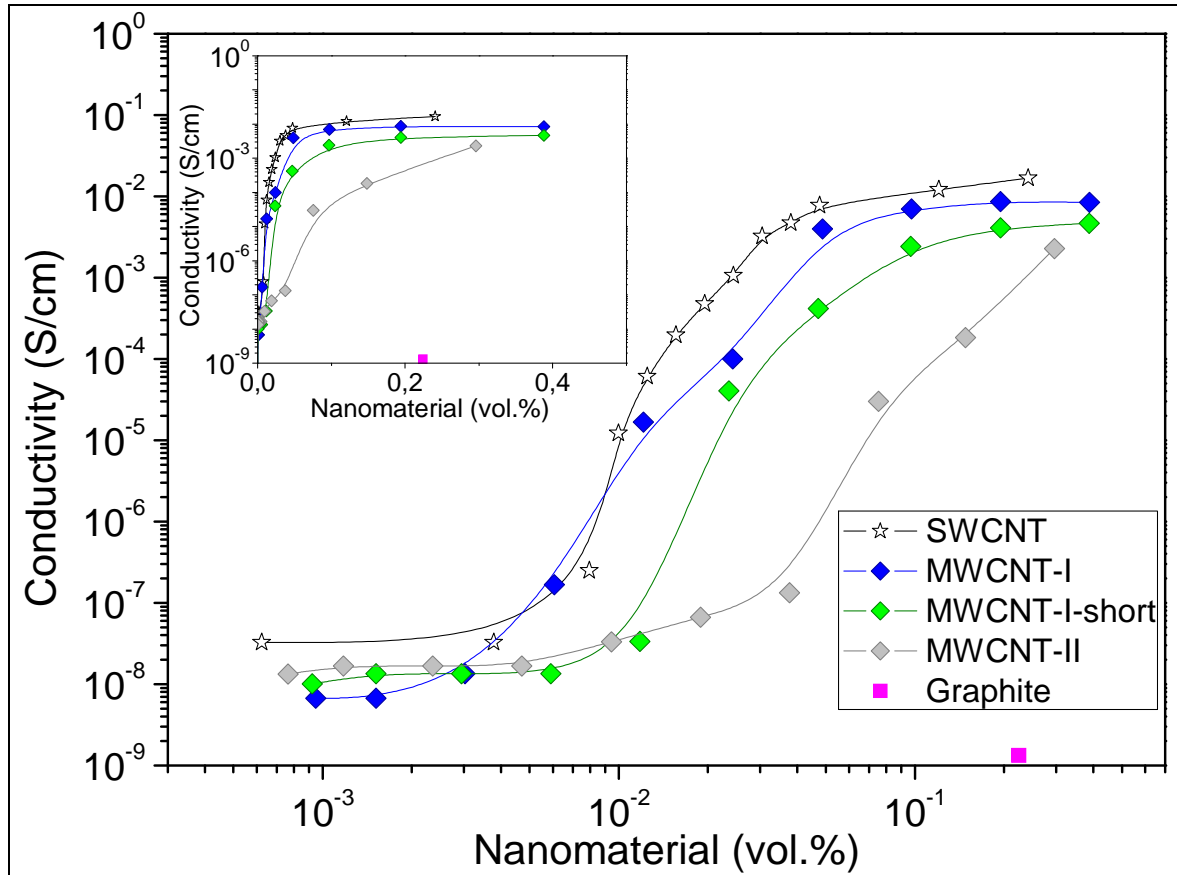


Figure 6.6 Electrical conductivity of the carbon suspensions in chloroform at 1.5 V DC (0.104 V/cm) during sonication: vol.% of nanomaterial (log scale) versus electrical conductivity (log scale). Inset: vol.% of nanomaterial (linear scale) versus electrical conductivity (log scale).

Under sonication, the configuration of CNTs in suspension is similar to that in solid composites: the CNTs are mixed randomly and no “alignment effect” takes place. The percolation thresholds found for the dynamic networks should therefore reflect that which could be obtained in solid composites with the same concentration of randomly dispersed CNTs [47]. However, it is important to note that the low percolation thresholds in the dynamic networks have also a contribution from dipole momentum and ionic conductivity of the particles in movement.

From Figure 6.6 it is possible to estimate the percolation threshold of some carbon materials and it allows the calculation from Equation 4.8

$$\left(\frac{\pi d}{2}\right)L^2 + \left[\pi d^2 \left(2 + \frac{V_{ex}}{4 \ln(1 - \phi_{CVF})}\right)\right]L + \frac{\pi d^3}{3} \left(4 + \frac{V_{ex}}{2 \ln(1 - \phi_{CVF})}\right) = 0$$

of the aspect ratio of these materials. Table 6.2 presents the estimated critical percolation thresholds for HiPco SWCNT, MWCNT-I and MWCNT-I-short products, as well as the aspect ratios calculated from Equation 4.8. However, the dynamic movement of the particles should yield to a lower percolation threshold (dipolar momentum plus ionic

conductivity); this effect, therefore, would need to be more deeply studied. The percolation thresholds measured by our novel method are one order of magnitude lower than the typical percolation threshold values obtained for CNTs in insulator matrix composites, usually around 0.1-0.4 wt.% [160]. However, using special techniques, such as *in-situ* polymerization, McLachlan *et. al* achieved a very low percolation threshold of 0.05 wt.% [125], for HiPco SWCNTs. This value is slightly higher than that found here for the HiPco material under sonication (~0.015 wt%, considering density of chloroform of 1.483 g/cm³). The advantages of the proposed method are most clearly demonstrated by the results of electrical conductivity measurements for various MWCNT suspensions. For example, to achieve a conductivity of 1x10⁻⁵ S/cm, the amount of MWCNT-II material required is six times higher than that for MWCNT-I material for a given volume of suspension, which, as explained before, might be to either a superestimation of the CNT aspect ratio by the producer or due to a higher presence of disordered carbon than in MWCNT-I (most probably, as evidenced by the high I_{D/G}: 1.75 against 1.69).

From Equation 4.8 it is possible to demonstrate that the percolation threshold volume fraction is inversely proportional to the aspect ratio (exception: sample MWCNT-II that, according to TEM images and I_{D/G} in Raman spectroscopy, probably has a lot of disordered carbon lowering the whole aspect ratio of the material in contrast to aspect ratio of the CNTs contained in this material). Longer CNTs will present a percolation threshold lower than shorter CNTs, for straight CNTs with same diameter. In this way, it is possible to estimate the aspect ratio of the filler material. The random orientation of the CNTs in the suspension assured by probe sonication could be compared to that of solid (static) composites with random orientation of CNTs, with a defined percolation threshold.

When the values of V_{ex} predicted by the percolation theory for randomly oriented thin cylinders (1.4) are used [120], the calculated aspect ratios obtained are higher by a factor of 10-12 than those observed by microscopy (by producers) for a great part of the materials, with exception of MWCNT-II (less than factor of 3). To obtain the aspect ratio given by the producers it was calculated that the value of V_{ex} would be about 0.12 for SWCNT and MWCNT-I-short, while 0.14 for MWCNT-I and 0.54 for MWCNT-II. These differences between the aspect ratios might be related to the way used to estimate the aspect ratio of the CNTs, since it is a difficult task to have a good idea of a material by microscopy (few amount of material and the most

dispersed CNTs are the shortest CNTs) [72]. It should be also taken into account that the observed CNTs by the producers are most probably the shorter ones since they are more easily dispersed. Another explanation would be that a much reduced total exclude volume might be used instead of 1.4 due to a very high local anisotropy in the filler orientation [161], caused by the probe sonication.

Table 6.2 Observed aspect ratios for various commercial carbon materials, in comparison to the calculated aspect ratios through the observed critical volume.

Material	Aspect ratio provided by producers (average)	Observed critical volume, ϕ_{CVF} (%)	Calculated aspect ratio for $V_{ex} = 1.4$
SWCNT	550	0.01	7000
MWCNT-I	750	0.009	7770
MWCNT-I-short	370	0.016	4370
MWCNT-II	379	0.07	996

For concentrations lower than approximately 1 mg/mL, the behaviour of HiPco SWCNTs suspensions (*similar for other CNTs, as demonstrated in attachment the fittings for MWCNT-I and MWCNT-I-short in Figures 0.6 and 0.7, respectively*) follow Equation 4.4 ($\sigma\alpha(\phi_F - \phi_{CVF})^\tau$), as shown in Figure 6.7. There is a good power law correlation between the reduced volume fraction of CNTs and the electrical conductivity. The calculated τ for a critical volume of ~0.01% was estimated to be 1.855, which is quite close to the theoretical value for a 3D network (1.94 [47] - 2.05 [46]). At concentrations above 1 mg/mL the CNTNs surpassed the percolation threshold and the conductivity is dominated by the intrinsic conductivity of CNTs/bundles.

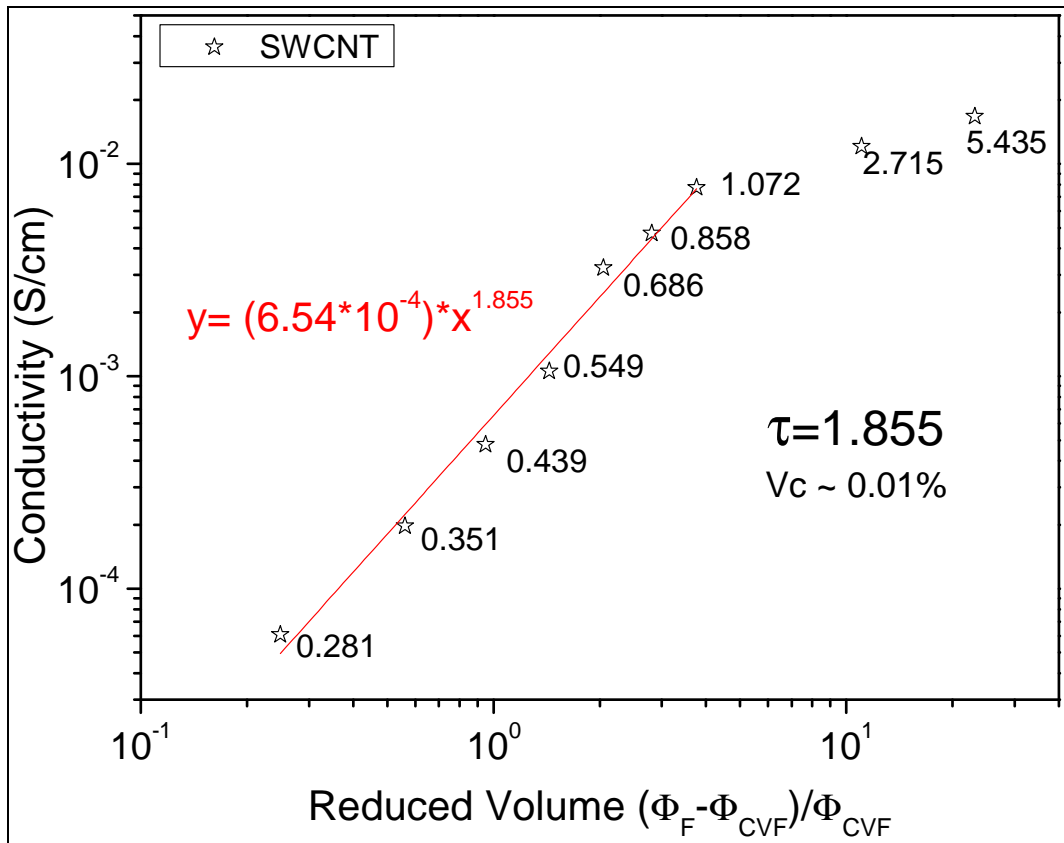


Figure 6.7 Conductivity *versus* reduced volume for HiPco SWCNTs (both in logarithmic scale). Below 1 mg/mL of CNTs (reduced volume = 3.7) the conductivity follows a linear correlation. The CNT concentration (mg/mL) is indicated for each point.

However, when the measured results of HiPco SWCNT are compared with the calculated electrical conductivity through the modified rule of mixtures (by Equation 6.1b: $\sigma_C = \alpha_1 \beta \sigma_{F1} \phi_{F1} + \alpha_2 \beta \sigma_{F2} \phi_{F2} + \sigma_M \phi_M$) using an aspect ratio of 7000 and β of 0.2 (Figure 6.8), it appears that the measured values are much lower (difference of about 10^3 S/cm above percolation threshold) than the linear relation suggested by the modified rule of mixtures even after the formation of the percolating network (difference of about five orders of magnitude). One important factor that plays a major role in the effective resistance and is not taken into account in the calculus is the interfacial resistance (intertube junction and in the interface of matrix and CNTs). Moreover, there are the characteristics of CNT material (defects/inhomogeneities, purity, waviness, metallic/semiconducting ratio modified by oxidative attacks during sonication) that affect the final conductivities, thus conductivity values of SWCNTs would have been superestimated. It should be also considered that all values estimated are very approximative.

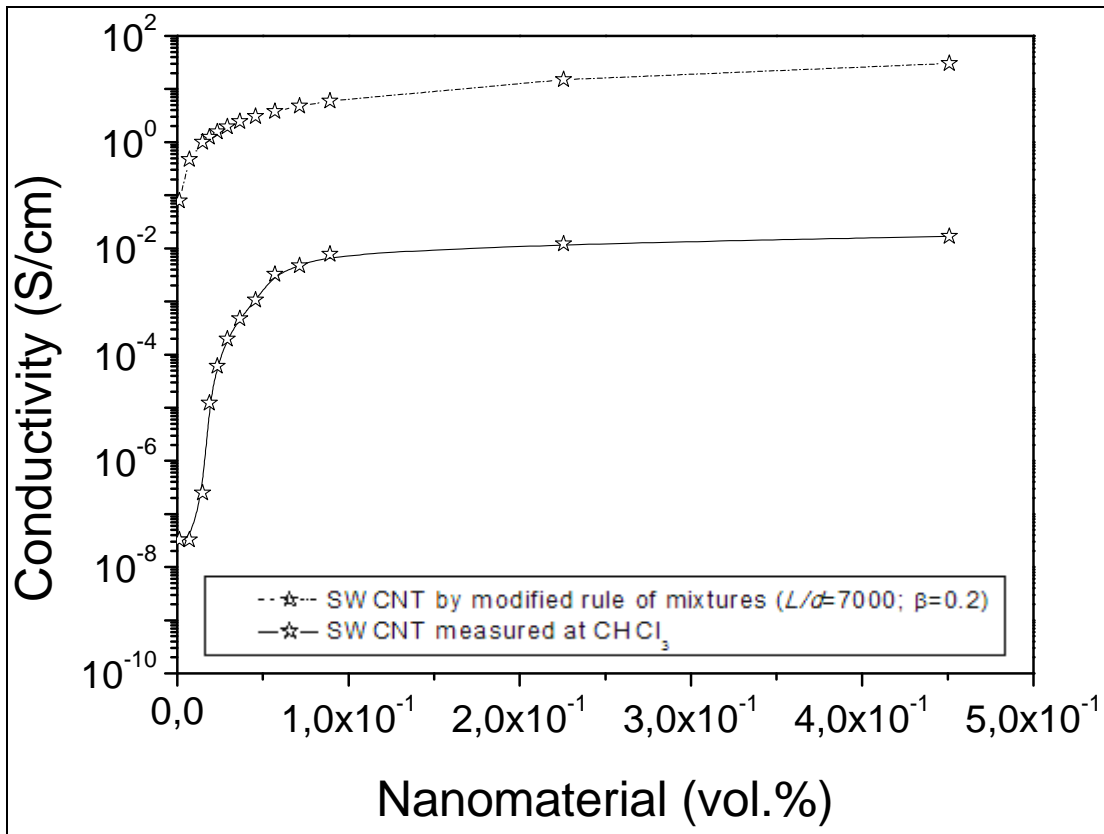


Figure 6.8 Measured conductivities of HiPco SWCNT dynamic 3D CNTNs in chloroform in comparison to calculated conductivities by modified rule of mixtures considering an aspect ratio (L/d) of 7000 and $\beta=0.2$.

Table 6.3 shows the electrical conductivity of free standing papers from CNTs materials, measured by the four-probe method, compared with the conductivities of the same carbon materials, measured in a liquid medium in the dynamic mode at 1.5 V (0.104 V/cm) for a concentration around 5 mg/mL. This concentration was chosen since it is above the percolation threshold. Due to the differences in porosity between the free standing papers, the electrical conductivities of the papers were normalized by their density and the ones of dynamic mode were normalized by their concentration (g/cm^3) to compare both in the same units. Free standing papers can be seen as extremely concentrated composites. In their case, the intrinsic electrical conductivity of the CNTs plays the dominant role. The normalized conductivities of the free standing paper of MWCNT-II materials is about $24 \text{ S}\cdot\text{cm}^2/\text{g}$, while MWCNT-I and MWCNT-I-short materials show normalized conductivities about $60\text{-}75 \text{ S}\cdot\text{cm}^2/\text{g}$. The results for the electrical conductivities of free standing papers are qualitatively in accordance (similar trend) to the values obtained for conductivity measurements in suspension at the highest concentration. The electrical conductivity measured for

HiPco SWCNT material is five times higher than that for MWCNT-I material, although in the suspensions with probe sonication, the HiPco SWCNT material exhibits conductivity only two times higher than that of the MWCNT-I material. This discrepancy could be explained by the fact that in composites (or CNTNs suspensions in liquid), the conductivity for smaller concentrations of CNTs is dominated by the electrical resistance of the contacts between the CNTs. On the other hand, for higher concentrations of CNTs, the intrinsic resistance of the CNTs starts to play the dominant role. Indeed, Skákalová *et al.* [58] reported that the thinnest SWNT 2D networks present a different electronic transport behavior than thick SWCNT 2D networks (free standing papers). They observed nonlinear I - V characteristics for thin SWCNT 2D networks at low temperatures, while thick free standing SWNT networks show linear I - V characteristics (much more metallic, retaining a large fraction of its conductance to very low temperatures). In contradiction to the fact that 1/3 of SWCNTs are metallic [33], while most of the DWCNTs or MWCNTs are metallic [56-58], SWCNTs have a higher specific conductivity than MWCNTs. This can be explained by: (i) the fact that SWCNTs are generally gathered in bundles, predominating a metallic character; (ii) the low $I_{D/G}$ of 0.05 (or, alternatively, I_{D/D^*} of 0.43) in comparison to MWCNTs used in this work ($I_{D/G}$ of 1.67-1.75), which is indicative of a less defective graphene structure.

Table 6.3 Electrical conductivity of free standing papers produced from different carbon materials, compared with the same materials' conductivities in liquid medium in the dynamic mode, at the highest concentration measured (around 5 mg/mL).

Material	Normalized σ_{DC} of self-standing paper of CNTs (S*cm²/g)	Normalized σ_{DC} in chloroform (S*cm²/g)
HiPco-SWCNT	390.3	3.079
MWCNT-I	73.2	1.661
MWCNT-I-short	64.6	0.916
MWCNT-II	24.5	0.453
Graphite	-	2.6×10^{-7}

6.1.1 Summary of characterization of the commercial CNTs

Commercial single- (from HiPco) and multi- (from Nanocyl and Baytubes) walled carbon nanotubes, which were all obtained by CCVD method, were characterized by TEM, Raman Spectroscopy and carbon analysis. The electrical conductivity of their respective networks as self-standing papers was measured (four probes) and the normalization by their density was outlined (the conductivity depends on the intertube contact, thus the packing during filtration to prepare self-standing papers). A new approach was developed during this work to evaluate their ability to form a percolating network by measurements (two probes) of the electrical conductivity of CNTs dynamic suspensions in chloroform. In the case of electrical conductivity, the amount of defects, the purity of the CNTs and their aspect ratio play a significant role in the final property and can be used to select the appropriate material.

The electrical conductivity of the suspensions in chloroform during ultrasonication follows a power law, as predicted by the classical percolation theory. It was observed smaller percolation threshold values (0.007-0.06 vol.%) than most reports about solid composites with randomly dispersed CNTs. A possible explanation for this is that, under dynamic conditions, the probability for the constantly moving CNTs in the suspension to form a percolation network is higher than under static conditions. A clear correlation was also found between the

conductivities measured for suspensions of CNTs in an insulator liquid, after reaching the percolation point, compared to those of free standing papers.

According to the characterizations of SWCNT product, it was possible to verify that: (i) the carbon content is the lowest in comparison to other commercial CNTs and slightly below ($81.3 (\pm 1.6)$ wt.%) the announced by the producer (85 wt.); (ii) Raman spectroscopy showed relatively low $I_{D/G}$ (~ 0.05 , alternatively I_{D/D^*} of 0.43), which is related to low graphitic defects; (iii) no structural defects was possible to see by TEM observations, but some (possibly) disordered carbon in the outer walls and encapsulated metal NPs (Fe as metal catalyst, according to producer) were visualized; (iv) TEM images also confirmed a diameter distribution in the range of 1-2 nm; (v) observed critical volume to percolate was found to be equal to 0.01 vol.%; (vi) their networks present high conductivities at high loads in chloroform (1.67×10^{-4} S/cm at 5 mg/mL, i.e., 0.24 vol.%, which corresponds to a normalized conductivity of $3.08 \text{ S}\cdot\text{cm}^2/\text{g}$) in good agreement to the normalized conductivity of self-standing papers ($390 \text{ S}\cdot\text{cm}^2/\text{g}$).

As far as MWCNTs are concerned, the characterizations showed that even though the carbon content in MWCNT-II ($95.6(\pm 1.9)$ wt.%) is higher than MWCNT-I ($90.4(\pm 1.8)$ wt.%) or MWCNT-I-short ($87.7(\pm 1.8)$ wt.%), Raman spectroscopy indicated that the first one has the highest $I_{D/G}$ intensity ratio (1.75 against 1.67 or 1.68, respectively). As expected, MWCNT-I presented an observed critical volume to percolate at much lower content (0.009 vol.%) than MWCNT-I-short (0.016 vol.%), as well as higher normalized conductivities of self-standing paper ($73.2 \text{ S}\cdot\text{cm}^2/\text{g}$ against $64.6 \text{ S}\cdot\text{cm}^2/\text{g}$) and of suspension ($1.661 \text{ S}\cdot\text{cm}^2/\text{g}$ against $0.916 \text{ S}\cdot\text{cm}^2/\text{g}$ both at 5 mg/mL, i.e., 0.39 vol.%). However, MWCNT-I-short can percolates at lower loads than MWCNT-II (0.07 vol.%), thus the second one has the smallest aspect ratio among the CNTs studied. MWCNT-II also showed the lowest normalized dynamical conductivity of suspensions ($0.453 \text{ S}\cdot\text{cm}^2/\text{g}$ at 5 mg/mL, i.e., 0.30 vol.%) and normalized conductivity of self-standing paper ($24.5 \text{ S}\cdot\text{cm}^2/\text{g}$). These facts might be also related to the highest $I_{D/G}$ observed for MWCNT-II. One should take into account not only the carbon content, but also the amount of disordered carbon (or defects in CNTs structure), which is much less conductor than CNT along its axis.

Finally, it was shown that the electrical conductivity evaluation of dynamic networks in chloroform could be an interesting tool to select the most appropriate CNT to prepare conductive nanocomposites. For the preparation of 2D CNTNs, the higher maximal conductivities and the availability of material and literature data led to select SWCNTs to prepare 2D CNTNs.

6.2 CNTNs in 2D system

Figure 6.9 presents the performance of the various networks over glass, characterized by electrical surface resistance and by optical transmittance measured at 550 nm wavelength. Here the values reported by Kaempgen *et al.* [136] of spray-coated HiPco SWCNTs networks and a commercial ITO glass were compared with the SWCNTs networks prepared in this work by the four deposition methods previously described. The results obtained for the networks deposited by filtration method (FM), spray-coating (SC) and electrophoretic deposition (ED) follow the same trend as the results obtained by Kaempgen *et al.* [136] by SC using similar materials. The exception is for the CNTNs prepared by dip-coating (DC): for example, the value of surface resistance at transmittance of 85-86 % is one order of magnitude lower ($\sigma_{//}$ of 0.18 k Ω /sq and σ_{\perp} of 0.28 k Ω /sq) than the values obtained for the other methods (3 k Ω /sq for FM, while 5 k Ω /sq for ED and SC). The better performance of CNTNs deposited by DC than others (after removal of surfactant in all cases) is attributed to the fact that this method produces smooth networks (Table 6.4), with partially aligned CNTs (Figure 6.10). The partial alignment of the CNTs can substantially improve the conductance in the direction along the CNTs [162]. For the dip-coating process, nanotubes are initially adsorbed during immersion and then aligned during the drying process by combined hydrodynamic and capillary forces. Several adsorbed layers are needed to percolate and probably each dipping decrease alignment (the first adsorbed layer is more aligned, but does not form percolating pathways as evidenced by Figure 0.9 in attachment) as can be observed (Figure 6.9) by the decrease of variation between σ_{\perp} and $\sigma_{//}$ with the number of dippings (at transmittance of 90% the difference factor is 1.7, while at 85-86% it is 1.5). This is probably because at each dipping the next CNTs adsorbed might realign parallel to

the previous CNTs adsorbed (strong Van der Waals interaction). Some nanotube loops can be sometimes visualized (red arrows in Figure 6.10) and they might be associated to the bending of the trapped carbon nanotube along the shrinking circumference of the drying liquid microdroplet [163].

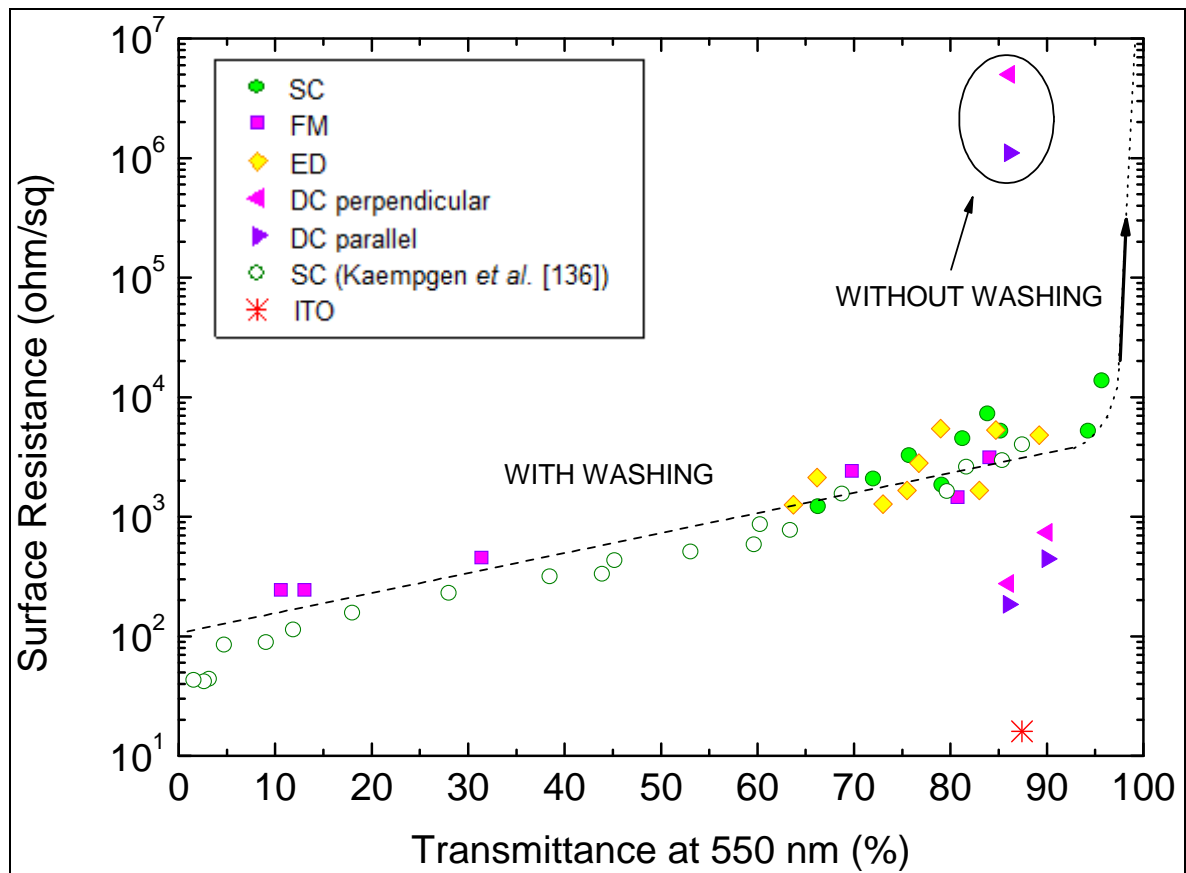


Figure 6.9 Surface resistance (log scale) versus transmittance of a commercial ITO and other data from literature [136] in comparison to several CNTNs prepared through different techniques using similar material of literature (HiPco SWCNTs): dip-coating (DC), filtration method (FM), spray-coating (SC) and electrophoretic deposition (ED). Eye-guide auxiliary line to visualize the tendency.

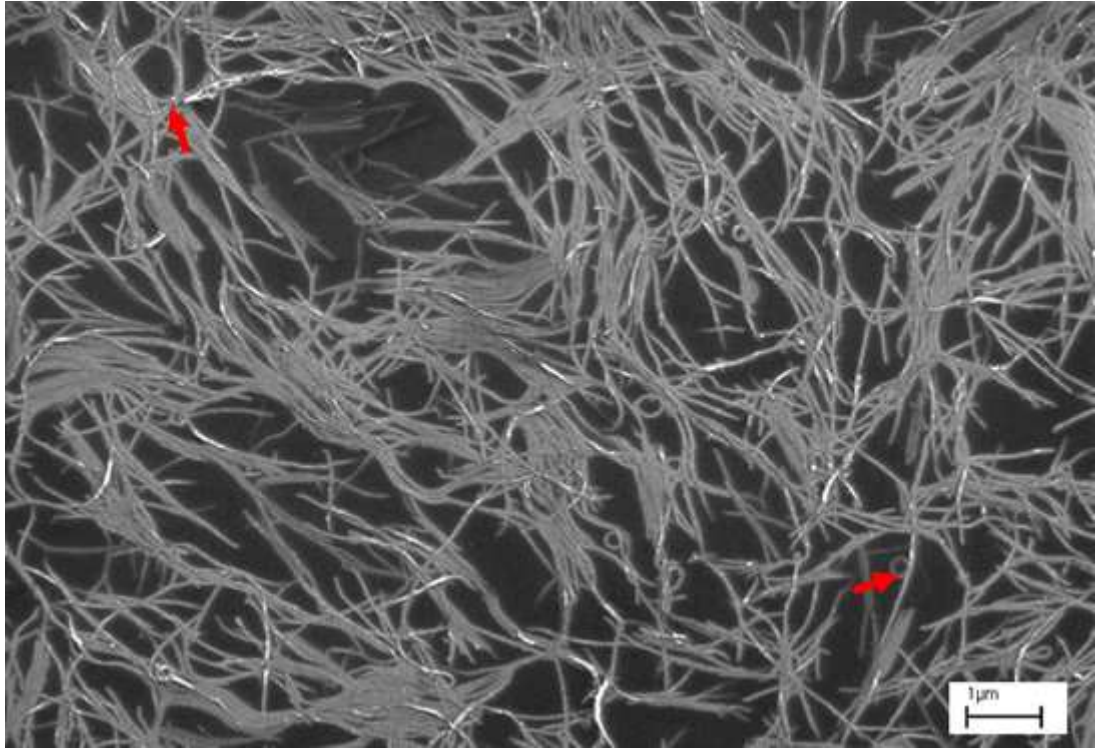


Figure 6.10 FESEM micrograph at 25 kx of magnification of a dip-coated CNTN (red arrow: CNT loop).

By Equation 4.9 ($P_{CNT} = \frac{\ln T}{-\alpha_{CNT}}$) and assuming the absorbance coefficient

α_{CNT} is $1.15 \times 10^{-5} \mu\text{m}^2$ for a light wavelength of 550 nm (measured by Kaempgen *et al.*) [136], it was calculated the concentration of CNTs per area (CNT/ μm^2) for the CNTNs prepared by SC, DC, FM and ED (Figure 6.11). As it was expected, these results are in good agreement with the measurements of Kaempgen *et al.* [136] since the material used was the same and, therefore, the α_{CNT} should be similar from their measurements. This validation of the α_{CNT} for the prepared CNTNs, allowed plotting the surface conductance *versus* concentration of CNTs per area in Figure 6.12. It can be observed that at a concentration of about 19000 CNTs per squared micrometer, CNTs already form a percolation pathway in 2D CNTNs.

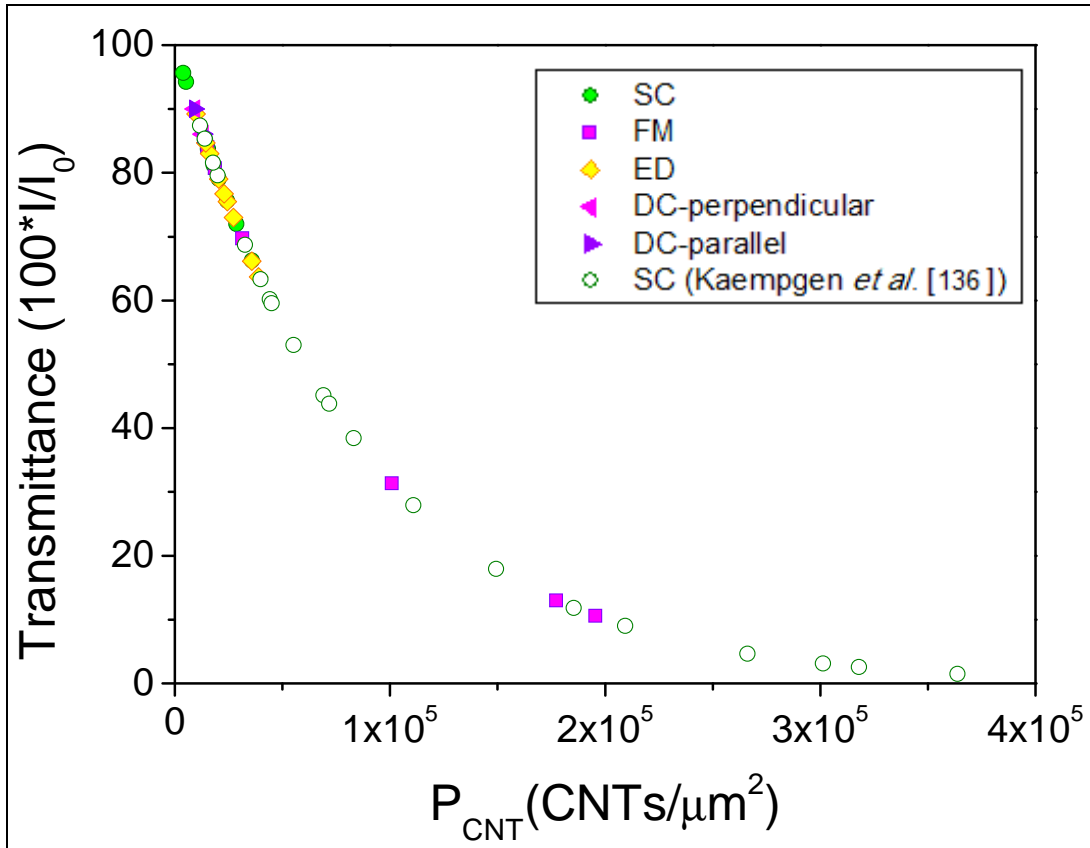


Figure 6.11 Transmittance (%) versus concentration per area of several CNTNs prepared through different techniques with HiPco SWCNTs in comparison with other data from literature using similar material [136].

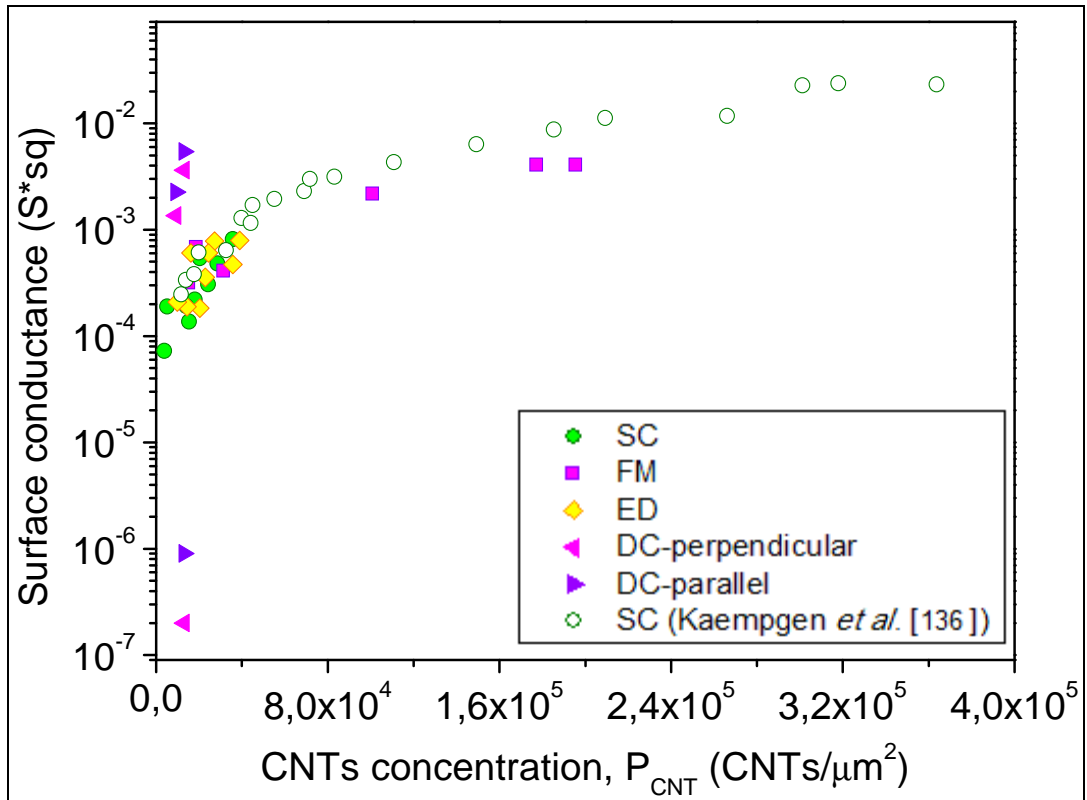


Figure 6.12 Surface conductance (log scale) versus concentration per area of several CNTNs prepared through different techniques with HiPco SWCNTs in comparison with other data from literature using similar material [136].

By considering only the authentic randomly aligned CNTNs with HiPco SWCNTs, which exclude the CNTNs obtained by DC, Figure 6.13 allowed to estimate for 2D CNTNs the coefficient τ to be around 1.29, which is in agreement with the theoretical predictions (1.1-1.4) [48].

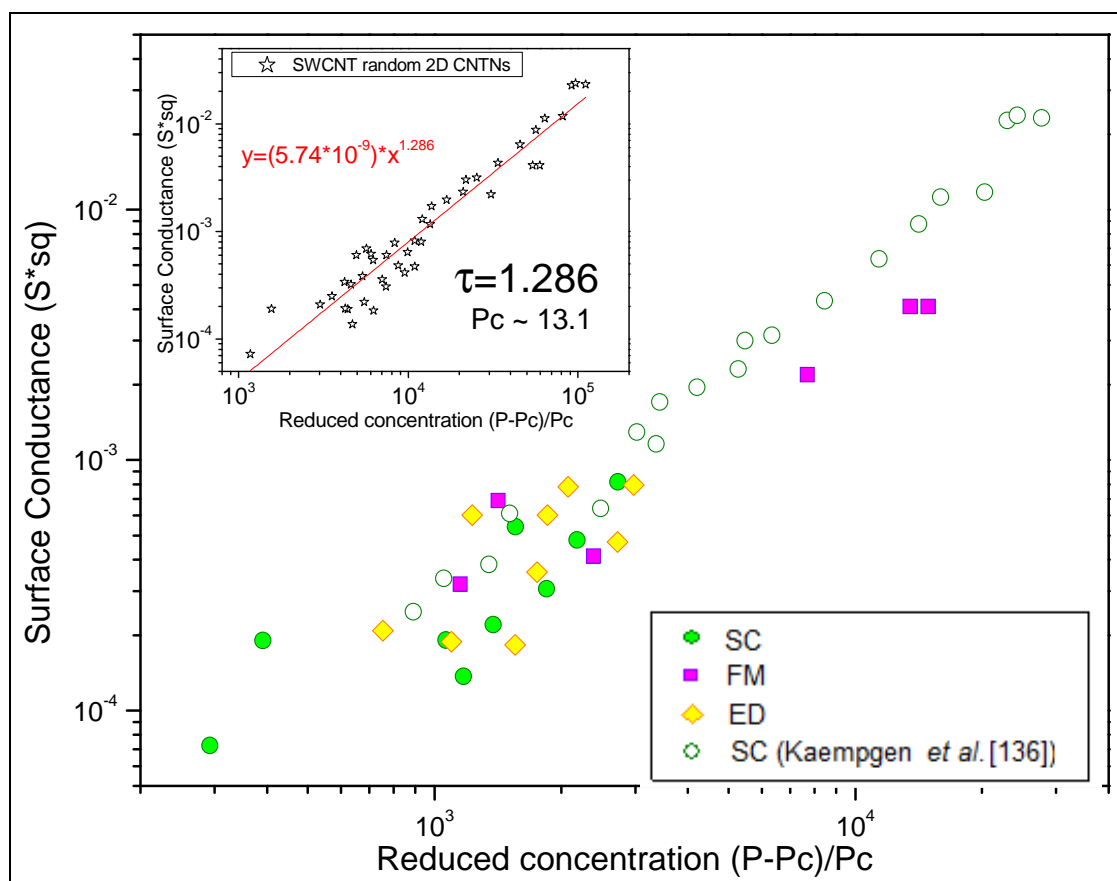


Figure 6.13 Surface conductance (log scale) versus reduced concentration (log scale) of several CNTNs prepared through different techniques with HiPco SWCNTs in comparison with other data from literature using similar material [136]. Inset: Power law fitting of the surface conductance (log scale) of SWCNT random 2D networks versus reduced concentration to obtain the constant of dimensionality.

Another result of this study is the effect of the presence of residual surfactant in the CNTNs, as shown in Figure 6.14. Without rinsing with deionized water, the surface resistance values for the DC network, for example, were more than four orders of magnitude higher than those when the network was thoroughly rinsed in deionized water after each cycle of dipping. The dried surfactant might not only decrease the transmittance, but, more importantly, wrapping CNTs with insulator molecules of surfactant can exclude the possibility of direct inter-tube contact and strongly hinders electron transport along the network. Therefore, rinsing the networks

eliminates a great part of the surfactant and improves the inter-tube contacts. Indeed, Bryning *et al.* [36] have already reported that the use of surfactant should be avoided since it remains in the nanocomposite and could decrease transport properties by increasing the intertube resistance.

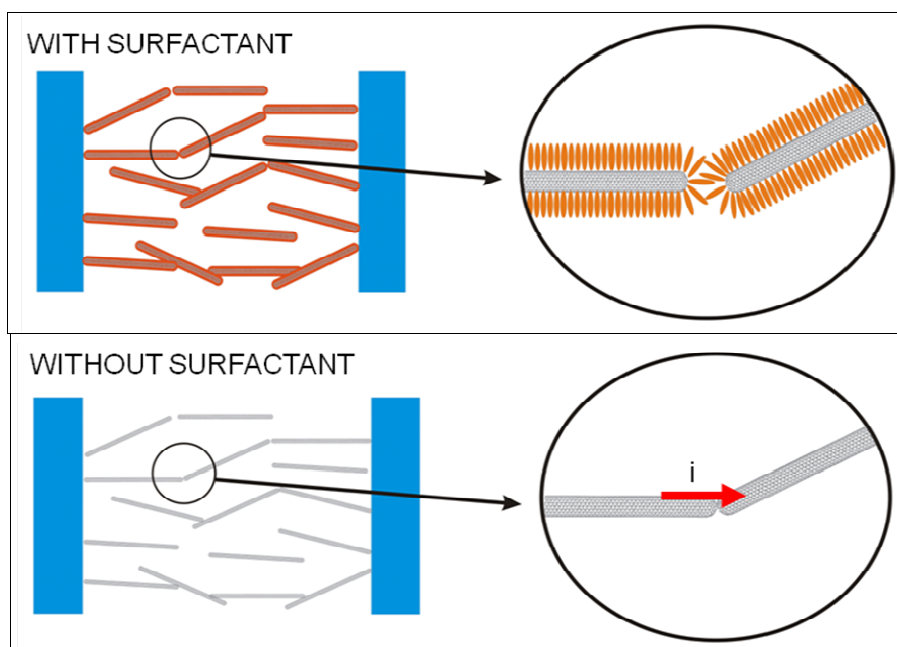


Figure 6.14 Schematic diagram (*note: CNTs and surfactant are not in the real proportions*) of the effect in the electrical conductivity of CNTNs with and without surfactant.

For some applications, like opto-electronic devices in solar cells for example, the roughness of the CNTNs can play an important role because, in thin layered configurations, unpacked CNTs would cause a short circuit [164]. The average thickness of solar cells is in the order of 200 nm and CNTs are generally micrometer long, so unpacked CNTNs might cause a short circuit if a metallic CNT reach the other electrode. Furthermore, the roughness of the CNTNs is also an indicative of the homogeneity of the network on a desired substrate. In this sense, particularly good results were achieved using the technique of ED. The networks fabricated by the ED method show the lowest value of average roughness (Table 6.4), almost comparable to that of ITO glass. In spite of the excellent homogeneity of the ED network, the surface resistance *versus* transmittance relation does not reflect the expectation. The reason for the lower performance of ED networks might be due to the scattering of light by the aluminum oxide layer formed during the electrophoresis process, which consequently limits the transmittance [156].

Table 6.4 Comparison of the average roughnesses of commercial ITO over glass with CNTNs using HiPco SWCNTs and prepared by different techniques (all with similar transparency, around 85 % at 550 nm): dip-coating (DC), filtration method (FM), spray-coating (SC) and electrophoretic deposition (ED). Size of each analyzed area: 210.25 μm^2 .

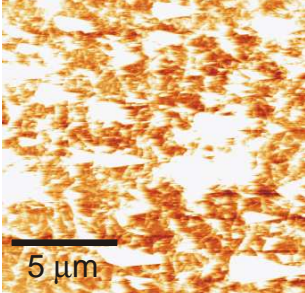
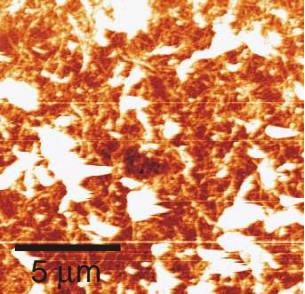
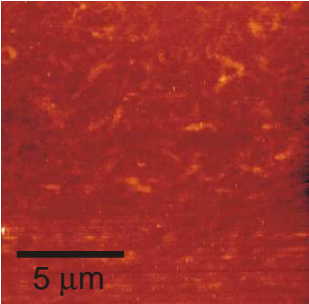
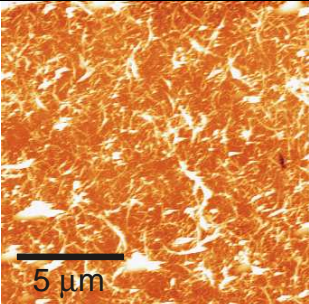
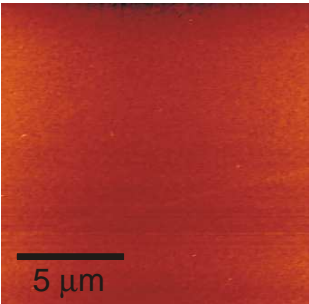
	Average roughness Ra (nm)	Example of atomic force micrograph (z_{max} at 100 nm)
SC	52.62 (\pm 24.14)	
FM	43.1 (\pm 5.23)	
ED	5.49 (\pm 3.37)	
DC	11.64 (\pm 4.68)	
ITO	1.58 (\pm 0,06)	

Figure 6.15 compares the properties of the networks deposited by FM, using different CNTs: SWCNT and MWCNT-I. From these results it follows that the surface resistance of CNTNs with MWCNT-I product is around ~2.6 times lower than CNTNs with HiPco SWCNT. The possible explanations for the superiority of the MWCNT-I in comparison with SWCNT are: (i) the metallic/semiconducting CNTs ratio [22a,39,58] (lower metallicity that SWCNT typically present in comparison with MWCNTs); (ii) more bundling of SWCNTs; (iii) the lower aspect ratio of the SWCNT material used in this work in comparison with MWCNT-I.

However, the CNTNs obtained in this work with filtration method present surface resistances higher than that reported by M.W. Rowell *et al.* [83] that achieved surface resistance of 200 Ohm/sq at 85% of transmittance (at 550nm). This is probably because the commercial AD-SWCNTs (Carbon Solutions, Inc.) used in that work might contain less impurities, fewer defects in the graphitic structure (due to the higher temperature of synthesis of CNTs) and doped semiconducting CNTs to some extent (by nitric acid treatment) [43] in comparison to those used to prepare the CVD-CNTNs.

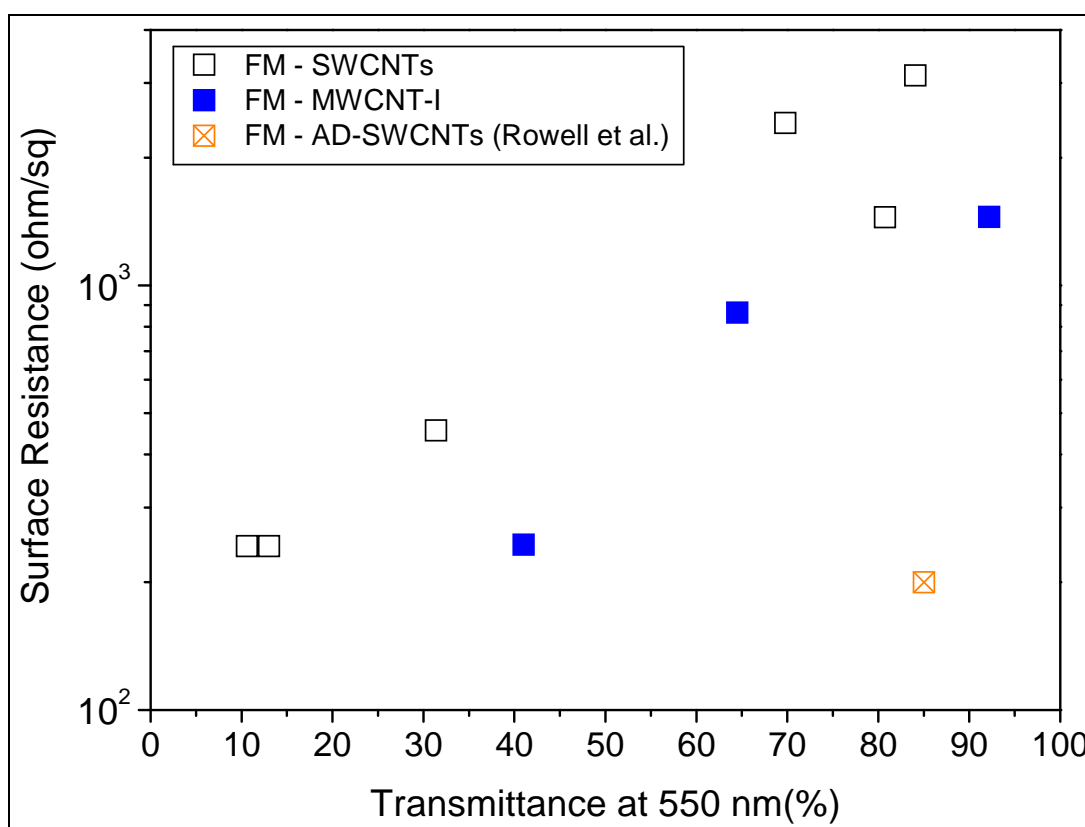


Figure 6.15 Surface resistance (log scale) versus transmittance of the pioneer work of M.W. Rowell *et al.* [83] reported using Arc-Discharge SWCNTs (AD-SWCNTs) in comparison to the CNTNs prepared by filtration method (FM) using different commercial CCVD CNTs: HiPco SWCNT, DWCNT-I and MWCNT-I.

By this study it was also possible to identify some possibilities of applications for 2D CNTNs (Figure 6.16). Among the possibilities of optically transparent and electrical conductive films the results obtained achieved the minimum requirements for the following applications: electrostatic dissipation, touch-screens panels, displays, solar cells and electromagnetic interference.

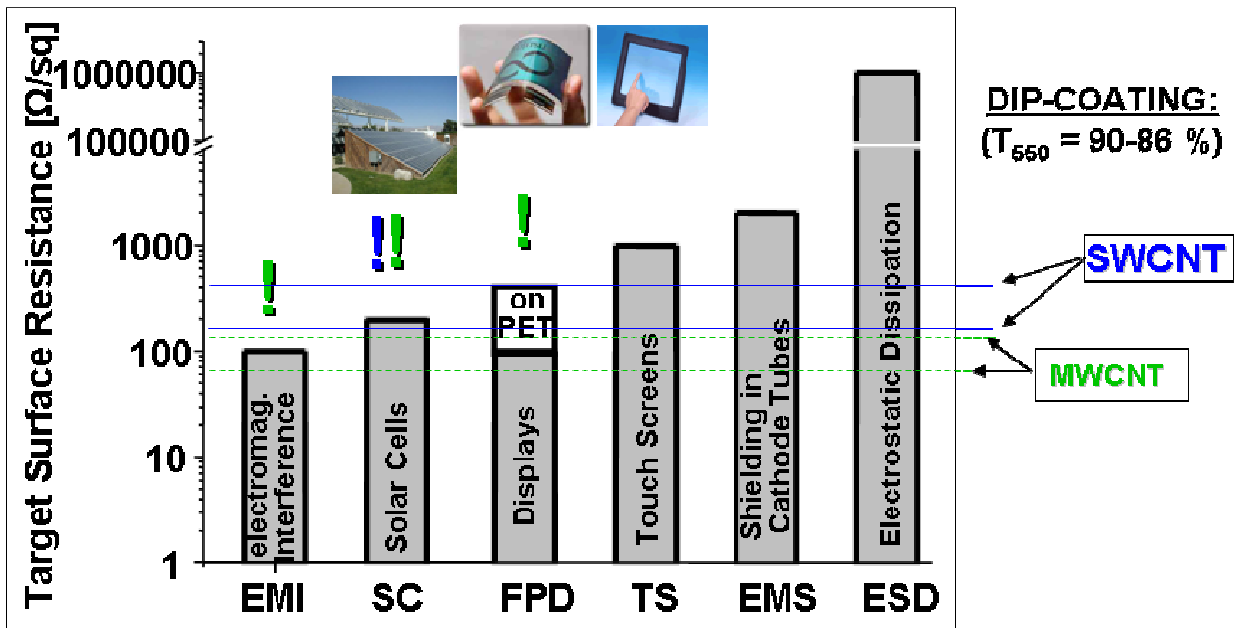


Figure 6.16 Possible applications for ultrathin CNTNs produced in this work (based on [136]).

For further works it would be interesting to study the adhesion of CNTNs to different substrates. Moreover, it could be studied the superposition of dip-coating (or other technique that yields relatively aligned CNTs) with a technique that gives more random CNTNs in order to increase interconnectivity. There is no doubt that additional steps of purification through thermal treatment (400-450°C) to eliminate others carbon structures that decrease the transparency and are less conductive than CNTs followed by doping would also certainly improve the results obtained in this work.

6.2.1 Summary of 2D CNTNs

Several techniques were compared: dip-coating, filtration, spray-coating and electrophoretic deposition. Dip-coating and electrophoretic deposition provided the smoothest CNTNs and might be an interesting option for solar cell applications, among others. It was outlined the importance of the removal of the surfactant from

the networks, as it decreases the resistance value by more than four orders of magnitude. As it was expected, the relatively smooth and aligned SWCNTNs obtained by DC showed the lowest surface electrical resistance for a given transparency ($\sim 186 \Omega/\text{sq}$ at $\sim 86\%T$). However, while this technique may be suitable for producing high performance networks, it is too time consuming at the laboratory scale in comparison with other techniques.

It was also confirmed that the most promising technique seems to be the electrophoretic deposition because it allows the preparation of a homogeneous, smooth and rigid deposit of CNTs, it is reproducible and it is fast. Besides the need for further studies, to decrease the effect of the residual aluminum oxide layer and to study the adhesion of the CNTNs in the substrate, it presents a great potential for applications that require the deposition of CNTs over complex shapes. Moreover, it might be possible to obtain CNTs relatively well aligned if CNTNs are deposited over a polymeric substrate and afterwards stretching it out.

Furthermore, it was showed that CNTNs prepared using MWCNT can improve the properties of the networks, and decrease costs at the same time. For future works, MWCNT should also be investigated, using DC and an optimized ED.

Moreover, the presented results show that the performance of the SWCNT networks by DC method reaches the parameters which may already make them suitable for applications in flat panel displays and solar cells.

6.3 CNTNs in 3D system: DWCNT-SiO₂ nanocomposites

6.3.1 DWCNTs synthesis and characterization

The use of SWCNTs allows achieving percolation with a lower load than with MWCNTs, but their functionalization would induce damages to their only wall which will compromise their electronic properties. In this context, double-walled carbon nanotubes (DWCNTs) were selected instead of SWCNT, while MWCNT were avoided since they would require higher load content to raise the percolation threshold for electrical conductivity. DWCNTs were produced at CIRIMAT by CCVD using the route developed by Flahaut *et al.* [154]. Firstly, a DWCNT-CoMo-MgO

composite powder is obtained by CCVD (using $\text{Mg}_{0.99}(\text{Co}_{0.75}\text{Mo}_{0.25})_{0.01}\text{O}$ as catalytic material and methane as carbon source) and then MgO and part of Co and Mo are dissolved by HCl giving extracted DWCNTs.

XRD patterns of the DWCNT-CoMo-MgO composite powder (typically 9-11 wt.% of carbon content according to flash combustion analysis carried out at CNRS, in good agreement with Flahaut *et al.* results [154,165,166]) and of the extracted DWCNTs were carried out to confirm the dissolution of MgO. These results are reported in Figure 6.17. Before acidic treatment, only Periclase is detected, but its peaks completely disappear after this process and then only cobalt and carbon are detected by XRD. Therefore, by comparing both XRD patterns it is possible to confirm that the magnesia (Periclase) is well dissolved by HCl. The concentric cylinders of stacked graphene sheets from DWCNTs or from some MWCNTs (3, 4 walls ...) or graphite are evidenced through the (002) peak of graphitic-like material. A peak corresponding to metallic cobalt (cubic, Fm-3m) is also observed and it can be associated to metallic NPs of the catalytic phase formed (together with molybdenum) during the synthesis of DWCNTs. No peaks of any Mo species are detected probably due to the low quantity of Mo (near the sensibility of XRD analyses). However, the light blue/green colour of the filtrated solution after extraction with HCl (Figure 6.17C) can be related to Co ions [167] and thus indicates that part of the metal NPs have been dissolved. Previous works have shown that some Co (and Mo) NPs remain enclosed in carbon capsules (and thus protected from the HCl dissolution) [154]. Indeed, elemental analyses performed at Service Central d'Analyse from CNRS in Lyon confirmed that after the extraction of DWCNTs from MgO about 3.65 wt.% of Co and 1.27 wt.% of Mo remain in the material. In spite of this, the flash combustion analysis of carbon method carried out at CNRS (Table 6.5) revealed an average carbon content in the range of 89-89.7 wt.% measured for 2-3 samples of each different batch of synthesis of DWCNTs (in very good agreement with Flahaut *et al.* [154,166]). Therefore, the other compounds (around 6 wt.%) are probably adsorbed oxygen and water.

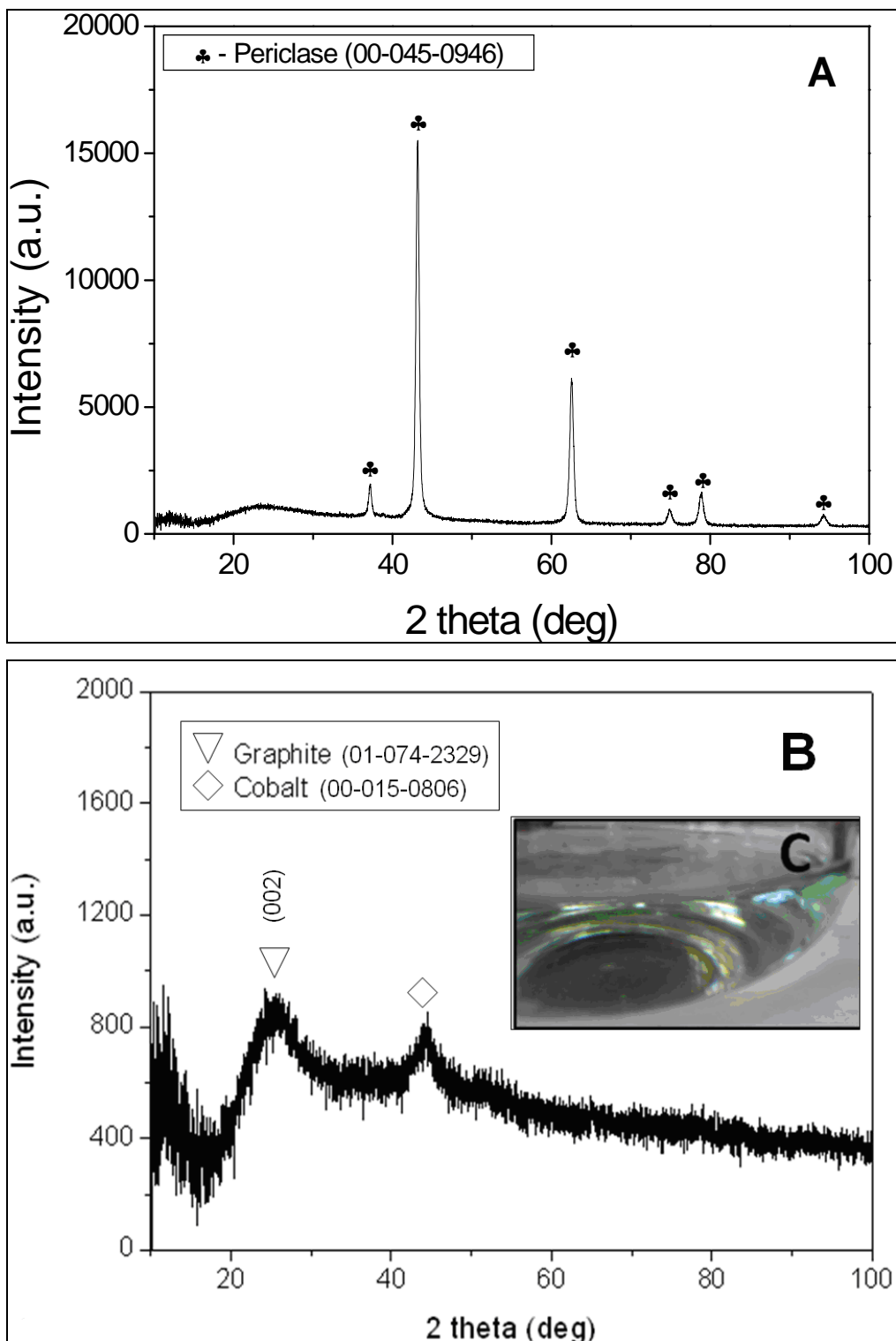


Figure 6.17 XRD patterns from DWCNTs: (A) before and (B) after extraction of magnesia (DWCNT), with an inset (C) of the filtrated solution after extraction with chloridric acid.

Figure 6.18 presents a TEM image (performed at TEMSCAN from Université Paul Sabatier in Toulouse) of the home-made DWCNTs after extraction with HCl, demonstrating many bundles of this material. According to Flahaut *et al.* [154] who characterized similar DWCNTs (96 measurements) produced by this method by high

resolution TEM, the mean outer diameter is of the order of 2 nm. According to them, about 77% of the CNTs are really DWCNTs (the rest are few SWCNT and some triplewalled-CNTs). Indeed, in Figure 6.18 it is possible to observe CNTs with an outer diameter distribution in the range of 1-3 nm. The TEM resolution does not enable to well visualize other carbon species. However, another work of Flahaut *et al.* [165] on similar materials reported the visualization (by HRTEM) of other carbon species, namely small crushed graphene sheets and some graphitic shells with encapsulated metal NPs. Indeed, in Figure 6.18 is possible to observe (blue arrows) some metal NPs (Co and/or Mo), indicating that they still remain in the material. Regarding defects, the TEM resolution allows to see only some bent DWCNTs (red arrows) and this is an indicative that DWCNT can have structural defects such as “kinks”.

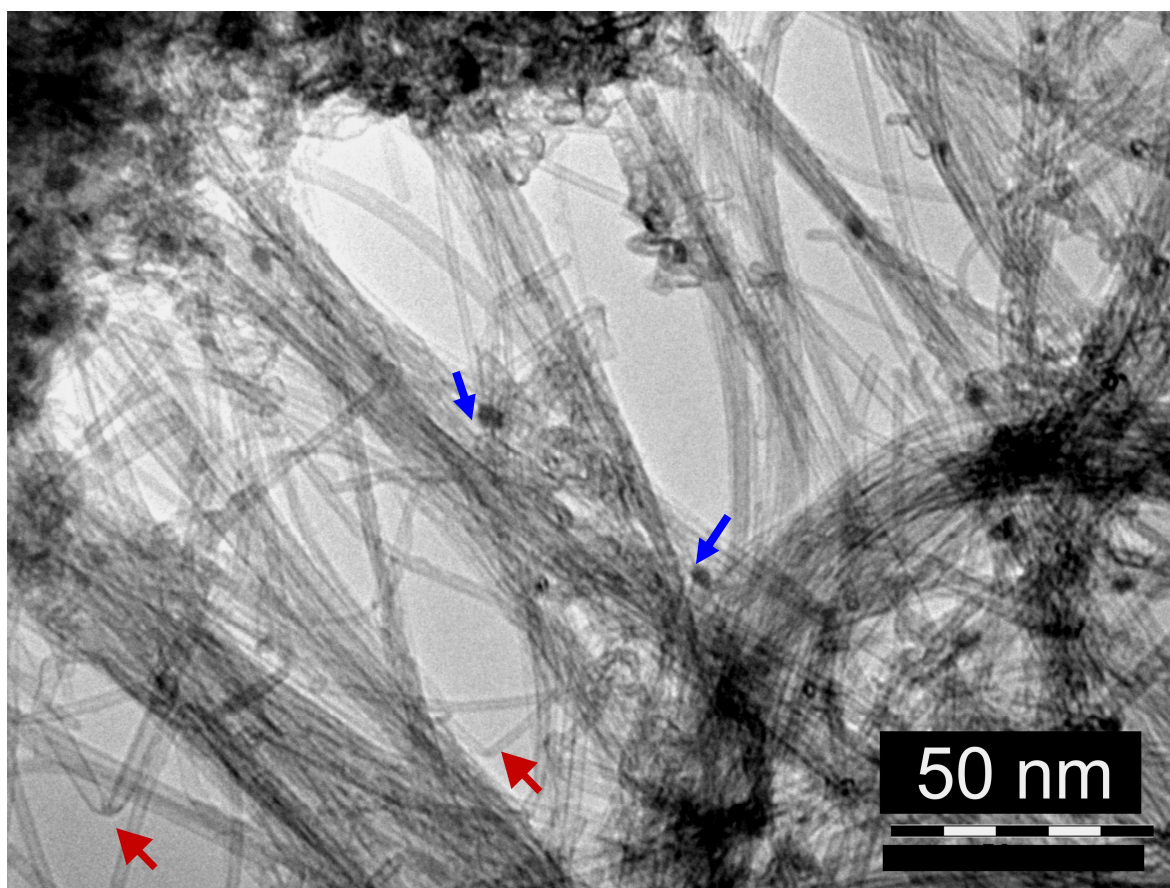


Figure 6.18 TEM micrographs of home-made DWCNTs after extraction with HCl. Red arrows as defects (“kinks”) and blue arrows as metal NPs.

Raman spectroscopy was also used to check the presence of disordered carbon in the extracted DWCNTs. The analysis was conducted on several synthesis

batches. Figure 6.19 shows three spectra obtained in different areas (coloured lines) of the sample DWCNT-C (i.e. the batch which gave the highest average: $I_{D/G}=17\%$) and also the average Raman spectrum (black line in the insets). As could be expected, the typical features visualized in SWCNT material can be observed in DWCNTs: *RBM*, *D* mode, *G* mode and *D** mode. The several Raman features at low frequencies (100-400 cm^{-1}) are outlined as left inset in Figure 6.19. These frequencies are inversely proportional to the tube diameters, but it is not representative of the CNTs population since only some of the CNTs are in resonance at 632.82 nm (1.96 eV). To estimate the diameter of the main tubes which are in resonance with this wavelength the following equation relates a diameter dependence on *RBM* frequency for DWCNTs [168]: $\omega=\alpha/d$, where ω is *RBM* frequency (cm^{-1}), α is a constant (related to van der Waals tube-tube interactions between inner and outer tubes or bundles) and d is the diameter. By using $\alpha=224 \text{ cm}^{-1}$ [168], it follows from the main *RBM* peaks outlined in the average Raman spectrum (black line) in the *RBM* region that peaks in the range of 148-336 cm^{-1} correspond to diameters between 0.7 nm and 1.9 nm. This range is in good agreement with the inner (0.53-2.53 nm) and outer (1.2-3.23 nm) diameters ranges determined from HRTEM by Flahaut *et al.* [154]. The ratio between the intensities of the *D* and the *G* bands, here called $I_{D/G}$, of other batches of synthesis of DWCNTs (Table 6.5) are in the range of 0.10-0.17, with exception of the batch corresponding to DWCNT-A with $I_{D/G}$ of 0.05. Therefore, the low $I_{D/G}$ variations (in the order of only ± 0.07) might be related to few differences of relative quantities of disordered carbon content (or defects) in the batches of DWCNTs. The observed $I_{D/G}$ ratios show that almost all batches (excepted DWCNT-A) contain more structural defects or disordered carbon than HiPco SWCNT material ($I_{D/G} = 0.05$) and much less than any MWCNT sample (lowest $I_{D/G} = 1.67$ for MWCNT-I). For the materials obtained in the same conditions in different batches, it was already reported $I_{D/G}$ of 0.089 [154], which is slightly below most of the batches obtained in this work. However, it was also reported $I_{D/G}$ of 0.25 for similar materials [168]. Variations among the spectra in different regions of samples DWCNT-B, DWCNT-C and DWCNT-D can be observed and almost no difference was observed in samples DWCNT-A and DWCNT-E. This indicates a higher homogeneity in the amounts of the materials separated for analysis (mixture of DWCNTs and disordered carbon, but also in the intensity of the

RBM peaks) in samples A and E than in the others. It is a proof that good homogenization is required before its use.

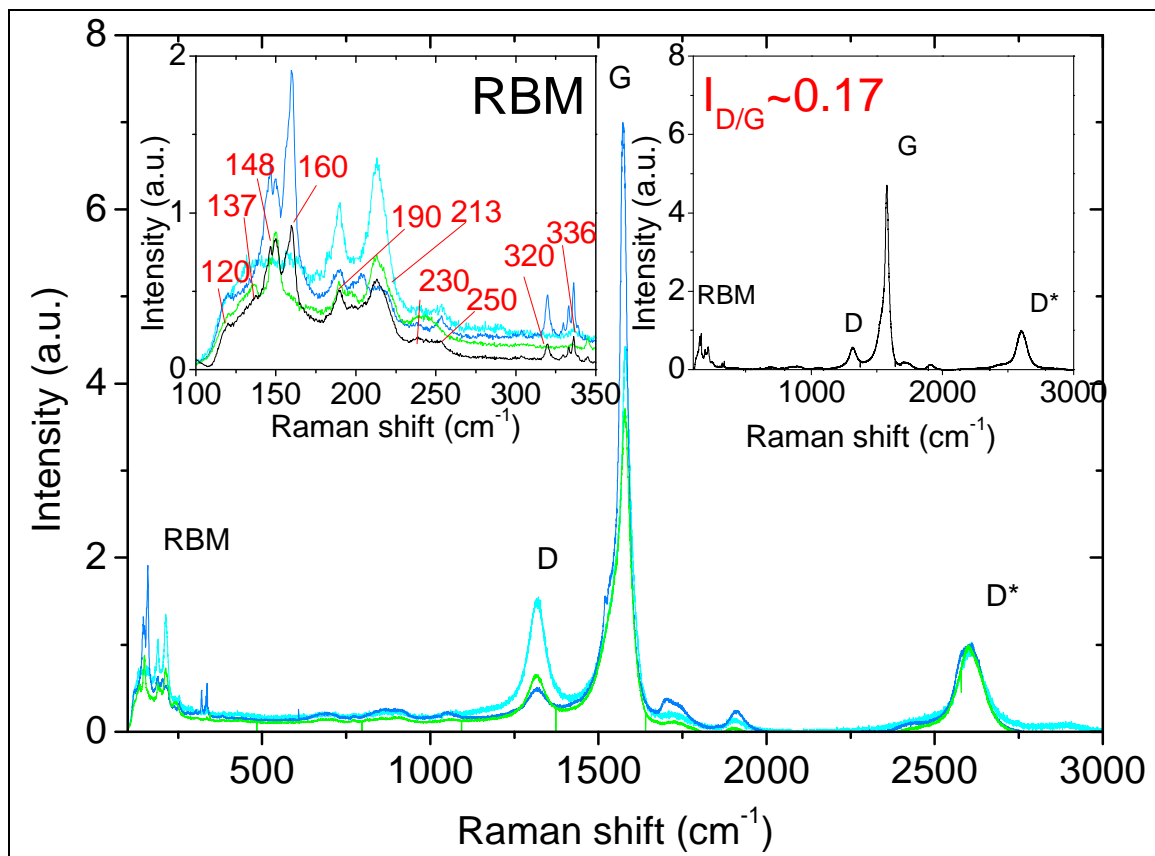


Figure 6.19 Raman spectra at different regions from DWCNT-C (DWCNT sample with the highest average $I_{D/G}$: 17%). Inset left: *RBM* spectra at different regions (coloured lines) and average *RBM* (black line). Inset right: average Raman spectrum.

Table 6.5 Main characteristics of the DWCNTs studied in this work: average carbon content wt.% (measured by flash-combustion method: two measurements for each sample) and calculated D/G ratios measured by Raman spectroscopy ($\lambda = 632$ nm) for the carbon materials in comparison with a graphite.

	Average carbon content wt.% (± 1.8)	Average $I_{D/G}$ (Raman)
DWCNT-A	89.0	0.05
DWCNT-B	89.5	0.10
DWCNT-C	89.1	0.17
DWCNT-D	-	0.10
DWCNT-E	89.7	0.16

Suspensions of DWCNTs at different concentrations in chloroform were used to measure the electrical conductivities of dynamic (during probe sonication) 3D networks of DWCNTs, using two copper electrodes at 1.5V DC. More details about this technique are described in the experimental procedure section of this work and elsewhere [158]. These measurements enabled to evaluate the electrical conductivity of the dynamic 3D networks of DWCNT in chloroform as a function of the CNTs content (vol.%), which have been calculated taking into account the values of density of DWCNTs as 1.8 g/cm^3 [12,126]. The results are reported in Figure 6.20. Besides all batches of DWCNTs samples presented similar maximum conductivities (around 10^{-2} S/cm), the percolation threshold for DWCNT-A, DWCNT-B and DWCNT-C was observed at much higher concentrations (about 0.01-0.012 vol.%) than for DWCNT-D and DWCNT-E (about 0.0025 and 0.003 vol.%, respectively). This fact might be related to more bundling and/or presence of aggregates in DWCNT-A, DWCNT-B and DWCNT-C than in DWCNT-D and DWCNT-E. Difference in the conductivity at low concentration (below the percolation thresholds) were also observed (for example, $\sim 7 \times 10^{-7} \text{ S/cm}$ in the case of DWCNT-D, while $\sim 3 \times 10^{-8} \text{ S/cm}$ for DWCNT-E) and it can be caused by any ionic contaminant (in the chloroform or in the material itself).

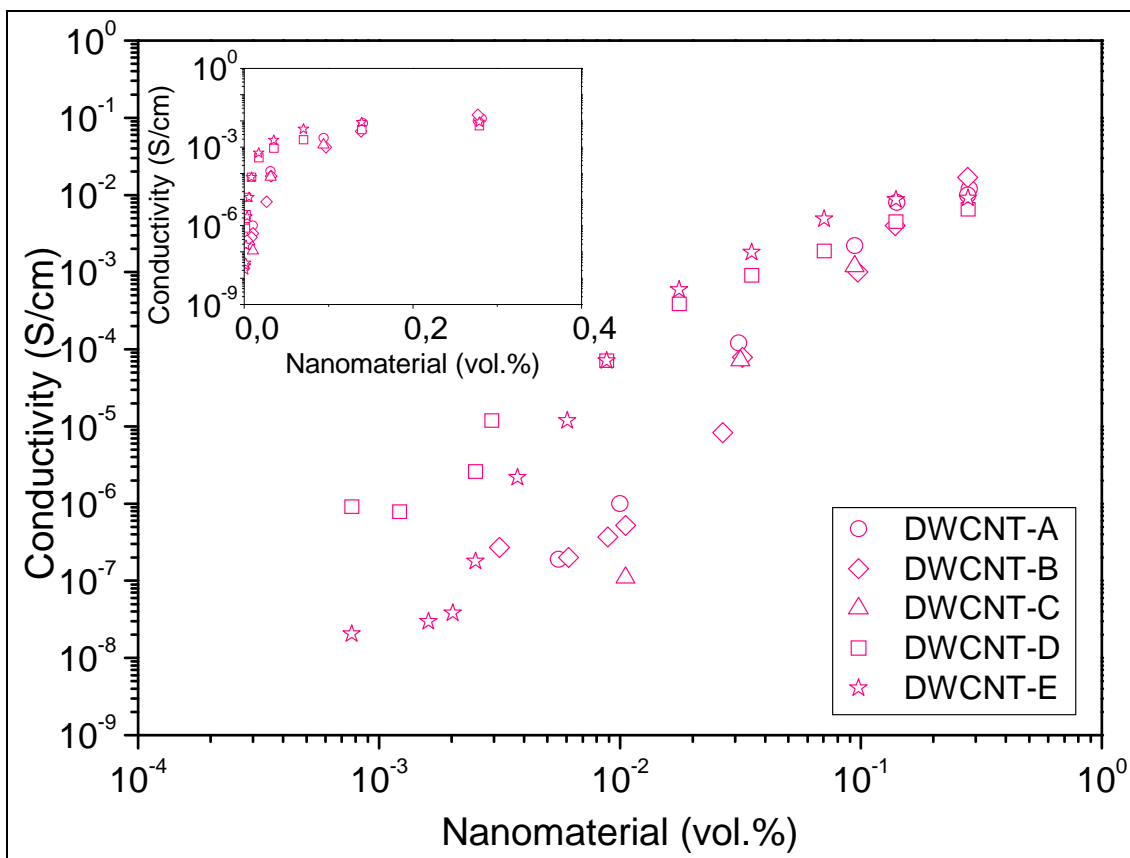


Figure 6.20 Electrical conductivity of the carbon suspensions (volume percent) in chloroform at 1.5 V DC (0.104 V/cm) during sonication (dynamic network) of different batches of DWCNTs.

The percolation threshold for DWCNT-E (sample used further for the wet route) is 0.002-0.003 vol.% (Figure 6.22), value lower than that observed for SWCNT (Figure 6.7: 0.01 vol.%) and for MWCNT-I (Figure 6.6: 0.009 vol.%) samples. The maximum electrical conductivity achieved (normalized conductivity, i.e., measured conductivity [S/cm] divided by the concentration [g/cm³] of material: $\sim 1.808 \text{ S}\cdot\text{cm}^2/\text{g}$) was similar to that obtained with MWCNT-I (Table 6.3: $1.661 \text{ S}\cdot\text{cm}^2/\text{g}$) but lower than that obtained with SWCNTs (Table 6.3: $3.079 \text{ S}\cdot\text{cm}^2/\text{g}$). It is difficult to calculate the aspect ratio of DWCNTs because of the difficulties to measure by microscopic techniques the length of very long individual filaments with diameter smaller than 5 nm. Some DWCNTs bundles were followed on lengths up to 100 μm but it is not established that some individual DWCNTs are so long. If we retain length values of a few tens of micrometers, the aspect ratio can be estimated to be in the range 5000-10000 which is almost ten times that of the SWCNTs and MWCNTs previously used in this study. That explains the low percolation threshold obtained in the better case (DWCNT-E). But the difference with other CNTs is not as high as that expected probably because of the higher bundling of DWCNTs (Figure 6.18) in comparison to

MWCNTs (Figure 6.3a) which decrease the effective aspect ratio. By using the Equation 4.8:
$$\left(\frac{\pi d}{2}\right)L^2 + \left[\pi d^2\left(2 + \frac{V_{ex}}{4\ln(1-\phi_{CVF})}\right)\right]L + \frac{\pi d^3}{3}\left(4 + \frac{V_{ex}}{2\ln(1-\phi_{CVF})}\right) = 0$$
 and considering the observed critical volume (ϕ_{CVF}) of about 0.002-0.003 vol.% and considering $V_{ex} = 1.4$ for randomly oriented infinitely thin cylinders [120], an aspect ratio of 35000-23330 was calculated, while if $V_{ex} = 0.3$ for very high local anisotropy in the filler orientation [158,161], the aspect ratio is around 7500-5000 (in better correlation with the estimated aspect ratio value). As explained in section 6.1.1, a V_{ex} of 0.3 in Equation 4.8 was also calculated for the case of a very high local anisotropy in the filler orientation [158], caused by the probe sonication. These results confirm that their high aspect ratio favours the use of less weight of DWCNT-E than MWCNT. Furthermore, even though HiPco SWCNTs present (by measurements performed with same electric field and similar maximum content of material) a higher maximum normalized (i.e. measured conductivity divided per quantity of material) conductivity (around 3.08 S*cm²/g) than DWCNTs (around 1.28 S*cm²/g for DWCNT-E, for example), their lower percolation threshold result of a higher conductivity at lower weight contents of carbon than the previous one. For example, around 0.018-0.019 vol.%, the conductivities of HiPco SWCNT and DWCNT-E are 1.2 x 10⁻⁵ S/cm and 5.9 x 10⁻⁴ S/cm, respectively.

As it could be expected, the conductivity values measured for DWCNT-E above percolation threshold are lower (five orders of magnitude) than those calculated by the modified rule of mixtures (by Equation 6.2b: $\sigma_C = \alpha_1\beta\sigma_{F1}\phi_{F1} + \alpha_2\beta\sigma_{F2}\phi_{F2} + \sigma_M\phi_M$) using an aspect ratio of 23300 and β of 0.2 (Figure 6.21). Below the percolation threshold, region that the aspect ratio of CNTs/bundles dominates, the values have not exactly the same trend and this can be because the modified rule of mixtures does not take into account the contact resistances. As previously mentioned, in a SWCNT metal-metal junctions can be in the order of 100-400 K Ω [148], while in metallic/semiconducting junction can be two orders of magnitude higher than this according to theoretical calculations [119]. Above percolation threshold, region that the intrinsic conductivity of CNTs/bundles dominates, the measured values and the calculated ones have both similar trend, but there is a shift of about 10³ S/cm between them. This shift could be explained by the fact that: (i) it can be assumed that DWCNTs in chloroform are not all individually

suspended, so the effective content of filler contributing to conductivity is lower than its potentiality; (ii) the assumed conductivity of an unique DWCNT might have been superestimated; (iii) the modified rule of mixtures does not take into account the intertube resistance.

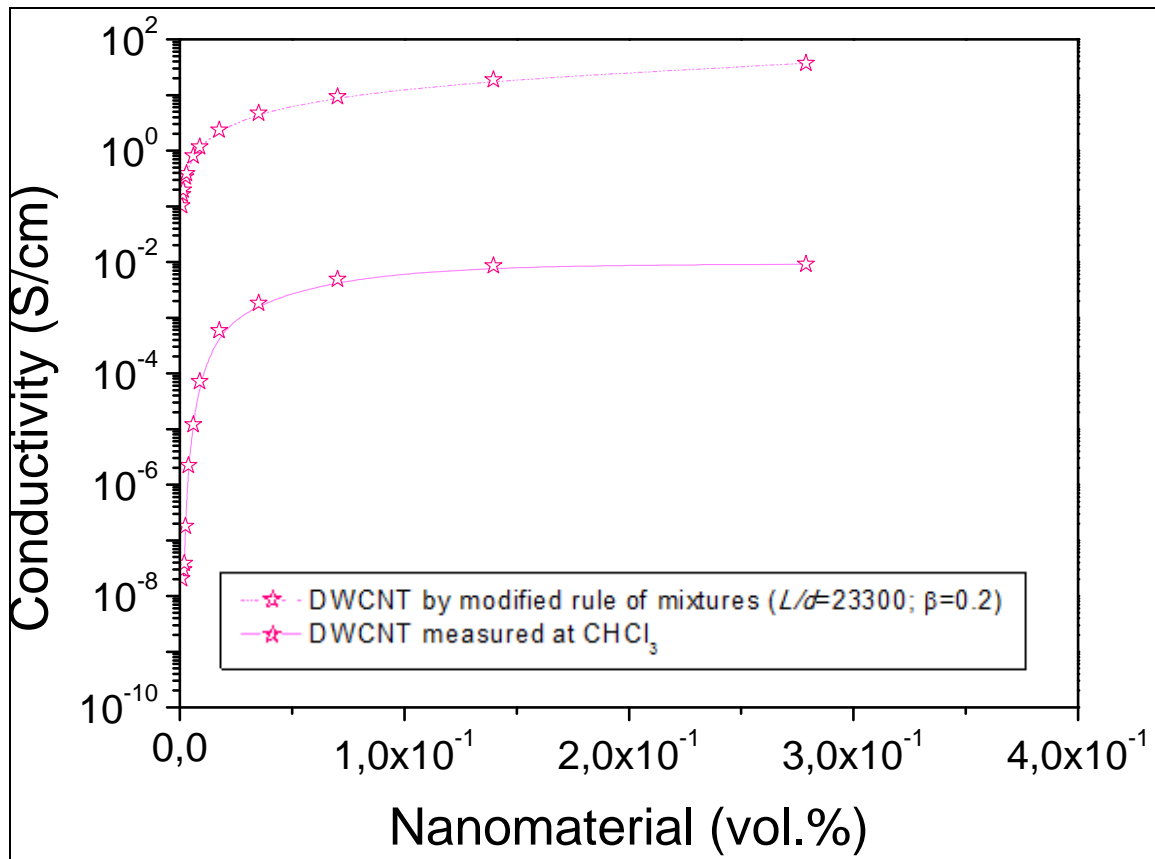


Figure 6.21 Measured conductivities of DWCNT-E dynamic 3D CNTNs (used for wet route) in chloroform in comparison to calculated conductivities (modified rule of mixtures) considering an aspect ratio (L/d) of 23300.

In order to verify that these results are in good agreement with the percolation law, the logarithm of conductivity was plotted versus the logarithm of the normalised filler volume fraction $(V-V_c)/V_c$ of DWCNT-E in Figure 6.22. For concentrations lower than approximately 1 mg/mL, the suspensions follow Equation 4.4 $(\sigma\alpha(\phi_F - \phi_{CVF})^\epsilon)$. There is a good power law correlation between the reduced volume fraction and the conductivity. In the case of DWCNT-E, with critical volume fraction of $\sim 0.003\%$, the dimensional parameter is 1.823, value which is similar of that calculated (section 6.1.1) for HiPco SWCNTs (1.82).

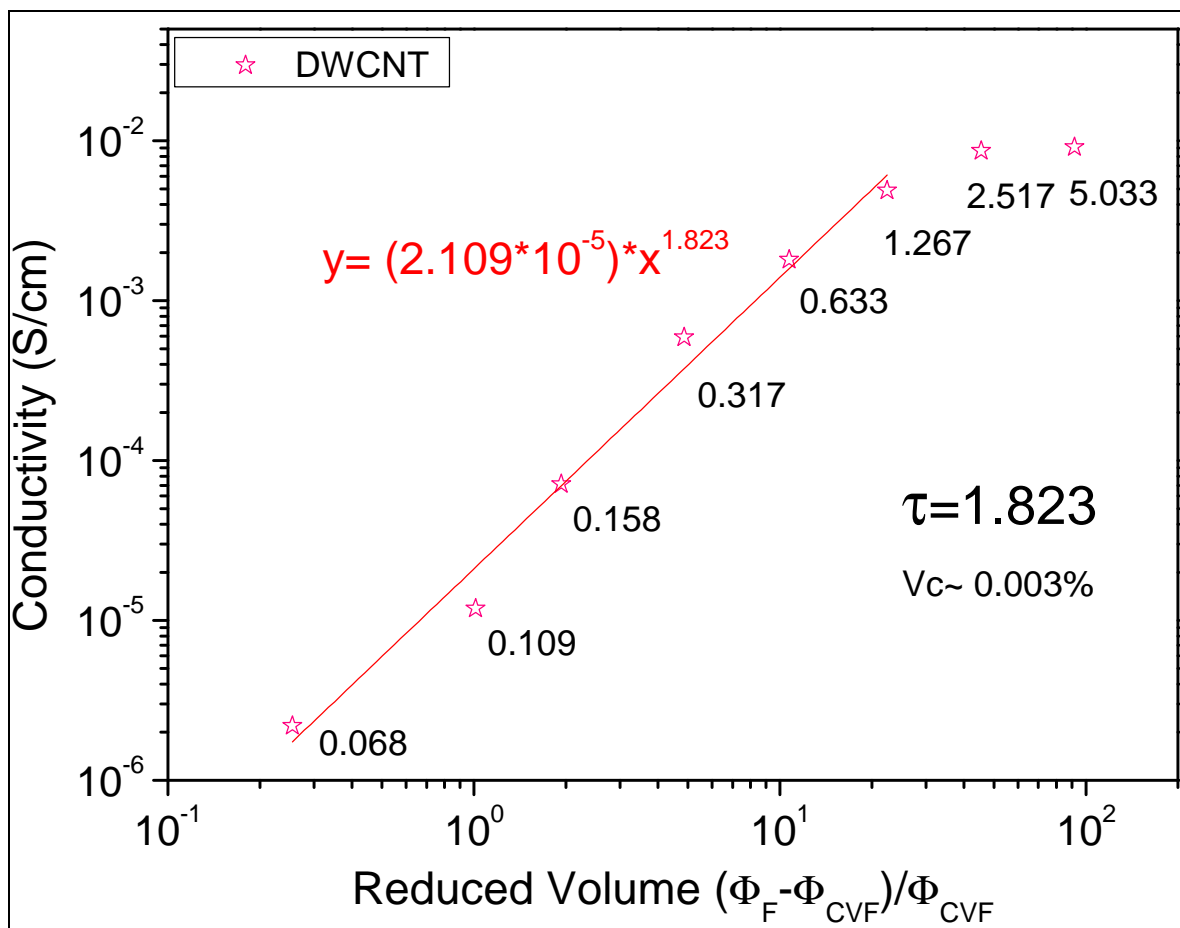


Figure 6.22 Conductivity versus reduced volume for DWCNT-E (both in logarithmic scale). The CNT concentration (mg/mL) is indicated for each point.

On the basis of these results, it was concluded that:

(i) the acidic treatment of raw CNT-CoMo-MgO composites powders with HCl well dissolved magnesia, but only a part of Co and Mo NPs and gave typical extracted materials containing 89-89.7 wt% of carbon, which is composed mainly by long DWCNTs with rare defects and heaps of DWCNTs; Raman spectra in different areas on each sample can sometimes present regions with various characteristics of *RBM*, which is a consequence of the distribution of DWCNT diameter (1-3 nm), and also different $I_{D/G}$ values never higher than 0.17 (similar differences are found between the several batches, with $I_{D/G}$ variations of ± 0.07);

(ii) the measured dynamic percolation threshold of DWCNTs in liquid was in the range of 0.0025 - 0.012 vol.%, indicating a lack of reproducibility probably related to CNT aggregation or insufficient dispersion; however the best dispersed samples gave lower percolation thresholds (0.002-0.003 vol.%) than SWCNTs or MWCNTs;

(iii) the high aspect ratio of DWCNTs associated with their extra outer walls, in comparison to SWCNTs, make them suitable for applications in composites in which it is required electrical conductivity at low concentrations of material;

(iv) the modified rule of mixtures did not allow us to predict the electrical conductivity of the studied 3D networks of CNTs which can be due to an imperfect mixing and desaggregation of CNTs bundles and heaps of CNTs;

(v) the electrical conductivities of 3D CNTNs in liquid present a good correlation with the percolation theory (power law between the reduced volume and the conductivity).

6.3.2 DWCNTs Functionalization

Functionalization (covalent or non-covalent) of CNTs (followed by sonication) is required in order to prepare a stable aqueous suspension with CNTs (necessary to synthesize *in-situ* the ceramic matrix around the dispersed CNTs). As already explained in the bibliographic revision section, even though the use of surfactant (non-covalent functionalization) to disperse CNTs preserves their electronic structure, the disadvantage is that it remains in the nanocomposites. Besides surfactant is greatly used to prepare nanocomposites, probably due to its simplicity, it might be avoided for electrical conductivity purposes. Indeed, according to Bryning *et al.* [36] the wrapping of CNTs by surfactants might even raise the resistivity by increasing the intertube resistance.

Therefore, initially some of the mostly used [74] nitro-sulphuric based covalent functionalizations were evaluated in the pH domain where sol-gel syntheses are conducted (acid medium) by Zeta potential measurements. Figure 6.23 presents Zeta potential curves of DWCNTs with different kinds of chemical oxidation that involved reflux of different acids or acid mixtures in comparison with non-functionalized DWCNTs. The threshold in Zeta potential, so called isoelectric point, is the point at which the charge is neutralized and the dispersion is the less stable. In the case of CNTs it can vary according to the type of functionalization applied. The Zeta curve of non-functionalized DWCNTs in this study is similar to that presented by other authors [169,170], but quite different from that presented by Jiang *et al.* [171]. It is important to outline that the oxidation of C atoms in the defects of CNTs (or eventual presence of disordered carbon) in non-functionalized CNTs can also alter

the behaviour of Zeta potential as a function of pH. As it can be observed, at pH below 2, all the suspensions of CNTs (before or after covalent functionalization) present the lowest modulated values of Zeta potential compared to measurements at different pH, which can be correlated to low charge repulsion between CNTs. As expected [76], the presence of carboxylic functional groups in the *F*-DWCNTs generated negative Zeta potential in all range of pH. In spite of this, at pH 4 all the functionalized CNTs present a high negative potential (around -50 mV), which is generally correlated with a good stability of the suspension. Therefore, this study demonstrated that the repulsion forces caused by the three different covalent functionalizations are not significantly different within the tested oxidations. Furthermore, the Zeta potential curves also demonstrate that the best optimal pH to work, in the case of an acidic route for sol-gel, would be around pH=4 (or more, but then with consequence of longer time to gelify by acidic route of sol-gel for a given temperature).

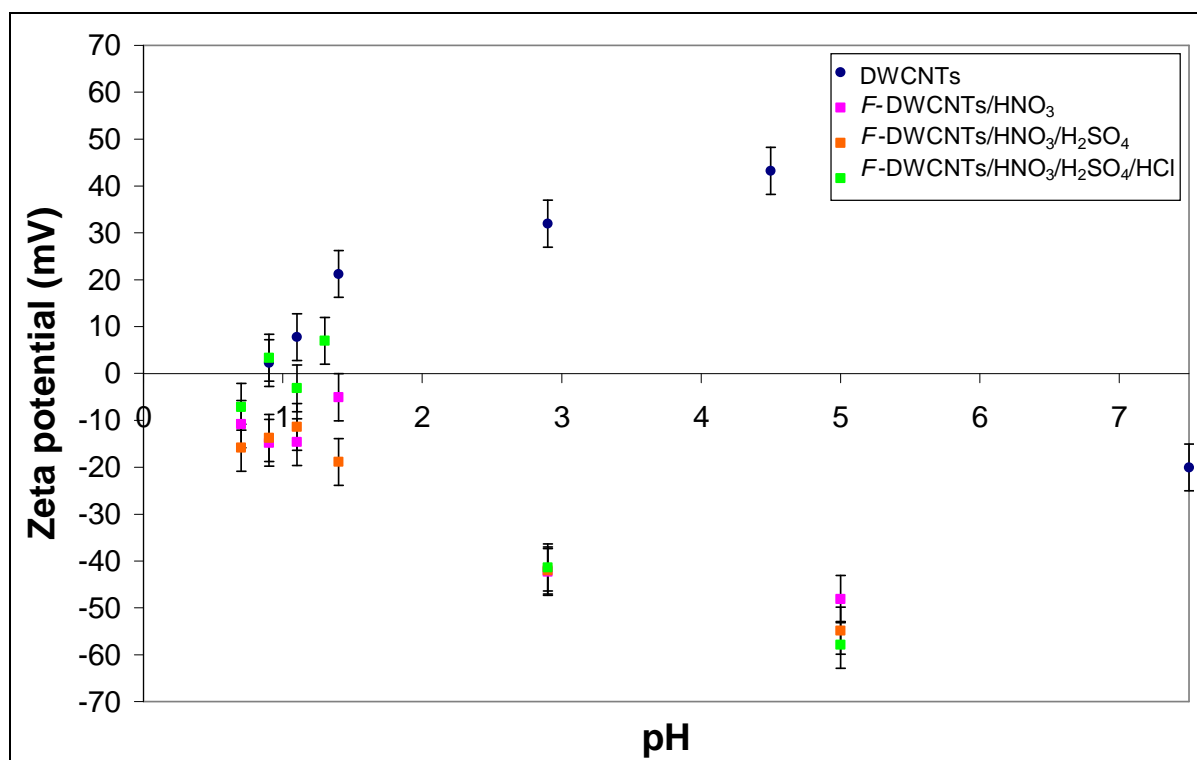


Figure 6.23 Zeta potential curve of CNTs non-functionalized (DWCNTs) and functionalized (using a reflux step) with acid nitric (*F*-DWCNTs/HNO₃), with acids nitric and sulphuric (*F*-DWCNTs/HNO₃/H₂SO₄) and with acids nitric, sulphuric and chloridric (*F*-DWCNTs/HNO₃/H₂SO₄/HCl).

However, the reflux step generally used during the chemical oxidation leads to breakage in the graphitic structure (eventually followed by shortening of the CNTs) as

reported by Liu *et al.* [172] and Datsyuk *et al.* [173]. In order to decrease the deleterious effects, bath sonication has been adopted instead of reflux, as suggested by Chen *et al.* [95]. Little modifications were done in comparison to their work. Briefly, the extracted CNTs were kept in contact with a mixture of nitric and sulphuric acids during bath sonication for about 1 h (in an ice bath) followed by 24 h of magnetic stirring. After that, chloridric acid was added for 10 min while stirring according to Chen *et al.* [95], then the medium was neutralized using ammonium hydroxide (in an ice bath) and finally abundantly rinsed with deionized water. Chen *et al.* [95] related that the addition of chloridric acid in nitro-sulphuric functionalization would cause an increase of the quantity of carboxylic (–COOH) groupments. Indeed, tests of stability of a suspension at pH near 4 for concentration of 1 mg/mL were carried out in our work for this adapted soft functionalization and are shown in Figure 6.24. As can be seen, the adapted soft chemical oxidation based on the work of Chen *et al.* [95] can allow a good stability of CNTs suspensions up to one week even at pH around 3.6. This good stability of suspension with time is also confirmed by Osorio [74] by the study of nitro-sulphuric based functionalizations (also using bath sonication, 2h followed by 15h of stirring, to prepare them). In their work they confirmed that an extra addition of chloridric acid at the last step of covalent functionalization can improve the stability at neutral pH: up to 20 days *F*-SWCNTs were still dispersed. This was evidenced by an increase of the intensity of the bands corresponding to carboxylic groupments observed by Infrared spectroscopy for the samples prepared with an extra addition of HCl than without this step and also by tests of stability of aqueous suspensions (containing 0.1 mg/mL of *F*-DWCNTs) at neutral pH up to 20 days.

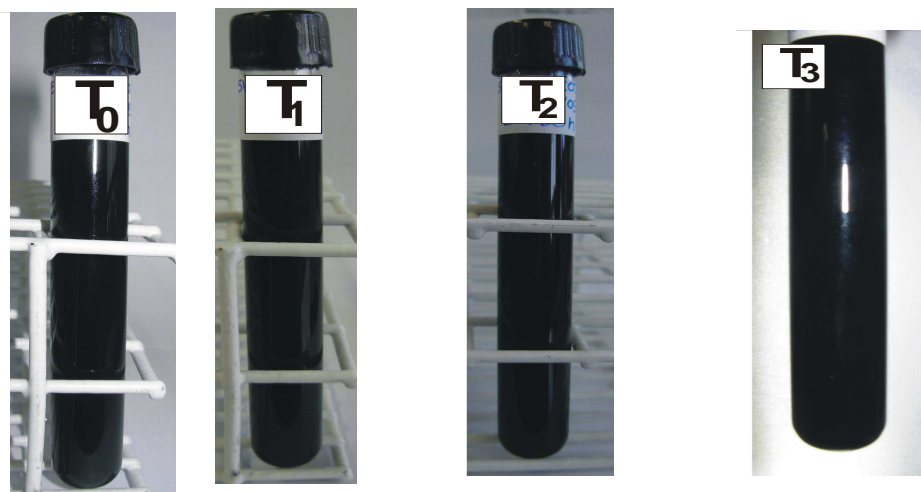


Figure 6.24 Qualitative stability test at pH 3.6 for functionalization with $\text{HNO}_3/\text{H}_2\text{SO}_4\text{-HCl}$ (aqueous suspension with ~ 1 mg/mL) at different times: T_0 is just after preparation of suspension, T_1 is after 24h, T_2 is after 48h and T_3 is after one week.

Figure 6.25a presents the XRD pattern of the DWCNTs after treatment by the functionalization method selected during this work. XRD pattern shows still some remaining Co and the wide (002) peak of graphitic-like material. As it can be observed, neither the treatment with HCl (Figures 6.17 and 6.18) nor the treatment of functionalization has completely eliminated the cobalt metal NPs. Indeed, the elemental analysis of the functionalized material (carried out at Service Central d'Analyse from CNRS in Lyon) revealed that there is about 2.86 wt.% of remaining Co and 0.38 wt.% of Mo after functionalization (against 3.65 wt.% of Co and 1.27 wt.% of Mo before), indicating that there is also a loss of metal particles during this treatment. Besides it was expected that cobalt metal NPs would be eliminated after the contact with nitric acid during chemical oxidation [174], the presence of metal NPs is confirmed by TEM observations (Figure 6.26). The acidic function (-COOH) can react with carbon preferentially in disordered carbon and at the defect of graphitic structure and thus can dissolve part of the metal NPs encapsulated. The remaining particles are probably protected against the acidic attack by graphitic shells (as extensively reported by Flahaut *et al.* [165] in previous works with similar materials) or CNTs (as shown in Figure 6.18) The inset in Figure 6.25 shows typical yellowish/brownish first filtrated solution. It can be related to the fragments of graphitic carbon (and maybe some CNTs) that pass through the membrane of filtration due to chemical oxidation.

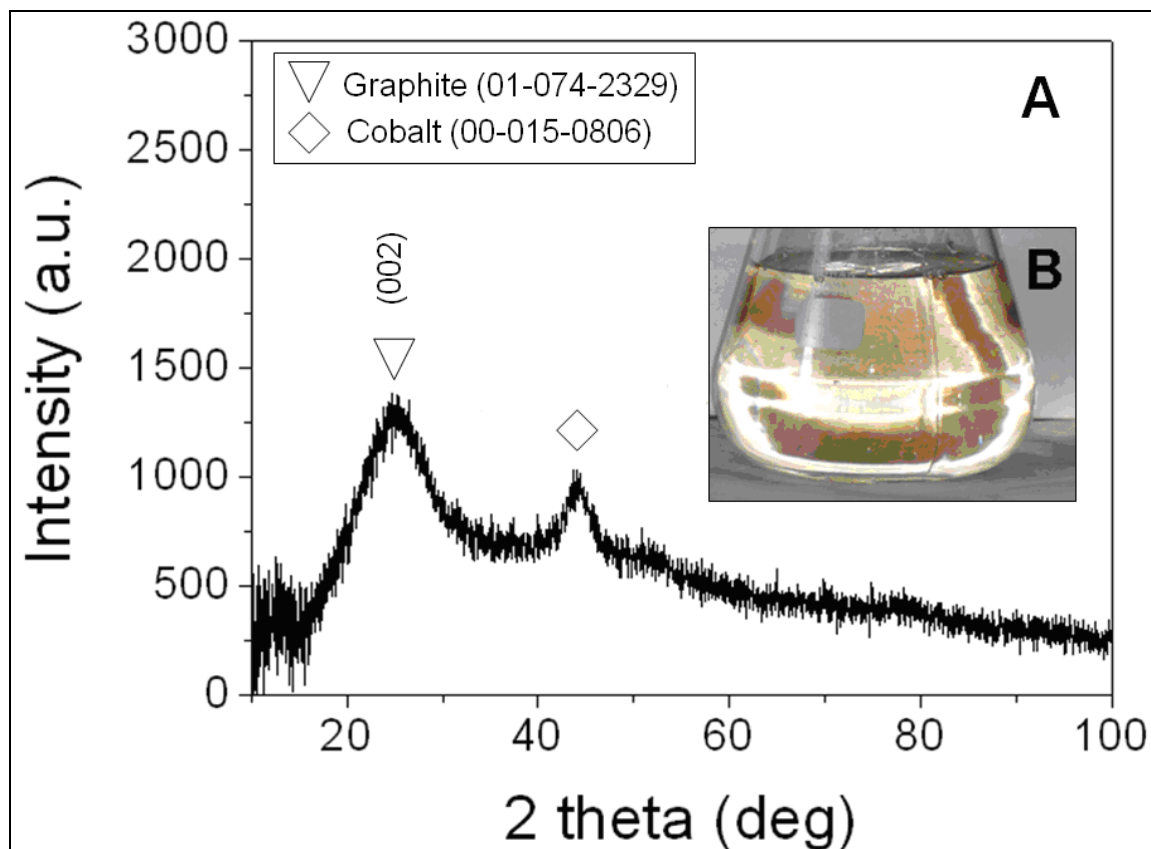


Figure 6.25 *F*-DWCNT: (a) XRD pattern of the material after rinsing with deionized water and (b) first filtrated solution after the chemical oxidation step.

TEM images (Figure 6.26) show that even though the DWCNTs were submitted to a chemical oxidation, this treatment was not so severe. When it is too strong, most CNTs are cut and opened [173], but in the present work with this adapted functionalization process, most CNTs are as long as originally (except for few of them: probably cut in the “defects” of the original graphitic structure of the CNTs since it was a soft functionalization). TEM images of *F*-DWCNTs show that graphitic heaps or shells (black arrows) can be visualized, as well as encapsulated metal NPs (blue arrows) and few structural defects (red arrows: only “kinks” were observed), which is also confirmed by Raman spectroscopy by analysis of *D/G* ratio of intensities, $I_{D/G}$ (Table 6.6). The non-homogeneous disordered carbon visualized in the outer walls of *F*-DWCNTs (Figure 6.26) is most probably remaining disordered carbon from the original sample (Figure 6.18). Disordered carbon is more reactive than CNTs, therefore would be the first to be functionalized. After functionalization, the material was submitted to bath sonication in order to prepare the grids. During the sonication probably some of the functionalized disordered carbon migrated to the

outerwalls of the *F*-DWCNT. It is also important to outline in TEM images that bundling is still observed after functionalization.

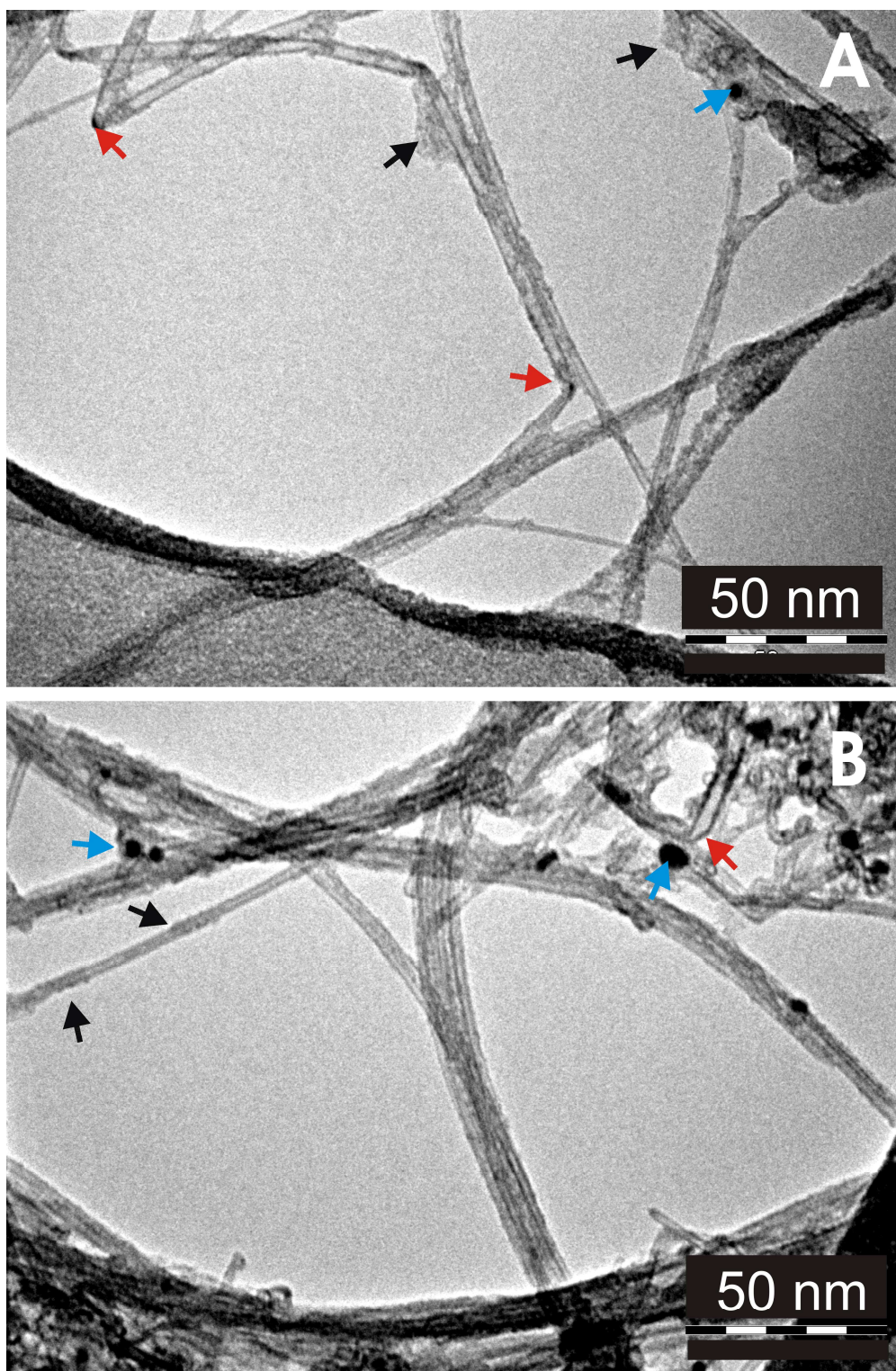


Figure 6.26 TEM images of (a) *F*-DWCNT-B and (b) *F*-DWCNT-E (material used for wet route). Red arrows as defects (“kinks”), black arrows as other carbon impurities and blue arrows as metal NPs.

Average Raman spectra from different batches of *F*-DWCNTs (normalized to D^*) are presented in Figure 6.27. Radial Breathing Modes (*RBM*) peaks were

observed in all cases and the $I_{D/G}$ ratio increases slightly (Table 6.6) after the step of soft functionalization, but never reached values higher than 0.20. This increase in $I_{D/G}$ is a consequence of the opening of some C-C bonds [71]. Therefore, this breakage of bonds can contribute to an increase in the proportion of sp^3 -like carbon (generally attributed to presence of more structural defects). After functionalization, the $I_{D/G}$ of all batches remained quite low and with small differences (minimum 0.16 and maximum 0.20) can be observed among the different batches of functionalizations. The differences in the carbon content (from 61.4 wt. % to 74.5 wt. %) associated to small variance in $I_{D/G}$ might be related to the fact of different relative amount of encapsulated (in graphitic shells or CNTs) metallic NPs or grafted functions. The carbon analysis evidenced a strong decrease of carbon content (from about 89.3 wt.% to 60-70 wt. %) after the functionalization step. This might be a consequence not only of the O and H atoms from functionalization, but also of a loss of disordered carbon during the process (accompanied by the only partial removal of cobalt and molybdenum, thus increasing their relative content: Co/C weight ratio before functionalization is 0.041 and after is 0.044). An upshift ($16\text{-}26\text{ cm}^{-1}$) of the D^* band (originally ca. 2608 cm^{-1}) was observed after almost all DWCNTs were functionalized (excepted DWCNT-C, insignificant upshift of 2 cm^{-1} considering that the uncertainty in reading the position of peaks is $\pm 1\text{ cm}^{-1}$). This probably reflects a charge transfer (electrons from the CNT to the COOH groupments) caused by the chemical oxidation [175]. On the basis of the findings described above, the chemical oxidation adopted can be considered as not severe and the differences in $I_{D/G}$ and D^* upshifts among different batches of functionalization might be related to limited reproduction of this step in the damage of graphitic structure, which might also depend on the relative quantity of sp^3 -like carbon in the original material. Alternatives to overcome this might be: (i) use of an unique batch of functionalized material; (ii) homogenization by milling together several batches of functionalization; (iii) thermal oxidation to eliminate disordered carbon previously to its use.

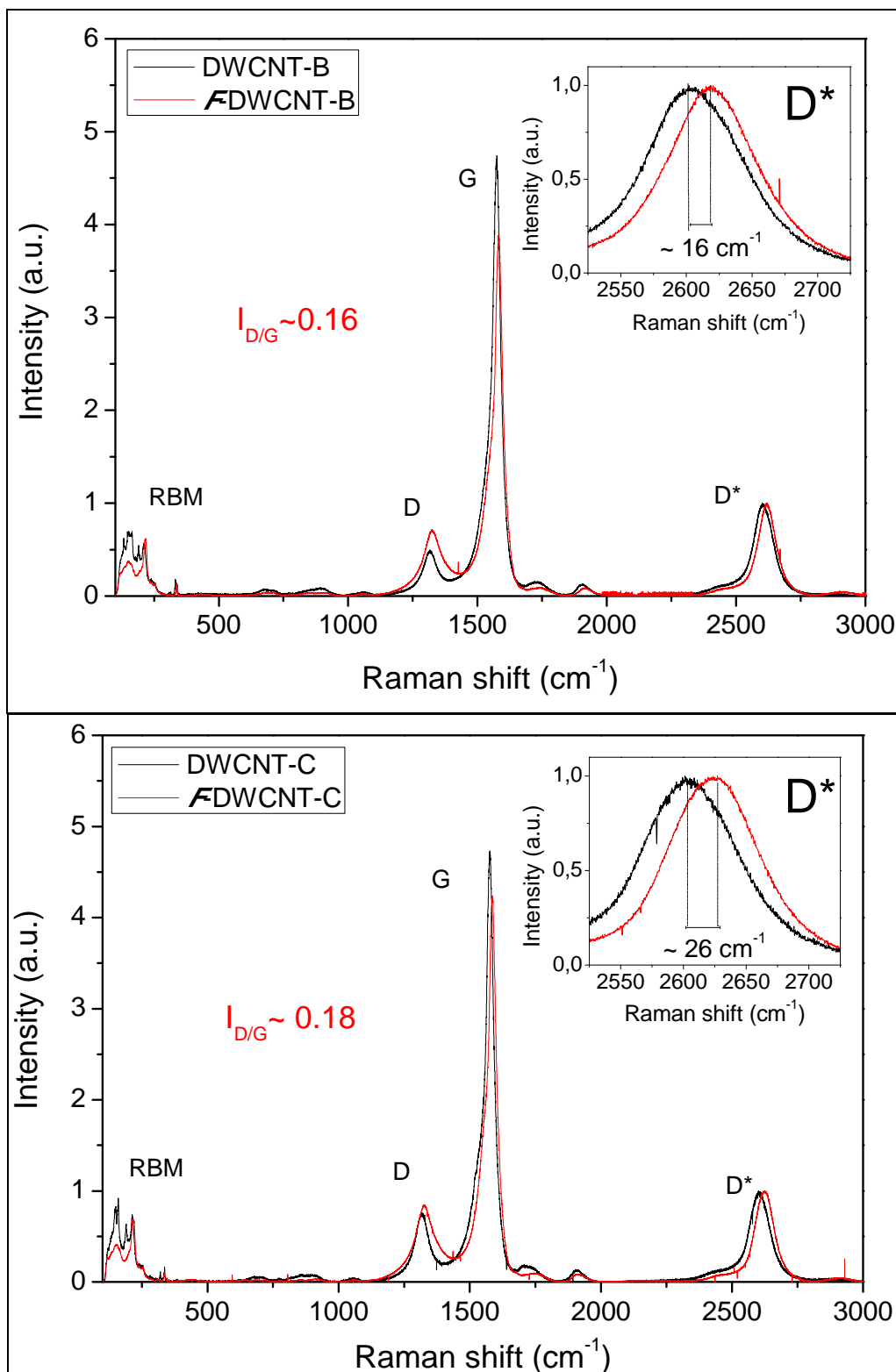


Figure 6.27 Average Raman spectra at $\lambda = 632.8 \text{ nm}$ (normalized to D^*) of F -DWCNT samples from different batches in comparison to original material. Inset: upshift in D^* after functionalization.

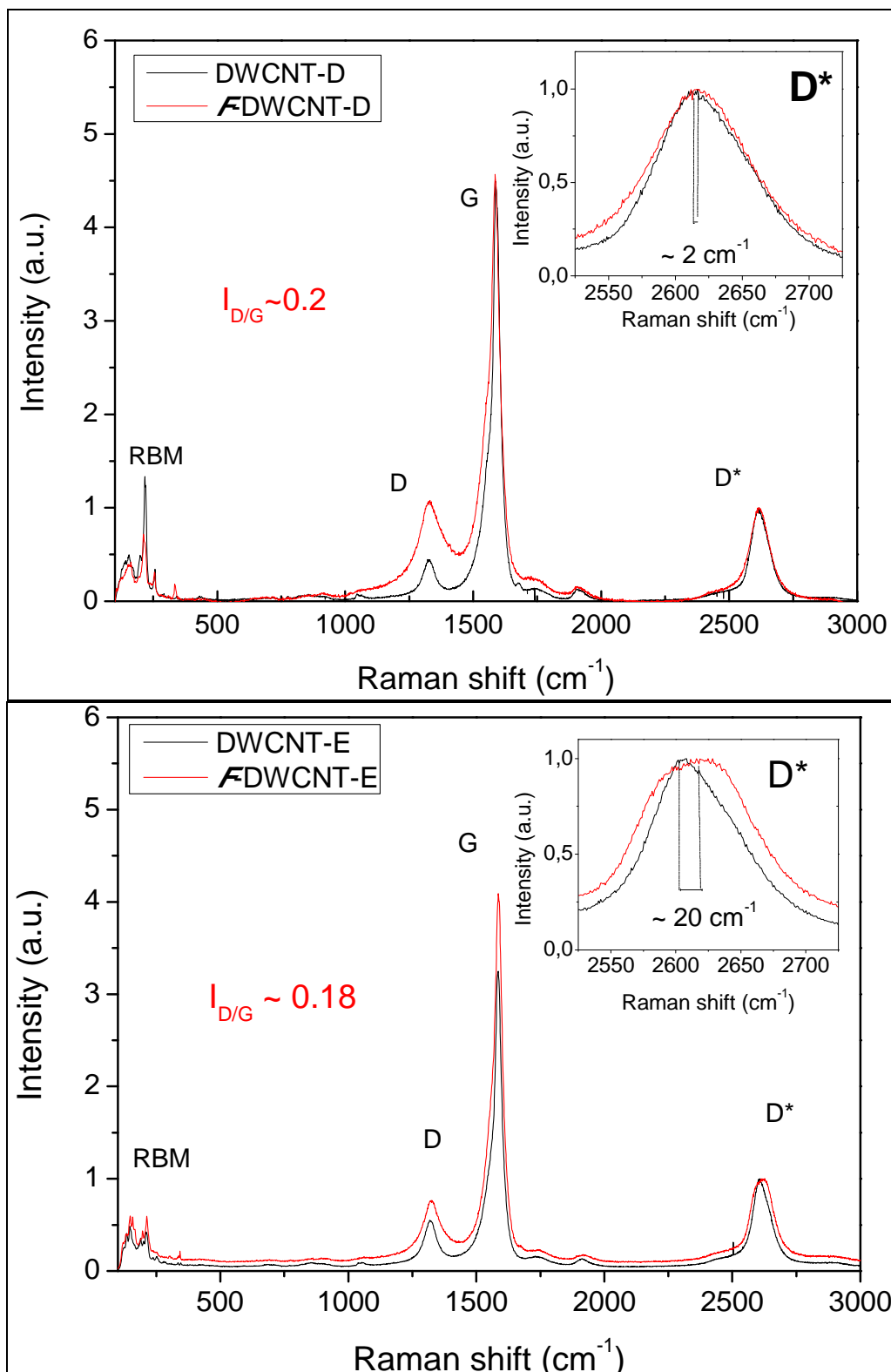


Figure 6.27 (Continued)

Table 6.6 Main characteristics of the DWCNTs after their functionalization: average carbon content wt.% (measured by flash-combustion method: two measurements for each sample) and average $I_{D/G}$ ratios measured by Raman spectroscopy ($\lambda = 632$ nm) for the carbon materials in comparison to original material.

	Average carbon content wt.%	$I_{D/G}$ ratio (Raman)	$I_{D/G}$ ratio of original material (Raman)
F-DWCNT-B	63.5 ± 1.3	0.16	0.10
F-DWCNT-C	61.4 ± 1.2	0.18	0.17
F-DWCNT-D	-	0.20	0.10
F-DWCNT-E	74.5 ± 1.5	0.18	0.16

Infrared spectra of DWCNTs and F-DWCNTs (Figure 6.28) revealed O-H ($3200-3600$ cm^{-1} and $2900-3200$ cm^{-1}), C-H ($2850-3000$ cm^{-1}), C=O ($1720-1740$ cm^{-1}), C=C ($1450-1670$ cm^{-1}), OH and C-O ($1000-1300$ cm^{-1}) bands, as well as an unknown band (1385 cm^{-1}). As can be seen, the spectra are in good agreement with Raman spectroscopy and TEM analyses since it shows just a slight increase of the ratio of the bands C=O to C=C after the chemical oxidation of the DWCNTs. The non-negligible presence of C=O in DWCNTs is due to the presence of defects in the original product (red arrows in Figure 6.18) that are oxidized in contact with air/water (which can be related to the missing 6 wt.% in the chemical analysis together with some O or OH in different forms). Chemical oxidation of the CNTs generates oxygen-containing groups, characterized by OH- bending and C-O-C stretching bonds ($1000-1300$ cm^{-1}), that also stabilize the structure [176]. The C-H bands observed in the range of $2850-3000$ cm^{-1} are typical from alkyl groupments and could be associated to the O-H stretching bands at $3200-3600$ cm^{-1} , which are probably alcohol from preparation of KBr pills. The C=C bands are typically in the region $1450-1670$ cm^{-1} and fundamental CNT mode is in the range $1550-1650$ cm^{-1} [176]. The 1385 cm^{-1} band is an unknown functional group rather than a CNT mode [71], probably assigned to some impurity from the KBr used to prepare the pills (as evidenced in the blank spectra on KBr without CNT in attachment: Figure 0.10). The band at 1435 cm^{-1} can be related to alkyl groupments. The C=O stretching band ($1720-1740$ cm^{-1}) [71] at low frequency (1723 cm^{-1}) is due to a high density of C=O groups caused by the -COOH addition and it is accompanied by presence of O-H

stretching bands of the carboxylic groupments ($2900-3200\text{ cm}^{-1}$). Treatments with concentrated nitric and sulphuric acids generate an electrochemical oxidation of CNTs that leads to a spontaneous charge transfer reaction accompanied by a mass increase of the CNTs sample [177], which explains the lower carbon content in samples after functionalization (Table 6.6). Peaks around $2300-2400\text{ cm}^{-1}$ are rather due to artefact from CO_2/air .

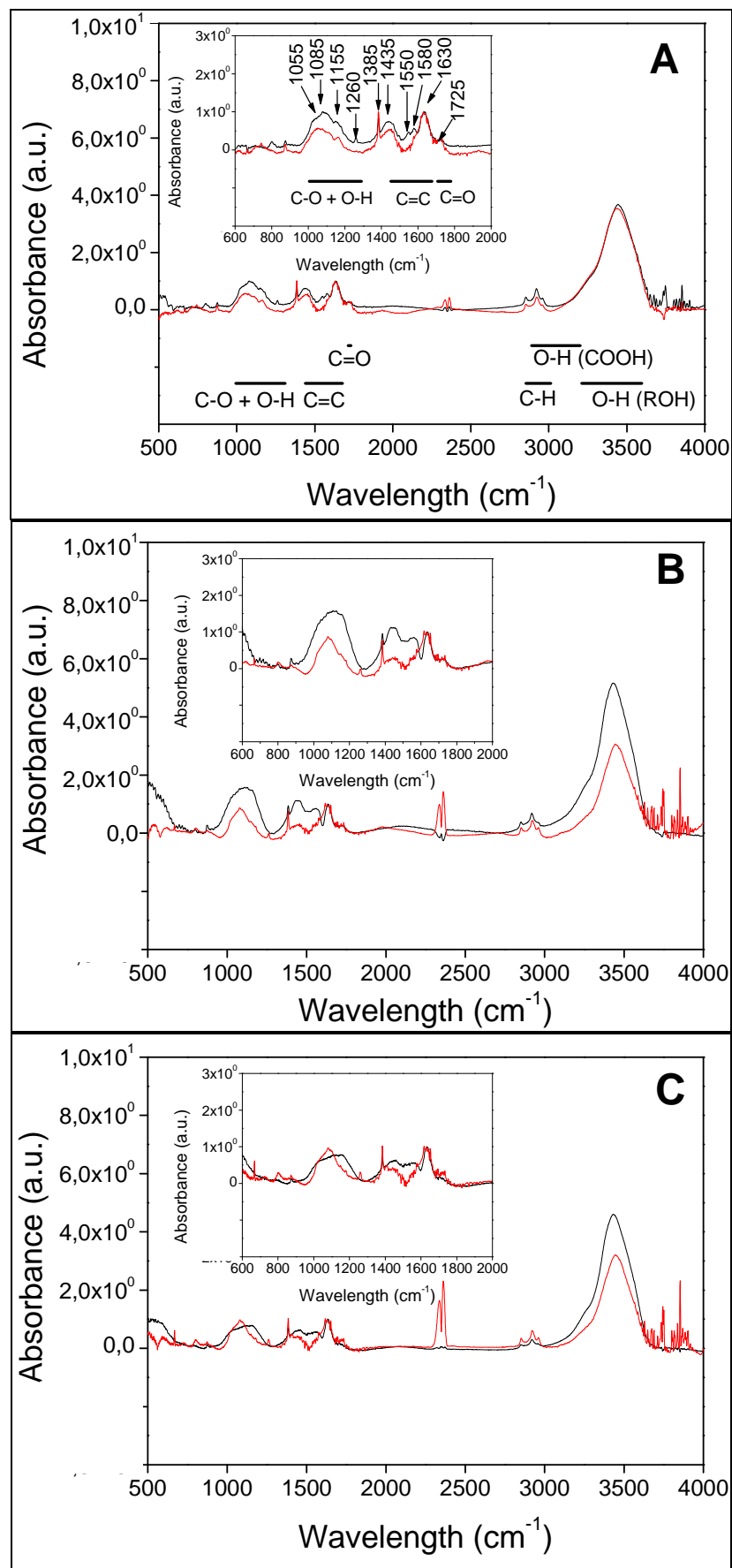


Figure 6.28 Normalized (by the mass and then by C=C peak at $\sim 1630\text{cm}^{-1}$) Infrared spectra of DWCNTs-II before (black line) and after (red line) chemical oxidation from (a) DWCNTs-E, (b) DWCNTs-B and (c) DWCNTs-C.

Measurements of conductivity in liquid (chloroform) of *F*-DWCNTs dynamic networks were carried out to check the effect of the covalent functionalization of the extracted DWCNTs on their electrical conductivity (Figure 6.29). In the case of functionalized materials dried in stove at about 80-100°C and with concentrations around 0.03-0.04 vol.%, the electrical conductivity reached 7.9×10^{-8} S/cm like for *F*-DWCNT-B, while 5.4×10^{-6} S/cm is achieved for *F*-DWCNT-C. On the other hand, when the used materials have been dried at room temperature in a vacuum dessicator, the conductivity is much higher and reached 5.06×10^{-4} S/cm (*F*-DWCNT-D sample) and up to 1.59×10^{-3} S/cm (*F*-DWCNT-E sample) for concentrations of 0.03-0.04 vol.%. Thus, the drying in stove, i.e. at a higher temperature than in dessicator probably results into harder aggregates/agglomerates. Due to the higher content needed to reach percolation and low values of conductivities in comparison to others, samples *F*-DWCNT-B and *F*-DWCNT-C were not used in the further studies. Moreover, these data also evidenced the necessity of working with an unique batch of functionalization of CNTs. Alternatively, an homogenization of several batches would be required.

Therefore, the drying of the CNTs in stove about 80-100°C, especially after functionalization, should be avoided, because hard agglomerates seem to be always formed during drying. It was observed that the agglomerates formed with dried functionalized CNTs are much harder to break by manual grinding (thus, by sonication as well) than the ones formed with non-functionalized CNTs. This is not surprising since dried functionalized CNTs, with more carboxylic groupments and more defects than non-functionalized ones, present outer walls with high reactivity that contribute to the formation of hard agglomerates after drying. As previously stated, a region of 10 nm in contact of two non-functionalized SWCNTs, for example, already present a bond energy of about 250 kJ (or 0.5 eV/nm for SWCNT-SWCNT contact) [7,101], so functionalized ones would interact between each other with a much more intense energy.

Indeed, the chemically inert surface of CNTs is converted into a reactive surface after chemical oxidation by inserting more carbonyl (-CO) and carboxylic (-COOH) groupments. Therefore, even if the functionalization step could be reproduced, not necessarily the conductivity achieved with similar concentration of CNTs could be reproduced since the dispersion and size of aggregates would not be necessarily the same. However, a decrease of almost one order of magnitude of the

conductivity of functionalized DWCNTs (dried in dessicator) at concentrations above percolation was observed in comparison to its original material. For example, DWCNT-E before functionalization shows a conductivity of 9.1×10^{-3} S/cm at 0.28 vol.%, while after functionalization it decreases to 1.92×10^{-3} S/cm at a similar content. This could be explained by the fact that: (i) defects act as scattering centres and, therefore, are detrimental to the electron transport of electrons; (ii) maybe also intertube contacts are injured by the presence of carboxylic groupments; (iii) short segments of intact outer walls would difficult two functionalized DWCNTs to contact electrically with the inner tubes [50]; and (iv) the possibility of an inner tube to be metallic is approximately 1/3 [50].

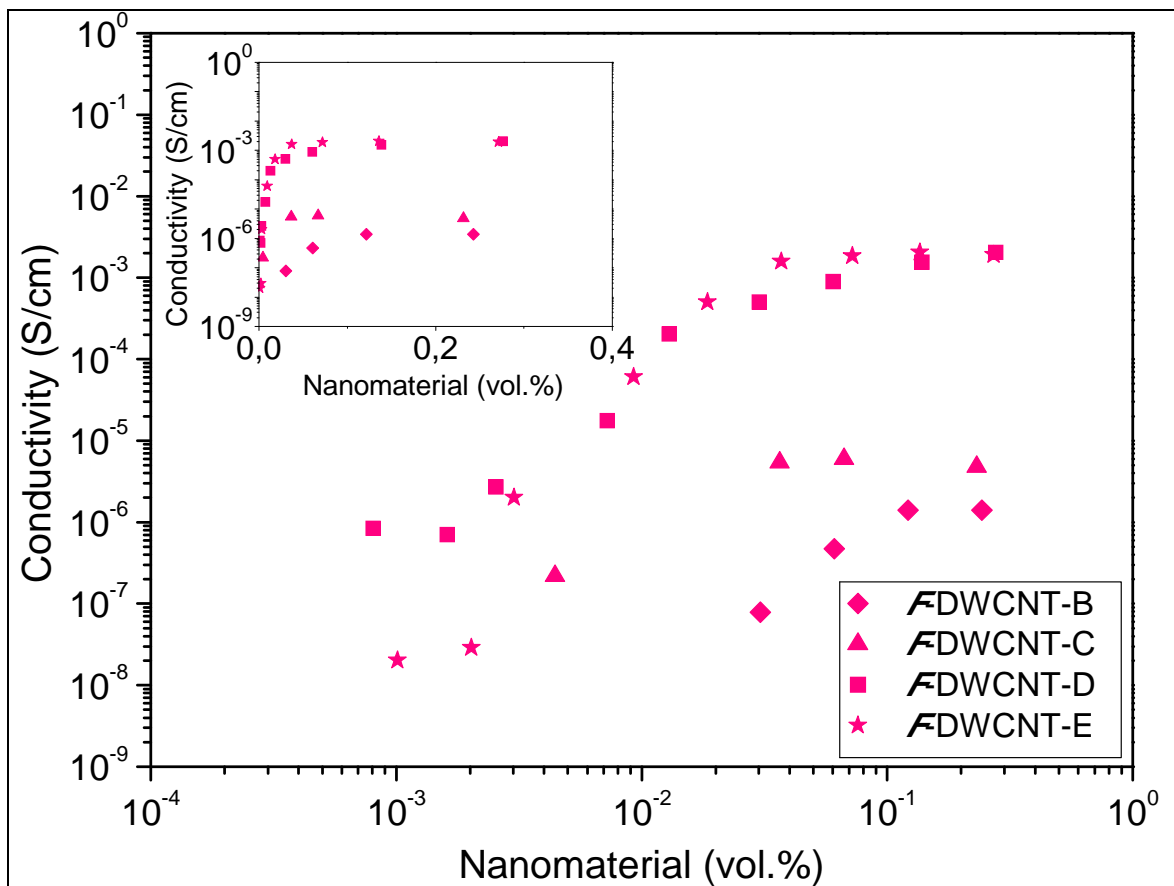


Figure 6.29 Electrical conductivity of the carbon suspensions in chloroform at 1.5 V DC (0.104 V/cm) during sonication of different batches of *F*-DWCNTs: dried in stove (*F*-DWCNT-B and *F*-DWCNT-C) and dried in dessicator (*F*-DWCNT-D and *F*-DWCNT-E).

From these results, it was concluded that:

- (i) The conductivity of functionalized CNTs can lack of reproducibility, which might depend on the amount of sp^3 -like carbon (before and after functionalization) as well as the drying of *F*-DWCNTs itself. During the manipulations it was observed that the drying step after chemical oxidation of the DWCNTs makes them difficult to disperse in the aqueous solution, requiring a manual grinding to break the hard aggregates before dispersing with probe sonication. Therefore, in spite of using the same functionalization treatment, different batches would lead to different dispersion states of CNTs in the silica matrix. This fact can be due to the drying step that decreased the efficiency of loading of *F*-DWCNTs (aggregation) associated to different chiralities attacked during functionalization. Samples dried at high temperature (80-100°C) lead to lower final conductivities (for example, at 0.03-0.04 vol.% conductivities are around 5×10^{-6} S/cm and 8×10^{-8} S/cm) than samples dried in dessicator at room temperature (conductivities at 0.03-0.04 vol.% around 5×10^{-4} S/cm and 1.6×10^{-3} S/cm) due to the formation of hard aggregates in the first ones. Thus, the step of drying of *F*-DWCNTs demonstrated to affect more than the batch of functionalization in the final conductivity. Alternatively, a batch of *F*-DWCNT was maintained wet for preparation of a set of composites in order to avoid these difficulties.
- (ii) The percolation threshold seems to be similar before (0.0025-0.012 vol.%) and after (0.0026-0.04 vol.%) functionalization and only the electrical conductivity is decreased. This would confirm that functionalization treatment does not damage the tubes (similar aspect ratio), but creates more defects (which act as scattering centers for transport of electrons) or increase the contact resistance (-COOH groups might decrease the proportion of direct intertube contacts).

6.3.3 Nanocomposite powders

Two routes were tested to prepare the nanocomposite powders: dry route and wet route. In the first case the DWCNTs were dried in vacuum dessicator (at room temperature) or stove (at 80-100°C) after acidic treatment, while in wet route it was tested not to dry the CNTs to avoid agglomeration of *F*-DWCNTs due to interaction between the carboxylic groupments on their surface. Samples with *F*-DWCNTs dried in stove were quite insulating even at carbon contents above the value of percolation threshold observed by conductivity in liquid. Thus, the stove dried route was abandoned. Samples dried in dessicator after functionalizations will be called D (dried) while for the wet route they will be called W (wet).

In the case of the dry route, *F*-DWCNTs-SiO₂ nanocomposites were prepared using different batches of functionalization (only samples D1-D3 were prepared using the same batch of functionalization), but difficulties in reproducibility were observed (see below). Moreover, dried *F*-DWCNTs form strong agglomerates that should be broken in a mortar previously to their dispersion in aqueous solution because probe sonication is not sufficient.

In the case of the wet route, a set of *F*-DWCNTs-SiO₂ nanocomposites was prepared using the same batch of functionalization (and of synthesis) to try to improve the reproducibility. Briefly, after *F*-DWCNTs from the same batch of functionalization were rinsed with deionized water, they were maintained humid until their dispersion in aqueous solution (wet route).

To prepare *F*-DWCNTs-SiO₂ nanocomposites, wet *F*-DWCNTs were firstly dispersed in acidic aqueous solution with the aid of probe sonication for not longer than 35 min and using an ice bath (heating is deleterious for the dispersion, which is confirmed by fluorescence tests of Heller *et al.* [178]). Finally, the prepared aqueous solution was incorporated, while magnetic stirring, into an alcoholic solution containing tetraethylorthosilicate and let it gelify.

In order to select the working pH for the gelification of the sol, a compromise between the time needed for gelification and the stability of the suspension was investigated. Indeed, a more acidic pH would gelify faster, but a too acidic pH would be deleterious for the stability of the *F*-DWCNT suspension (as shown by Zeta

potential curves). Therefore a pH around 3.6 was used for the preparation of the composites. A high proportion of molar content of water per TEOS, the so called r ratio, of 20 was used in order to facilitate the incorporation of high loadings of F -DWCNTs. Then, a molar ratio of ethanol to TEOS was fixed around 0.3 based on Brinker *et al.* results [25]. They reported this molar ratio of ethanol to TEOS for similar molar ratios of water to TEOS (r ratio of 20). The nanocomposite powders were let to gelify with constant stirring at room temperature. In order to remove the organic compounds, thermal treatments at 400°C for 2h were carried out (higher temperatures in oxidizing atmosphere were avoided to preserve CNTs), followed by XRD analyses of the nanocomposite powders. As can be expected, after these calcinations of the nanocomposite powders, the silica matrix is amorphous.

It is quite difficult to visualize by FESEM the CNTs in nanocomposite powders (probably because they are surrounded by silica) and generally, CNTs are visualized only at high loadings. Some FESEM images (observations at TEMSCAN in Université Paul Sabatier) of the nanocomposite powders obtained by dry or wet route at the highest loadings of carbon - 2.97 vol.% and 6.43 vol.%, respectively - (after the calcination step) are reported in Figures 6.30a and 6.30b, respectively. In both cases, F -DWCNTs are presented in the form of thin bundles (d_{MAX} around 20 nm for D and W routes), which seems rather well dispersed within silica grains. No aggregates were observed on the images of the powders. However, we will see later one that some were observed on SEM images of dense nanocomposites.

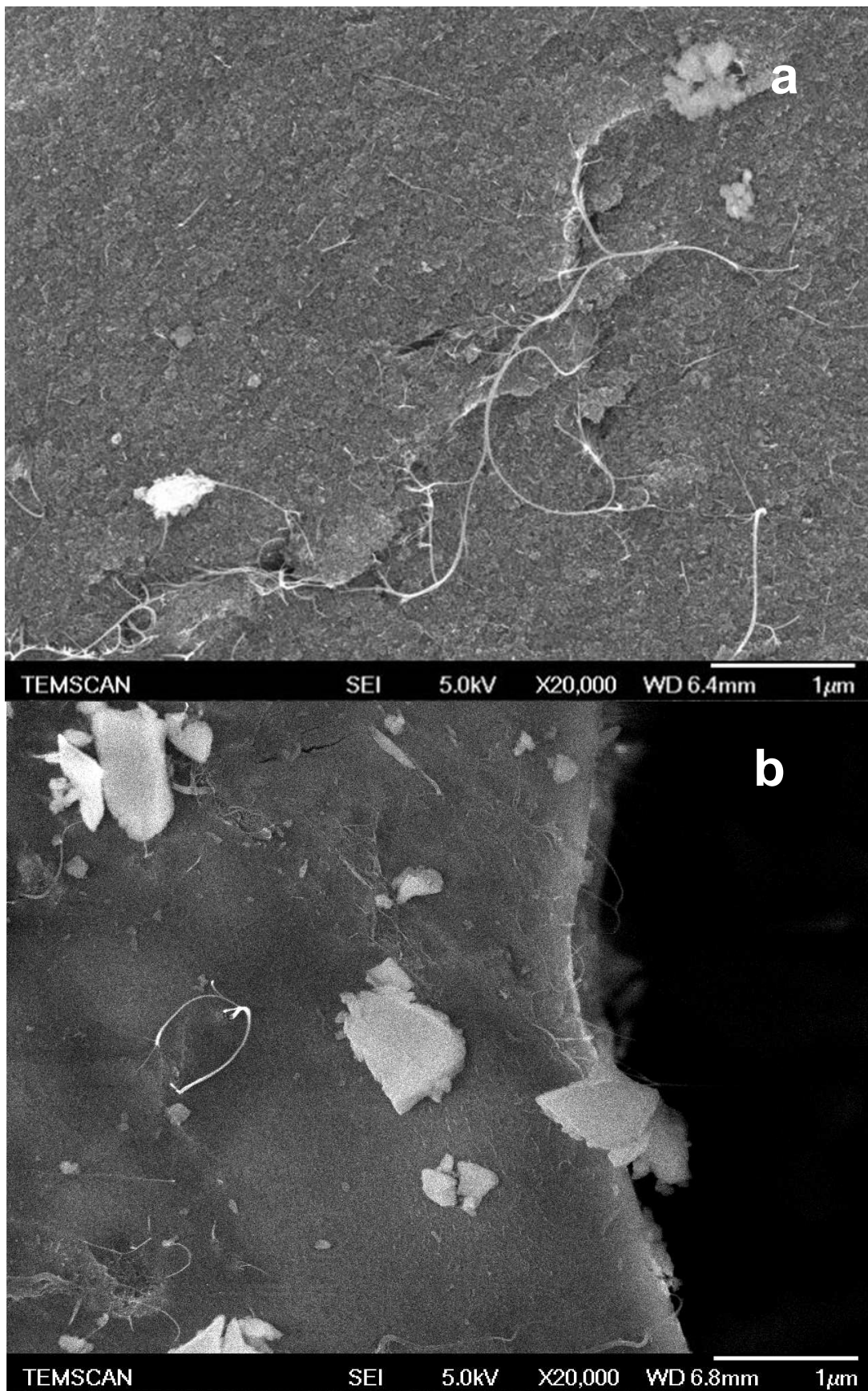


Figure 6.30 FESEM image of a nanocomposite powders D (a) and W (b) prepared using dry (2.97 vol.% of average carbon content) or wet (6.43 vol.% of average carbon content) DWCNTs, respectively.

Moreover, in order to check the presence of CNTs in the calcinated nanocomposite powders, Raman spectroscopy was also performed (at Service d'Analyse from CNRS-UPS). The Raman spectra of the nanocomposite powders prepared by dry or wet route at the highest loadings are reported in Figures 6.31A and 6.31B, respectively.

The spectra of the D nanocomposite powder with the highest carbon content (2.97 vol.%) shows typical DWCNTs features: *RBM* (peaks around 161, 195, 204, 224 and 256 cm^{-1}), *D* ($\sim 1332 \text{ cm}^{-1}$), *G* ($\sim 1595 \text{ cm}^{-1}$) and *D** ($\sim 2635 \text{ cm}^{-1}$) band. The $I_{D/G}$ ratio (0.17) is similar to the value calculated for *F*-DWCNTs before incorporation into silica ($I_{D/G}$ of 0.16), which indicates that the dispersion step using probe sonication does not significantly increase the amount of defects on *F*-DWCNTs in spite of the fact that sonication is known to damage CNTs [179]. Besides the lineshapes were preserved, the frequencies of *D* (*F*-DWCNTs originally at $\sim 1327 \text{ cm}^{-1}$) and *G* (*F*-DWCNTs originally at $\sim 1586 \text{ cm}^{-1}$) upshifted 5 cm^{-1} and 9 cm^{-1} , respectively; while *D** (*F*-DWCNTs originally at $\sim 2617 \text{ cm}^{-1}$) upshifted 18 cm^{-1} in comparison to the functionalized material. These upshifts can be related to a negative charge transfer from the DWCNT to the silica matrix, thus a high interaction between CNTs and the silica matrix is evidenced. Similar upshifts in *D* and *G* bands were already reported in the case of doping of graphene/CNTs [180] (probably there is a p-doping of *F*-DWCNTs since in silica there is a lot of available oxygen), while *D** upshift was observed for other composites and attributed to a strong interaction of CNTs with the matrix [99,102].

The spectra of the W nanocomposite powder with the highest carbon content (6.43 vol.%) shows typical DWCNTs features: *RBM* (peaks around 119, 133, 153, 166, 198, 220 and 256 cm^{-1}), *D* ($\sim 1327 \text{ cm}^{-1}$), *G* ($\sim 1588 \text{ cm}^{-1}$) and *D** ($\sim 2625 \text{ cm}^{-1}$) band. The $I_{D/G}$ ratio is 0.22, which indicates that the dispersion step using probe sonication might have slightly increased the amount of defects on *F*-DWCNTs (*F*-DWCNT-E has $I_{D/G}$ of 0.18). It is also important to note that the frequencies of *D* (*F*-DWCNTs originally at $\sim 1324 \text{ cm}^{-1}$) and *G* (*F*-DWCNTs originally at $\sim 1585 \text{ cm}^{-1}$) both upshifted 3 cm^{-1} (the uncertainty on reading position of peaks is $\pm 1 \text{ cm}^{-1}$), while *D** (*F*-DWCNTs originally at $\sim 2618 \text{ cm}^{-1}$) upshifted 7 cm^{-1} in comparison to the functionalized material. The fact that the composite prepared by the wet route with the highest carbon content (5.32 wt.%) present a lower upshift in *D** than the nanocomposite prepared by the dry route with the highest carbon content (2.44 wt.%)

might be related to the presence of aggregates. Indeed, the higher is the carbon content, the higher is the probability of presence of aggregates, which in turn decrease the amount of *F*-DWCNT interacting with the matrix and thus are constrained.

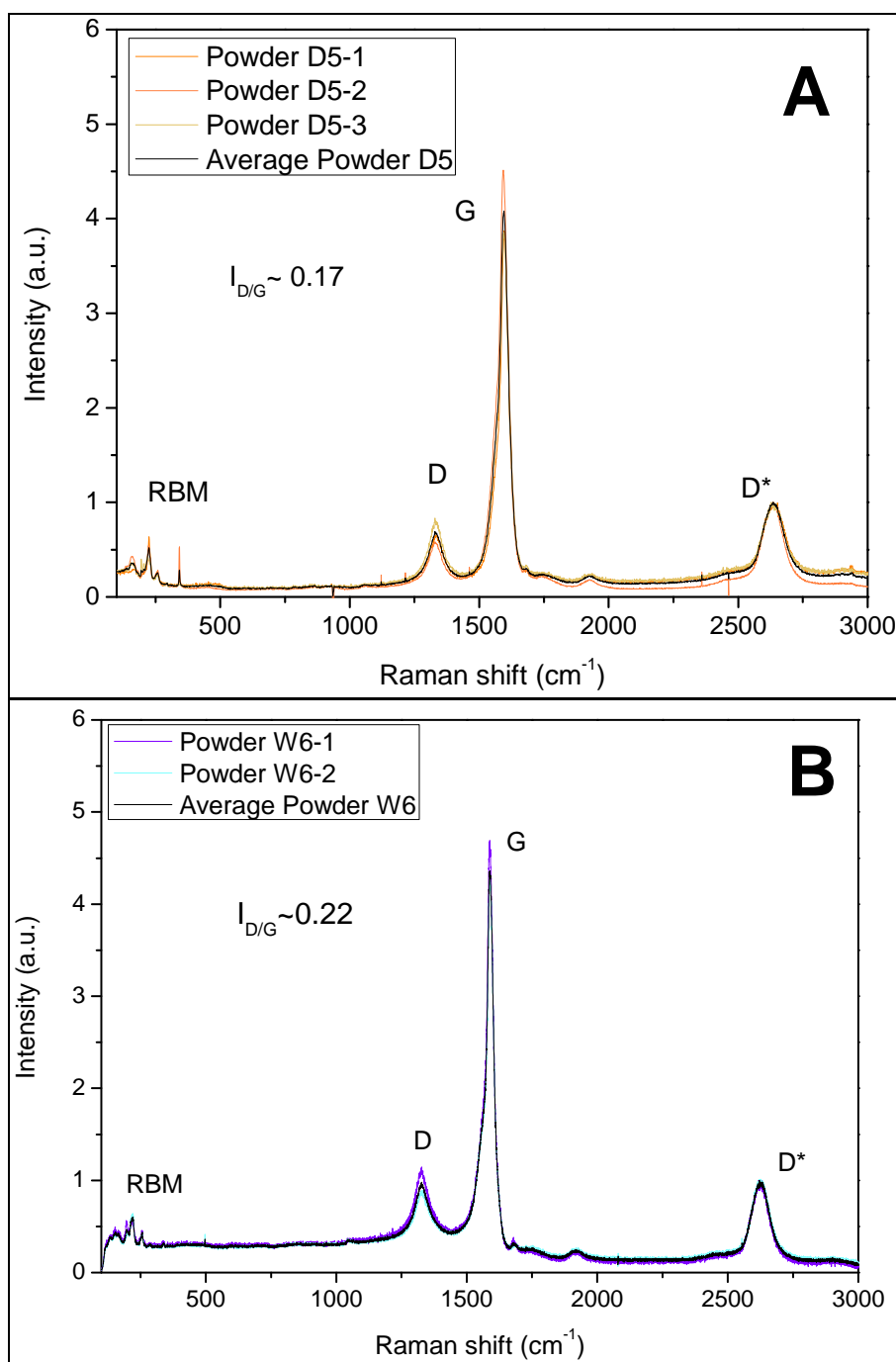


Figure 6.31 Raman spectra at $\lambda = 632.8$ nm (normalized to D^*) of a nanocomposite powder obtained by (A) dry route and (B) wet route (containing 6.43 vol.% of carbon): coloured lines are spectra from different regions of the same sample and black line is the average spectra.

6.3.4 Dense F-DWCNT-SiO₂ Nanocomposites

- Study of the influence of SPS parameters on silica

Since SPS is a relatively new technique of densification (and there is not a full consensus about the mechanisms involved during the process), this study with pure silica was necessary to pre-select the SPS parameters that would be used to further densify the nanocomposites. A preliminary study was conducted using pure silica (based on the work of Mayerhöfer *et al.* [181] who densified commercial fumed silica by SPS) to optimize the SPS parameters for the densification of sol-gel silica. During these tests of densification with pure silica, many challenges were surpassed, like delamination of the material (due to a not efficient pre-compaction of the powder), as well as heterogeneous crystallization of the material probably due to residual water (likely caused by a non efficient storage of the calcinated powders which led to the adsorption of humidity from atmosphere).

Table 6.7 presents some results of this study. Initially, sample with fumed silica (sample S1) was densified based on the work of Mayerhöfer *et al.* [181] with few modifications. Briefly, the differences are that pressure was applied just when reaching the dwell temperature and the step of thermal treatment at 900°C in air for 5h to remove graphite was replaced by a polishing of the samples to remove the graphite layer contaminating their surface. In our study a transparent compacted silica sample was obtained with a relative density (R.D.) of 98.3(±1.4)% (density of 2.16(±0.03) g/cm³, calculated using a density of 2.20 g/cm³ for pure amorphous silica [98]). Besides Mayerhöfer *et al.* [181] achieved a transmittance of ~63% (within the whole range of 200 nm up to 1000 nm), the sample prepared in the present work using fumed silica under similar conditions seems to be more transparent (see Table 6.7). This could be related to microstructural characteristics of the starting powder. For example, Mayerhöfer *et al.* [181] demonstrated (by Infrared and Raman spectroscopies) that the silica glass they prepared by SPS (using silicic acid as silica source) contains a great quantity of hydroxyls groups. That is not surprising since the inorganic route of sol-gel uses quite high amounts of water, even higher molar ratios H₂O:SiO₂ than the organic route of sol-gel [99] and it would be probably be more difficult to eliminate OH groups from in the first case (using silicic acid). Moreover, the fact that Mayerhöfer *et al.* [181] applied pressure of 50 MPa while heating might have

also contributed to keep more closed porosity inside the sample leading to higher opacity of their samples compared to ours.

It was possible to prepare, using fumed silica, a quite dense ($99.9(\pm 0.4)\%$ or $2.20(\pm 0.01)$ g/cm³) and transparent compact sample (sample S2) using a same applied pressure, but a much lower temperature (950°C) and an increased dwell time (15 min).



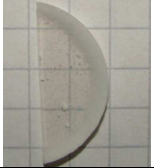


For silica powders prepared by the sol-gel route, firstly a formulation using formamide (samples S3 and S4) was prepared according to the chemical route defined by Estournès *et al.* [182]. By this route it was demonstrated that at 950°C for 5 min and a pressure of 50 MPa, transparent and fully dense samples are obtained for S3 and S4 (same values of densities, taking into account the uncertainties in Table 6.7). To achieve full densification with colloidal commercial silica, Guo *et al.* [183] used similar sintering parameters, excepted a higher temperature (1050°C). Later, the same group [184] reported the full densification using the same commercial colloidal silica and similar conditions than those used for S3 and S4. Therefore, the high relative densities achieved with S3 and S4 in these conditions are not surprising, since it would be expected that the sol-gel route would give silica with a decreased activation energy for sintering (particle's surface energy is the driving force for densification), due to its high specific surface area ($580(\pm 17)$ m²/g after calcination at 400°C for 2h) in comparison to fumed silica (measured $200(\pm 6)$ m²/g). However, due to toxicity of formamide, another set of samples was prepared without formamide.




Therefore, similar conditions of sintering were tested with a calcinated xerogel powder originally obtained by sol-gel without formamide (sample S5). The obtained relative density (R.D.) is $91.9(\pm 3.6)\%$ ($2.02(\pm 0.08)$ g/cm³) if we consider that silica is fully amorphous. However, this sample was opaque (non-transparent) which indicates porosity or some crystallization (a unique pure silica sample, which is not reported in Table 6.7, showed a slight beginning by an unique small peak of crystallization: see Figure 0.11 in the attachment section), and thus a super-estimation of the relative density. The small decrease in relative density might be related to the presence of more hydroxyls than when formamide is used. However, it was observed that similar sintering conditions can lead to different transparencies of the compact samples (samples S6 and S7), which was later correlated with some humidity adsorbed after the calcination step. In spite of the fact that sample S6 has

distributed small white spots in the sample (related to heterogeneous crystallization), its R.D. (in comparison to amorphous silica) is $99.2(\pm 0.9)\%$ ($2.18(\pm 0.02) \text{ g/cm}^3$). In the case of sample S7, which is totally transparent, its R.D. (in comparison to amorphous silica) is $99.5(\pm 0.4)\%$ ($2.19(\pm 0.01) \text{ g/cm}^3$). If sample S8 considered fully amorphous, it has a R.D. of $99.0(\pm 0.9)\%$ ($2.18(\pm 0.02) \text{ g/cm}^3$), but the crystallization concentrated in the borders indicates that it is super-estimated. The nucleation probably started at the interfaces of residual humidity in the powder, which tends to diffuse from the central part to the borders. Therefore, if the densification occurs previously to degassing, sintering occurs with concurrent crystallization. Other problems of sintering can also be correlated to inefficient pre-compaction (sample S9), leading to partition of the sample (by formation of thin flakes).

From the results described above, we conclude that full densification can be achieved even at 950°C for 5 minutes at a pressure of 50 MPa for silica powders obtained by sol-gel (followed by calcination). However, in the case of fumed silica, longer dwell times and higher pressures than for powders prepared by sol-gel are required to obtain similar densifications. This can be explained by the higher specific surface areas of the xerogel powders, which decrease the activation energies for their sintering, in comparison to fumed silica.

Table 6.7 Examples of studies of sintering parameters by SPS with pure silica: silica powder, SPS parameters, final density by Archimedes, relative density (considering amorphous silica) and general aspect.

Sample	Powder	SPS parameters			$\rho_{\text{ARCHIMEDES}}$ (g/cm ³)	Relative density (%)	General aspect (diameter ~ 20 mm)
		T (°C)	P (MPa)	t (min)			
S1	Fumed silica calcinated at 400°C for 2h	600	-	3	2.16 (±0.03)	98.3 (± 1.4)	
		1100	100	5			
S2	Fumed silica calcinated at 400°C for 2h	950	100	15	2.20 (±0.01)	99.9 (± 0.4)	NO PHOTO
S3	Xerogel powder obtained with formamide calcinated at 500°C for 2h	950	50	5	2.20 (±0.04)	≅100 (± 1.8)	
S4	Xerogel powder obtained with formamide calcinated at 500°C for 2h	900	50	5	2.20 (±0.05)	99.8 (± 2.3)	
S5	Xerogel powder obtained without formamide calcinated at 500°C for 2h	900	50	5	2.02 (±0.08)	91.9 (± 3.6)	
S6	Xerogel powder obtained without formamide calcinated at 400°C for 4h	950	100	15	2.18 (±0.02)	99.2 (± 0.9)	

Sample	Powder	SPS parameters			$\rho_{\text{ARCHIMEDES}}$ (g/cm ³)	Relative density (%)	General aspect (diameter ~ 20 mm)
		T (°C)	P (MPa)	t (min)			
S7	Xerogel powder obtained without formamide calcinated at 400°C for 2h	950	100	15	2.19 (±0.01)	99.5 (± 0.4)	
S8	Xerogel powder obtained without formamide calcinated at 400°C for 2h	900	100	5	2.18 (±0.02)	99.0 (± 0.9)	
S9	Xerogel powder obtained without formamide calcinated at 400°C for 2h	950	100	15	-	-	

- SPS densification of *F*-DWCNT-silica nanocomposites

Table 6.8 shows the relative densities (R.D., considering all silica amorphous) of nanocomposites prepared by D (using *F*-DWCNTs dried in dessicator) and W (using wet *F*-DWCNTs) routes in relation with the SPS parameters and carbon contents (varied from 0.12(\pm 0.01) wt.% to 5.32(\pm 0.11) wt.%). Variations in temperature (950°C/1000°C), dwell time (5 min/15 min) and applied pressure (50 MPa/100 MPa) were carried out.

Preliminary sintering tests were performed on nanocomposites samples synthesised using the D route with the SPS parameters leading to dense and transparent compacts for calcinated (400°C for 2h) pure sol-gel silica (sample S7). As can be observed, nearly full densification for these nanocomposites (Table 6.8) can be reached at temperatures of 950-1000°C by a slight modification of the SPS parameters in comparison to pure silica (Table 6.7). Indeed, dense (R.D. around 94.9(\pm 0.91)-96(\pm 0.45)%) compacts of nanocomposites were obtained at 950°C for 15 min at 100 MPa (samples D1 and D2). By decreasing the applied pressure to 50 MPa and maintaining temperature (950°C) and dwell time (15 min) to densify a nanocomposite powder with same carbon content (sample D3), the relative density decreased to 90.2(\pm 4.09)%. Besides an increase of temperature accompanied by a lower dwell time generated a nanocomposite containing 0.29(\pm 0.5) wt.% (sample D4) with a R.D. of 96.1(\pm 2.73)%, it was evidenced that the increase of applied pressure is more efficient to densify these nanocomposites. For example, a nanocomposite containing 2.44(\pm 0.5) wt.% (sample D5) presented a R.D. of 98.0(\pm 0.91)% after sintering by SPS at 950°C for 5 min and 100 MPa of applied pressure. As it can be noted, even at just 50°C above the conditions of sintering of a sample with pure silica, in the presence of CNTs it was possible to achieve densification near the theoretical one.

Table 6.8 Densities of *F*-DWCNT silica nanocomposites measured by Archimedes method with their statistic deviation between brackets in comparison to their SPS parameters, carbon content and relative density (by considering full silica amorphous).

		Average [C]		SPS (T,t,P)	$\rho_{\text{ARCHIMEDES}}$ (g/cm ³)	Relative density (%)
		(wt.%)	(vol.%)			
DRY ROUTE	D1	0.22(±0.004)	0.27(±0.005)	950°C/15'/100MPa	2.09 (±0.02)	94.9(±0.9)
	D2	0.22(±0.004)	0.27(±0.005)	950°C/15'/100MPa	2.11 (±0.01)	96.0(±0.5)
	D3	0.22(±0.004)	0.27(±0.005)	950°C/15'/50MPa	1.98 (± 0.09)	90.2(±4.1)
	D4	0.29(±0.006)	0.35(±0.007)	1000°C/5'/50MPa	2.12 (±0.06)	96.1(±2.7)
	D5	2.44(±0.049)	2.97(±0.059)	950°C/5'/100MPa	2.15 (±0.02)	98.0(±0.9)
WET ROUTE	W1	0.12(±0.002)	0.15(±0.003)	950°C/5'/100MPa	2.09 (± 0.03)	95.0(±1.4)
	W2	0.15(±0.003)	0.19(±0.004)	950°C/5'/100MPa	2.26 (± 0.06)	≅100
	W3	0.47(±0.009)	0.58(±0.011)	950°C/5'/100MPa	2.15 (± 0.06)	97.7(±2.7)
	W4	0.48(±0.010)	0.59(±0.012)	950°C/5'/100MPa	2.07 (± 0.11)	94.1(±5.0)
	W5	1.27(±0.025)	1.55(±0.031)	950°C/5'/100MPa	2.09 (± 0.01)	95.0(±0.5)
	W6	5.32(±0.106)	6.43(±0.127)	950°C/5'/100MPa	2.19 (± 0.01)	≅100

Based on these results, we finally chose the parameters reported in Figure 6.32 as the most appropriate ones (among the tested conditions) for the densification of *F*-DWCNTs nanocomposites by SPS since it enables to achieve a high densification at a short dwell time (5 min: decreasing possibility of oxidation of *F*-DWCNTs) and at relatively low temperature (950°C) and applied pressure (50 MPa). The temperature used is quite lower than the range of temperatures at which can occur the carboreduction of silica (1500-1700°C) [157]. As the incorporation of any fiber in glasses makes difficult their densification [185], differences in the relative densities were expected between pure silica and nanocomposites (from W or D route) even using similar SPS parameters. For example, 95.0(±1.4)% and 95.0(±0.5)% of theoretical densifications were achieved for W1 and W5, respectively (Table 6.8), compared to 99.0(± 0.9)% for S8 (Table 6.7). Thus, besides the slight increase of specific surface area (measured 591(±18) m²/g) of the nanocomposite powders in comparison to the silica powder (582(±17) m²/g) the incorporation of CNTs into silica glass is detrimental to densification. This can be explained by the fact that it slows the sintering mechanisms (mainly viscous flow for the present material) as any fiber does in a glass matrix [185].

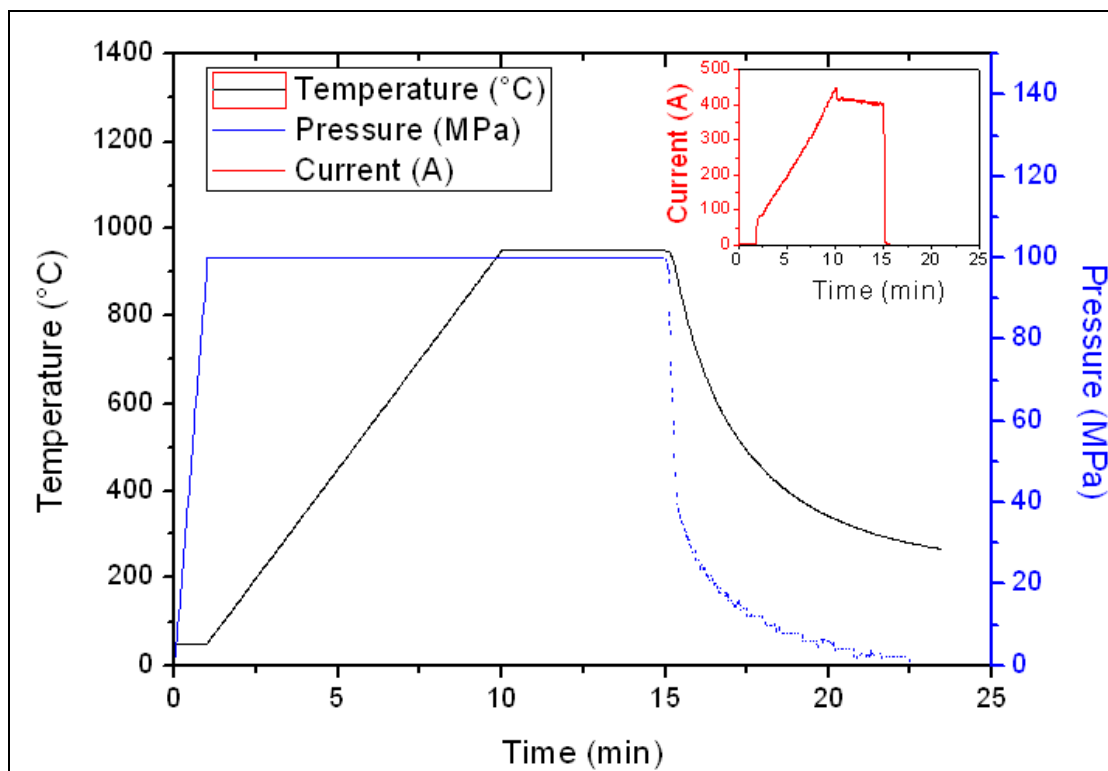


Figure 6.32 SPS parameters used to densify the W set of nanocomposites. Inset: electric current applied during SPS densification.

Besides the smaller relative densities of nanocomposites in comparison to pure silica samples, all the obtained relative densities achieved for the nanocomposites are higher than 94% (excepted 90.2(\pm 4.1)% for the sample D3), reflecting low porosities. Further work would be necessary to optimize the densification of the nanocomposites with special attention in avoiding the adsorption of humidity between the calcination and sintering steps (dessicator would be suggested). The residual water can cause a concurrent crystallization during sintering [25], which inhibits the densification. Moreover, a slight increase in the temperature of sintering would probably aid to increase the densification.

These results also show that to achieve theoretical densities above 90% by SPS with the calcinated (at 400°C for 2h) xerogel nanocomposite powders prepared in this work, it urges to apply a pressure twice higher than that used by the group of Guo *et al.* [30,183,184] to fully densify MWCNT-SiO₂ nanocomposites by SPS at same temperature and dwell time to those used in this work (950°C). In those works [30,183,184], the authors used a colloidal commercial silica and the nanocomposite powders were previously calcinated at 600°C in N₂ and sieved at 75 μ m mesh.

- **Microstructure of *F*-DWCNT-silica nanocomposites**

- ***X-ray diffraction***

X-ray diffraction analyses were carried out to check the crystallinity of the nanocomposites after their densification by SPS. The XRD patterns (in attachment: Figure 0.12) reveal peaks around 26.5-26.9 degrees for the most samples (exception sample W1) and an extra peak at 44.3 degrees only for W5 sample. This means a possible presence of alpha-quartz, but we can not discriminate from possible peaks of graphite coming from residual papyex (the 002 peak from CNTs would be very large, which is not the case here).

Other works [30,100c,100d,183,184] already reported the crystallization of silica in the presence of CNTs, however the intensities of the main peak (26.5-26.9 degrees) are not in correlation with the CNTs content. Therefore, in our case it is likely that residual water [25] plays a higher role in the heterogeneous crystallization than the presence of CNTs as reported by Ning *et al.* [100d] and also believed by us previously [186] or it is the superposition with peaks of graphite. If it is only from alpha-quartz that might be a consequence of the non-appropriate storage of the powder after its calcination until its sintering. Sol-gel materials typically present quite high surface areas, which tend to adsorb moisture at room temperature. Even after precompaction and preparation of sample in the graphitic mould, it probably would be recommended for future works to store them in a dessicator.

- ***Raman spectroscopy***

Raman spectroscopy of densified *F*-DWCNT-SiO₂ was carried out in order to observe any possible interaction between the silica matrix and the *F*-DWCNT as well as the possible damage of the later. The images in Figures 6.33 and 6.34 display average Raman spectra obtained for different regions for each nanocomposite sample (black line) and the original spectra (coloured lines as inset images) prepared by dry and wet route, respectively. As it can be noted, in general, a typical spectrum of CNT-SiO₂ nanocomposite is composed by a broad peak due to fluorescence of silica (only in a few ones: Figures 6.33c and 6.33d) and the main features of CNTs spectrum are clearly observed at relative high load

contents. These observations are in good agreement with other reported works on CNT-SiO₂ nanocomposites [99,102]. A G band upshift (1-13 cm⁻¹) is observed in all spectra. At the same time, a D* upshift (2-13 cm⁻¹) is observed in almost all nanocomposites of D and W route (excepted samples D1, D2, D3 and D5). Puech *et al.* [187] showed through *in-situ* Raman spectroscopy of DWCNTs in a diamond anvil cell that there is a linear dependence between the shift in the frequency of the G-band and the applied isostatic pressure up to 12 GPa. Thus, these results could suggest that the F-DWCNT remain constrained in the matrix, which could also reflect the good interaction between the SiO₂ and CNTs mentioned in other studies [97,99,100d,102]. In a previous work with F-SWCNTs-SiO₂ composites (using a non-commercial CCVD-SWCNT material [188]) prepared by sol-gel and densified by isostatic high pressure [102] we also observed a G band upshift and a correlation between the residual stress in the CNTs and good affinity with the matrix was also suggested. Moreover, D* band upshift also suggests a good interaction between F-DWCNT and silica matrix [102].

Most of the densified F-DWCNT-SiO₂ nanocomposites prepared by the dry route shows common RBM peaks at about 199 cm⁻¹, 153 cm⁻¹, 215 cm⁻¹ and 255 cm⁻¹. The few exceptions are sample D4 with its unique RBM peak around 215 cm⁻¹, which corresponds to the most intense peak in other samples, and sample D5 with its extra peak around 245 cm⁻¹. Probably the regions analyzed in sample D4 contained less CNTs, thus the fluorescence of silica masked some of the other peaks from RBM.

It is difficult to evaluate the ratio $I_{D/G}$ due to the fluorescence of silica. Thus, a manual subtraction (using 10 points) of the broad fluorescence band from the spectra using the software *Origin Pro 8* to calculate $I_{D/G}$.

Thus, it was calculated $I_{D/G}$ of ~0.04 in samples D1 and D2 (Figures 6.33a and 6.33b, respectively), while $I_{D/G}$ ~0.06 in samples D3 and D5 (Figures 6.33c and 6.33e, respectively) and $I_{D/G}$ ~0.10 for sample D4 (Figure 6.33d).

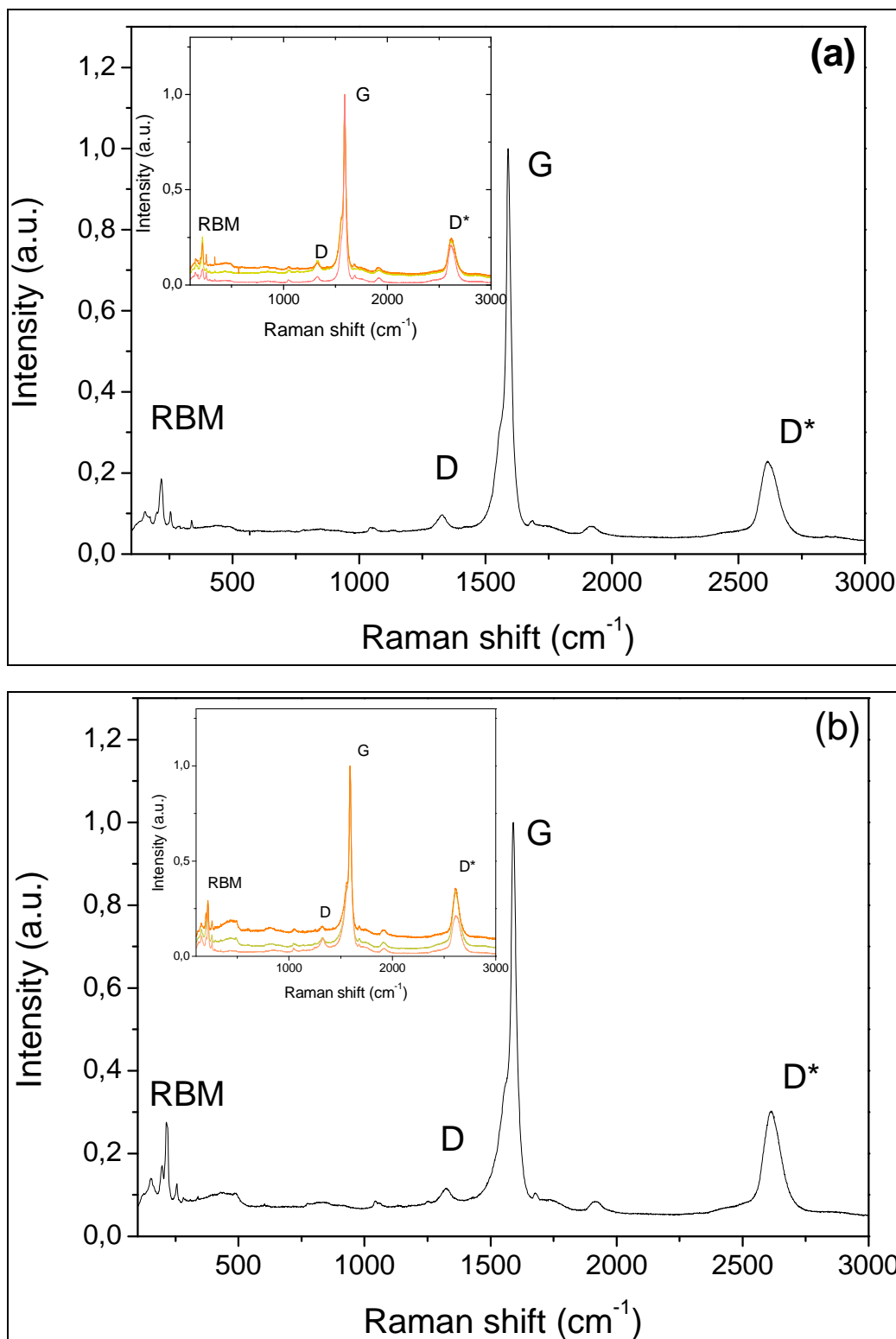


Figure 6.33 Raman spectra at $\lambda = 632.8$ nm normalized by G band done in different regions of the sample (coloured lines as inset) for each sample from dry route: (a) D1 (0.22 wt.%); (b) D2 (0.22 wt.%); (c) D3 (0.22 wt.%); (d) D4 (0.29 wt.%); (e) D5 (2.44 wt.%). Black line: Average Raman spectra of the respective densified F-DWCNT-SiO₂ nanocomposites.

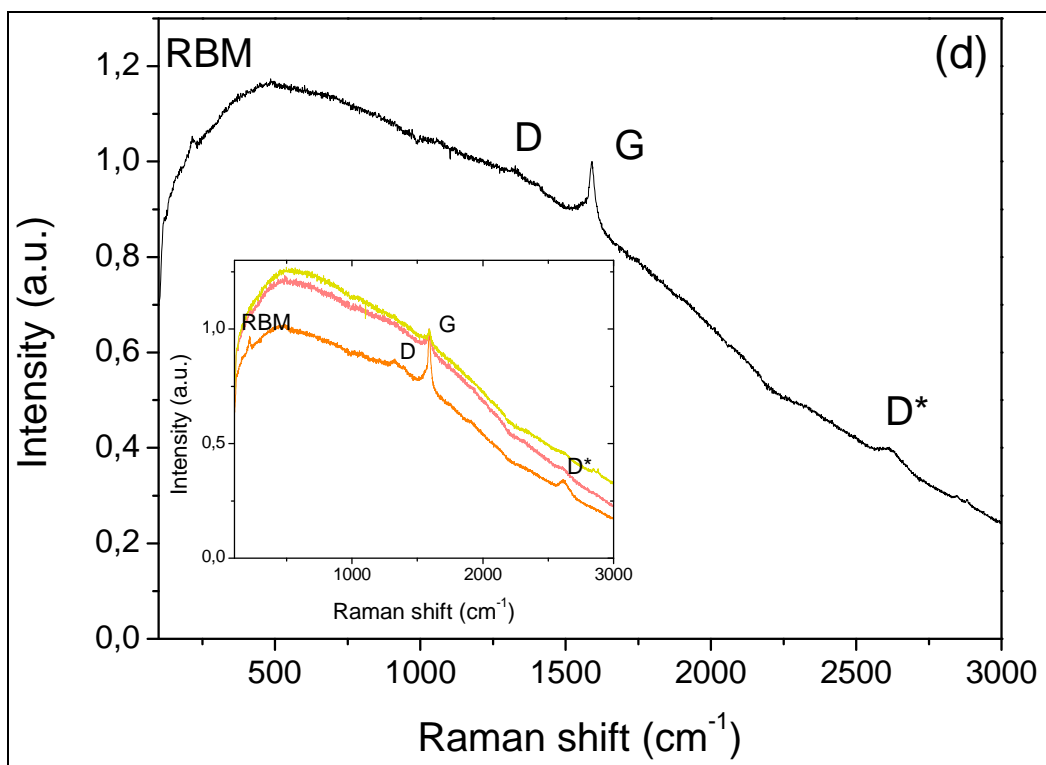
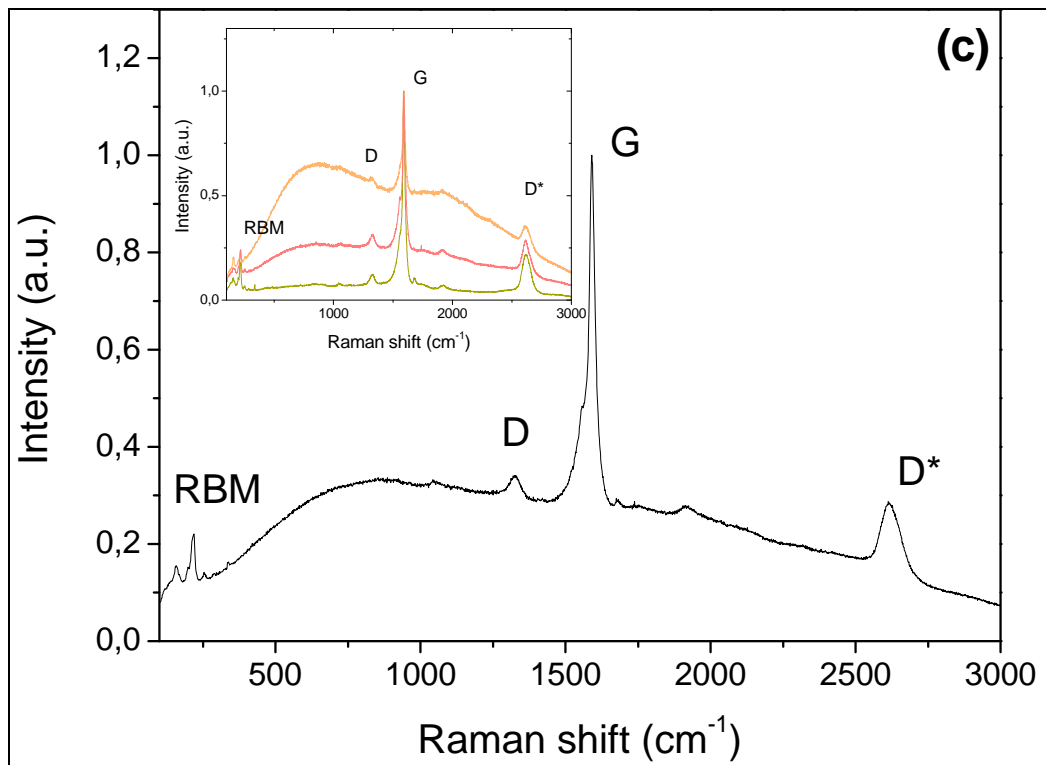


Figure 6.33 (Continued)

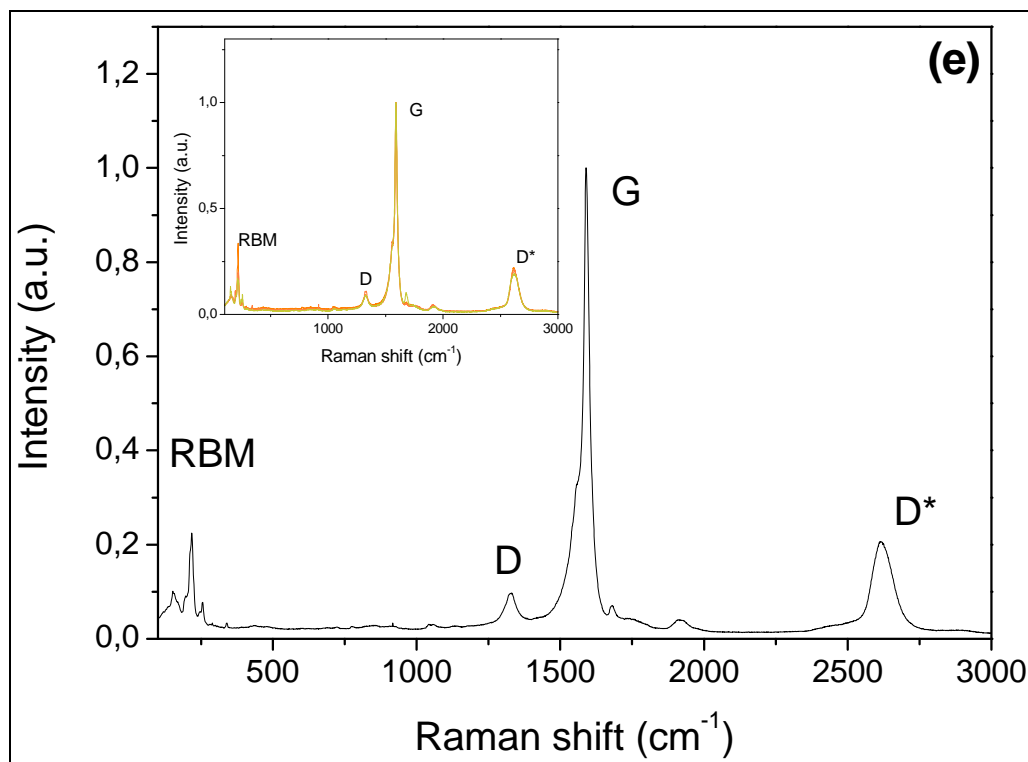


Figure 6.33 (Continued)

In the case of the wet route, the most intense *RBM* peaks observed for *F*-DWCNTs are still detected in most parts of the nanocomposites (except for the sample W1 with 0.12 wt.% where the fluorescence of the silica masked any other information). For example, *RBM* peaks can be identified at about 128, 152, 218 and 254 cm⁻¹ for the sample containing 0.15 wt.% of filler (sample W2, Figure 6.34b), while for sample W3 with concentration of 0.47 wt.% of filler (Figure 6.34c, except in one region of the sample) the peaks are at 133, 153, 198, 218 and 255 cm⁻¹. Similar observations (Figures 6.34d and 6.34e) can be done for samples W4 (carbon content of 0.48 wt.%) or W6 (carbon content of 5.32 wt.%): peaks at 146, 197, 217 and 254 cm⁻¹ are detected for the first, while peaks at 130, 148, 214 and 254 cm⁻¹ are observed in the later. As it can be noticed, for W6 as example, a downshift in *RBM* peaks occurred. In relation to the *D* band intensity, after the manual subtraction of the fluorescence, it was calculated a $I_{D/G}$ ratio of 0.09 for W2 sample, $I_{D/G}$ of 0.24 for W3 sample, $I_{D/G}$ of 0.35 for W4 sample and $I_{D/G}$ of 0.36 for W6 sample. It is observed an increase of $I_{D/G}$ for higher loads of CNTs after the preparation and densification of the nanocomposites by SPS. This can indicate that some defects in CNT structure were introduced during sintering by SPS. The higher $I_{D/G}$ of W samples in comparison to D samples might be explained by the

fact that W samples have more surface areas of CNTs exposed to acids during functionalization than D samples (hard aggregates partially grinded would lead to lower exposed area of CNTs).

For other samples, it is possible to confirm the quite good dispersions of CNTs in the matrix (similar pattern in all regions). An exception is observed in sample containing about 0.47 wt.% of *F*-DWCNTs since one spectrum demonstrates a higher fluorescence of silica than other regions, indicating a lower content of CNTs in that region. Raman spectroscopy shows that CNTs are found in all area of the samples, which traduces a rather good dispersion of CNTs in the matrix (with few exceptions). Moreover, as already mentioned, D^* upshift also suggest a good interaction of *F*-DWCNTs with silica matrix.

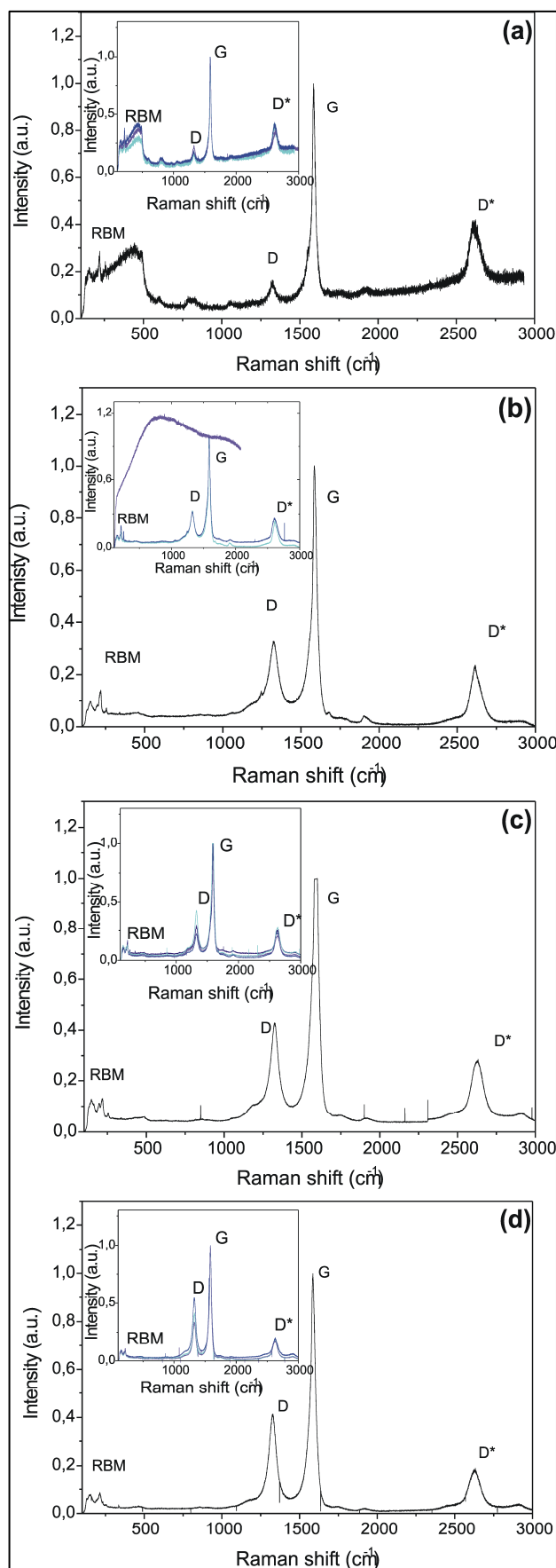


Figure 6.34 Raman spectra at $\lambda = 632.8$ nm normalized by G band done in different regions of the sample (colored lines as inset) for each sample from wet route: (a) W2 (0.15 wt.%); (b) W3 (0.47 wt.%); (c) W4 (0.48 wt.%); (d) W6 (5.32 wt.%). Average Raman (black line) spectra of samples from respective densified *F*-DWCNT-SiO₂ nanocomposites.

-FESEM characterization

FESEM observations of fractured surfaces of *F*-DWCNTs-SiO₂ nanocomposites (Figures 6.35 and 6.36 for D samples and Figure 6.37 for W samples) were carried out at TEMSCAN from Universite Paul Sabatier. The fracture surfaces of silica is rather flat and CNT bundles (9-20 nm in diameter) emerge from the matrix with variable lengths, probably after variable degrees of pulling-out, which is indicative of cohesion between CNT and matrix. This cohesion is also evidenced by the 2 CNT bundles which bridge a flaw in D5 (Figure 6.35g). The FESEM resolution allows the visualization of smaller diameter filaments (a few nm in diameter) but no ones were visualized, so it seems that most or all CNTs are not individual but gathered in bundles. The bundles are more or less well dispersed and some aggregates are evidenced in some of D samples (D4 – Figure 6.35f) and in most of W samples (W3-W6, Figure 6.37b-h).

To improve the comparison between samples images as a function of the DWCNT content and of the preparation route (D or W, time of gelification), several qualitative and quantitative microstructural characteristics have been determined and reported in Table 6.5. In order to that bundles and aggregates from several FESEM images were measured with the aid of the imaging software ImageJ. Two parameters of dispersity named Bdl (related to size of bundles) and Agg (related to the size and frequency of aggregates) are defined and have been evaluated (integer, between 1 and 5 from the thinner to the larger bundle diameter, and from the less/smaller aggregates to more/larger ones).

In D nanocomposites (D1-D5, 0.27-2.97 wt.% carbon), prepared using *F*-DWCNTs dried with a dessicator at room temperature, images (Figure 6.35) and microstructural characteristics (Table 6.6) reveal that *F*-DWCNTs bundles have average diameters in the range of 12-19 nm, which corresponds to around 30-65 CNTS/bundle and that aggregates are only scarcely observed: small in D2 (< 1 μm², Figure 6.35c) and larger in D4 (> 10 μm², Figure 6.35f). On the images shown in Figure 6.35, the distribution of the CNT bundles in the silica matrix seems quite good. However, some parts of area without CNTs bundles do exist (right down corner in Figure 6.35a) and we determined on smaller magnification images that their sizes can sometimes reach several tens of square micrometers. Both the existence of such area and the detection of aggregates prove that the

state of dispersion of CNT bundles is not ideal and thus could be improved.

Moreover, differences between samples with similar carbon contents can be evidenced (Figures 6.35a-d). For example, we determined that sample D3 (Figure 6.35d), which contains 0.22 wt.% of carbon, shows smaller regions with no CNTs in the 2D planes (~36% of total area contain CNT bundles) than other nanocomposites with similar carbon contents (D1 and D2: Figures 6.35a,b and 6.35c, respectively, for which ≈12 % and ≈6% of total area contain CNT bundles, respectively). These differences are also proved by the parameters of dispersity (Table 6.5 – Bd between 1 and 3, Agg between 1 and 3 for similar CNT contents) which suggests a lack of reproducibility for D samples, prepared using dried CNTs.

Surprisingly, no more quantity of CNTs is observed in D5 (Figures 6.35g and 6.35h) than in previous samples (in a same surface area) in spite of the much higher overall carbon content (2.44 instead of 0.22-0.29 wt.% carbon), which allows to suspect the presence of aggregates probably of large size (and consequently very rare) in D5 (like the one found in D4 sample).

The image of D4, already reported in Figure 6.35, has been enlarged in Figure 6.36a with an inserted detail Figure 6.36b taken at a much higher magnification which is representative of the interaction between CNT bundle and the matrix. This detail is evidenced through the contact angle that there is a good wettability of the *F*-DWCNT bundle by the silica matrix. Moreover, the length of the CNT bundles emerging from the fractured surface, similar to the lengths of all other bundles (Figure 6.36a) is short reflecting a binding not very strong (because the pulling out operate) but sufficient to possibly mechanically reinforce the matrix. This confirms the good interaction previously demonstrated by Raman spectroscopy (*D** band and *G* band upshifts).

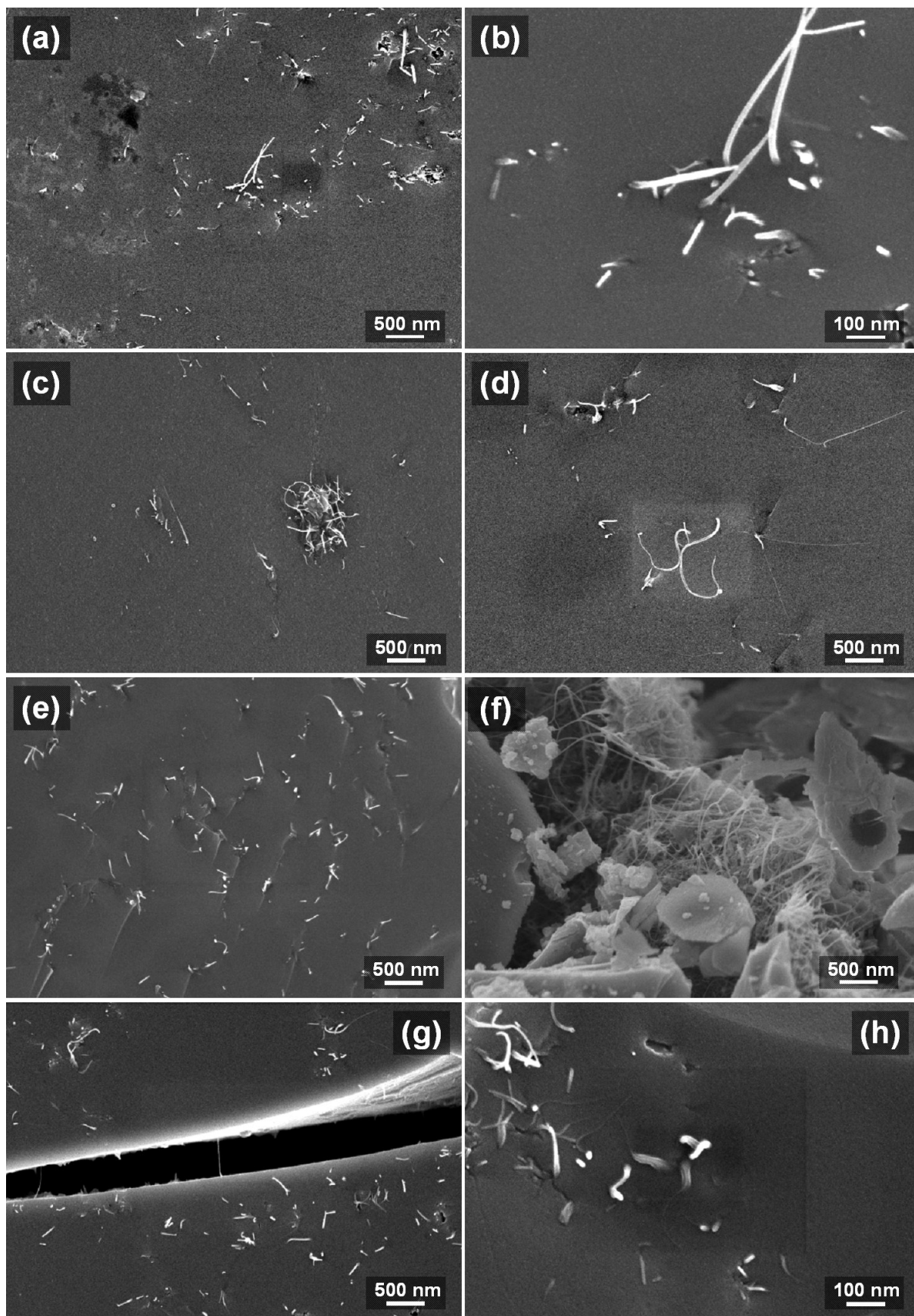


Figure 6.35 FESEM image of a fractured surface of *F*-DWCNT-SiO₂ nanocomposite obtained by dry route: (a,b) sample D1 (0.22 wt.%); (c) sample D2 (0.22 wt.%); (d) sample D3 (0.22 wt.%); (e,f) sample D4 (0.29 wt.%); (g,h) sample D5 (2.44 wt.%).

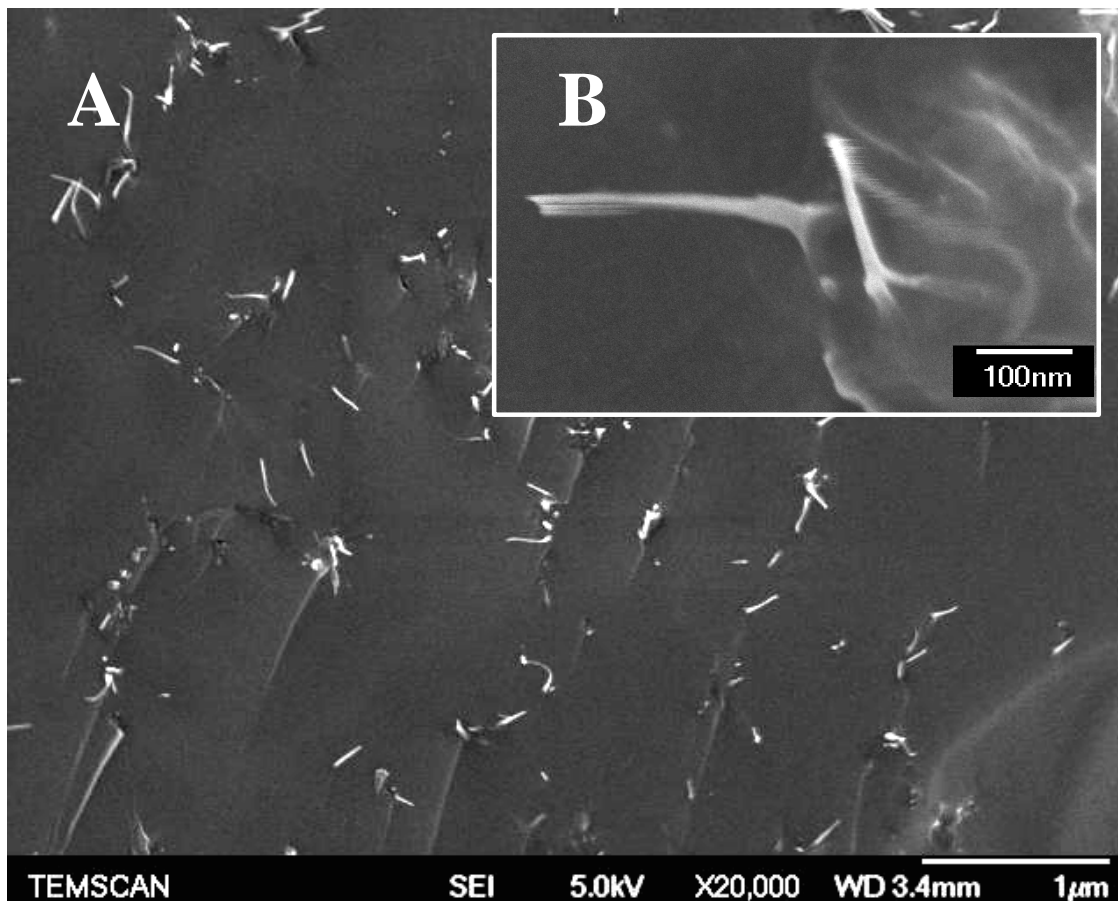


Figure 6.36 (A) FESEM image of a fractured surface of *F*-DWCNT-SiO₂ (0.29 wt.% of carbon) nanocomposite obtained by dry route; (B) Evidence of wettability of the *F*-DWCNT by the silica matrix.

For *W* samples, FESEM images of fractured surfaces (Figure 6.37) and microstructural parameters (Table 6.5) reveal significant differences in comparison with *D* samples. Firstly, except *W*1 (0.12 wt.% - Figure 6.37a) or *W*2 (0.15 wt.% of carbon – not shown, similar to *W*1) which present almost no aggregates, flat aggregates are present in all area of all other *W* samples (Figure 6.37b-h). These flat aggregates are mostly aligned in a unique direction which we think to be perpendicular to the axis of applied pressure. So, these aggregates have been flattened during the SPS treatment and had probably an isotropic shape in the starting powder. Most of the CNT bundles are found within these aggregates and only a few ones are dispersed between them. Secondly, except also for *W*1, CNT bundles have smaller diameters than in *D* samples (Table 6.5) which indicates a better separation of bundles or/and a lesser bundling.

From *W*3, as a function of the CNT contents, the aggregates are of similar sizes but more and more frequent, especially for *W*6 (5.32 wt.% carbon), and the mean diameters of CNTs bundles remain similar, excepted for *W*1.

Even though it was easier to disperse in aqueous solution wet *F*-DWCNTs (the formation of hard aggregates is avoided in *W* samples) than dried ones (*D* samples), in dense nanocomposites, most of the CNT bundles are found within well distributed flattened aggregates with rather similar sizes in *W* samples (Table 6.5: *W3-W6*). The flattened shape of aggregates results of the pressing during the SPS treatment, but we infer that the initially isotropic aggregates have been formed during the gelification process. Indeed, for *W3-W6* samples, the observed periods of gelification were longer (3-6 days instead of 2 days for other samples) giving more time to a possible aggregation. During the sol-gel process, the duration of gelification step depends on many factors, including ambient conditions (area exposed to atmosphere, humidity, temperature and pH of solution) and solvent content. Before the sol does gelify, *F*-DWCNTs/bundles or small aggregates are able to migrate through the solution in order to decrease their surface area. According to the time given before their immobilization through the gelification, these bundles and small aggregates unbroken with sonication present in the sol can form big aggregates. In further works, the use of special procedures to shorten the gelification would be wished as that reported by Brinker *et al.* [25]: smaller amount of solvent (optimal ratio *r* and small quantity of EtOH), work with small volumes, use a base (with caution to maintain the spherical silica particles in suspension by using a non-covalent functionalization, for example) or other acids as catalysts in order to increase the speeds of hydrolysis and condensation occurring in such process (with attention not to work at too acid pH since the dispersion would be more unstable) increase temperature. Moreover, the silica alkoxyde can be pre-hydrolyzed prior to the CNT solution is incorporated in the mixture, and knowing the gelification time the CNT can be added at different steps of the sol-gel process in order to avoid their aggregation.

From the FESEM analysis of several images of nanocomposites obtained by *D* (dry route) and *W* (wet route) presented in Table 6.9 it can be concluded that in general: (i) *W* series shows smaller mean diameter of bundles (12.8 nm against 15 nm); (ii) at contents of 0.47 wt.%, bigger and flattened aggregates are visualized in samples from *W* route presented than in samples from *D* series. Therefore, it can be inferred that smaller diameter of bundles in *W* series might be indicative that the CNT were initially better separated than in *D* series. In the case of the *D* route with similar functionalization and sonication conditions, the manual grinding may have contributed to more finely divide the aggregates. The observation of more aggregates

in composites prepared by the W route shows that this procedure must be optimised. In this way, we propose some possible solutions: (i) a shortening of the gelification step; (ii) a more severe dispersion through strong or more complex functionalization of DWCNTs, adding a second step to insert amines (positively charged) at the extremities of CNTs; (iii) prolonged time of (bath or probe) sonication; (iv) use a base as catalyst in the sol-gel process to flocculate spherical silica particles (Stöber synthesis) [25] since it seems that it would not disturb the dispersion of *F*-DWCNTs (as evidenced by Zeta potential results), but the functionalisation of silica would be probably required to maintain the silica particles well dispersed in the medium (since the spherical particles would tend to precipitate at the bottom of the vessel).

Table 6.9 D and W samples microstructural analysis (selected only “clean” type of fracture for these analyses).

	Average [C]		Time for gelification (days)	Average diameter of bundles (nm)	Number of CNT/bundle	Presence of aggregates	Biggest aggregate dimensions observed ($\mu\text{m} \times \mu\text{m}$)	Geometry of aggregates	Criter of dispersion	
	(wt.%)	(vol.%)							Bdl	Agg
D1	0.22(± 0.004)	0.27(± 0.005)	2	12	32	NOT OBSERVED	-	-	1	1
D2	0.22(± 0.004)	0.27(± 0.005)	2	19	84	ONE OBSERVED	1 x 0,73	Rectangular	3	2
D3	0.22(± 0.004)	0.27(± 0.005)	2	14	50	NOT OBSERVED	-	-	2	1
D4	0.29(± 0.006)	0.35(± 0.007)	2	14	47	ONE OBSERVED	-	-	2	2
D5	2.44(± 0.049)	2.97(± 0.059)	2	16	65	NOT OBSERVED	-	-	2	1
W1	0.12(± 0.002)	0.15(± 0.003)	2	20	99	ONE OBSERVED	5 x (0,2-0,5)	very flat	5	1
W2	0.15(± 0.003)	0.19(± 0.004)	2	CNT NOT OBSERVED	-	NOT OBSERVED	-	-	-	-
W3	0.47(± 0.009)	0.58(± 0.011)	3	11	27	YES	5,39 x (0,13-0,82)	Flattened (ellipse/rectangle)	1	2
W4	0.48(± 0.010)	0.59(± 0.012)	6	9	18	YES	13,22 x 0,77	Flattened (ellipse/rectangle)	1	2
W5	1.27(± 0.025)	1.55(± 0.031)	5	11	29	YES	11,22 x (0,06-0,37)	Flattened (ellipse/rectangle)	1	2
W6	5.32(± 0.106)	6.43(± 0.127)	4	13	38	YES	12,17 x (0,42-3,22) OR 242,94 x (162,53-229,12)	Flattened (ellipse/rectangle)	1	5

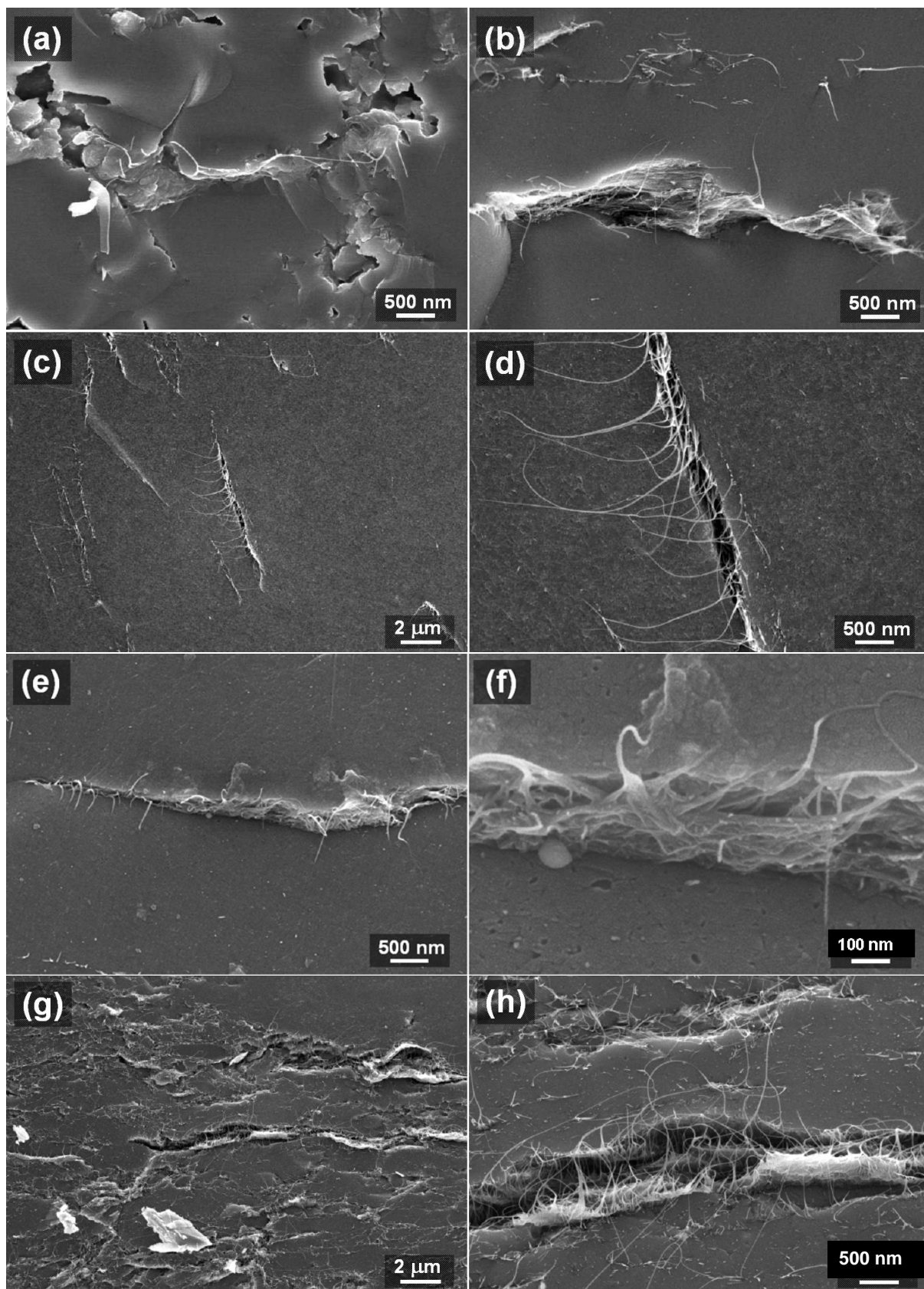


Figure 6.37 FESEM images of the fracture surface of *F*-DWCNT-SiO₂ nanocomposites obtained through the wet route: (a) sample W1 (0.12 wt.%); (b) sample W3 (0.47 wt.%); (c,d) sample W4 (0.48 wt.%); (e,f) sample W5 (1.27 wt.%); (g,h) sample W6 (5.32 wt.%).

- Electrical Conductivity

Electrical conductivities of sintered nanocomposites obtained by the dry route from different batches of synthesis and of functionalizations are shown in Table 6.10. As it can be observed, for same or similar carbon contents, quite different conductivities were measured: while samples D1 and D2 present an insulating behaviour ($\sim 10^{-7}$ S/cm), the percolation of CNTs seems to be observed for sample D3 ($\sim 10^{-5}$ S/cm) and D4 can be considered as a conductive sample (10^{-4} S/cm). However, the conductivity of the sample D5 ($\sim 10^{-5}$ S/cm) is smaller than that of D4 ($\sim 10^{-4}$ S/cm) in spite of its much higher carbon content.

These variations in conductivity are not in correlation with the dispersion parameters (Bd and Agg – Table 6.6) because D1 which has the better dispersity parameters (thinner bundles, no aggregates detected by SEM) is the less conductive whereas D4, which is the more conductive, has smaller dispersity parameters. Compared to D3, the increase in conductivity of D4 could be explained by the small increase of the carbon content if the values are near the percolation threshold. Moreover, the low relative density of D3 (90.2(\pm 4.1)%) which indicates the presence of open porosity where CNTs could percolate with low interaction with the silica matrix could account for the high conductivity observed compared to the other D samples which exhibit higher relative densities (between 94.9(\pm 0.9)% and 98.0(\pm 0.9)%).

D5 is less conductive than D4 sample in spite of its highest CNT content and highest dispersity parameters. For D5 sample, besides its aggregates were not visualized by SEM, we note that the quantity of observed CNT bundles seemed low regards to the high carbon content (2.44 wt.%) which could be explained only by the presence of some large aggregates. Only long FESEM investigations on a lot of sample fractures could be able to verify that.

The electrical conductivity of nanocomposites could also vary with the degree of functionalization of the DWCNTs used, *i.e.* the number of carboxylic groups on the DWCNT walls, because it is detrimental to the intrinsic electrical conductivity of CNTs [189]. So, the unexplained differences in conductivity between nanocomposites,

particularly for similar CNT contents, could be rather due to the lack of reproducibility of the functionalization step which has been previously reported in this work.

Therefore, the differences in electrical conductivity among these samples can be due to variations: (i) of batches of *F*-DWCNTs used (which also depends on the original sample); (ii) the degree/states of dispersion of bundles and to the quantity of hard aggregates which are only partially crushed during the manual grinding previously to their dispersion and (iii) to the densification. No doubt that further work with X-ray tomography, focused ion beam and 4D electron tomography would be necessary to confirm these assumptions.

Table 6.10 Electrical conductivity of *F*-DWCNT-SiO₂ nanocomposites obtained by the dry (D samples) and wet (W samples) routes measured by two-probe method.

	Average [C]		Electrical conductivity (S/cm)	Relative density (%)	Criter of dispersity	
	(wt.%)	(vol.%)			Bundles	Aggregates
D1	0.22(±0.004)	0.27(±0.005)	2.97x 10 ⁻⁷	94.9(±0.9)	1	1
D2	0.22(±0.004)	0.27(±0.005)	4.1 x 10 ⁻⁷	96.0(±0.5)	3	2
D3	0.22(±0.004)	0.27(±0.005)	1.28 x 10 ⁻⁵	90.2(±4.1)	2	1
D4	0.29(±0.006)	0.35(±0.007)	1 x 10 ⁻⁴	96.1(±2.7)	2	2
D5	2.44(±0.049)	2.97(±0.059)	3.36 x 10 ⁻⁵	98.0(±0.9)	2	1
W1	0.12(±0.002)	0.15(±0.003)	3 x 10 ⁻⁷ / 7 x 10 ⁻⁷	95.0(±1.4)	5	1
W2	0.15(±0.003)	0.19(±0.004)	8.18 x 10 ⁻⁷	≅100	-	-
W3	0.47(±0.009)	0.58(±0.011)	0	97.7(±2.7)	1	2
W4	0.48(±0.010)	0.59(±0.012)	4.2 x 10 ⁻⁶ / 3.8 x 10 ⁻⁷	94.1(±5.0)	1	2
W5	1.27(±0.025)	1.55(±0.031)	1.54 x 10 ⁻³ / 1.58 x 10 ⁻³	95.0(±0.5)	1	2
W6	5.32(±0.106)	6.43(±0.127)	1.56	≅100	1	5

Figure 6.38 shows the electrical conductivities of the *F*-DWCNT-SiO₂ nanocomposites obtained through the wet route (W series) or by the dry route (D series). In comparison with electrical conductivities obtained in chloroform suspension using *F*-DWCNT dried in dessicator (Figure 6.29), for similar CNT contents (*i.e.* for values < 1 vol.%), the values are at least one order of magnitude

smaller (10^{-4} S/cm against around $>10^{-3}$ S/cm). In *F*-DWCNT-SiO₂ nanocomposites, the probable higher quantities of *F*-DWCNTs aggregates formed than in suspensions in chloroform could explain that fewer filaments contribute efficiently to the percolation network in the first, giving rise to a percolation threshold at higher concentrations (~0.30 vol.% by dry route and ~0.70 vol.% by wet route) and to lower electrical conductivities than in suspension. Moreover, in chloroform, the constant sonication should limit the (re-)aggregation of *F*-DWCNTs and contribute to dynamic percolation. Another hypothesis to explain the difference in conductivity can be due to the fact that bundles of *F*-DWCNTs are thinner in the suspensions (and maybe some filaments are individual *F*-DWCNTs, but this is not obvious) than those observed in silica nanocomposites. Therefore, many reasons can explain that there are more filaments effectively available to contribute to form a 3D network pathway for the electrical current with lower *F*-DWCNT contents (smaller percolation threshold) in the suspension with *F*-DWCNT dried in dessicator than in the nanocomposites.

The comparison of electrical conductivities of D and W samples (Figure 6.38) shows that the percolation threshold seems to have been reached at lower loadings of *F*-DWCNT in the D samples than in the W samples (D3 and D4 compared to W3). This can be explained by the fact that in W3 (0.47 wt.% carbon), it is already possible to observe flattened aggregates and regions with few *F*-DWCNTs (Figure 6.37b), while in D4 (0.29 wt.% carbon), CNT bundles seem to be well distributed (Figure 6.36) and aggregates are rarely visualized (Figure 6.35f - Table 6.5).

On the other hand, the electrical conductivity of W5 is much higher than that of D5 in spite of the higher *F*-DWCNT loading of the second one (1.27 wt.% against 2.44 wt.% respectively). Thus, for loadings above 1 wt.%, the wet route could be preferable to the dry route, in spite of the systematic aggregation for the first one (Figures 6.37e and 6.37f). We infer that in W5, flat aggregates form a percolating network with the aid of the part of DWCNTs bundles with small diameters (mean diameter is 9 nm – Table 6.5) which are better distributed.

The sample W6 present a high electrical conductivity (1.56 S/cm) because of its high loading (5.32 wt.%), in spite of the presence of a lot of aggregates (Figures 6.37g and 6.37h) which can be as large as 30 μm^2 . For this sample, the percolating network appears to be denser than for W5 because a lot of bundles with a small

diameter (mean diameter 13 nm, ~38 CNTs/bundle) are well dispersed between the large aggregates of *F*-DWCNTs (Figures 6.37g and 6.37h).

Therefore, even though the good reproducibility is difficult to achieve, a tendency becomes apparent that at carbon contents between 0.3-0.5 wt.% the D route would lead to composites more electrically conductive than composites from using W route, while at higher loadings, an opposite behaviour is observed. Indeed, for example, by using D route at 2.44 wt.% of carbon content the conductivity achieved of the samples is about two hundred times lower than that of the samples prepared using W route at around half of this content. By comparing these conductivities (Figure 6.38) and criterious of dispersity (Table 6.9) of D5 (2.44 wt.% of carbon content) and W5 (1.27 wt.% of carbon content) we conclude that at high carbon contents (above 0.48 wt.%) with the W route the aggregates tend to be more dispersed than with the D route (might be more rare and bigger than if wet *F*-DWCNTs are used). On the other hand, by the W route at a carbon content of 0.48 wt.%, the conductivity can be 10 to 100 times lower than that by D route with only 0.29 wt.% of filler. This can be explained by the fact that W4 presents big flattened aggregates (Table 6.9: could reach 13.22 μm x 0.77 μm), thus decreasing the effective amount of fillers contributing to form percolating network.

However, the highest electrical conductivity for 0.27 vol.% of *F*-DWCNT (ca. 1.28×10^{-5} S/cm, achieved for D3, *i.e.*, dried in dessicator) is lower than for *F*-DWCNT (also dried in dessicator) measured in chloroform suspension with constant sonication at same concentration of filler (around 2×10^{-3} S/cm). This discrepancy is due to the higher number of percolating pathways in the suspension than in the nanocomposite. However, when comparing the conductivities of these silica nanocomposites to *F*-DWCNTs dried in stove (c.a. 6×10^{-6} S/cm and 7.9×10^{-8} S/cm, for *F*-DWCNT-B' and *F*-DWCNT-B, respectively), an opposite behaviour is observed (*i.e.* probably bigger and rare aggregates are present in *F*-DWCNTs dried in stove and measured by conductivity in liquid). Moreover, the obtained *F*-DWCNTs-SiO₂ prepared by this wet route presented a percolation threshold (around 0.70 vol.% of carbon) at a higher concentration (about two orders of magnitude) than those measured through conductivity in liquid (chloroform) for (*F*-)DWCNT dynamic network (Figures 6.20 and 6.29). The fact that the electrical percolation in the nanocomposites of *F*-DWCNT embedded in silica matrix occurs at

higher concentrations (about one order of magnitude) than in liquid can be explained by the probable higher presence of aggregates (evidenced on FESEM images: Figures 6.35c, 6.35f, 6.37b and 6.37h) and bundling of *F*-DWCNTs (bundles of tens of *F*-DWCNTs). The presence of bundles containing tens of CNTs would represent a quantity of filaments contributing to conductivity ten times smaller than if the CNTs were individually dispersed. Even most important, the presence of aggregates not only decreases the quantity of CNTs available for conductivity, but also can act as defects (like pores), eventually increasing the fragility of silica matrix. For the same reason, a conductivity similar to that measured in the 3D CNTN in chloroform with 0.028 vol.% of *F*-DWCNTs (10^{-3} S/cm) was only achieved in the 3D CNTN embedded in silica matrix at a concentration about 1.55 vol.% of CNTs (sample W5). In the other hand, the electrical conductivity achieved with the 3D CNTNs in silica nanocomposites (D1-D3 samples) at a carbon content (0.27 vol.%) similar to the maximum concentration in chloroform (0.28 vol.%) is between four and two orders of magnitude lower (2.97×10^{-7} S/cm to 1.28×10^{-5} S/cm, respectively) than that in dynamic tests in chloroform ($\sim 2 \times 10^{-3}$ S/cm).

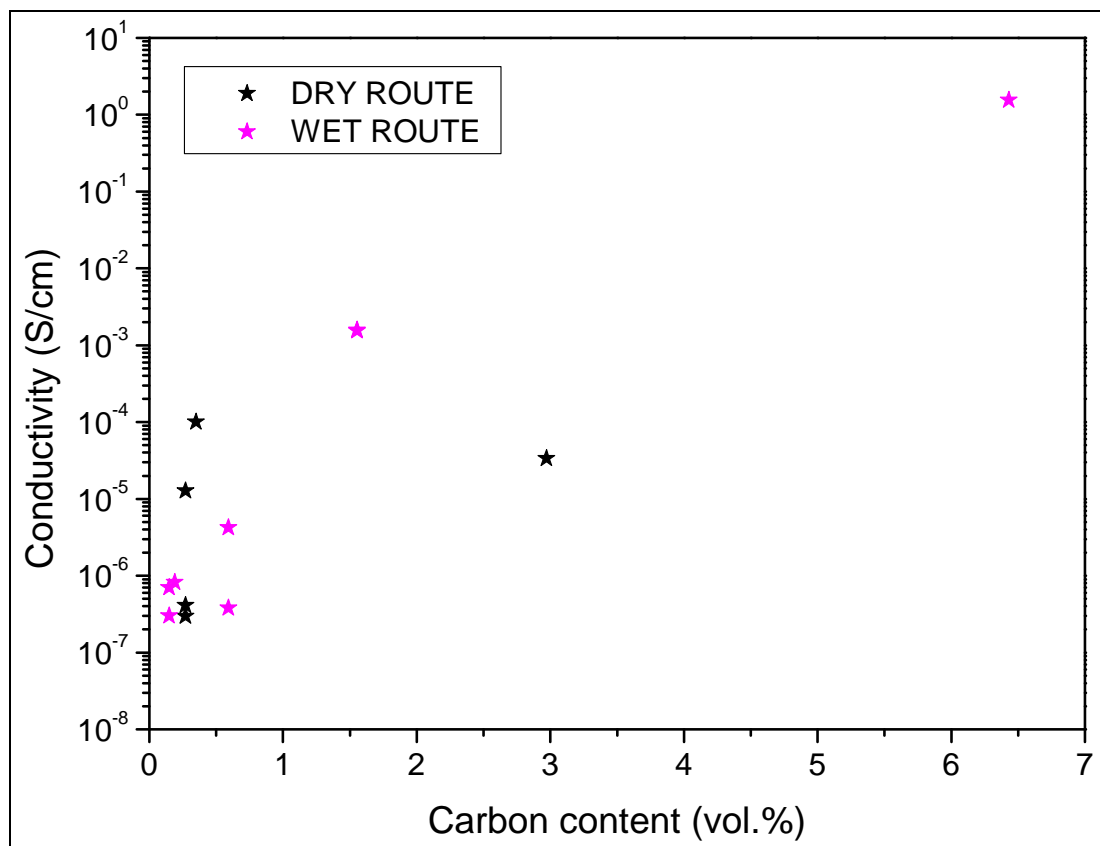


Figure 6.38 Electrical conductivity measured for the *F*-DWCNT-silica nanocomposites (D and W series) measured by two-probe method.

The electrical conductivities of the sintered nanocomposites prepared by the wet route are presented in Figure 6.39 in comparison to probability of percolation (Equation 4.2) and the expected from modified rule of mixtures (Equation 6.3b: $\sigma_C = \alpha_1 \beta \sigma_{F1} \phi_{F1} + \alpha_2 \beta \sigma_{F2} \phi_{F2} + \sigma_M \phi_M$). It shows the tendency that increasing CNT content to above the expected critical percolation, the probability to form pathways for the conduction of electrons leads to an increase of conductivity in several orders of magnitude (conductivity of pure silica sample was even not measurable, but according to literature it is around 10^{-20} S/cm [98]).

Moreover, as it occurred in the case of dynamic network, the conductivity expected through the modified rule of mixtures (even considering an aspect ratio much below the real aspect ratio) is several orders higher than the measured conductivities of the prepared nanocomposites. This fact might be also related to: (i) intrinsic conductivity of the metallic *F*-DWCNT lower than the assumed; (ii) ratio of metallic/semiconducting is modified (note: *conductivity values were calculated assuming 2/3 metallic*) by oxidative attacks (*preferential attack of metallic CNTs with functionalization* [189]); (iii) interfacial resistances are not taken into account (intertube or rather at the interface of silica and DWCNT, while the last might also contribute to conduction by tunnel effect [49]) and, most probably, (iv) dispersion of *F*-DWCNT in the matrix is not optimal (thus, can not enable to confirm the prediction of modified rule of mixtures); (v) effect of the residual stress in the conductivity of the CNT might affect the conductivity in the same way of defects, as scattering centers.

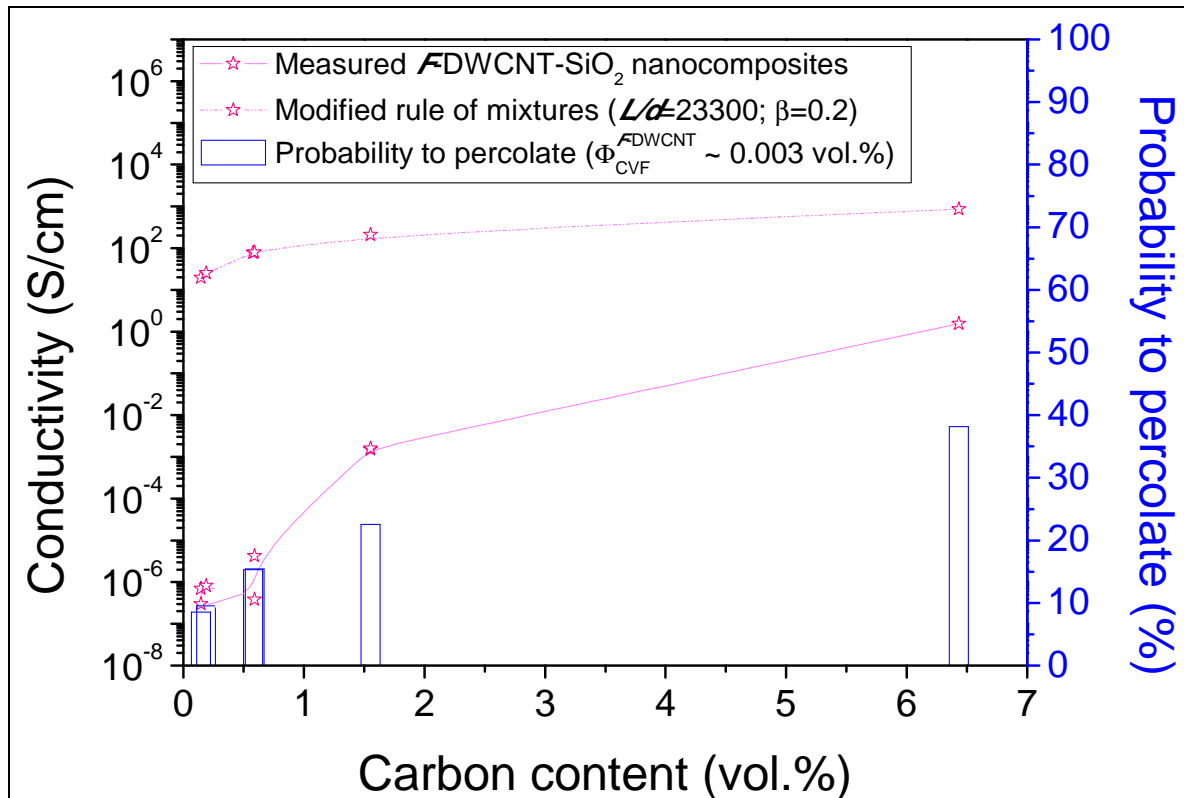


Figure 6.39 Electrical conductivity measured for the *F*-DWCNT-silica nanocomposites measured by two-probe method (straight line below) in comparison to expected from modified rule of mixtures (dash-dot line above) using a $L/d=23300$ and $\beta=0.2$ (Equation 4.13b) and its probability of percolation (Equation 4.2), considering critical volume fraction ($\Phi_{CVF}^{F-DWCNT} \sim 0.003$ vol.%) of *F*-DWCNT measured by dynamic percolation (0.003 vol.%).

The Figure 6.40 shows a comparison between the *F*-DWCNT-SiO₂ nanocomposites prepared using the dry and wet routes and data from literature on CNT-SiO₂ nanocomposites and others insulating ceramic matrices (borosilicate, alumina, magnesia and magnesium aluminate spinel).

For a given amount of CNT, the electrical conductivity achieved with densified *F*-DWCNT-SiO₂ nanocomposite were higher than all others previously reported for CNT-SiO₂ nanocomposites [29,30,99,100b,102]. For example, the nanocomposite prepared at the highest carbon content (sample W6: 6.43 vol.%) presents an electrical conductivity (1.56 S/cm) higher than the most conductive MWCNTs-SiO₂ nanocomposites fully densified by SPS (SPS parameters: 1100°C and 50 MPa for 5 minutes) prepared by Guo *et al.*: twenty times higher than that containing 5 vol.% MWCNTs (8×10^{-2} S/cm) and twice higher than that containing 10 vol.% MWCNTs (6.5×10^{-1} S/cm) [30]. In the same way, for much lower carbon contents ($[CNT] < 0.58$ vol.%), samples D1-D4 and W1-W3 are also more conductive than the 1 vol.% MWCNT-SiO₂ nanocomposite (1×10^{-10} S/cm) prepared by Xiang *et al.*

[100b]. Sample W6 containing 6.43 vol.% was about 3 times more conductive (1.56 S/cm) than the most conductive sample prepared by Xiang *et al.* (0.574 S/cm at 10 vol.% of MWCNTs) in a further work [29]. However, even if the electrical conductivities obtained in the present work are higher than those reported in literature for such kind of nanocomposites, it might be possible to increase their values, for a given CNTs content, by improving their dispersion, thus creating more possibilities of conduction paths. Probably the results achieved might be due not only to the high aspect ratio of the DWCNTs used (calculated as 35000-23300 for $V_{ex} = 1.4$ or 7500-5000 for $V_{ex} = 0.3$ against 33-1000 [30] and 100–1000 [100b] for MWCNTs used by other reports in silica matrix), but also because it was used a soft functionalization step and a more efficient process of densification (short dwell time at a moderate temperature in comparison to some of these reports) [99,100b]. Indeed, for similar carbon contents, DWCNTs give much higher total length of filament than MWCNTs, which gives rise to a much dense 3D CNTN. However, the bundling of DWCNTs is detrimental because wide MWCNTs (with a lot of walls) do not tend to form easily bundles.

Glass nanocomposites with borosilicate as matrix (electrical conductivity of 10^{-15} S/cm and density of 2.23 g/cm³ [98]) and 10 wt.% of MWCNTs (~11 vol.% assuming density of MWCNTs as 2 g/cm³ [7]) as fillers were prepared by Boccaccini *et al.* [190] using a conventional powder processing route followed by uniaxial hot pressing. By this methodology, the final nanocomposite achieved an electrical conductivity of 7.7×10^{-2} S/cm. This value is much lower than that obtained in the present work by the wet route: 1.56 S/cm with 6.43 vol.% of *F*-DWCNTs.

In general, for CNT nanocomposites with amorphous matrices, the obtained electrical conductivities remain relatively low in comparison to those that have been reported for others CNT-ceramic nanocomposites with insulating polycrystalline matrices (Al₂O₃, MgO and MgAl₂O₄) at similar CNT contents [94,126,191-196,199,200]. In the first publication on electrical conductivities of CNT-alumina nanocomposites (few-walls CNTs synthesized *in-situ* by CCVD in Al₂O₃ or MgAl₂O₄, materials partially densified by hot-pressing) Flahaut *et al.* [94] reported electrical conductivities between 0.4 and 4.0 S/cm for 4.8-5.7 wt.% CNT in Al₂O₃ and 1.5–1.8 S/cm for 4.9 wt.% CNT in MgAl₂O₄. These values are similar or slightly higher than that we obtained for similar CNT contents (1.56 S/cm for W6, which contains 5.32 wt.% DWCNTs). For lower CNT contents, our results are lower than those achieved

in SWCNT-MgAl₂O₄ nanocomposites (SWCNTs synthesized *in-situ* by CCVD) by Rul *et al.* [191] (1.54×10^{-3} S/cm for 1.55 vol.% DWCNTs against 0.0087 S/cm for 1.27 vol.% SWCNTs). Zhan *et al.* [192] dispersed SWCNTs (HIPco) in alumina (powder processing with 24 h ball-milling followed by SPS at 1150°C) and reported higher electrical conductivities (10.5, 15.1 and 33.45 S/cm for 5.7, 10 and 15 vol.% of SWCNTs, respectively). It is quite intriguing to obtain such a high electrical conductivity since this long ball-milling probably damage CNTs. But these SWCNTs form large diameter bundles in which inner SWCNTs could be protected by the outer SWCNTs and SEM images show that the dispersion of CNTs bundles is quite good. Inam *et al.* [193] used a colloidal processing to disperse MWCNTs in alumina and obtained an electrical conductivity near 2 S/cm for 4.65 vol% MWCNT. In a further work [194], they improved the colloidal process (high power sonication during 2h in dimethylformamide followed by bath sonication and then ball milling with the alumina powder) and obtained a maximal electrical conductivity (5.76 S/cm for 9.48 vol.% MWCNTs) quite comparable to that achieved by Zhan *et al.* [192] for SWCNT-Al₂O₃ composites. This result demonstrates that their processing route leads to a good dispersion (thus percolating pathways) since MWCNTs generally require higher weight load than using SWCNTs to obtain a same length of filament. Another explanation is the high trend of bundling of SWCNTs, which reduces the total length of filament available for the network, in comparison to that would give individual MWCNTs, for the same carbon content.

Kumari *et al.* [195] prepared MWCNT-Al₂O₃ nanocomposites by *in-situ* growth using cobalt NPs as catalysts and obtained quite high electrical conductivities for high CNT contents (7.05–33.36 S/cm for 12.81-33.12 vol.% MWCNT). Compared with Inan *et al.* recent results [194], the values are comparable at similar CNT contents. This shows that the approach of dispersion of CNTs used by Inam *et al.* [194] was probably quite efficient and the relative quantity of filler contributing to percolation played a major role than the eventual shortening of their CNTs.

Recently, Ahmad and Pan [196] prepared MWCNT-Al₂O₃ nanocomposites by ultrasonic mixing alumina with MWCNTs followed by 24h of ball milling. However, this process probably severely damaged the MWCNTs and led to their shortening since lower conductivities were achieved (σ_{MAX} of 3.545×10^{-2} S/cm for 5 wt.% of MWCNTs), in comparison to both polycrystalline and glass matrices.

Shi and Liang [197] prepared MWCNT-3Y-TZP and obtained a percolation threshold of 1.7 wt.% (~5.0 vol.% assuming density of 2 g/cm³ for MWCNTs [7] and of 6.08 g/cm³ for 3Y-TZP [198]), which corresponds to a higher CNT loading needed to achieve a percolating network than for other ceramic insulating matrices (at room temperature). Indeed, lower percolation thresholds were obtained by other authors: 0.45 wt.% MWCNT and 0.64 vol.% SWCNTs for CNT-Al₂O₃ [196] and SWCNT-MgAl₂O₄ [191] nanocomposites respectively. A recent study from Peigney *et al.* [199] with an *in-situ* route and consolidation by spark-plasma-sintering of DWCNT-Co/Mo-MgO nanocomposites showed that the increase of DWCNTs content (2.3 wt.% to 7.1 wt.%, corresponding to 4.5 vol.% and 13.2 vol.%, respectively, by assuming density of 3.58 g/cm³ for MgO [98]) increase the conductivity (1.9–2.1 S/cm to 6.3–6.9 S/cm) and decrease the matrix grain size (200 nm to 60-70 nm). Indeed, the blocking of matrix grain growth by nanotubes was previously reported in other work of the group using similar materials, and higher electrical conductivities were reached (12-17 S/cm) for nanocomposites containing 7 wt% of DWCNTs [126] (corresponding to 13.2 vol.%). In the same group, Santanach recently published his work on highly densified (98%) DWCNT-Fe-Al₂O₃ nanocomposites prepared by *in-situ* growth of CNTs followed by densification by SPS and achieved a maximal conductivity of 8 S/cm for nanocomposite containing about 7.1 wt.% of CNTs [200].

Studies of aligned CNTs embedded in insulating ceramic matrices to produce conductive samples with anisotropic conductivities were reported by Peigney *et al.* [201] and Zhu *et al.* [202]. Peigney *et al.* [201] prepared anisotropic SWCNT-Fe/Co-MgAl₂O₄ nanocomposites by high temperature extrusion, while Zhu *et al.* [202] prepared anisotropic MWCNT-Al₂O₃ nanocomposites through the application of a DC electric field. As expected, the conductivity in the direction parallel to the aligned CNTs is much higher than that measured in the transverse direction. In the case of SWCNT-Fe/Co-MgAl₂O₄ (hot extrusion), the parallel conductivity was around 30 times higher than the perpendicular one (20 S/cm against 0.95 S/cm for 4.9 wt.% of SWCNTs), while in the case of MWCNT-Al₂O₃ (electric field) the parallel conductivity was seven orders of magnitude higher than the perpendicular one (6.2 x 10⁻⁴ S/cm against 6.8 x 10⁻¹¹ S/cm for 2 wt.% of MWCNTs). These results indicate that the CNTs bundles are well interconnected and that they are partially aligned. Moreover, induced electric DC field seems very efficient for the partial alignment of CNTs. Furthermore, as could be expected, the maximum conductivities

for CNTs nanocomposites with insulating matrices can be reached in the parallel direction of partially aligned CNTs when anisotropy is present (σ_{MAX} of 20 S/cm for 4.9 wt.% of SWCNTs). However, a full alignment would be detrimental for the connectivity of the network since it would increase the threshold.

The previous discussion and comparisons show that the conductivities of CNT- Al_2O_3 nanocomposites (and that with other insulating oxide matrices) are always higher than that of CNT- SiO_2 nanocomposites, at similar CNT contents. That could indicate that the good wettability of the CNTs bundles by the SiO_2 matrix is probably deleterious for the intertube contact (a conduction by tunnelling effect might occur), increasing the local resistance. More generally, besides the difficulty of available comparisons, it seems that CNTs embedded in polycrystalline materials have a tendency to achieve higher conductivities as polycrystalline nanocomposites than as glassy nanocomposites.

Taking this considerations into account and considering that *F*-DWCNT- SiO_2 prepared in this work present electrical conductivities similar to other CNT-ceramic nanocomposites already reported, it can be concluded that besides the difficulty of reproducibility in functionalization step, CNTs silica matrix nanocomposites can reach low percolation thresholds and high electrical conductivities using the high aspect ratio and soft functionalized DWCNTs and the following route: (i) dispersion aided by ultrasonic tip probe; (ii) *in-situ* formation of the matrix; (iii) spark-plasma sintering at relatively low temperature and with a short dwell time to achieve the full densification. However, great efforts are still needed to achieve performances similar to those obtained with polymer matrices or on CNT-ceramic nanocomposites when the ceramics are insulating polycrystalline oxides [94,126,191-196,199,200].

On the other hand, Bauhofer and Kovacs [49] mentioned nanocomposites using SWCNTs [124] (with L/d of 55-321 and of 153-668) and MWCNTs [129] (L/d of 500) embedded in polyepoxy ($\sigma < 10^{-12}$ S/cm [98]) with percolation thresholds at lower concentrations (two orders of magnitude: 0.0052 vol.%, 0.0085 vol.% and 0.0025 wt.%, respectively) than in the *F*-DWCNT- SiO_2 composites. This evidences that most probably further improvements in the dispersion of CNTs are still needed especially in the case of ceramic nanocomposites.

In a recent review on CNT-polymer nanocomposites, Bauhofer and Kovacs [49] reported that to achieve a low percolation threshold and a high electrical

conductivity, the type and production method of CNTs is less important than the type of matrix and the dispersion method. For ceramic matrices, the tendency of higher conductivities in polycrystalline matrices than in amorphous matrices as well as the results obtained with different preparation methods support a similar conclusion.

In the present work, for the sample prepared by the wet route the percolation threshold is observed at slightly higher loads (~1.5 vol.%) than that observed by Rul *et al.* [191] in MgAl₂O₄ matrix (0.69 vol.%) and quite similar to the observed by Ahmad and Pan [196] in Al₂O₃ matrix (0.45 wt.% ~0.89 vol.%). Besides in dry route the percolation threshold is observed at lower content (~ 0.35 vol.%) than W samples and the conductivity can be higher (~10⁻⁴ S/cm) at contents lower than 1 vol.% in comparison to them, the opposite is true at loadings around 3 vol.%. The highest conductivities observed by Rul *et al.* [191] in the range of 1-3 vol.% in comparison to other ceramic nanocomposites containing randomly oriented CNTs is an indicative of the effective methodology used by them to obtain a well dispersed CNTN by *in-situ* growing of CNTs. In the other hand, the procedure used in this work is as efficient as that used by Ahmad and Pan [196].

The high conductivities observed by Zhan *et al.* [192] and Inam *et al.* [193,194] above 3 vol.% in comparison to others also indicate that their methodology might be promising, but the lack of compositions near the percolation does not allow any further conclusion on their results about the percolation threshold of the CNTN. In relation to the percolation threshold of non-aligned 3D CNTNs, CNT-ceramics nanocomposites are reported to present connectivity of CNTN at higher loadings (Figure 6.40b: typically in the range of 1-2 vol.% CNTs) than in CNT-polymer nanocomposites (generally below 1 vol.% [49]), but with similar or often higher maximal electrical conductivities than in the case of polymer matrices. The lower concentration of CNTs to percolation threshold in most polymers might be related to: (i) the higher facility/efficiency of dispersion of CNTs in some polymers (solubility) than in ceramics (powder suspension or, alternatively, sol-gel process); (ii) low percolation thresholds are probably kinetically produced (particle movement by diffusion, convection, shearing or external fields and re-aggregation) [49]; (iii) ceramics generally require high temperatures for densification, while in polymers it is generally a room temperature processing, avoiding any oxidation of CNTs. On the other hand, the maximal electrical conductivity in polymers is possibly affected by: (i) the wettability of CNT by some polymer (insulating polymer coatings of different

thicknesses on CNT: tunnelling through polymer barriers) [49], increasing contact resistance, in comparison to great part of polycrystalline ceramic matrices.

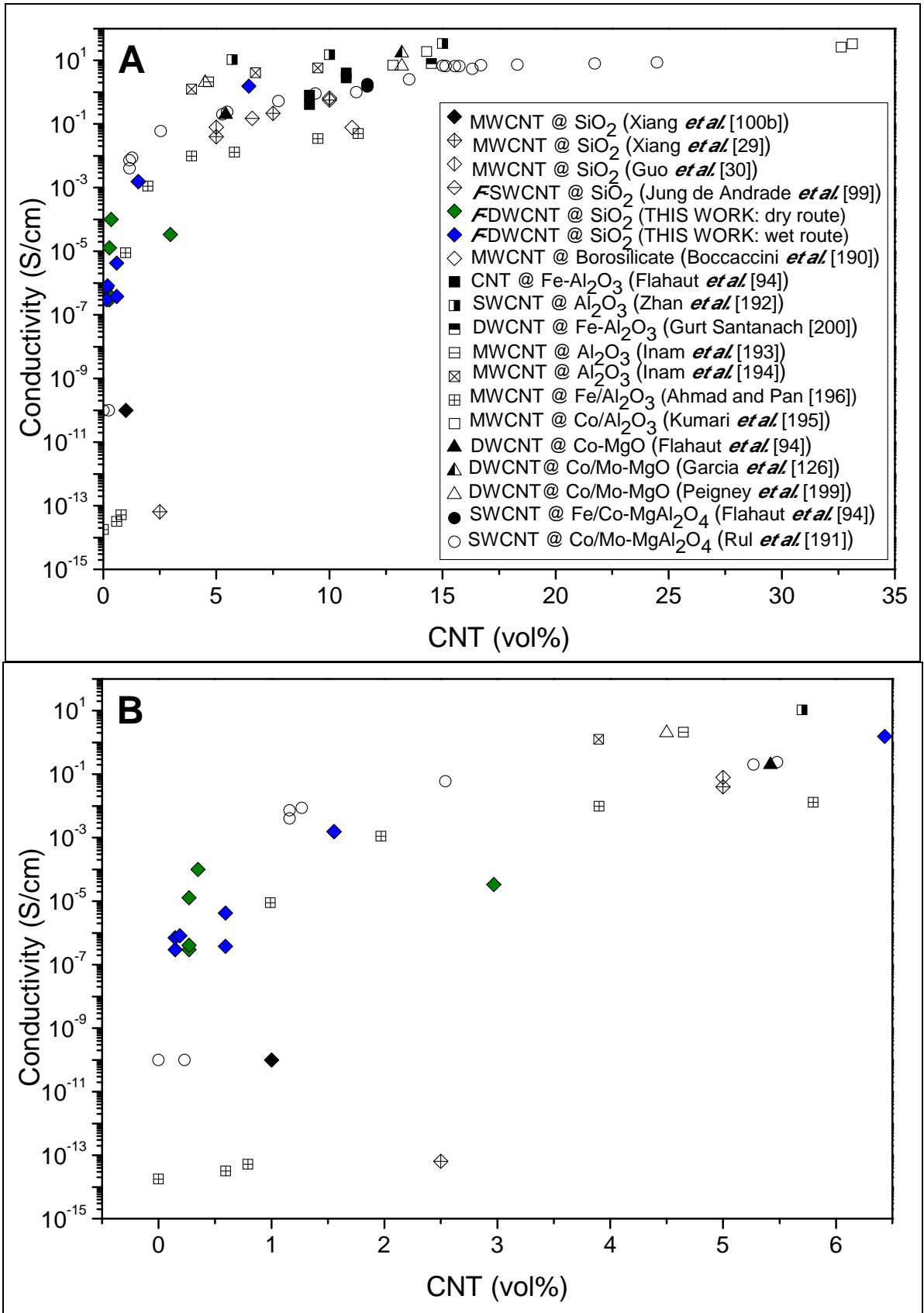


Figure 6.40 (A) Electrical conductivity versus various CNT content (vol.%) for CNT-ceramic nanocomposites (non-aligned CNTNs) in insulator matrices (*note: assuming densities of 3.98 g/cm³ and 2.23 g/cm³ for alumina and borosilicate, respectively* [98]): F-DWCNT-SiO₂ nanocomposites from this work in comparison with data from literature [29,30,94,99,100b,126,190-196,199,200]. (B) Same enlarged graph for the low contents.

6.3.5 Summary of 3D CNTNs

DWCNTs synthesis and characterization:

According to the characterizations, DWCNTs were successfully produced at CIRIMAT by CCVD using route developed by Flahaut *et al.* [154]. The carbon contents of the extracted DWCNTs are high (from 89 wt.% to 90 wt.%) and different batches present few differences, which traduces a rather good reproducibility. However, Raman spectroscopy showed some differences in $I_{D/G}$ (from 5% to 17%) between different batches which traduce variations of quantity of sp^3 defects or of content of disordered carbon. TEM observations evidenced outer diameter distribution in the range of 1-3 nm with few structural defects (only few “kinks”) accompanied by some disordered carbon (probably formed by small heaps of crushed graphene sheets and some graphitic shells, as observed in previous works of Flahaut *et al.* [154,165,166]) and some remaining metal NPs (Co and/or Mo). Raman spectroscopy also confirmed the relatively lower amount of defects and other disordered carbon than in MWCNTs previously used in this work.

Chemical functionalization:

A soft functionalization of the DWCNTs was operated by chemical oxidation at room temperature. Raman ($I_{D/G}$ in the range of 16-20%) and Infrared spectroscopies, as well as TEM and carbon analysis (from 61 wt.% to 74 wt.%) showed that *F*-DWCNT prepared in different batches can have some differences in characteristics and thus, probably, in electrical conductivities (*F*-DWCNT-A, *F*-DWCNT-B and *F*-DWCNT-C). However, the drying step seems to play the most important role in the final conductivity of suspensions or composites since it has a great influence on the aggregation degree, which affects directly the effective amount of filler contributing to form a percolating pathway for the electron transport. This soft functionalization did not cause any strong damage since only rare shortened CNT were observed by TEM and this is also confirmed by a low increase in $I_{D/G}$ and little differences observed comparing the Infrared spectra obtained for the DWCNTs before and after functionalization (only peaks of CNT mode are more defined before the functionalization).

Electrical conductivity of (*F*-)DWCNT suspension in chloroform:

Measurements of the electrical conductivity of DWCNT suspensions showed that these CNTs are potentially more interesting for the production of electrical conductive composites than other CNTs previously studied in this work.

However, the measurements of dynamic electrical conductivity have shown that suspensions made with different synthesis batches of DWCNTs present different percolation thresholds (varying from 0.01-0.012 vol.% for DWCNTs-A, -B and -C samples to 0.0025-0.003 vol.% for DWCNTs-D and -E samples) and conductivity values. These facts can be related to the differences in the amount of disordered carbon and to a non complete disaggregation. For example, at low CNT loadings (before percolation threshold), a peak on the conductivity can be observed on the curve obtained for sample DWCNT-D, which might probably be due to the breaking of big aggregates, while for sample DWCNT-E the CNTs smoothly form a percolating network which can indicate that the sample probably contained smaller aggregates than sample DWCNT-D. Samples DWCNTs-A, B and C were not used in the following studies of preparation of nanocomposites due to the lower percolation threshold of their suspensions in comparison to that of samples DWCNTs-D and -E.

These studies also demonstrated that the soft functionalization did not cause any strong damage (i.e., no severe shortening) because similar percolation thresholds are obtained before (samples dried in desiccator) and after the functionalization step for a given batch of CNT. The fact that at the lower CNTs contents (below 0.003 vol.%) the conductivity of sample D is higher than others (but still quite insulating) is most probably due to contamination of some ions in chloroform. However, at the higher CNTs contents the conductivities of suspensions of *F*-DWCNTs are lower than that of non-functionalized one probably due to the creation of defects that can act as scattering centers for electron transport. Moreover, drying of *F*-DWCNTs in stove (at 80-100°C) lead to the formation of hard aggregates which require manual grinding. Consequently, the drying at room temperature in a desiccator is preferable.

Nanocomposite powders:

DWCNT-SiO₂ nanocomposite powders were successfully obtained by a classical organic sol-gel method. Zeta potential measurements showed that a pH around 4 would be a good compromise to obtain a not too long gelification time and a good stability of suspensions. Molar ratios water/TEOS and ethanol/TEOS were fixed to 20 and 0.3 respectively to enable high loadings of CNTs as high as possible in the final nanocomposite.

It was quite difficult to visualize CNTs in nanocomposite powders by FESEM because they are surrounded by silica and thus CNTs were scarcely imaged only for high loadings, which did not allow evaluating the state of CNT dispersion. Raman spectroscopy of calcinated *F*-DWCNTs-SiO₂ nanocomposite powders indicated that the dispersion step using probe sonication might have slightly increased the amount of defects on *F*-DWCNTs ($I_{D/G}$ from 0.18 to 0.22). It also revealed (D^* upshift) an interaction of CNTs with the silica matrix.

Dense nanocomposites:

SPS experiments outlined the importance to well stock the CNT-SiO₂ nanocomposite powders (in desiccator, for example) after its calcination in order to avoid it to adsorb humidity from the ambient air, due to its high specific surface area. This precaution can aid to avoid heterogeneous crystallization of silica.

Densification of CNT-SiO₂ nanocomposites by SPS was achieved at relatively low temperature (950°C) with short dwell time (5 min) and an applied pressure of 100 MPa. It was observed that CNTs slows the predominant sintering mechanism (viscous flow) as any fiber does in a glass matrix, but few modifications on SPS parameters were needed (in comparison to parameters used with pure silica). It was also demonstrated by FESEM (angle of contact shows wettability) and Raman spectroscopy (G and D^* bands upshifted after densification indicate CNTs under residual pressure in the matrix) that CNT preserve a good interaction with silica after its densification.

In some samples, the crystallization of some α -quartz grains was suspected but not proved by XRD since the main peak of this phase is superimposed with the main peak of graphite (coming from residues of graphite foils used for sintering or

from CNTs). We also concluded that the residual humidity in the powders has a major role in the transparency, which is not always achieved due to either residual porosity or heterogeneous crystallization. Thus, an appropriate storage (desiccator) of the CNT-SiO₂ powder is necessary after its calcination, until its sintering.

On Raman spectra of sintered nanocomposites, when the silica fluorescence signal is subtracted an increase in $I_{D/G}$ (from 0.22 to 0.36), is noticed which could reflect some extra damage by oxidation of *F*-DWCNTs by silica during SPS treatment at 950°C.

About the dispersion of CNTs in the silica matrix, it was shown that it is important to well homogenise each batch of functionalization and that the state of the *F*-DWCNTs (wet or dry) prior to its incorporation in a suspension greatly influences the final dispersion in the nanocomposites. In general, W series (wet) show smaller mean diameter of bundles (12.8 nm against 15 nm), but at the same time presented more aggregates than D series (dry). The smaller diameter of bundles in W series might be an indicative that they were initially better dispersed than D series. We infer that, for W series, an aggregation of CNTs occurs during gelification which was generally longer than for D series. These aggregates (> 10 μm² observed by FESEM for CNTs contents ≥ 0.59 vol.%) are well dispersed in the composites (flattened probably during the uniaxial pressure application during SPS), and connected by CNT bundles. To avoid this CNT bundle aggregation during the wet route, it was suggested: (i) to use a basic sol-gel route (since it seems that it would not disturb the dispersion as evidenced by Zeta potential results) or (ii) to work with a more complex functionalization of DWCNTs, adding a second step to insert amines (positively charged) at the extremities of CNTs.

The electrical conductivity measurements of *F*-DWCNT-SiO₂ nanocomposites show an increase of almost 7 orders of magnitude in electrical conductivity (from 3×10^{-7} S/cm to 1.56 S/cm) from 0.15 vol.% to 6.43 vol.% *F*-DWCNTs. However, the initial state of *F*-DWCNTs (wet or dried at room temperature) seem to cause variations in conductivity for similar *F*-DWCNTs contents and this was assigned to the different degrees of dispersion of *F*-DWCNTs. In the same way, the percolation threshold also depends on the initial state of *F*-DWCNTs: ~0.35 vol.% with *F*-DWCNTs previously dry and grinded (dry route) against ~0.70 vol.% with wet *F*-DWCNTs (wet route). These differences are a consequence of the better dispersion state at low carbon contents in D samples than in W samples (for example, at 0.15

vol.% of *F*-DWCNTs by *W* route, some aggregates with area larger than $2 \mu\text{m}^2$ were observed, while in *D* samples, up to 0.27 vol.% of *F*-DWCNTs, the larger one has an area of $0.73 \mu\text{m}^2$). As a consequence, it has been demonstrated that it is possible to observe a tendency that up to carbon contents between 0.3-0.5 wt.% the *D* route would lead to composites more electrically conductive (10^{-4} S/cm for 0.35 vol.% of *F*-DWCNTs) than those from *W* route (4.2×10^{-6} S/cm for 0.35 vol.% of *F*-DWCNTs). In the other hand, at higher loadings than this, the opposite is true ($1.5\text{-}1.6 \times 10^{-3}$ S/cm for 1.55 vol.% against 3.36×10^{-5} S/cm for 2.97 vol.% of *F*-DWCNTs by *W* and *D* route, respectively). A percolating network is formed in *D* samples at slightly lower loadings of DWCNTs than *W* samples due to the presence of flattened aggregates (observed from contents of 0.47 wt.% of DWCNT in composites from *W* series). However, the good distribution of aggregates in *W* samples demonstrates that even at high carbon contents (6.43 vol.%) *W* series can achieve high electrical conductivity, while in *D* series the conductivity greatly decreased (from 10^{-4} S/cm to 3.36×10^{-5} S/cm when increasing filler content from 0.35 vol.% to 2.97 vol.%, respectively) probably due to great and rare aggregates formed at high content (above percolation threshold). The highest electrical conductivity was possible through *W* route as well as the highest CNT contents.

The significant differences found between measured conductivities, for similar CNTs contents and within a given route are related to: (i) different batches of *F*-DWCNTs (which also depends on the original sample); (ii) different states of dispersion related to different dispersion of aggregates (those formed during the drying step are more difficult to divide after the functionalization step); (iii) different sizes of aggregates in suspension.

For a given load of CNTs, nanocomposites have an electrical conductivity below that of suspensions in liquid, probably because the constant sonication of liquid suspensions limits the formation of aggregates (more filaments, probably DWCNT bundles, are thus effectively available to contribute to form a 3D network pathway for electrical current).

It was not possible to verify if the modified rule of mixtures is appropriate to forecast the conductivity of CNT networks in chloroform or in silica and this fact could be explained by the facts that: (i) the intrinsic conductivity of the metallic *F*-DWCNTs is lower than that assumed; (ii) the dispersion of CNTs is not optimal; (iii) the

interfacial resistivities are not taken into account (intertube and, especially, at the interface of silica and DWCNT) through modified rule of mixtures; (iv) the metallic/semiconducting ratio can vary with the preferential oxidation of metallic DWCNTs; (v) effect of the residual stress in the conductivity of the CNT might affect in the same way of defects, as scattering centers.

Compared with data from literature the maximal electrical conductivity (1.56 S/cm at 6.43 vol.% of *F*-DWCNTs against 0.65 S/cm at 10 vol.% of MWCNTs [30] achieved in this work is higher than all others studies previously reported on CNTs randomly oriented in glassy matrices [30,99,100b,190]. In the same way, at low contents (< 0.5 vol.%) the conductivities of *F*-DWCNTs-SiO₂ were also higher than all others studies previously reported with silica and borosilicate matrices [30,99,100b,190], which is explained by a percolation threshold smaller (~0.30 vol.% by dry route and ~0.70 vol.% by wet route) than any value obtained. Several reasons explain these improved results: (i) the particular characteristics of used DWCNTs, particularly their very high length and aspect ratio; (ii) the functionalization step which was sufficiently mild to avoid important damages to DWCNTs; (iii) the efficiency of densification by SPS at a moderate temperature. But these values could be increased by improving the DWCNT dispersion.

Compared with most results of literature on other CNT-ceramic nanocomposites with insulating polycrystalline matrices, *F*-DWCNT-SiO₂ of the present work generally present, for same CNT contents, quite lower electrical conductivities (at the higher CNT contents) than polycrystalline matrices. The good wetting of CNTs by amorphous silica might increase the intertube contact resistance and thus lower the conductivity of the material.

The achieved maximal electrical conductivities for the nanocomposites by dry and wet routes are both enough to the use of these materials as antielectrostatic [27] or heating applications [28], for example. For the wet route (W samples), in order to lower the percolation threshold and to increase the electrical conductivity at similar CNT contents, we proposed the following solutions: (i) the shortening of the gelification step; (ii) a more severe dispersion through strong functionalization or a prolonged time of (bath or probe) sonication.

CONCLUSIONS

We have prepared 2- and 3-dimensional carbon nanotubes networks (CNTNs), over silica glass substrate and in silica matrix respectively, and studied their electrical conductivity as a function of the CNT content and in relation with the CNTs characteristics and their dispersion. Different kinds of CNTs, which were all produced by a CCVD method, were characterized (TEM, Raman Spectroscopy, carbon analysis). In a first time, their abilities to form a percolating network were compared by measurement of the electrical conductivity of CNTs dynamic suspensions in chloroform. Then, thin pure CNTs films over silica glass substrates were prepared and the surface resistance *versus* transparency was studied. Finally, 3D CNTNs in the form of CNT-silica nanocomposites were prepared and their conductivities were studied and correlated with microstructure.

In the different parts of the work, we used SWCNTs, DWCNTs and three kinds of MWCNTs which differ by their mean diameters (1.2 - 15 nm), their lengths (660 nm to more than 10 μm) and consequently by their aspect ratios (370 to more than 5000), their presence either mostly under the form of bundles (SWCNTs and DWCNTs) of rather individual (MWCNTs) and the quantity of defects in their walls (few in SWCNTs and DWCNTs, much more in MWCNTs). All the used CNTs formed percolating networks in dynamic suspensions in chloroform and, for SWCNTs and DWCNTs, the electrical conductivities well followed the power law, as predicted by the percolation theory, with an exponent of 1.82-1.85 near the theoretical value for a 3D network [46,47]. Among all suspensions, that with SWCNTs present the higher maximum normalized conductivity (3.08 $\text{S}\cdot\text{cm}^2/\text{g}$) due to their specific electrical conductivity which is higher than that of DWCNTs and MWCNTs. Consequently we chose to use SWCNTs for the preparation of 2D CNTNs. However, the lower percolation thresholds (0.002-0.06 vol.%) were obtained for suspensions of DWCNTs mainly due to their aspect ratio higher than that of other used CNTs. For this reason and also because their outer tube would allow their covalent functionalization while preserving the inner tube [50], we selected DWCNTs for the preparation of 3D CNTNs in solid (CNT-silica nanocomposites). For all suspensions, the percolation thresholds were

found to be lower than most of that reported for solid nanocomposites containing randomly aligned CNTs.

To prepare thin pure films of CNTs over (previously amino silanized) silica glass substrates, we used several techniques, spray-coating, dip-coating, electrophoretic deposition and filtration method and only one SWCNT aqueous suspension. We compared the surface resistance of the films at similar transparencies. For the films prepared by spray-coating, electrophoretic deposition or filtration method, the surface resistances versus transparencies were quite similar to those obtained by Kaempgen *et al.* [136]. However, quite different conductivities were obtained for the films prepared by dip-coating which was explained by difference in the alignment of the CNTs: while dip-coating showed some partial alignment, the others techniques present random distribution of CNTs. Moreover, it was outlined the importance of well rinsing the 2D CNTNs to remove the surfactant which can act as barriers for intertube contacts. The smoothest CNTNs were obtained by electrophoretic deposition, but their surface resistances *versus* transparencies were below the expected ones and that was possibly due to higher opacity of the CNTNs caused by oxidation of the aluminium layer. Most of the 2D CNTNs formed a percolating network whose electrical conductivity well followed the power law, with an exponent around 1.29, which is in agreement with the theoretical predictions (1.1-1.4 [48]). The properties of the SWCNT networks prepared by the dip-coating method reach parameters which may already make them suitable for applications in flat panel displays and solar cells. It was also shown that MWCNT films prepared by the filtration method present a lower surface resistance, for a given transparency, than SWCNT films.

For the preparation of DWCNTs-silica nanocomposites, a soft chemical functionalization was developed. Two batches of DWCNTs, prepared by a dry or a wet route respectively, presenting the lowest percolation thresholds (0.002-0.003 vol.%) in chloroform suspension were selected and functionalized. The functionalized DWCNTs (*F*-DWCNTs) were incorporated in the matrix by a sol-gel technique and thermally treated to remove the organics. Then, nanocomposites materials were fully densified by spark-plasma sintering (SPS). The main parameters of SPS (pressure, dwell temperature and time) were previously studied on pure silica and then adjusted for nanocomposites. The microstructures of the materials, particularly the dispersion

of DWCNTs, were characterized by FESEM observations and were correlated to their respective conductivities. For low carbon contents (up to 0.3-0.5 wt.%), the dispersion state of samples prepared by the dry route was better than that prepared by the wet route, while it was the opposite for higher contents. In good correlation with the dispersion states, the percolation threshold was lower for samples prepared by the dry route (~0.35 vol.% of *F*-DWCNTs) than for that prepared by the wet route (~0.70 vol.% with *F*-DWCNTs) but the higher conductivity was obtained for the latter samples (1.56 S/cm for 6.43 vol.% of *F*-DWCNTs). The obtained percolation threshold is the lower value and the maximal conductivity is the higher value compared with that reported in literature for CNT-silica nanocomposites, and these values are similar to that reported for other CNT-ceramic nanocomposites. The achieved maximal electrical conductivities of DWCNT-silica nanocomposites are enough to the use of these materials in antielectrostatic or heating applications.

For future work, the preparation of 2D CNTNs using MWCNTs should be more investigated, using dip-coating and an optimized electrophoretic deposition, to obtain improved properties and decrease the costs at the same time. A higher transparency of 2D CNTNs obtained by electrophoretic deposition could be obtained by using alternative conductive films or by removing the alumina films. Films with higher conductivities could also be obtained by using doped CNTs or batches of CNTs in which disordered carbon has been removed through thermal treatments.

Also for future work the dispersion of DWCNTs in the silica matrix can be still improved. Firstly, the formation of CNTs aggregates during the wet route should be avoided by shortening the gelification time. The *in-situ* growing of CNTs within a silica powder is an alternative route which could lead to a better dispersion of CNTs but the difficulty will be the lower control of the characteristics of the obtained CNTs, and thus of their properties. These routes could allow obtaining transparent and conductive samples in enhancing the dispersion state of the CNT inside the silica matrix leading in such a way to a decrease of the CNT amount necessary to reach the percolation threshold or the maximal conductivity. The DWCNT dispersion in composites could be further studied from the nm to the micron or mm scale (because of possible agglomeration) by using not only FESEM, but also X-ray tomography, focused ion beam and 4D electron tomography.

ATTACHMENTS

SURFACTANT FOR 2D CNTNs

Erreur ! Signet non défini.

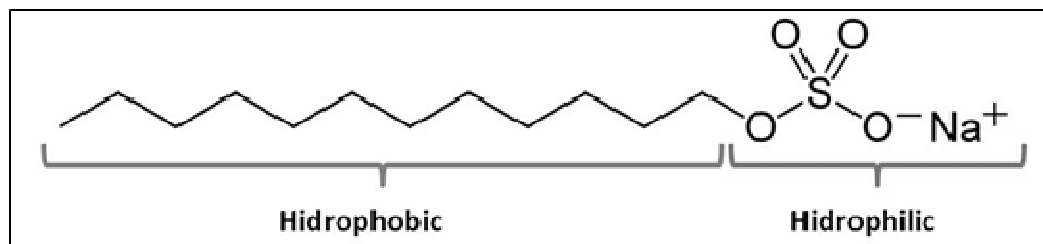


Figure 0.1 Schematic diagram of the molecule of sodium dodecyl sulfate, SDS.

SUBSTRATE FOR 2D CNTNs

SUPRASIL®, from Heraeus Quarzglas, is a high purity synthetic amorphous silica material manufactured by flame hydrolysis. This synthetic fused silica is practically free from bubbles and inclusions (Table 0.1) with outstanding optical characteristics in the deep UV and the visible wavelength range (Figure 0.2). In addition, the material provides excellent resistance to damage by high energy UV laser radiation.

Table 0.1 Main characteristics of substrate used for the deposition of 2D CNTNs.

Refractive Index	Bubbles and Inclusions
$n_c = 1.45637$ at 656.3 nm $n_d = 1.45846$ at 587.6 nm $n_F = 1.46313$ at 486.1 nm $n_g = 1.46669$ at 435.8 nm $n = 1.50855$ at 248 nm At 20°C, 1 bar atmospheric pressure Accuracy: $\pm 3 \cdot 10^{-5}$	(Bubbles ≤ 0.08 mm diameter are disregarded) Bubble class: better than 0 (as per DIN 58927 2/70) i.e. total bubble cross section within the volume is $\leq 0.03 \text{ mm}^2 / 100 \text{ cm}^3$ Maximum bubble diameter ≤ 0.20 mm

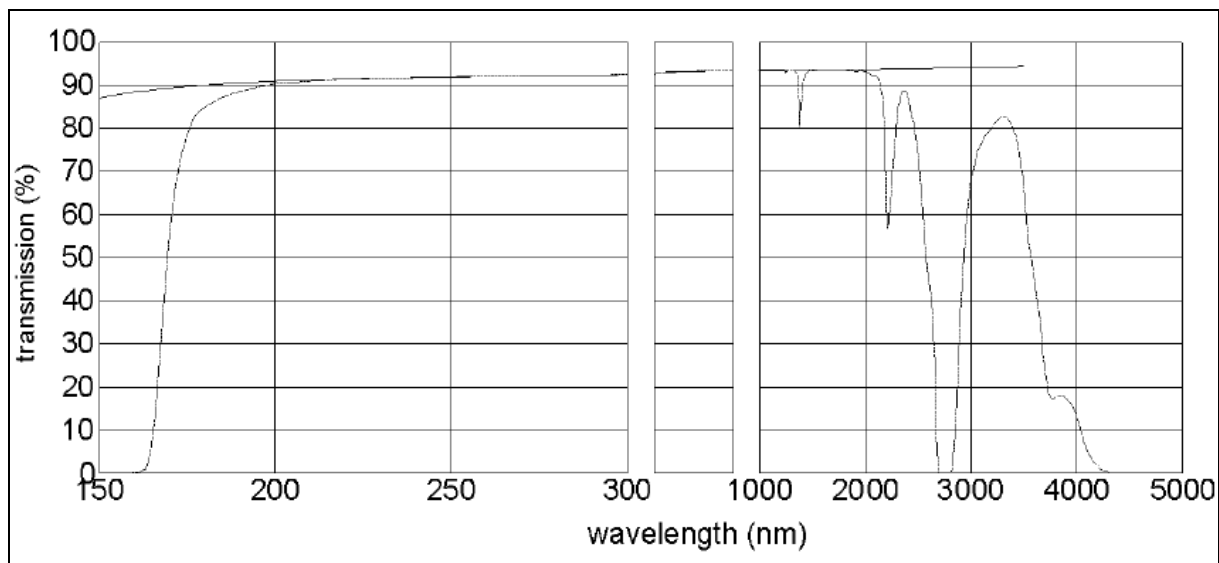


Figure 0.2 Typical spectral transmission including Fresnel reflection loss. The uppermost nearly straight line indicates the calculated Fresnel reflection loss of two uncoated surfaces. Path length of 10 mm.

SILANIZATION OF THE SUBSTRATE FOR 2D CNTNs

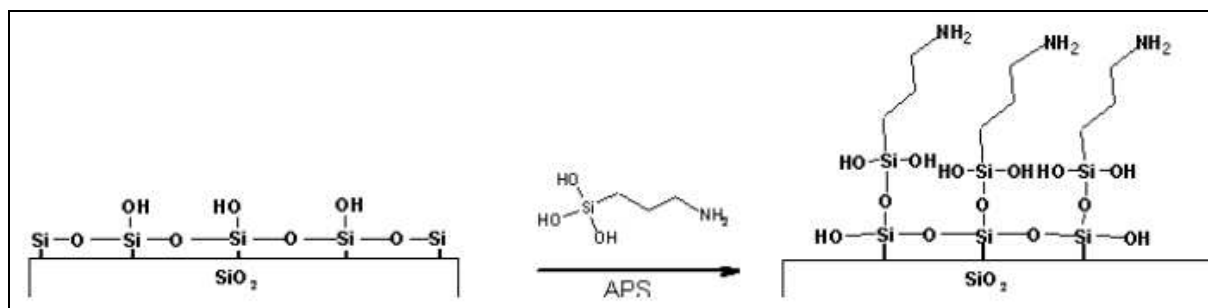


Figure 0.3 Schematic diagram of the reaction of silanization of the surface of silica glass substrate by reacting with 3-Aminopropyltriethoxysilan (APS).

ELETROPHOTRETIC DEPOSITION FOR 2D CNTNs

During the electrophoretic deposition the aluminium layer is oxidized and, therefore the electrical current is reduced along the time, as it is shown in Figure 0.4.

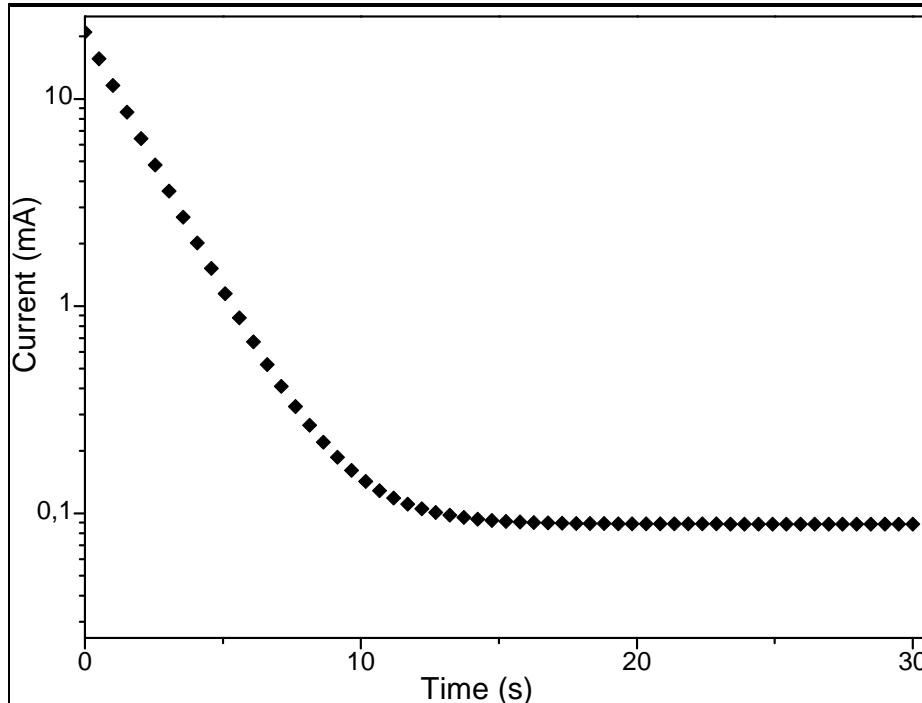


Figure 0.4 Schematic diagram of the reaction of silanization of the surface of silica glass substrate by reacting with 3.Aminopropyltriethoxysilan (APS).

ELECTRICAL CONDUCTIVITY IN LIQUID ALONG TIME

It is possible to note that HiPco material have a conductivity along time quite stable, while DWCNT needed more time to achieve a plateau of steady conductivity. This might be due to a higher grade of packing in comparison to HiPco, but further studies are needed to elucidate.

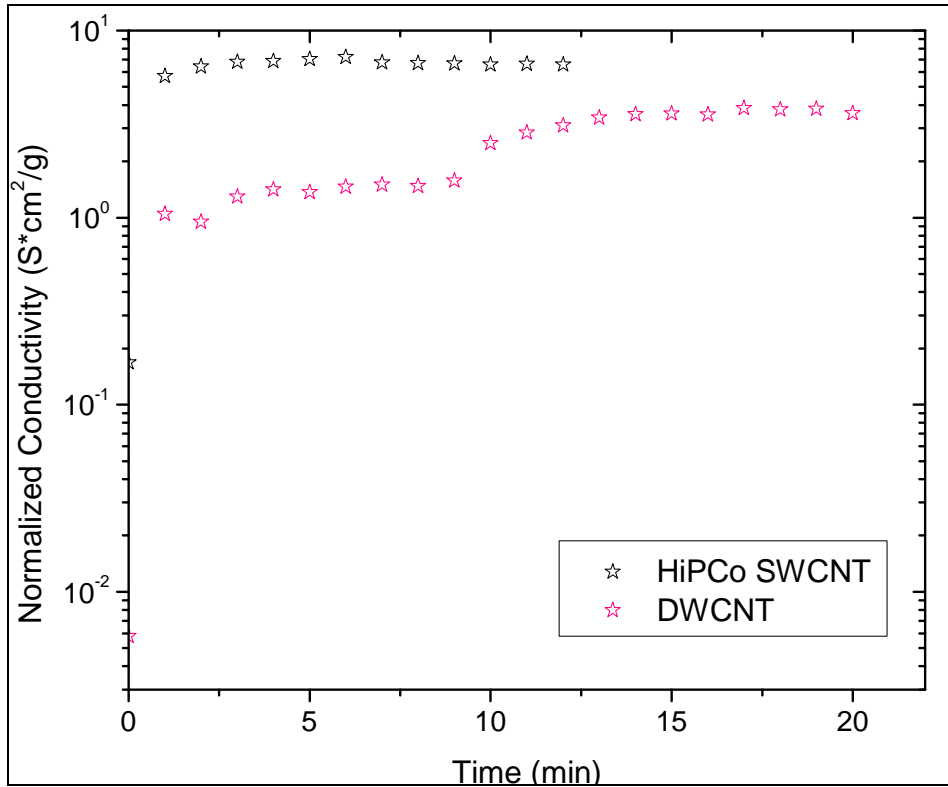


Figure 0.5 Normalized electrical conductivity (~1 mg/mL) of the carbon suspensions in chloroform at 1.5 V DC (0.104 V/cm) during sonication of HiPco-SWCNT and DWCNT along time.

CONDUCTIVITY OF DYNAMIC SUSPENSIONS OF MWCNTs

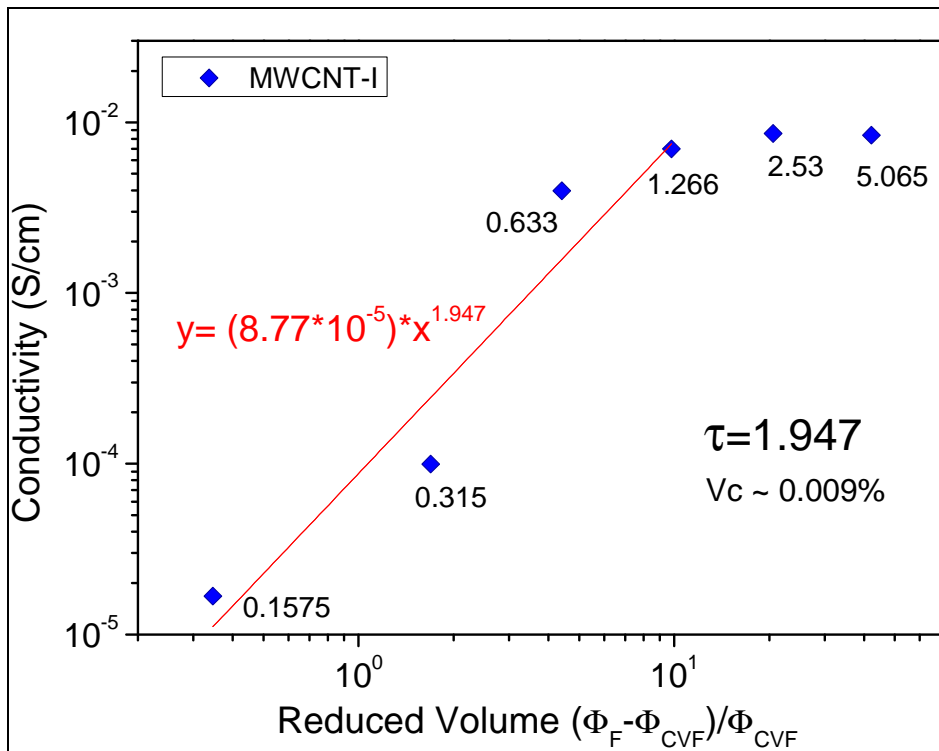


Figure 0.6 Conductivity of MWCNT-I suspensions in chloroform *versus* its reduced volume (both in logarithmic scale). The CNT concentration (mg/mL) is indicated for each point.

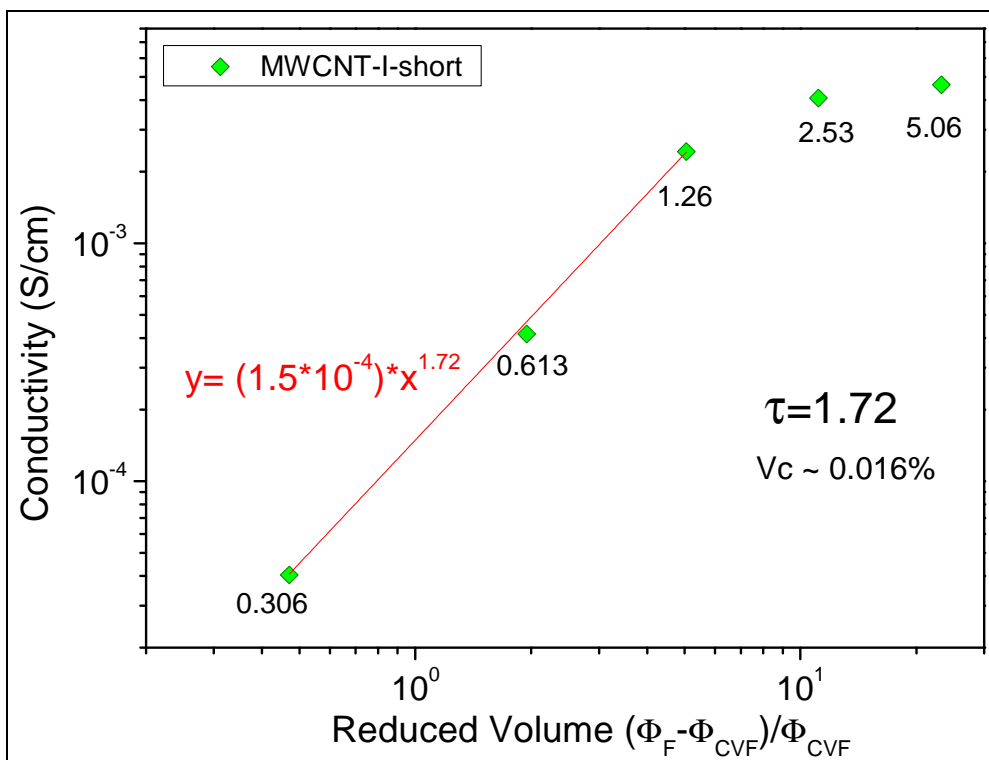


Figure 0.7 Conductivity of MWCNT-I-short suspensions in chloroform *versus* its reduced volume (both in logarithmic scale). The CNT concentration (mg/mL) is indicated for each point.

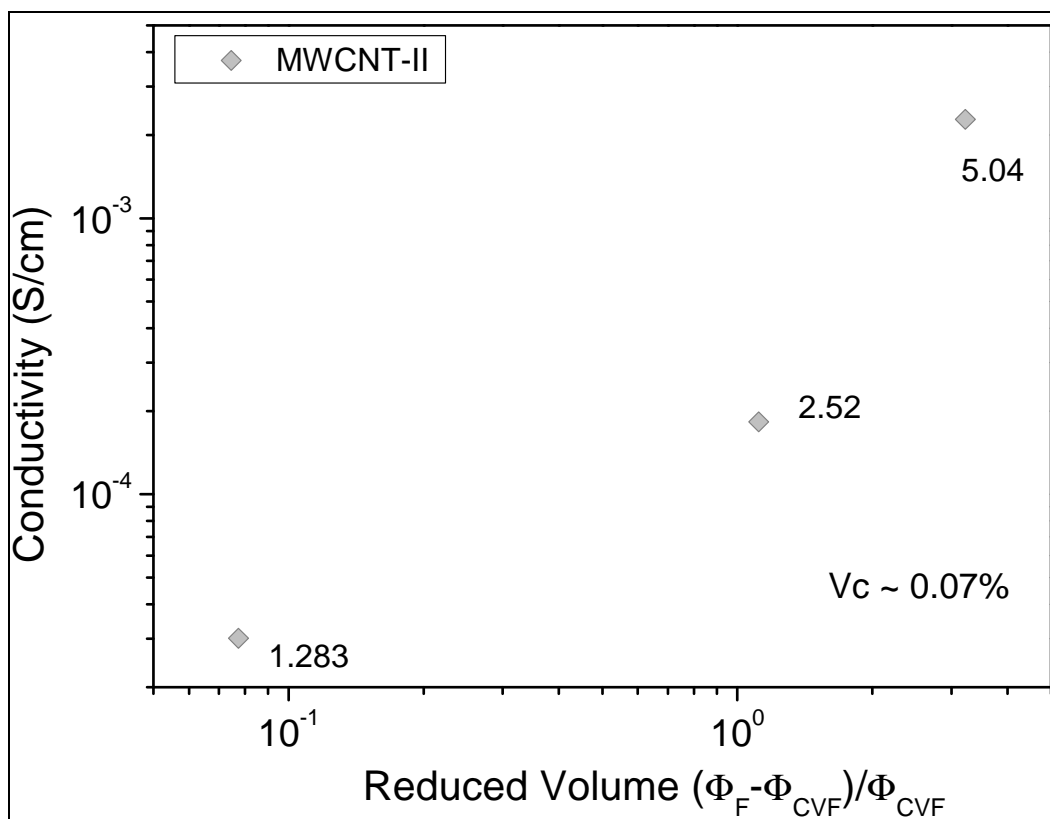


Figure 0.8 Conductivity of MWCNT-II suspensions in chloroform *versus* its reduced volume (both in logarithmic scale). The CNT concentration (mg/mL) is indicated for each point.

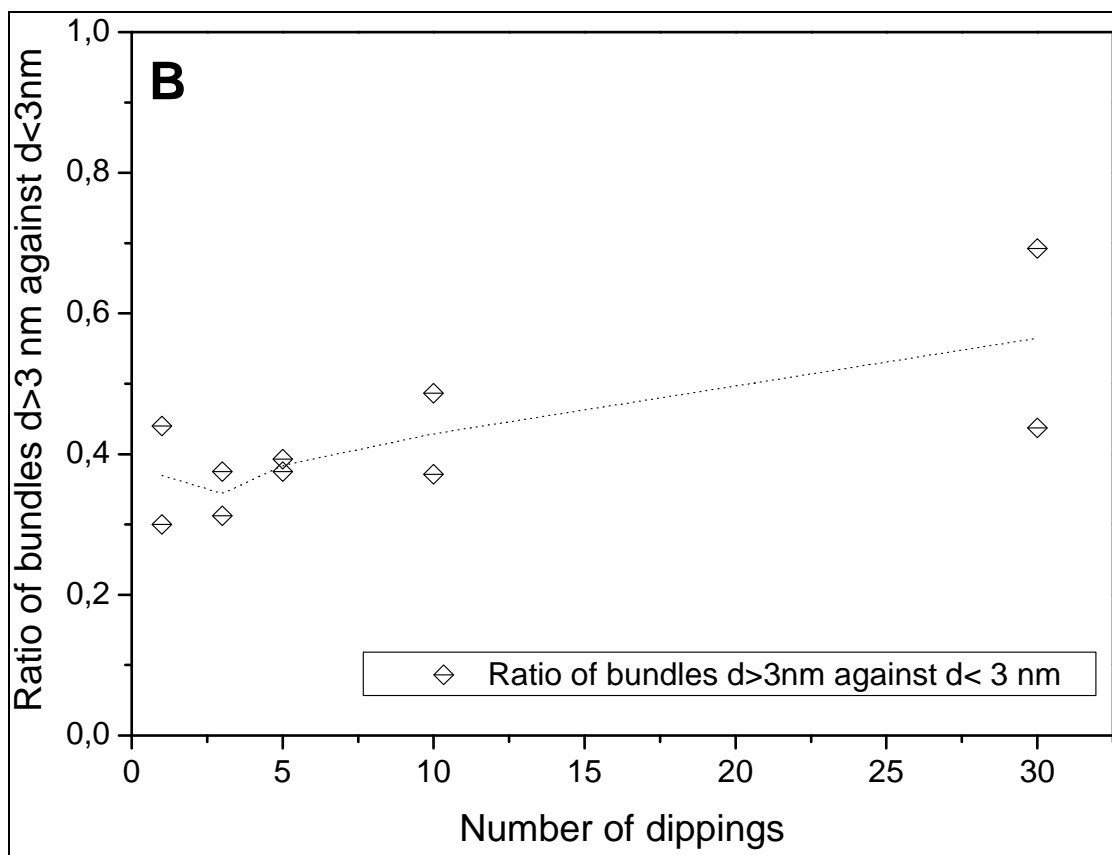
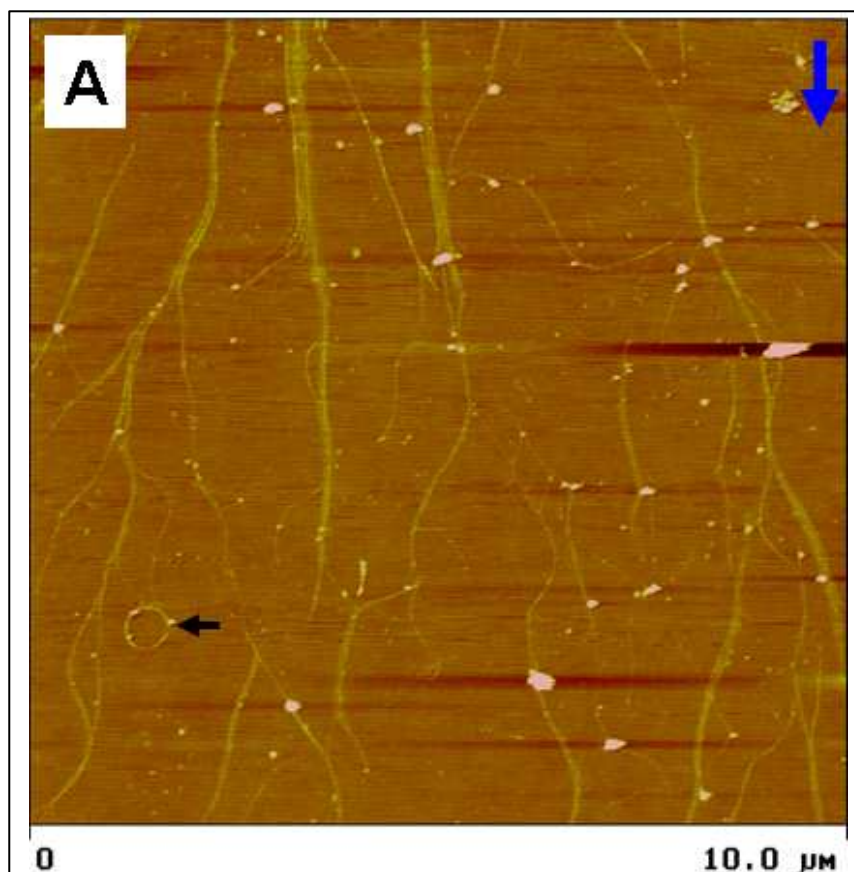


Figure 0.9 (A) AFM image (height data type with Z range of 30 nm) evidence of alignment of dip-coating first adsorbed layer (blue arrow is the direction of dipping and black arrow shows CNT loop); (B) and increase of bundling with number of dippings.

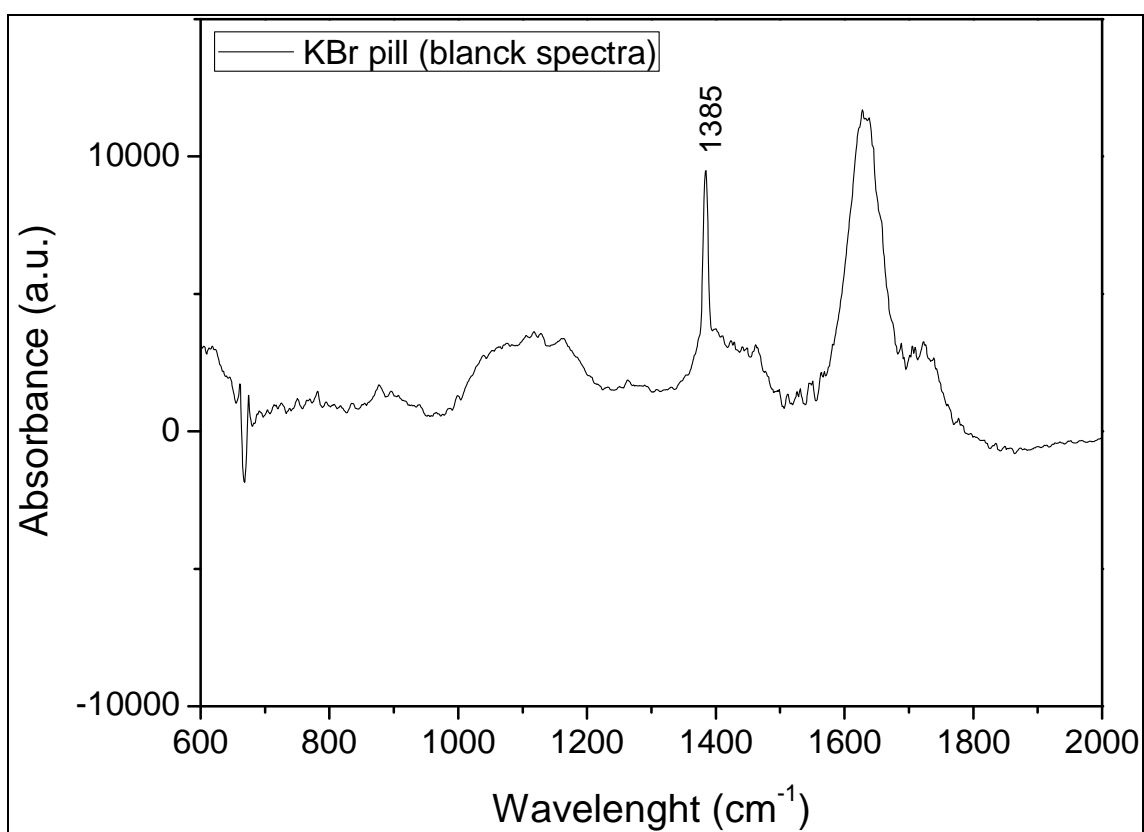


Figure 0.10 Infrared spectra of KBr pill without CNTs.

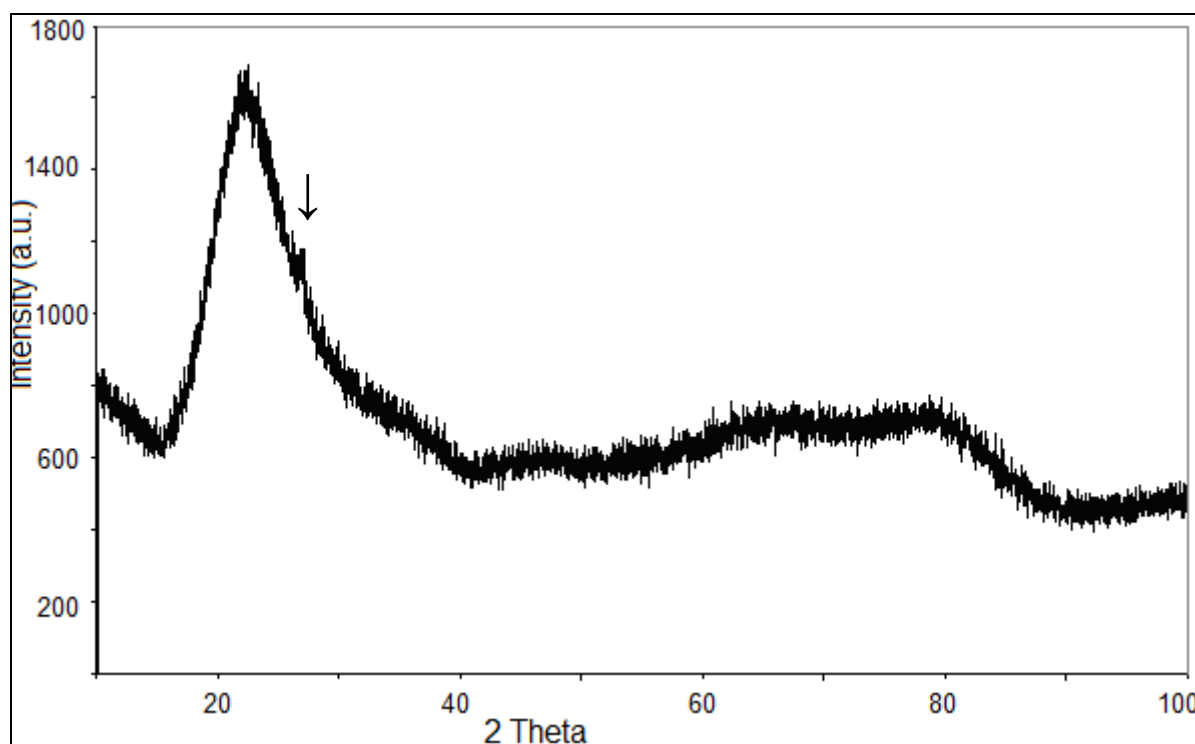


Figure 0.11 XRD pattern of a pure silica sample with apparent slight beginning of crystallization (black arrow).

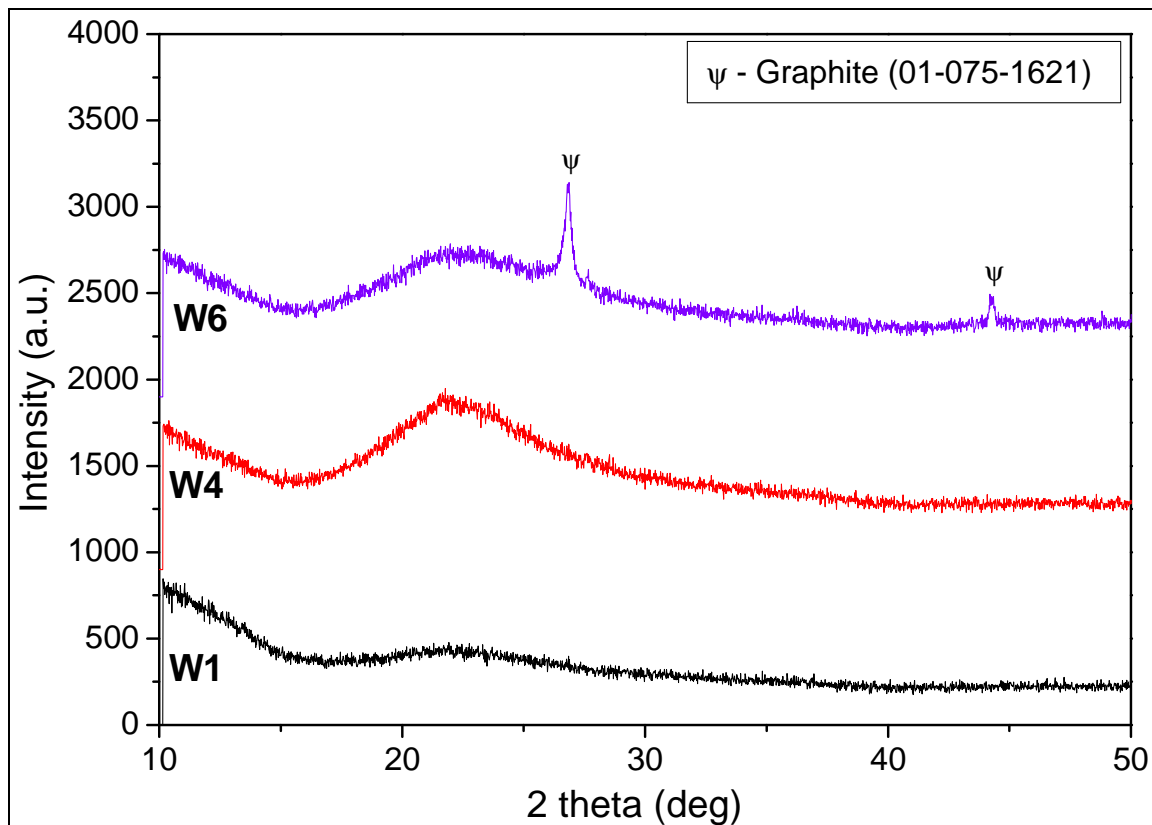


Figure 0.12 XRD patterns of the *F*-DWCNT-SiO₂ materials after consolidation by SPS composites obtained by wet route.

REFERENCES

- [1] RADUSHKEVICH, L.V.; LUKYANOVICHV.M., *Zurn Fisic Chim*, 26 (1952) 88–95.
- [2] HUGHES, T.V.; CHAMBERS, C.R., *US Patent* 405480, 1889.
- [3] OBERLIN, A.; ENDO, M.; KOYAMA, T., *J. Cryst. Growth*, 32 (1976) 335-343.
- [4] ABRAHAMSON, J.; WILES, P.G.; RHOADES, B.L., *Carbon*, 37 (1999) 1873-1874.
- [5] TENNENT, H.G., *US Patent* 4663230, 1987.
- [6] IJIMA, S., *Nature*, 354 (1991) 56-58.
- [7] O'CONNELL, M.J. (2006). *Carbon Nanotubes – Properties and Applications*. New York, USA: Taylor & Francis.
- [8] YE, J.T.; TANG, Z.-K., *Physical Review B*, 72 (2005) 045414.1-045414.4
- [9] LI, H.J.; LU, W.G.; LI, J.J.; BAI, X.D.; GU, C.Z., *Physical Review Letters*, 95 (2005) 086601.1-086601.4.
- [10] NEMES-INCZE, P.; DARÓCZI, N.; SÁRKÖZI, Z.; KOÓS, A.A.; KERTÉSZ, K.; TÍPRIGAN, O.; HORVÁTH, Z.E.; DARABONT, AL.; BIRÓ, L.P., *Journal of Optoelectronics and Advanced Materials*, 9 (2007) 1525 – 1529.
- [11] PEIGNEY, A.; LAURENT, Ch.; FLAHAUT, E.; BACSA, R.R.; ROUSSET. A., *Carbon*, 39 (2001) 507–514
- [12] LAURENT, Ch., PEIGNEY, A.; FLAHAUT, E., *Carbon*, 48 (2010) 2989–2999.
- [13] BEGTRUP, G.E.; RAY, K.G.; KESSLER, B.M.; YUZVINSKY, T.D.; GARCIA, H.; ZETTL, A., *Phys. Stat. Sol. (B)*, 244 (2007) 3960–3963.
- [14] LÓPEZ, M.J.; CABRIA, I.; MARCH, N.H.; ALONSO, J.A., *Carbon*, 43 (2005) 1371-1377.
- [15] GRUNER, G., *J. Mater. Chem.*, 16 (2006) 3533–3539.
- [16] HU, L.; GRUNER, G.; LI, D.; KANER, R.B.; CECH, J., *Journal of Applied Physics*, 101 (2007) 016102.1-016102.3.
- [17] LIU, Y.T.; XIE, X.M.; GAO, Y.F.; FENG, Q.P.; GUO, L.R.; WANG, X.H.; YE, X.Y., *Mater. Lett.*, 61 (2007) 334-338.
- [18] RAFFAELLE, R.P.; LANDI, B.J.; HARRIS, J.D.; BAILEY, S.G.; HEPP, A.F., *Mater.Sci.Eng. B*, 116 (2005) 233-243.
- [19] NOVAK, J.P.; LAY, M.D.; PERKINS, F.K.; SNOW, E.S., *Solid-State Electron*, 48 (2004) 1753-1756.
- [20] (a) BORGHETTI, J.; DERYCKE, V.; LENFANT, S.; CHENEVIER, P.; FILORAMO, A.; GOFFMAN, M.; VUILLAUME, D.; BOURGOIN, J.-P., *Adv. Mater.*, 18 (2006) 2535-2540.; (b) HUR, S.; KHANG, D.Y.; KOCABAS, C.; ROGERS, J.A., *Appl. Phys. Lett.*, 85 (2004) 5730-5732.
- [21] (a) SNOW, E.S.; PERKINS, F.K.; HOUSER, E.J.; BADESCU, S.C.; REINECKE, T.L., *Science*, 307 (2005) 1942-1945; (b) FERRER-ANGLADA, N.; KAEMPGEN, M.; ROTH, S., *Phys. stat. sol. (b)*, 243 (2006) 3519-3253.
- [22] (a) FANCHINI, G.; UNALAN, H.E.; CHHOWALLA, M., *Appl. Phys. Lett.*, 88 (2006). 191919.1-191919.3; (b) STAR, A.; LU, Y.; BRADLEY, K.; GRÜNER, G., *Nano Lett.*, 4 (2004) 1587-1591.
- [23] ZHOU, Y.; GAUR, A.; HUR, S.; KOCABAS, C.; MEITL, M.A.; SHIM, M.; ROGERS, J.A., *Nano Lett.*, 4 (2004) 2031-2035.
- [24] SIMMONS, T., *J. Am. Chem. Soc.*, 129 (2007) 10088–10089.
- [25] BRINKER, C.J.; SCHERER, G.W. (1990). *SOL-GEL SCIENCE – The Physics and Chemistry of Sol-Gel Processing*. New York, USA: Academic Press.
- [26] BOUSSAAD, S.; HARMER, M.A., *US Patent Application* 2006/0240238 A1, 2006.
- [27] FALLIS, S.; IRVIN, J.A., *US Patent*. 7108758, 2006.
- [28] MEIXNER, H.; SCHEBLER, A.; *US Patent*. 4371778, 1983.
- [29] XIANG, C.; PAN, Y.; GUO, J., *Ceram. Int.*, 33 (2007) 1293–1297.
- [30] GUO, S.; SIVAKUMAR, R.; KITAZAWA, H.; KAGAWA, Y., *Journal of the American Ceramic Society*, 90 (2007) 1667-1670.
- [31] LIU, L.Y.; YANG, Y.G.; ZHANG, Y.F., *Physica E*, 24 (2004) 343–348.
- [32] LISUNOVA, M.O.; LEOVKA, N.I.; MELEZHYYK, E.V.; BOIKO, Y.P., *J. Colloid Interface Sci.*, 299 (2006) 740–746.
- [33] AJAYAN, P.M., *Chem. Rev.*, 99 (1999) 1787-1799.
- [34] SAITO, R.; DRESSELHAUS, G.; DRESSELHAUS, M.S. (1998) *Physical Properties of Carbon Nanotubes*. London, England: Imperial College Press.
- [35] DENG, F.; ZHENG, Q.-S., *Appl. Phys. Lett.*, 92 (2008) 071902.1-071902.3

- [36] TANAKABA, K.; YAMABE, T.; FUKUI, K. (1999) *The Science and Technology of Carbon Nanotubes*. Oxford, England: Elsevier.
- [37] BRYNING, M.B.; MILKIE, D.E.; ISLAM, M.F.; KIKKAVA, J.M.; YODH, A.G., *Appl. Phys. Lett.*, 87 (2005) 161909.1-161909.3.
- [38] KANZAKI, K.; SUZUKI, S.; INOKAWA, H.; ONO, Y.; VIJAYARAGHAVAN, A.; KOBAYASHI, Y., *J. Appl. Phys.*, 101 (2007) 034317.1-034317.4.
- [39] DRESSELHAUS, M.S.; DRESSELHAUS, G.; AVOURIS, P. (2000) *Carbon Nanotubes*. Berlin, Germany: Springer-Verlag.
- [40] BANDARU, P.R., *J. Nanosci. Nanotechnol.* 7 (2007) 1239-1267.
- [41] SKÁKALOVÁ, V.; KAISER, A.B.; DETTLAFF-WEGLIKOWSKA, U.; HRNCARIKOVA, K.; ROTH S., *J. Phys. Chem. B*, 109 (2005) 7174-7181.
- [42] BEHNAM, A.; GUO, J.; URAL, A., *Journal of Applied Physics*, 102 (2007) 044313.1-044313.7
- [43] HECHT, D.; HU, L.; GRUNER, G., *Appl. Phys. Lett.*, 89 (2006) 133112.1-133112.3.
- [44] LYONS, P.E.; DE, S.; BLIGHE, F.; NICOLSI, V.; PEREIRA, L.F.C.; FERREIRA, M.S.; COLEMAN, J.N., *Journal of Applied Physics*, 104 (2008) 044302.1-044302.8.
- [45] LI, J.; MA, P.C.; CHOW, W.S.; TO, C.K.; TANG, B.Z.; KIM, J.-K., *Adv. Funct. Mater.*, 17 (2007) 3207–3215.
- [46] STAUFFER, D. (1985). *Introduction to Percolation Theory*. London, England: Taylor & Francis.
- [47] BALBERG, I.; BIBENBAUM, N.; WAGNER, N., *Phys. Rev. Lett.*, 52 (1984) 1465-1468.
- [48] FOYGEL, M.; MORRIS, R.D.; ANEZ, D.; FRENCH, S.; SOBOLEV, V.L., *Physical Review B*, 71 (2005) 104201.1-104201.8.
- [49] BAUHOFER, W.; KOVACS, J.Z., *Composites Science and Technology*, 69 (2009) 1486–1498.
- [50] BROZENA, A.H.; MOSKOWITZ, J.; SHAO, B.; DENG, S.; LIAO, H.; GASKELL, K.J.; WANG, Y.H. *J. Am. Chem. Soc.* 132 (2010) 3932–3938.
- [51] MIDGLEY, P.A.; DUNIN-BORKOWSKI, R.E., *Nature Materials*, 8 (2009) 271-280.
- [52] BELIN, T.; EPRON, F., *Materials Science and Engineering B*, 119 (2005) 105–118.
- [53] <http://www.nanointegris.com/en/technology-advantages>
- [54] REICH, S.; THOMSEN, C.; MAULTZSCH, J. (2004). *Carbon Nanotubes – Basic Concepts And Physical Properties*. Weinheim, Germany: Wiley-VCH Verlag GmbH & Co.
- [55] (a) ZÓLYOMI, V.; RUSZNYÁK, Á.; KÜRTI, J.; GALI, Á.; SIMON, F.; KUZMANY, H.; SZABADOS, Á.; SURJÁN, P.R. *phys. stat. sol. (b)* 243 (2006) 3476–3479; (b) ZÓLYOMI, V.; KOLTAI, J.; RUSZNYÁK, Á.; KÜRTI, J.; GALI, Á.; SIMON, F.; KUZMANY, H.; SZABADOS, Á.; SURJÁN, P.R. *Physical Review B*, 77 (2008) 245403.1-245403.10.
- [56] (a) KIM, D.-H.; SIM, H.-S.; CHANG, K.J. *Phys Rev B*, 64 (2001) 115409.1-115409.7; (b) KIM, D.-H.; CHANG, K.J. *Phys Rev B*, 66 (2002) 155402.1-155402.5; (c) MIYAMOTO, Y.; SAITO, S.; TOMÁNEK, D. *Phys Rev B*, 65 (2001) 041402.R1-041402.R4; (d) OKADA, S.; OSHIYAMA, A. *Phys Rev Lett*, 91 (2003) 216801.1-216801.4; (e) MAO, Y.L.; YAN, X.H.; XIAO, Y.; XIANG, J.; YANG, Y.R.; YU, H.L. *Phys Rev B*, 71 (2005) 033404.1-033404.4; (f) SONG, W.; NI, M.; JING, L.; GAO, Z.; NAGASE, S.; YU, D.; YE, H.; ZHANG, X. *Chem Phys Lett* 414 (2005) 429-433; (g) SHANAND, B.; CHO, K. *Phys Rev B*, 73 (2006) 081401.R1-081401.R4; (h) MORADIAN, R.; AZADI, S.; REFII-TABAR, H. *J. Phys.: Condens. Matter* 19 (2007) 176209.1-176209.10.
- [57] SINGER, P.M.; WZIETEK, P.; ALLOUL, H.; SIMON, F.; KUZMANY, H. *Phys Rev Lett* 95 (2005) 236403.1-236403.4.
- [58] SKÁKALOVÁ, V.; KAISER, A.B.; WOO, Y.-S.; ROTH, S., *Physical Review B*, 74 (2006) 085403.1-085403.10.
- [59] SHIOZAWA, H.; Pichler, T.; Kramberger, C.; Grüneis, A.; Knupfer, M.; Büchner, B.; Zólyomi, V.; Koltai, J.; Kürti, J.; Batchelor, D.; Kataura, H. *Phys Rev B*, 77(2008) 153402.1-153402.4.
- [60] PFEIFFER, R.; SIMON, F.; KUZMANY, H.; POPOV, V.N. *Phys Rev B*, 72 (2005) 161404R.1-161404R.4.
- [61] FLAHAUT, E., "Synthese par Voie Catalytique et Characterization de Composites Nanotubes de Carbone – Metal – Oxide. Poudres et Matériaux Denses.", Thesis; Université Paul Sabatier, 1999.
- [62] EBBESEN, T.W.; AJAYAN, P.M., *Nature*, 358 (1992) 220-222.
- [63] BETHUNE, D.S.; KLANG, C.H.; DE VRIES, M.S.; GORMAN, G.; SAVOY, R.; VAZQUEZ, J.; BEYERS, R., *Nature*, 363 (1993) 605 – 607.
- [64] GUO, T.; NIKOLAEV, P.; THESS, A.; COLBERT, D.T.; SMALLLEY, R.E., *Chem. Phys. Lett.*, 243 (1995) 49-54.
- [65] FLAHAUT, E.; BACSA, R.; PEIGNEY, A.; LAURENT, CH.; *Chem. Commun.*, (2003) 1442-1443.
- [66] VENEGONI, D.; SERP, P.; FEURER, R.; KIHN, Y.; VAHLAS, C.; KALCK, P., *J. Phys. IV France*, 12 (2002) Pr4.93-Pr4.98.
- [67] DAI, H.; WONG, E.W.; LIEBER, C.M., *Science*, 272 (1996) 523-526.

- [68] (a) NIKOLAEV, P.; THESS, A.; RINZLER, A.G.; COLBERT, D.T.; SMALLEY, R.E., *Chem. Phys. Lett.*, 313 (1999) 91–97.; (b) BRONIKOWSKI, M.J.; WILLIS, P.A.; COLBERT, D.T.; SMITH, K.A.; SMALLEY, R.E., *J. Vac. Sci. Technol. A*, 19 (2001) 1800-1805.
- [69] JORIO, A.; PIMENTA, M.A.; SOUZA FILHO, A.G.; SAITO, R.; DRESSELHAUS, G.; DRESSELHAUS, M.S., *New Journal of Physics*, 5 (2003) 139.1–139.17.
- [70] RASHEED, A.; HOWE, J.Y.; DADMUN, M.D.; BRITT, P.F., *Carbon*, 45 (2007) 1072–1080.
- [71] KIM, U.J.; FURTADO, C.A.; LIU, X.; CHEN, G.; EKLUND, P.C., *J. Am. Chem. Soc.*, 127 (2005) 15437-15445.
- [72] ITKIS, M.E.; PEREA, D.E.; NIYOGI, S.; RICKARD, S.M.; HAMON, M.A.; HU, H.; ZHAO, B.; HADDON, R.C., *Nano Lett.*, 3 (2003) 309–314.
- [73] GASS, M.H.; KOZIOL, K.K.K.; WINDLE, A.H.; MIDGLEY, P.A., *Nano Lett.*, 6 (2006) 376–379.
- [74] OSORIO, A.G. “*Funcionalização de Nanotubos de Carbono e sua Utilização como Reforço em Matriz de Hidróxiapatita*”, Diss.; Universidade Federal do Rio Grande do Sul, 2008.
- [75] GOYANES, S.; RUBIOLLO, G.R.; SALAZAR, A.; JIMENO, A.; CORCUERA, M.A.; MONDRAGON, I., *Diamond & Related Materials*, 16 (2007) 412–417.
- [76] HU, H.; YU, A.; KIM, E.; ZHAO, B.; ITKIS, M.E.; BEKYAROVA, E.; HADDON, R.C., *J. Phys. Chem. B*, 109 (2005) 11520-11524.
- [77] SKOOG, D.A.; HOLLER, F.J.; NIEMAN, T.A. (2007). *Principles of Instrumental Analysis*. 6th ed. Belmont, USA: Thomson Brooks/Cole.
- [78] KAEMPGEN, M.; DUESBERG, G.S.; ROTH, S., *Appl. Surf. Sci.*, 252 (2005) 425-429.
- [79] PARK, C.; OUNAIES, Z.; WATSON, K.A.; CROOKS, R.E.; SMITH, J.; LOWTHER, S.E.; CONNELL, J.W.; SIOCHI, E.J.; HARRISON, J.S.; CLAIR, T.L.S., *Chem.Phys.Lett.*, 364 (2002) 303-308.
- [80] <http://www.sciencedaily.com/releases/2007/07/070719011151.htm>
- [81] DE ANDRADE, M.J.; LIMA, M.D.; SKAKALOVA, V.; BERGMANN, C.P.; ROTH, S., *Physica Status Solidi (RRL) - Rapid Research Letters*, 1 (2007) 178-180.
- [82] WU, Z.C.; CHEN, Z.H.; DU, X.; LOGAN, J.M.; SIPPEL, J.; NIKOLOU, M.; KAMARAS, K.; REYNOLDS, J.R.; TANNER, D.B.; HEBARD, A.F.; RINZLER, A.G., *Science*, 305 (2004) 1273-1276.
- [83] ROWELL, M.W.; TOPINKA, M.A.; McGEHEE, M.D.; PRALL, H.J.; DENNLER, G.; SARICIFTCI, N.S.; HU, L.B.; GRÜNER, G., *Appl. Phys. Lett.*, 88 (2006) 233506.1-233506.3.
- [84] STAR, A.; LU, Y.; BRADLEY, K.; GRÜNER, G., *Nano Lett.*, 4 (2004) 1587-1591.
- [85] NG, M.H.A.; HARTADI, L.T.; TAN, H.; POA, C.H.P., *Nanotechnology*, 19 (2008) 205703.1-205703.5.
- [86] ZHANG, M.; FANG, S.; ZAKHIDOV, A.A.; LEE, S.B.; ALIEV, A.E.; WILLIAMS, C.D.; ATKINSON, K.R.; BAUGHMAN, R.H. *Science*, 309 (2005) 1215-1219.
- [87] GERDES, S.; ONDARÇUHU, T.; CHOLET, S.; JOACHIM, C., *Europhys. Lett.*, 48 (1999) 292-298.
- [88] LIMA, M.D.; de ANDRADE, M.J.; SKAKALOVA, V.; NOBRE, F.; BERGMANN, C.P.; ROTH, S., *Physica Status Solidi (RRL) - Rapid Research Letters*, 1 (2007) 165-167.
- [89] LAURENT, Ch.; PEIGNEY, A. (2004). *Encyclopedia of Nanoscience and Nanotechnology*. H. S. Nalwa, Am. Sci. Pub. 1: 635-653.
- [90] PEIGNEY, A.; LAURENT, Ch. (2006). *Ceramic Matrix Composites: Microstructure-Property Relationship*. Ed.I. Cambridge, England: M. Low, Woodhead Publishing Limited.
- [91] LOISEAU, A.; LAUNOIS, P.; PETIT, P.; ROCHE, S.; SALVETAT, J.P. (2006). *Understanding Carbon Nanotubes from Basics to Application*. Heidelberg, Germany: Springer.
- [92] WOODMAN, R.H.; KLOTZ, B.R.; DOWDING, R.J., *Ceramics International*, 31 (2005) 765–768.
- [93] GAVALAS, V.G.; ANDREWS, R.; BHATTACHARYYA, D.; BACHAS, L.G., *Nanoletters*, 1 (2001) 719-721.
- [94] FLAHAUT, E.; PEIGNEY, A.; LAURENT, Ch.; MARLIÈRE, Ch.; CHASTEL, F.; ROUSSET, A., *Acta Mater.*, 48 (2000) 3803–3812.
- [95] CHEN, Q.; SALTIEL, C.; MANICKAVASAGAM, S.; SCHADLER, L.S.; SIEGEL, R.W.; YANG, H., *Journal of Colloid and Interface Science*, 280 (2004) 91-97.
- [96] ROUSE, J.H. *Langmuir*, 21 (2005) 1055-1061.
- [97] (a) TSETSERIS, L.; PANTELIDES, S.T., *Phys. Rev. Lett.*, 97, (2006) 266805.1- 266805.4.; (b) WOJDEL, J.C.; BROMLEY, S.T., *J. Phys. Chem. B*, 109 (2005) 1387-1391.
- [98] CALLISTER, W.D.; RETHWISCH, D.G., *Fundamentals of Materials Science and Engineering – an Integrated Approach*. Wiley. Danvers, 2007.
- [99] DE ANDRADE, M.J.; LIMA, M.D.; STEIN, L.; BERGMANN, C.P.; ROTH, S., *Phys. Status Solidi B*, 244 (2007) 4218-4222.
- [100] (a) XIANG, C.; PAN, Y.; LIU, X.; SUN, X.; SHI, X.; GUO, J., *Appl. Phys. Lett.*, 87 (2005) 123103.1-123103.3.; (b) XIANG, C.; SHI, X.; PAN, Y.; GUO, J., *Key Eng. Mater.*, 280-283 (2005)

- 123-126.; (c) NING, J.; ZHANG, J.; PAN, Y.; GUO, J., *Ceram. Int.*, 20 (2004) 63-67.; (d) NING, J.; ZHANG, J.; PAN, Y.; GUO, J., *Materials Science and Engineering A*, 357 (2003) 392-396.
- [101] DYKE, C.A.; TOUR, J.M. *J. Phys. Chem. A*, 108 (2004) 11151-11159.
- [102] DE ANDRADE, M.J.; LIMA, M.D.; BERGMANN, C.P.; RAMMINGER, G.O.; BALZARETTI, N.M.; COSTA, T.M.H.; GALLAS, M.R., *Nanotechnology*, 19 (2008) 265607.1.
- [103] PASCUAL, M.J.; DURÁN, A.; PRADO, M.O.; ZANOTTO, E.D., *J. Am. Ceram. Soc.*, 88 (2005) 1427-1434.
- [104] TOKITA, M., *American Ceramic Society Bulletin*, 85 (2006) 32-34.
- [105] OLEVSKY, E.A.; KANDUKURI, S.; FROYEN, L., *Journal of Applied Physics*, 102 (2007) 114913.1-114913.12.
- [106] GROZA, J.R.; ZAVALIANGOS, A., *Materials Science and Engineering A*, 287 (2000) 171-177.
- [107] MAIZZA, G.; GRASSO, S.; SAKKA, Y.; NODA, T.; OHASHI, O., *Science and Technology of Advanced Materials*, 8 (2007) 644-654.
- [108] VANMEENSEL, K.; LAPTEV, A.; HENNICKE, J.; VLEUGELS, J.; VAN DER BIEST, O., *Acta Materialia*, 53 (2005) 4379-4388.
- [109] YAMAZAKI, K.; RISBUD, S.H.; AOYAMA, H.; SHODA, K., *Journal of Materials Processing Technology*, 56 (1996) 955-965.
- [110] CHEN, W.; ANSEMI-TAMBURINI, U.; GARAY, J.E.; GROZA, J.R.; MUNIR, Z.A., *Materials Science and Engineering A*, 394 (2005) 132-138.
- [111] ANSEMI-TAMBURINI, U.; GARAY, J.E.; MUNIR, Z.A., *Materials Science and Engineering A*, 407 (2005) 24-30.
- [112] CHAIM, R., *Materials Science and Engineering A*, 443 (2007) 25-32.
- [113] SONG, S.N.; WANG, X.K.; CHANG, R.P.H.; KETTERSON, J. B., *Phys. Rev. Lett.* 72 (1994) 697-700.
- [114] ANDO, Y.; ZHAO, X.; SHIMOYAMA, H.; SAKAI, G.; KANETO, K., *Inter. J. Inorg. Mater.*, 1 (1999) 77-82.
- [115] LANGER, L.; BAYOT, V.; GRIVEI, E.; ISSI, J.; HEREMANS, J.P.; OLK, C.H.; STOCKMAN, L.; VAN HAESSENDONCK, C.; BRUYNSERAEDE, Y., *Phys. Rev. Lett.*, 76 (1996) 479-482.
- [116] THESS, A.; LEE, R.; NIKOLAEV, P.; DAI, H.; PETIT, P.; ROBERT, J.; XU, C.; LEE, Y.H.; KIM, S.G.; RINZLER, A.G.; COLBERT, D.T.; SCUSERIA, G.; TOMÁNEK, D.; FISCHER, J.E.; SMALLEY, R.E., *Science*, 273 (1996) 483-487.
- [117] ZHANG, M.; ATKINSON, K.R.; BAUGHMAN, R.H., *Science*, 306 (2004) 1358-1361.
- [118] LAURENT, Ch.; CHEVALLIER, G.; WEIBEL, A.; PEIGNEY, A.; ESTOURNES, C., *Carbon*, 46 (2008) 1812-1816.
- [119] BULDUM, A.; LU, J.P. *Phys. Rev. B*, 63 (2001) 161403.1-161403.4.
- [120] CELZARD, A.; McRAE, E.; DELEUZE, C.; DUFORT, M.; FURDIN, G.; MARECHE, J.F., *Physical Review B*, 53 (1996) 6209-6214.
- [121] CLINGERMAN, M.L.; WEBER, E.H.; KING, J.A.; SCHULZ, K.H., *Journal of Applied Polymer Science*, 88 (2003) 2280-2299.
- [122] HWANG, J.; MUTH, J.; GHOSH, T., *Journal of Applied Polymer Science*, 104 (2007) 2410-2417
- [123] ARLEN, M.J.; WANG, D.; JACOBS, J.D.; JUSTICE, R.; TRIONFI, A.; HSU, J.W.P.; SCHAFFER, D.; TAN, L.-S.; VAIA, R.A., *Macromolecules*, 41 (2008) 8053-8062.
- [124] BRYNING, M.B.; ISLAM, M.F.; KIKKAWA, J.M.; YODH, A.G., *Advanced Materials*, 17 (2005) 1186-1191.
- [125] McLACHLAN, D.S.; CHITEME, C.; PARK, C.; WISE, K.E.; LOWTHER, S.E.; LILLEHEI, P.T.; SIOCHI, E.J.; HARRISON, J.S., *J. Polym. Sci., Part B: Polym. Phys.*, 43 (2005) 3273-3287.
- [126] GARCIA, F.L.; ESTOURNÈS, C.; PEIGNEY, A.; WEIBEL, A.; FLAHAUT, E.; LAURENT, Ch., *Scripta Materialia*, 60 (2009) 741-744.
- [127] BARRAU, S.; DEMONT, P.; PEIGNEY, A.; LAURENT, Ch.; LACABANNE, C., *Macromolecules*, 36 (2003) 5187-5194.
- [128] ALMASRI, A.; OUNAIES, Z.; KIM, Y.S.; GRUNLAN, J., *Macromol. Mater. Eng.*, 293 (2008) 123-131.
- [129] SANDLER, J.K.W.; KIRK, J.E.; KINLOCH, I.A.; SHAFFER, M.S.P.; WINDLE, A.H., *Polymer*, 44(2003) 5893-5899.
- [130] HU, G.J.; ZHAO, C.G.; ZHANG, S.M.; YANG, M.S.; WANG, Z.G., *Polymer*, 47 (2006) 480-488.
- [131] HARRIS, P.J.F. (1999). *Carbon Nanotubes and Related Structures*. Cambridge, UK: Cambridge University Press.
- [132] (a) COLLINS, P.G.; AVOURIS, P., *Scientific American*, 283 (2000) 62-69.; (b) HONG, S.; MYUNG, S., *Nature Nanotechnology*, 2 (2007) 207-208.
- [133] COLLINS, P.G.; ARNOLD, M.S.; AVOURIS, P., *Science*, 292 (2001) 706-709.
- [134] (a) KRUPKE, R.; HENNRICH, F.; LÖHNESEN, H.; KAPPES, M.M., *Science*, 301 (2003) 344-

- 347.; (b) ZHENG, M.; JAGOTA, A.; SEMKE, E.D.; DINER, B.A.; McCLEAN, R.S.; LUSTIG, S.R.; RICHARDSON, R.E.; TASSI, N.G., *Nat. Mater.*, 2 (2003) 338-342.; (c) CHATTOPADHYAY, D.; GALESKA, I.; PAPADIMITRAKOPOULOS, F., *J. Am. Chem. Soc.*, 125 (2003) 3370-3375.
- [135] ARNOLD, M.S.; GREEN, A.A.; HULVAT, J.F.; STUPP, S.I.; HERSAM, M.C., *Nature Nanotechnology*, 1 (2006) 60-65.
- [136] KAEMPGEN, M., „Eigenschaften Und Anwendungen Von Netzwerken Aus Kohlenstoff-Nanoröhren“ Thesis. University of Stuttgart, 2006.
- [137] THOSTENSON, E. T.; REN, Z.; CHOU, T.-W., *Composites Science and Technology*, 61 (2001) 1899-1912.
- [138] HENNRICH, F.; KRUPKE, R.; ARNOLD, K.; STIITZ, J. A. R.; LEBEDKIN, S.; KOCH, T.; SCHIMMEL, T.; KAPPES, M. M., *Journal of Physical Chemistry B*, 111 (2007) 1932-1937.
- [139] MARSHALL, M.W.; POPA-NITA S.; SHAPTER, J.G., *Carbon*, 44 (2006) 1137-1141.
- [140] YANG, C.M.; PARK, J.S.; AN, K.H.; LIM, S.C.; SEO, K.; KIM, B.; PARK, K.A.; HAN, S.; PARK, C.Y.; LEE, Y.H., *Jour. Phys. Chem. B*, 109 (2005) 19242-19248.
- [141] BOSE, S.; BHATTACHARYYA, A.R.; BONDRE, A.P.; KULKARNI, A.R.; TSCHKE, P.P., *Journal of Polymer Science: Part B: Polymer Physics*, 46 (2008) 1619-1631.
- [142] LARA, I., “Estudo teórico da influência de grupos carboxílicos em nanotubos de carbono” In: I WORKSHOP CNANO: Porto Alegre, 27-28 august 2009.
- [143] BARROS, E.B.; SOUZA FILHO, A.G.; LEMOS, V.; FILHO, J.M.; FAGAN, S.B.; HERBST, M.H.; ROSOLEN, J.M.; LUENGO, C.A.; HUBER, J.G., *Carbon*, 43 (2005) 2495–2500.
- [144] BROADBENT, S.R.; HAMMERSLEY, J.M., *Proc. Camb. Phil. Soc. LIII* (1957) 629.
- [145] BALBERG, I.; ANDERSON, CH.; ALEXANDER, S.; WAGNER, N., *Phys. Rev. B*, 30 (1984) 3933–3943.
- [146] GOJNY, F.H.; WICHMANN, M.H.G.; FIEDLER, B.; KINLOCH, I.A.; BAUHOFFER, W.; WINDLE, A.H.; SCHULTE, K., *Polymer*, 47 (2006) 2036-2045.
- [147] (a) DELANEY, P.; CHOI, H.-J.; IHM, J.; LOUIE S.G.; COHEN M.L., *Nature*, 391 (1998) 466-468.; (b) CHARLIER, J.-C.; GONZE, X.; MICHENAUD, J.-P., *Europhys. Lett.*, 29 (1995) 43-48.; (c) REICH, S.; THOMSEN, C.; ORDEJON, P., *Phys. Rev. B*, 65 (2002) 155411.1-155411.11.; (d) OUYANG, M.; HUANG, J.-L.; CHEUNG, C.L.; LIEBER, C.M., *Science*, 292 (2001) 702-705.
- [148] FUHRER, M.S.; NYGARD, J.; SHIH, L.; FORERO, M.; YOON, Y.G.; MAZZONI, M.S.; CHOI, H.J.; IHM, J.; LOUIE, S.G.; ZETTL, A.; MCEUEN, P.L., *Science*, 21 (2000) 494-497.
- [149] KWON, Y.-K.; TOMÁNEK, D., *Phys. Rev. B*, 58 (1998) R16001-R16004.
- [150] VIGOLO, B.; COULON, C.; MAUGEY, M.; ZAKRI, C.; POULIN, P., *Science*, 309 (2005) 920-923.
- [151] PEIGNEY, A., *Nature Materials*, 2 (2003) 15-16.
- [152] HULL, D.; CLYNE, T.W. (1996). *An Introduction to Composite Materials*, 2nd ed. Cambridge, UK: Cambridge University Press.
- [153] FANG, F.; ZHANG, Y.F., *J. Mater. Sci.*, 40 (2005) 2979-2980.
- [154] FLAHAUT, E.; BACSA, R.; PEIGNEY, A.; LAURENT, CH., *Chem. Commun.*, (2003) 1442-1443.
- [155] (a) GROSSIORD, N; REGEV, O; LOOS, J; MEULDIJK, J; KONING, CE *Anal.Chem.*, 77 (2005) 5135-5139; (b) CHENG, Q; DEBNATH, S; GREGAN, E; BYRNE, HJ. *J.Phys.Chem.C*, 114 (2010) 8821–8827; (c) LU, K.L.; LAGO, R.M.; CHEN, Y.K.; GREEN, M.L.H.; HARRIS, P.J.F.; TSANG, S.C. *Carbon*, 34 (1996) 814-816; (d) HENNRICH, F.; KRUPKE, R.; ARNOLD, K.; STIITZ, J.A.R.; LEBEDKIN, S.; KOCH, T.; SCHIMMEL, T.; KAPPES, M.M. *Journal of Physical Chemistry B*, 111 (2007) 1932-1937.
- [156] LIMA, M.D.; de ANDRADE, M.J.; BERGMANN, C.P.; ROTH, S., *J. Mater. Chem.*, 18 (2008) 776-779.
- [157] SOMIYA, S. (1989). *Advanced Technical Ceramics*. San Diego, USA: Academic Press Inc. pp 51.
- [158] LIMA, M.D.; de ANDRADE, M.J.; SKAKALOVA, V.; BERGMANN, C.P.; ROTH, S., *J. Mater. Chem.*, 17 (2007) 4846-4853.
- [159] MAUTZSCH, J.; REICH, S.; THOMSEN, C.; WEBSTER, S.; CZERW, R.; CARROLL, D.L.; VIEIRA, S.M.C.; BIRKETT, P.R.; REGO, C.A., *Appl. Phys. Lett.*, 81 (2002) 2647-2649.
- [160] SKAKALOVA, V.; DETTLAFF-WEGLIKOWSKA, U.; ROTH, S., *Synthetic Metals*, 152 (2005) 349-352.
- [161] BALBERG, I., *Physical Review B*, 31 (1985) 4053-4055.
- [162] FISCHER, J.E.; ZHOU, W.; VAVRO, J.; LLAGUNO, M.C.; GUTHY, C.; HAGGENMUELLER, R.; CASAVANT, M.J.; WALTERS, D.E.; SMALLEY, R.E., *Appl. Phys. Lett.*, 93 (2000) 2157-2163.
- [163] KO, H.; PELESHANKO, S.; TSUKRUK, V.V., *J. Phys. Chem. B*, 108 (2004) 4385-4393.
- [164] TENENT, R.C.; BARNES, T.M.; BERGESON, J.D.; FERGUSON, A.J.; TO, B.; GEDVILAS, L.M.; HEBEN, M.J.; BLACKBURN, J.L., *Advanced Materials*, 21 (2009) 3210-3216.

- [165] FLAHAUT, E.; PEIGNEY, A.; BACSA, W.S.; BACSA, R.R.; LAURENT, CH., *J. Mater. Chem.*, 14 (2004) 646-653.
- [166] FLAHAUT, E.; LAURENT, CH.; PEIGNEY, A., *Carbon*, 43 (2005) 375-383.
- [167] CHIANG, I.W.; BRINSON, B.E.; SMALLEY, R.E.; MARGRAVE, J.L.; HAUGE, R.H., *J. Phys. Chem. B*, 105 (2001) 1157-1161.
- [168] OSSWALD, S.; FLAHAUT, E. GOGOTSI, Y., *Chem. Mater.*, 18 (2006) 1525-1533.
- [169] KIM, B.; PARK, H.; SIGMUND, W.M., *Colloids and Surfaces A: Physicochem. Eng. Aspects*, 256 (2005) 123-127.
- [170] SUN, J.; GAO, L.; LI, W. *Chem. Mater.*, 14 (2002) 5169-5172.
- [171] JIANG, L.; GAO, L.; SUN, J., *Journal of Colloid and Interface Science*, 260 (2003) 89-94.
- [172] LIU, J.; RINZLER, A.G.; DAI, H.; HAFNER, J.H.; BRADLEY, R.K.; BOUL, P.J.; LU, A.; IVERSON, K. SHELIMOV, C.B. HUFFMAN, F. RODRIGUEZ-MACIAS, Y.-S. SHON, T.R. LEE, D.T. COLBERT, T.; SMALLEY, R.E., *Science*, 280 (1998)1253-1256.
- [173] DATSYUK, V.; KALYVA, M.; PAPAGELIS, K.; PARTHENIOS, J.; TISIS, D.; SIOKOU, A.; KALLITSIS, I.; GALIOTIS, C., *Carbon*, 46 (2008) 833-840.
- [174] DUJARDIN, E.; EBBESEN, T.W.; KRISHNAN, A.; TREACY, M.M.J., *Adv. Mater.* 10 (1998) 611-613.
- [175] BARROS, E.B.; SON, H.; SAMSONIDZE, GE.G.; SOUZA FILHO, A.G.; SAITO, R.; KIM, Y.A.; MURAMATSU, H.; HAYASHI, T., *Phys. Rev. B*, 76 (2007) 045425.1.- 045425.11.
- [176] KUBOTA, S.; NISHIKIORI, H.; TANAKA, N.; ENDO, M.; FUJII, T., *J. Phys. Chem. B*, 109 (2005) 23170-23174.
- [177] DUCLAUX, L., *Carbon*, 40 (2002) 1751-1764.
- [178] HELLER, D.A.; BARONE, P.W.; STRANO, M.S., *Carbon*, 43 (2005) 651-673.
- [179] MUKHOPADHYAY, K.; DWIVEDI, C.D.; MATHUR, G.N., *Carbon*, 40 (2002) 1369-1383.
- [180] (a) HALUŠKA, M.; OBERGFELL, D.; MEYER, J.C.; SCALIA, G.; ULBRICHT, G.; KRAUSS, B.; CHAE, D.H.; LOHMANN, T.; LEBERT, M.; KAEMPGEN, M.; HULMAN, M.; SMET, J.; ROTH, S.; VON KLITZING, K., *Phys. Stat. Sol. B*, 244 (2007) 4143-4146.; (b) COSTA, S.; BOROWIAK-PALEN E., *Acta Physica Polonica A*, 116 (2009) 32-35.
- [181] MAYERHÖFER, T.G.; SHEN, Z.; LEONOVA, E.; EDEN, M.; KRILTZ, A.; POPP, J., *Journal of Solid State Chemistry*, 181 (2008) 2442-2447.
- [182] LUTZ, T.; ESTOURNES, C.; MERLE J.C.; GUILLE J.L., *Journal of Alloys and Compounds*, 262-263 (1997) 438-442.
- [183] GUO, S.; SIVAKUMAR, R.; KAGAWA, Y., *Adv. Eng. Mat.*, 9 (2007) 84-87.
- [184] SIVAKUMAR, R.; GUO, S.; NISHIMURA, T.; KAGAWA, Y., *Scripta Materialia*, 56 (2007) 265-268.
- [185] PASCUAL, M.J.; DURÁN, A.; PRADO, M.O.; ZANOTTO, E.D., *J. Am. Ceram. Soc.*, 88 (2005) 1427-1434.
- [186] JUNG DE ANDRADE, M.; WEIBEL, A.; LAURENT, Ch.; ROTH, S.; PÉREZ BERGMANN, C.; ESTOURNÈS, C.; PEIGNEY, A., *Scripta Materialia*, 61 (2009) 988-991.
- [187] PUECH, P.; FLAHAUT, E.; SAPELKIN, A.; HUBEL, H.; DUNSTAN, D.J.; LANDA, G.; BACSA, W.S. *Phys. Rev. B*, 73 (2006) 23408.1-23408-4.
- [188] LIMA, M.D., "Síntese de Nanotubos de Carbono por Deposição Química de Vapor Catalisada: Correlação entre Parâmetros de Processo e Características Estruturais", Thesis, Universidade Federal do Rio Grande do Sul, 2007.
- [189] YANG, C.M.; PARK, J.S.; AN, K.H.; LIM, S.C.; SEO, K.; KIM, B.; PARK, K.A.; HAN, S.; PARK, C.Y.; LEE, Y.H., *J. Phys. Chem. B*, 109 (2005) 19242-19248.
- [190] BOCCACCINI, A.R.; THOMAS, B.J.C.; BRUSATIN, G.; COLOMBO, P., *J. Mater. Sci.*, 42 (2007) 2030-2036.
- [191] RUL, S.; LEFEVRE-SCHLICK, F.; CAPRIA, E.; LAURENT, Ch.; PEIGNEY, A., *Acta Materialia*, 52 (2004) 1061-1067.
- [192] ZHAN, G.D.; KUNTZ, J.D.; GARAY, J.E.; MUKHERJEE, A.K., *Appl. Phys. Lett.*, 83 (2003) 1228-1230.
- [193] INAM, F.; YAN, H.; REECE, M.J.; PEIJS, T., *Nanotechnology*, 19 (2008) 195710.1-195710.5.
- [194] INAM, F.; YAN, H.; JAYASEELAN, D.D.; PEIJS, T.; REECE, M.J., *Journal of the European Ceramic Society*, 30 (2009) 977-985.
- [195] KUMARI, L.; ZHANG, T.; DU, G.H.; LI, W.Z.; WANG, Q.W.; DATYE, A.; WU, K.H., *Ceramics International*, 35 (2009) 1775-1781.
- [196] AHMAD, K. and PAN, W., *Composites Science and Technology*, 69 (2009) 1016-1021.
- [197] SHI, S.L.; LIANG, J., *J. Am. Ceram. Soc.*, 89 (2006) 3533-3535.
- [198] HUANG, X.W.; WANG, S.W.; ZHAO S.K.; HUANG, X.X., *Materials Research Bulletin*, 37 (2002) 1709-1719.

- [199] PEIGNEY, A.; LEGORRETA GARCIA, F.; ESTOURNES, C.; WEIBEL, A.; LAURENT, CH., *Carbon*, 48 (2010) 1952–1960.
- [200] SANTANACH, J.G.; “*Frittage Reactif et Consolidation par Spark Plasma Sintering d’alumine Nanometriques et de Nanocomposites Metal-Alumine ou Nanotubes de Carbone-Metal-Alumine*”. Thesis, Université Paul Sabatier, 2009.
- [201] PEIGNEY, A.; FLAHAUT, E.; LAURENT, C.; CHASTEL, F.; ROUSSET, A., *Chem. Phys. Lett.*, 352 (2002) 20-25.
- [202] ZHU, Y.F.; SHI, L.; ZHANG, C.; YANG, X.Z.; LIANG, J., *Appl. Phys. A- Mater. Sci. Process.*, 89 (2007) 761-767.

Etude des propriétés électriques de réseaux bi- et tri-dimensionnels de nanotubes de carbone

Des réseaux de nanotubes de carbone (CNTs) en deux ou trois dimensions (2D- et 3D-CNTNs) ont été préparés respectivement sur substrat de silice amorphe et dans une matrice silice. Plusieurs types de CNTs (mono-, double- et multi-parois, respectivement SWCNTs, DWCNTs et MWCNTs) ont été caractérisés par microscopie électronique à transmission, spectroscopie Raman et analyse élémentaire du carbone, et leurs aptitudes à former un réseau percolant ont été comparées par mesure de la conductivité électrique de suspensions dynamiques de ces CNTs dans le chloroforme. La conductivité des suspensions de SWCNTs et de DWCNTs obéit à la loi de puissance de la théorie de percolation, avec un exposant proche de la valeur théorique d'un réseau 3D. Celle des suspensions de SWCNTs présentent une conductivité normalisée maximale (3.08 S.cm²/g) tandis que celle des suspensions de DWCNTs présente le plus faible seuil de percolation (0.002-0.06 vol.%) ce qui a conduit à choisir les SWCNTs pour la préparation des 2D-CNTNs et les DWCNTs pour la préparation des nanocomposites CNT-silice (3D CNTNs).

Les 2D-CNTNs ont été préparés par dépôt de suspensions aqueuses de SWCNTs contenant du dodecyl sulfate de sodium sur de la silice amorphe, par quatre techniques différentes : trempage, filtration, spray et dépôt électrophorétique. Les 2D-CNTNs forment un réseau percolant dont la conductivité électrique obéit à la loi de puissance, avec un exposant d'environ 1,29, ce qui est en bon accord avec les prédictions théoriques. Les dépôts effectués par trempage et les dépôts électrophorétiques conduisent aux films les plus lisses et peuvent constituer une option intéressante pour des applications dans les cellules solaires. La conductance de surface et la transparence obtenues dans l'UV laissent espérer des applications possibles dans les écrans d'affichage, les écrans tactiles, les tubes cathodiques et les films destinés à dissiper les charges électrostatiques.

Les nanocomposites CNT-silice (3D-CNTNs) ont été préparés par sol-gel, en utilisant des DWCNTs qui furent d'abord soumis à un traitement doux de fonctionnalisation, leur dispersion étant réalisée par sonication avec une sonde. Les matériaux ont été ensuite complètement densifiés par "spark-plasma sintering". Les états de dispersion des CNTs ont été évalués par microscopie électronique à balayage à émission de champ et corrélés aux propriétés électriques. La comparaison de deux variantes de la méthode de préparation (i.e.: DWCNT séchés ou non séchés après leur fonctionnalisation) a conduit à une bonne corrélation entre les états de dispersion (présence et taille des agrégats de CNTs) et les seuils de percolation. Pour la voie sèche, la percolation intervient pour seulement 0,35 vol.% DWCNT, ce qui est plus faible que les valeurs publiées pour les nanocomposites CNT-silice. Pour la voie humide, le matériau le plus conducteur présente une conductivité électrique (1,56 S/cm) plus élevée que celles publiées pour des matériaux similaires. Bien que l'état de dispersion des CNTs puisse encore être amélioré, la conductivité électrique obtenue pour ces nanocomposites est déjà suffisamment élevée pour leur utilisation pour évacuer les charges électrostatiques ou comme éléments chauffants.

Mots clés : Nanotubes de carbone, nanocomposites, silice, Spark Plasma Sintering, percolation, propriétés électriques.

Study of electrical properties of 2- and 3-dimensional carbon nanotubes networks

Two and three dimensional carbon nanotube networks (2D- and 3D-CNTNs) were prepared over silica glass substrate and in silica matrix, respectively. Several types of CNTs (single-, double- and multi-walled carbon nanotubes, SWCNTs, DWCNTs and MWCNTs, respectively) were characterized by transmission electron microscopy, Raman spectroscopy and carbon analysis, while their aptitudes to form a percolating network were compared by measurement of their electrical conductivity in dynamic suspensions in chloroform. The conductivity of SWCNTs and DWCNTs suspensions well follow the power law of the percolation theory, with an exponent close to the theoretical value of a 3D network. The SWCNTs suspensions present the higher maximum normalized conductivity (3.08 S.cm²/g) whereas the DWCNTs suspensions present the lower percolation thresholds (0.002-0.06 vol.%) which led to choose SWCNTs for the preparation of 2D-CNTNs and DWCNTs for the preparation of CNT-silica nanocomposites (3D-CNTNs).

To produce 2D-CNTNs, SWCNTs aqueous suspensions containing sodium dodecyl sulphate were deposited over amorphous silica substrates using four different techniques : dip-coating, filtration, spray-coating and electrophoretic deposition. Most of the 2D-CNTNs formed a percolating network whose electrical conductivity well followed the power law, with an exponent around 1.29, which is in agreement with theoretical predictions. Dip-coating and electrophoretic deposition provided the smoothest CNTNs and might be an interesting option for solar cell applications. The obtained characteristics of surface conductance and transparency in the UV also demonstrated their possible applications in displays, touch screens, shielding in cathode tubes and electrostatic dissipation.

CNT-silica matrix nanocomposites (3D-CNTNs) were prepared by the sol-gel route, using DWCNTs which were previously submitted to a mild functionalization, their dispersion being carried out by probe sonication. The materials were fully densified by spark-plasma sintering. The dispersion state of CNTs was evaluated by field emission scanning electron microscopy and correlated with the electrical properties. The comparison of two variations in the preparation route (ie: the DWCNT were dried or not after their functionalization) led to a good correlation between the dispersions states (presence and size of CNTs aggregates) and the percolation thresholds. For the "Dry" route, the percolation operates at only 0.35 vol.% DWCNT, which is lower than the values reported for CNT-silica nanocomposites. For the "Wet" one, the more conductive material shows an electrical conductivity (1.56 S/cm) higher than the values reported for similar materials. In spite that the dispersion of CNTs could be still improved, the achieved electrical conductivity of these nanocomposites is still high enough for their use in antielectrostatic or heating applications.

Keywords : Carbon nanotubes, nanocomposites, silica, Spark Plasma Sintering, percolation, electrical properties.